“Study of near-borehole thermo-hydro-mechanical processes”

Von der Fakultät für Georessourcen und Materialtechnik der
Rheinisch-Westfälischen Technischen Hochschule Aachen

zur Erlangung des akademischen Grades eines

Doktors der Naturwissenschaften

genehmigte Dissertation

vorgelegt von

Wen Luo, M. Sc.

Berichter: Univ.-Prof. Dr. rer. nat. Florian Amann
Prof. Dr. Phil Vardon

Tag der mündlichen Prüfung: 25.02.2026

This doctoral research has been carried out in the context of an agreement on joint doctoral supervision between Delft University of Technology, the Netherlands, and RWTH Aachen University, Germany.

Diese Dissertation ist auf den Internetseiten der
Universitätsbibliothek online verfügbar

STUDY OF NEAR-BOREHOLE THERMO-HYDRO-MECHANICAL PROCESSES

STUDY OF NEAR-BOREHOLE THERMO-HYDRO-MECHANICAL PROCESSES

Dissertation

for the purpose of obtaining the degree of doctor
at Delft University of Technology
by the authority of the Rector Magnificus, Prof. dr. ir. H. Bijl,
chair of the Board for Doctorates
to be defended publicly on Wednesday 25th February 2026, at 12:30

by

Wen LUO

This dissertation has been approved by the promotors

Composition of the doctoral committee:

Rector Magnificus,	chairperson
Prof. dr. P. J. Vardon,	Delft University of Technology, promotor
Prof. dr. rer. nat. F. Amann,	RWTH Aachen, Germany, promotor
Dr. ir. G. G. Drijkoningen,	Delft University of Technology, promotor
Dr. ir. A. C. Dieudonné,	Delft University of Technology, copromotor

Independent members:

Prof. dr. D. F. Bruhn,	Delft University of Technology
Prof. dr. F. Wellmann,	RWTH Aachen, Germany
Prof. dr. F. M. Wagner,	RWTH Aachen, Germany
Prof. dr. R. Fuentes,	RWTH Aachen, Germany
Prof. dr. M. A. Hicks,	Delft University of Technology, reserve member

This doctoral research has been carried out in the context of an agreement on joint doctoral supervision between RWTH Aachen University, Germany, and Delft University of Technology, the Netherlands.







Keywords: Geothermal energy, thermo-hydro-mechanical processes, cohesive interface element, soft stimulation, micro-seismic monitoring, distributed acoustic sensing, source mechanism

Printed by: Gildeprint Drukkerijen - Enschede

Copyright © 2026 by Wen Luo
Email: W.Luo@tudelft.nl

ISBN: 978-94-6518-247-6

An electronic version of this dissertation is available at
http://repository.tudelft.nl/.

To my beloved family and everyone who helped me

CONTENTS

Summary xi

Samenvatting xiii

Zusammenfassung xv

1 Introduction 1
- 1.1 Geothermal energy in the world and in the Netherlands . . . 2
- 1.2 Problem statement . . . 3
- 1.3 Modelling cyclic thermo-hydro-mechanical processes . . . 6
  - 1.3.1 Near-borehole coupled THM processes . . . 6
  - 1.3.2 Numerical methods for modelling discontinuity problems . . . 7
  - 1.3.3 Cohesive zone model with fatigue damage variable . . . 8
- 1.4 Micro-seismic monitoring using distributed acoustic sensing . . . 10
  - 1.4.1 Micro-seismic monitoring methods . . . 10
  - 1.4.2 Source localisation and mechanisms . . . 12
- 1.5 EASYGO project . . . 14
- 1.6 Motivation and research objectives . . . 15
- 1.7 Outline of the thesis . . . 15

2 Literature review on the mechanisms causing injectivity changes in geothermal projects 17
- 2.1 Introduction . . . 18
- 2.2 History and regulation of re-injection of geothermal fluids . . . 18
- 2.3 Injectivity decline during re-injection . . . 22
  - 2.3.1 Physical processes . . . 25
  - 2.3.2 Chemical processes . . . 28
  - 2.3.3 Biological processes . . . 29
  - 2.3.4 Strategy to avoid and recover injectivity decline . . . 31
- 2.4 Injectivity enhancement during re-injection . . . 32
  - 2.4.1 Individual mechanisms . . . 35
  - 2.4.2 Combined mechanisms . . . 37
- 2.5 Conclusion . . . 38

3 Coupled THM cohesive interface element: Theory, verification and qualitative validation 39
- 3.1 Introduction . . . 40
- 3.2 Numerical model . . . 40
  - 3.2.1 Modelling approach . . . 40
  - 3.2.2 Governing equations for the continuum porous medium . . . 41
  - 3.2.3 Governing equations for the discontinuities . . . 42

3.3 Verification against analytical solutions . . . 46
3.3.1 Thermo-hydraulic coupling in a single fracture . . . 46
3.3.2 Hydro-mechanical processes - KGD model . . . 50
3.4 Validation . . . 52
3.4.1 Recap of the experiment . . . 52
3.4.2 Numerical model . . . 55
3.4.3 Comparison between simulation and experimental results . . . 56
3.4.4 Sensitivity analysis . . . 60
3.5 Conclusions . . . 63

4 Simulation of fatigue damage under cyclic coupled thermo-hydro-mechanical processes 65
4.1 Introduction . . . 66
4.2 New elasto-damage law . . . 68
4.3 Validation against cyclic Brazilian test . . . 70
4.3.1 Description of the experiment . . . 70
4.3.2 Numerical model . . . 71
4.3.3 Numerical simulation of the static Brazilian test . . . 73
4.3.4 Numerical simulation of the cyclic Brazilian test . . . 76
4.4 Validation against cyclic hydraulic fracturing test . . . 76
4.4.1 Description of the experiment . . . 76
4.4.2 Numerical model . . . 80
4.4.3 Numerical simulation of the monotonic injection tests . . . 80
4.4.4 Simulation results of the cyclic injection tests . . . 81
4.5 Validation against cyclic thermo-hydraulic fracturing test . . . 83
4.5.1 Description of the experiment . . . 83
4.5.2 Numerical model . . . 85
4.5.3 Results and discussion . . . 87
4.6 Conclusions . . . 89

5 Numerical study of the soft stimulation scenarios 91
5.1 Introduction . . . 92
5.2 Synthetic reservoir with clogged near-borehole zone . . . 93
5.3 Method . . . 94
5.3.1 Numerical model . . . 94
5.3.2 Investigated scenarios . . . 99
5.4 Results and discussion . . . 102
5.4.1 Monotonic stimulation (*M*1 - *M*3) . . . 102
5.4.2 Stepwise stimulation (*S*1 - *S*2) . . . 106
5.4.3 Cyclic stimulation (*C*1 - *C*3) . . . 107
5.4.4 Combined cyclic and stepwise stimulation (*CS*1 - *CS*2) . . . 111
5.5 Conclusion . . . 112

6 Feasibility study of the application of a dual-cable DAS to micro-seismic monitoring **113**
6.1 Introduction . . . 114
6.2 Generating DAS signals . . . 115
6.3 Localisation method . . . 115
6.3.1 Introduction to the localisation method . . . 115
6.3.2 Base example . . . 118
6.3.3 Sensitivity analysis . . . 119
6.4 Moment tensor resolvability . . . 127
6.4.1 Construction of the resolution matrix . . . 128
6.4.2 Moment-tensor resolvability from a single DAS cable in a vertical borehole . . . 129
6.4.3 Moment-tensor resolvability from dual DAS cable in a vertical borehole . . . 132
6.5 Discussion . . . 135
6.6 Conclusion . . . 140

7 Conclusions and recommendations **141**
7.1 Conclusions . . . 142
7.1.1 A numerical tool to study near-borehole cyclic and coupled THM processes . . . 142
7.1.2 Performance of different stimulation schemes . . . 143
7.1.3 Feasibility of the dual-cable DAS in a single vertical well . . . 143
7.2 Limitations and future recommendations . . . 144
7.2.1 Numerical methods for coupled THM processes with discontinuous problems . . . 145
7.2.2 Stimulation strategy for geothermal reservoirs . . . 145
7.2.3 Micro-seismic monitoring using DAS . . . 146

A Finite element procedure **147**
A.1 Initial and boundary conditions . . . 148
A.2 Weak form . . . 149
A.3 Discretisation and intrinsic coordinates . . . 151
A.4 Global solution and stiffness matrix . . . 153

B Method to reduce hydraulic and thermal artificial compliance **155**

C Simulation of the normal injection scenario **159**

D Moment tensor decomposition **163**

References **165**

Acknowledgements **191**

Curriculum Vitæ **193**

List of Publications **195**

SUMMARY

Near-borehole coupled thermo-hydro-mechanical (THM) processes are critical in defining the success or failure of geothermal projects. Injectivity decline due to clogging or the increased viscosity of cold water reduces the safe operational window of geothermal projects. However, near-borehole fracturing, a result of near-borehole coupled thermo-hydro-mechanical (THM) processes, is thought to possibly be able to contribute to maintaining or improving the re-injection performance. Understanding and being able to simulate the fracturing processes is therefore of great significance for both analysing re-injection and designing stimulation operations. This thesis presents a geo-mechanical tool, based on the finite element method and cohesive zone model, to simulate the fracture initiation and propagation under THM loadings. The geo-mechanical tool is used to study several stimulation scenarios, including monotonic, stepwise, cyclic, and stepwise combined with cyclic stimulation. To monitor such stimulation processes, this thesis proposes a dual-cable distributed acoustic sensing (DAS) system in a single vertical well and investigates its feasibility to localise and understand near-borehole cracking events.

In the numerical method, possible discontinuities are represented by zero-thickness triple-nodded interface elements, which allow solid elements to separate with mechanical damage and the simulation of longitudinal and transversal fluid/heat flow in the discontinuity. The cubic law is used to simulate the fracture transmissivity changes, while an elasto-damage law is used to characterise the mechanical response of the discontinuity. To simulate the fracture initiation and propagation from high-permeability intact rock, interface elements are inserted in-between all the solid elements, with high stiffness and transversal hydraulic coefficient assigned to reduce artificial compliance. An artificial heat conductivity is introduced to stabilise the numerical solution, in which high Péclet numbers lead to numerical divergence. Substantial verifications and validation are implemented to demonstrate the performance of the developed method.

A new elasto-damage law is developed by incorporating a fatigue damage variable into the tensile branch, in order to account for the fatigue effects during the simulation of cyclic (thermal) stimulation to geothermal reservoirs. The fatigue damage variable is calibrated using the number of loading cycles and fatigue life at different load intensities, with Palmgren-Miner's rule used to account for varying-amplitude cyclic loading. The proposed model is validated against extensive laboratory tests, including cyclic Brazilian test, cyclic hydraulic fracturing test and cyclic thermo-hydraulic fracturing test. The validation results show good agreement with the experimental data, demonstrating that the proposed model is capable of handling fatigue damage under cyclic and coupled THM loadings.

The developed tool is then used to study stimulation to a synthetic sedimentary reservoir, which, according to regional experience, is assumed to be clogged in the near-borehole region. THM simulations of various stimulation strategies - monotonic, stepwise, cyclic, and stepwise combined with cyclic - demonstrate that the stepwise stimulation

yields the most favourable outcomes. Specifically, it enables a significantly lower peak injection pressure with more near-borehole damage. This performance is not achievable using either monotonic or cyclic strategies (assuming same Q_{inj} and T_{inj}). Conversely, cyclic-injection-rate stimulation slightly underperforms (under high injection rate) or slightly outperforms (under low injection rate) the monotonic stimulation. A combined approach incorporating both cyclic and stepwise strategies may lead to slightly better stimulation performance, showing lower peak pressure, compared to corresponding monotnic stimulation, but is inferior to the stepwise stimulation alone.

The feasibility of using a single-well dual-cable DAS to fully localise and understand the near-borehole micro-seismic events is investigated based on synthetic signals, assuming homogenous and isotropic media. A localisation method is introduced to determine the source depth, epicentral distance and azimuth. Sensitivity analysis shows that the localisation accuracy is not sensitive to source with frequency varying from 50 Hz to 200 Hz. But a low signal-to-noise ratio and/or source-to-receiver azimuth close to 0° can lead to decreasing accuracy. Moreover, resolvability analysis suggest that non double-couple moment tensor components M_{xx}, M_{yy} and M_{zz} can be reliably resolved with an epicentral distance within 20 meters, showing improvement on the case of only one cable in a well. A discussion based on the geo-mechanical simulation demonstrates that the single-well dual-cable DAS can be used to understand near-borehole tensile fractures induced during thermal stimulation, with a limited epicentral distance, which implies it is well suited to monitoring stimulation operations.

This thesis contributes to the energy transition by developing a geo-mechanical model to simulate cyclic and coupled THM processes, including the development of fractures, around the near field of the wellbore which can allow the design of novel cyclic thermal stimulation and by proposing a single-well dual-cable DAS configuration that is demonstrated to be feasible to localise and understand near-borehole micro-seismic events to monitor thermal stimulation operations.

SAMENVATTING

Gekoppelde thermo-hydro-mechanische (THM) processen in het gebied rondom het boorgat zijn van cruciaal belang voor het succes of falen van geothermische projecten. Een afname van de injectiviteit, bijvoorbeeld als gevolg van verstopping of de verhoogde viscositeit van koud injectiewater, verkleint het veilige operationele venster van geothermische systemen. Daarentegen wordt verondersteld dat breukvorming rondom het boorgat, als gevolg van gekoppelde THM-processen, kan bijdragen aan het behouden of zelfs verbeteren van de herinjectieprestaties. Het begrijpen en numeriek kunnen simuleren van deze breukprocessen is daarom van groot belang, zowel voor de analyse van herinjectiegedrag als voor het ontwerp van stimulatie-operaties.

Dit proefschrift presenteert een geomechanisch instrument, gebaseerd op de eindige-elementenmethode en het cohesieve-zone-model, waarmee de vorming en voortplanting van breuken onder gekoppelde THM-belastingen kunnen worden gesimuleerd. Het instrument wordt toegepast om verschillende stimulatiescenario's te onderzoeken, waaronder monotone, stapsgewijze, cyclische en stapsgewijs gecombineerde cyclische stimulatie. Ter monitoring van dergelijke stimulatieprocessen wordt een dual-cable Distributed Acoustic Sensing (DAS)-systeem in een verticaal boorgat voorgesteld, en wordt de haalbaarheid onderzocht om breukgerelateerde gebeurtenissen rondom het boorgat te lokaliseren en te beoordelen.

In het numerieke model worden potentiële breuken gerepresenteerd door nul-dikte interface-elementen met drie knooppunten. Deze benadering stelt ons ertoe in staat om mechanische schade aan het grondcontinuüm te simuleren, terwijl stroming van vloeistof en warmte langs de ontstane breuk doorlopend wordt gemodelleerd. De kubuswet wordt toegepast om veranderingen in breukdoorlaatbaarheid te beschrijven, terwijl het mechanische gedrag van de breuk wordt gekarakteriseerd met een elastische schadewet. Om breukvorming en -voortplanting in intacte, sterk doorlatende gesteenten te simuleren, worden interface-elementen geplaatst tussen alle solide elementen, waaraan een hoge stijfheid en transversale hydraulische coëfficiënt worden toegekend om numerieke compliantie te beperken. Daarnaast wordt een effectieve warmtegeleidingscoëfficiënt geïntroduceerd om de numerieke oplossing te stabiliseren, aangezien hoge Péclet-getallen anders tot numerieke divergentie kunnen leiden. Uitgebreide verificatie- en validatiestudies tonen de prestaties van de ontwikkelde methode aan.

Om vermoeiingseffecten tijdens cyclische, al dan niet thermische, stimulatie van geothermische reservoirs te beschrijven, is een vermoeiingsschadevariabele opgenomen ter beschrijving van het grondgedrag onder trekbelasting in het numerieke model. Deze vermoeiingsschadevariabele wordt gekalibreerd op basis van het aantal belastingscycli en de vermoeiingslevensduur bij verschillende belastingniveaus, waarbij de regel van Palmgren–Miner wordt toegepast om het effect van cyclische belastingen met variërende amplitudes in rekening te brengen. Het voorgestelde model is gevalideerd aan de hand van uitgebreide laboratoriumproeven, waaronder de cyclische Braziliaanse test,

de cyclische hydraulische breuktest en de cyclische thermo-hydraulische breuktest. De validatieresultaten tonen een goede overeenstemming met experimentele gegevens en laten zien dat het model in staat is vermoeiingsschade onder cyclische en gekoppelde THM-belastingen adequaat te beschrijven.

Het beschreven numerieke model wordt vervolgens gebruikt om de stimulatie van een synthetisch sedimentair reservoir te simuleren waarvan, op basis van regionale ervaring, wordt aangenomen dat het gebied rondom het boorgat is verstopt. De THM-simulaties worden uitgevoerd met verschillende stimulatiestrategieën, waaronder monotone, stapsgewijze en cyclische strategieën, evenals een combinatie van stapsgewijze en cyclische stimulatie. Deze laten zien dat stapsgewijze stimulatie de meest gunstige resultaten oplevert. Deze strategie maakt een aanzienlijk lagere piekinjectiedruk mogelijk, in combinatie met meer schade rondom het boorgat. Dit prestatieniveau kan niet worden bereikt met uitsluitend monotone of cyclische strategieën bij een gelijk injectiedebiet en -temperatuur. Cyclisch variërende injectiestrategieën presteren daarentegen iets slechter bij hoge injectiesnelheden of juist iets beter bij lage injectiesnelheden dan monotone stimulatie. Een benadering waarin zowel cyclisch als stapsgewijs wordt gestimuleerd kan leiden tot een lichte prestatieverbetering ten opzichte van monotone stimulatie, maar blijft inferieur aan uitsluitend stapsgewijze stimulatie.

De haalbaarheid van het gebruik van een dual-cable DAS-systeem in één enkele put om microseismische gebeurtenissen nabij de boorput volledig te lokaliseren en te karakteriseren, wordt onderzocht op basis van synthetische signalen, uitgaande van een homogeen en isotroop medium. Een lokalisatiemethode wordt geïntroduceerd om de brondiepte, de epicentrale afstand en het azimut te bepalen. Gevoeligheidsanalyse toont aan dat de lokalisatienauwkeurigheid niet gevoelig is voor de bronfrequentie in het bereik van 50 Hz tot 200 Hz. Een lage signaal-ruisverhouding en/of een bron-ontvangerazimut dicht bij 0° kan echter leiden tot een afnemende nauwkeurigheid. Bovendien suggereert de resolvabiliteitsanalyse dat niet–double-couple momenttensorcomponenten M_{xx}, M_{yy} en M_{zz} betrouwbaar kunnen worden bepaald voor een epicentrale afstand kleiner dan 20 meter, wat een verbetering betekent ten opzichte van het geval met slechts één kabel in de put. Een discussie op basis van geomechanische simulaties toont aan dat een single-well dual-cable DAS kan worden gebruikt om trekbreuken nabij de boorput te analyseren die worden geïnduceerd tijdens thermische stimulatie, binnen een beperkte epicentrale afstand, wat impliceert dat deze configuratie bijzonder geschikt is voor het monitoren van stimulatie-operaties.

Samenvattend levert dit proefschrift een bijdrage aan de energietransitie door de ontwikkeling van een geomechanisch model dat cyclische en gekoppelde THM-processen rondom het boorgat simuleert, inclusief breukvorming. Hierdoor kunnen mogelijk nieuwe cyclische thermische stimulatiestrategieën worden ontwikkeld. Daarnaast wordt een single-borehole, dual-cable DAS-configuratie voorgesteld en wordt via een haalbaarheidsstudie aangetoond dat deze kan worden ingezet om microseismische gebeurtenissen rondom het boorgat te lokaliseren en te begrijpen. Daarmee heeft deze methode de potentie om waardevolle ondersteuning te bieden bij het monitoren en optimaliseren van thermische stimulatie-operaties.

ZUSAMMENFASSUNG

Nahe-Bohrloch gekoppelte thermo-hydro-mechanische (THM) Prozesse sind entscheidend für den Erfolg oder Misserfolg geothermischer Projekte. Ein Rückgang der Injektivität infolge von Verstopfung oder der erhöhten Viskosität von kaltem Wasser verringert das sichere Betriebsfenster geothermischer Projekte. Demgegenüber wird angenommen, dass Frakturierung im Nahbereich des Bohrlochs, als Folge von gekoppelten THM-Prozessen, möglicherweise dazu beitragen kann, die Re-Injektionsleistung aufrechtzuerhalten oder zu verbessern. Das Verständnis und die Simulation solcher Frakturierungsprozesse sind daher von großer Bedeutung – sowohl für die Analyse der Re-Injektion als auch für die Planung von Stimulationsmaßnahmen. Diese Dissertation stellt ein geomechanisches Werkzeug vor, das auf der Finite-Elemente-Methode und dem Cohesive-Zone-Modell basiert, um die Initiierung und Ausbreitung von Rissen unter THM-Belastungen zu simulieren. Das geomechanische Werkzeug wird eingesetzt, um verschiedene Stimulationsszenarien zu untersuchen, darunter monotone, schrittweise, zyklische sowie schrittweise-zyklisch kombinierte Stimulation. Zur Überwachung solcher Stimulationsprozesse schlägt diese Dissertation ein Doppelkabel-basiertes Distributed Acoustic Sensing (DAS)-System in einem vertikalen Bohrloch vor und untersucht dessen Eignung, um Rissbildungsereignisse im Nahbereich des Bohrlochs zu lokalisieren und zu verstehen.

In der numerischen Methode werden mögliche Diskontinuitäten durch null-dicke dreiknotige Interface-Elemente dargestellt. Diese erlauben die Trennung von Festkörperelementen mit mechanischer Schädigung sowie die Simulation von longitudinalem und transversalem Wärme- und Flüssigkeitstransport durch die Diskontinuität. Das Kubikgesetz wird zur Modellierung der Rissdurchlässigkeit verwendet, während ein elasto-schadensmechanisches Gesetz das mechanische Verhalten der Diskontinuität beschreibt. Um Rissbildung in hochpermeablen intakten Gesteinen zu simulieren, werden Interface-Elemente zwischen alle Festkörperelemente eingefügt. Diese erhalten eine hohe Steifigkeit und einen hohen transversalen hydraulischen Leitwert, um künstliche Nachgiebigkeit zu vermeiden. Eine künstliche Wärmeleitfähigkeit wird eingeführt, um die numerische Lösung zu stabilisieren, da hohe Péclet-Zahlen zu numerischer Divergenz führen können. Umfangreiche Verifikations- und Validierungsmaßnahmen zeigen die Leistungsfähigkeit der entwickelten Methode.

Ein neues elastizitäts-schädigungsgesetz wurde entwickelt, indem eine Ermüdungsschädigungsvariable in den Zugzweig integriert wurde, um die Ermüdungseffekte während der Simulation der zyklischen (thermischen) Stimulation geothermischer Reservoire zu berücksichtigen. Die Ermüdungsschädigungsvariable wird anhand der Anzahl von Belastungszyklen und der Ermüdungslebensdauer bei unterschiedlichen Belastungsintensitäten kalibriert, wobei die Palmgren-Miner-Regel angewendet wird, um zyklische Belastungen mit variierender Amplitude zu erfassen. Das vorgeschlagene Modell wird anhand umfangreicher Laborversuche validiert, darunter der zyklische Brasilianische Test, der zyklische hydraulische Bruchtest und der zyklische thermo-hydraulische Bruchtest.

Die Validierungsergebnisse zeigen eine gute Übereinstimmung mit den experimentellen Daten und belegen, dass das vorgeschlagene Modell in der Lage ist, Ermüdungsschädigungen unter zyklischen und gekoppelten THM-Belastungen zu beschreiben.

Das entwickelte Werkzeug wird anschließend eingesetzt, um die Stimulation eines synthetischen Sedimentreservoirs zu untersuchen, das – basierend auf regionalen Erfahrungen – als im nahen Bohrlochbereich verstopft angenommen wird. THM-Simulationen verschiedener Stimulationsstrategien – monoton, schrittweise, zyklisch sowie schrittweise in Kombination mit zyklisch – zeigen, dass die schrittweise Stimulation die günstigsten Ergebnisse liefert. Insbesondere ermöglicht sie einen deutlich niedrigeren Spitzeninjektionsdruck bei gleichzeitig stärkerer Schädigung im nahen Bohrlochbereich. Dieses Leistungsniveau kann mit ausschließlich monotonen oder zyklischen Strategien (bei gleichen Werten von Q_{inj} und T_{inj}) nicht erreicht werden. Im Gegensatz dazu schneidet die zyklische Injektionsratenstimulation etwas schlechter ab (bei hoher Injektionsrate) oder geringfügig besser (bei niedriger Injektionsrate) als die monotone Stimulation. Ein kombinierter Ansatz, der sowohl zyklische als auch schrittweise Strategien einbezieht, kann zu einer leicht verbesserten Stimulationsleistung führen – charakterisiert durch einen niedrigeren Spitzendruck im Vergleich zur entsprechenden monotonen Stimulation – bleibt jedoch der ausschließlich schrittweisen Stimulation unterlegen.

Die Machbarkeit des Einsatzes eines Dual-Kabel-DAS-Systems in einem Einzelbohrloch zur vollständigen Lokalisierung und Analyse mikro-seismischer Ereignisse im Nahbereich wird anhand synthetischer Signale untersucht, unter der Annahme eines homogenen und isotropen Mediums. Eine Lokalisierungsmethode wird vorgestellt, um Quelltiefe, Epizentraldistanz und Azimut zu bestimmen. Sensitivitätsanalysen zeigen, dass die Lokalisierungsgenauigkeit unempfindlich gegenüber Quellfrequenzen im Bereich von 50 Hz bis 200 Hz ist. Eine geringe Signal-Rausch-Verhältnis und/oder ein Quell-Empfänger-Azimut nahe 0° können jedoch die Genauigkeit beeinträchtigen. Die Analyse der Auflösbarkeit legt nahe, dass nicht-doppelkoppelte Momententensor-Komponenten M_{xx}, M_{yy} und M_{zz} bei Epizentraldistanzen unter 20 Metern zuverlässig bestimmt werden können – eine Verbesserung gegenüber der Ein-Kabel-Lösung. Eine Diskussion auf Basis geomechanischer Simulationen zeigt, dass das Einzelbohrloch-Dual-Kabel-DAS-System zur Analyse von durch thermische Stimulation verursachten Zugrissen im Nahbereich des Bohrlochs eingesetzt werden kann – jedoch mit begrenzter Epizentraldistanz. Dies deutet darauf hin, dass es gut für die Überwachung von Stimulationsmaßnahmen geeignet ist.

Diese Dissertation leistet einen Beitrag zur Energiewende, indem sie ein geomechanisches Modell zur Simulation zyklischer und gekoppelter THM-Prozesse – einschließlich der Rissbildung im Nahfeld des Bohrlochs – entwickelt, das die Planung neuartiger zyklischer thermischer Stimulationsstrategien ermöglicht. Darüber hinaus wird eine Einzelbohrloch-Dual-Kabel-DAS-Konfiguration vorgeschlagen, deren Eignung zur Lokalisierung und Analyse mikro-seismischer Ereignisse im Nahbereich zur Überwachung von thermischen Stimulationsmaßnahmen nachgewiesen wird.

1

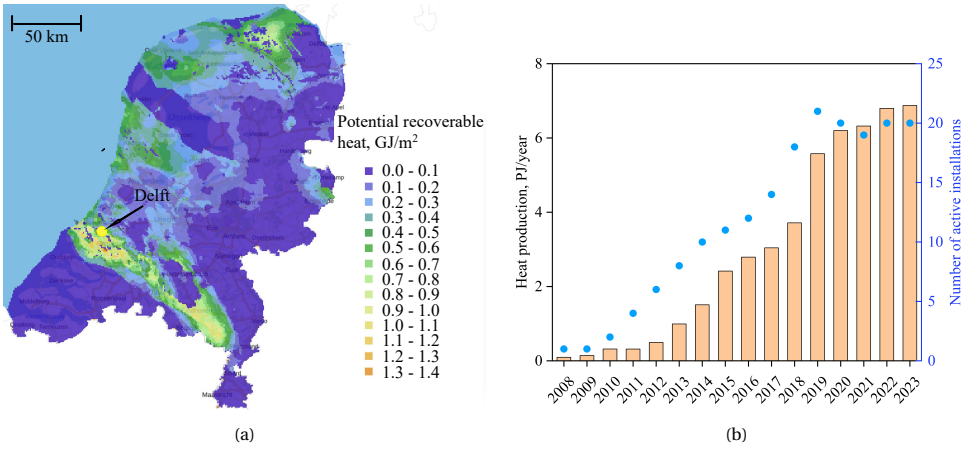
INTRODUCTION

1

1.1. GEOTHERMAL ENERGY IN THE WORLD AND IN THE NETHERLANDS

Geothermal energy, the thermal energy resource under the surface of the earth, is one of the most promising renewable energy sources for the 21st century. Its reliability and low carbon emissions make it widely applicable for heating, cooling, and power generation. In 2023, the total installed geothermal heating and cooling capacity (from 88 countries) was approximately 173 303 MWt, with a total produced energy of 1 476 312 TJ per year, while the total installed geothermal electric production capacity (from 30 countries) was approximately 16 211 MW with a total generated power of approximately 347 602 TJ (IGA, 2024). In terms of consumption, geothermal energy use reached 5 exajoule (EJ), representing approximately 0.8% of global energy demand in 2023 (IEA, 2024a). By 2050, the global geothermal electricity production capacity is expected to reach 60 GW, while tripling the use of geothermal resources for heating (IEA, 2024a,b).

The Netherlands, nearly half of the final energy use is used for heating and is primarily obtained from natural gas (Planbureau voor de Leefomgeving, 2020), has ample geothermal resources with heat sources estimated to be 821 000 PJ (Kramers *et al.*, 2012), demonstrated in Fig. 1.1a. As of 1st January 2024, the total geothermal energy production installations (i.e. a doublet, a pair of wells) amounts to 33, among which 20 were operating and contributed to a total heat production of 6.875 PJ in 2023 (TNO, 2024). Fig. 1.1b shows the changes in annual heat production from geothermal energy and number of operating installations in the Netherlands, seeing a significant increase since 2018 (TNO, 2024). Although only 1% increase in heat production compared to 2022, a record number of 13 new geothermal wells were completed in 2023, demonstrating measurable progress in achieving the goal of the Dutch government of 15 PJ by 2023 and the ambition of 200 PJ by 2050 (Platform Geothermie *et al.*, 2018; TNO, 2024), which is equivalent to around 700 installations (Platform Geothermie *et al.*, 2018).



(a) (b)

Figure 1.1: (a) Dutch geothermal potential recoverable heat (TNO - GDN, 2024), and (b) annual heat production and number of active installations since 2013, reproduced from TNO (2024), with data between 2008-2013 originally from Centraal Bureau voor de Statistiek (2014).

Geothermal energy in the Netherlands has predominantly been extracted from high-permeability sedimentary aquifers of Cenozoic, Upper Jurassic-Lower Cretaceous, Triassic, Rotliegend and Lower Carboniferous - Dinantian ages, at depths between 500 m and 3000 m (Mijnlieff, 2020; www.nlog.nl, 2025). The reservoir temperatures typically range from 40°C to around 100°C, and the high transmissivity of these reservoirs has led to an average extraction/injection flow rate of around 200 m^3/h within a wide range of 50 m^3/h to 400 m^3/h, depending on the season and system (Mijnlieff, 2020; www.nlog.nl, 2025). Most of the recent Dutch geothermal systems are doublets, consisting of a pair of wells drilled into the same reservoir (Mijnlieff, 2020), as shown in Fig. 1.2a. This open-loop system therefore enables the extraction of hot water from one well for heating, while the cooled-down water is re-injected into the same reservoir through another well, ensuring a sustainable and environmentally friendly operations.

The Geothermie Delft project (schematically shown in Fig. 1.2a), a doublet drilled in 2023 on the TU Delft campus, was designed for both research and commercial thermal energy supply (Vardon *et al.*, 2024). This project is typical of projects installed in the Netherlands and is used as an example later in the thesis. The two wells target the early Cretaceous Delft sandstone formation, located at approximately 2 km below the surface, whose distribution across the Netherlands and broad estimation of transmissivity are shown in Fig. 1.2b. The wells both have an approximately 800 m vertical section, from where the two wells deviate from each other so that water can be pumped between them over a horizontal distance of around 1.3 km at reservoir depth (Vardon *et al.*, 2024). Hot water will be produced at around 80 °C with an initial rate of up to 350 m^3/h, and the cooled-down water will be re-injected to the same reservoir at a temperature that can be as low as 20°C (Vardon *et al.*, 2024). This project includes a comprehensive research programme, involving the installation of a wide range of instruments alongside extensive logging and coring programmes and monitoring work (Vardon *et al.*, 2024). A fibre optic cable will be installed in the producer well down to the reservoir section to monitor the operations, with a local seismic monitoring network being installed in the surrounding area. In addition to the scientific ambitions, the whole project aims to supply a peak of around 25 MW of thermal energy (Vardon *et al.*, 2024).

1.2. PROBLEM STATEMENT

Ensuring the sustainability of a geothermal project is the key aspect both for economic reasons and for stable energy supply. As shown in Fig. 1.2a, a typical geothermal project comprises a producer well and an injector well where the produced fluid is returned to the reservoir after the thermal energy has been extracted. Long-term successful re-injection operations are therefore required, which replenish the reservoir, sustain reservoir pressure and ensure environmentally responsible disposal of the fluid (Kaya *et al.*, 2011). One of the challenges in the re-injection operations is to maintain the injectivity (the ratio of injection rate to injection pressure). Injectivity decline is a common issue that, sometimes, leads to the abandonment of wells (Ungemach, 2003; Markó *et al.*, 2024), and potentially failure of the whole project (Guinot & Marnat, 2021). Stimulation technologies are often required to restore reservoir injectivity. However, conventional methods, such as hydraulic fracturing, raise concerns regarding either safety or effectiveness. Consequently, there is a need to explore and evaluate innovative stimulation approaches, alongside the development of

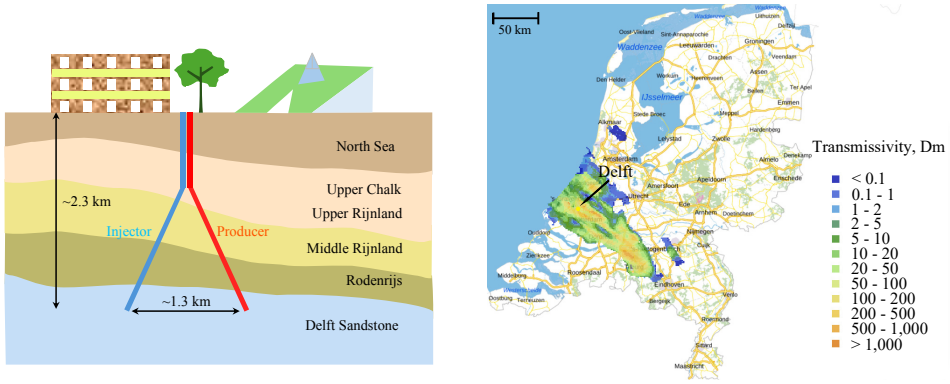


Figure 1.2: (a) Schematic description of a typical geothermal doublet in the Netherlands (showing the Geothermie Delft project as an example) and (b) transmissivity map of the Delft Sandstone Formation and Alblasserdam Formation (Vrijlandt *et al.*, 2019; TNO - GDN, 2024).

novel monitoring technologies to improve the understanding of subsurface processes during stimulation.

Injecting water substantially colder than the ambient reservoir temperature results in a complex multi-physics problem immediately around the borehole. Fluid pressures are elevated and cooling results in thermal-contraction, both processes are overplayed on the mechanical disturbance caused by drilling. The radial fluid and heat flows lead to large pressure and temperature gradients near the borehole. The significant near-borehole pressure and temperature changes can trigger bio-chemo-physical processes, including mineral dissolution or precipitation, fines migration and clay swelling, biofilm formation and gas entrapment, thermal matrix shrinkage or thermal cracking, etc (Burté *et al.*, 2019; Kamila *et al.*, 2021; Song *et al.*, 2020; Yuan & Wood, 2018). These processes can largely influence the injection well performance. Yet, understanding these processes is not an easy task, since it involves the interactions of various problems.

Sandstone reservoirs have been long reported to suffer from decreased injectivity during operations. Moderate injectivity decrease is expected from injecting cooled water, arising from the viscosity increase (Veldkamp *et al.*, 2016b). More significant injectivity decline has also been reported, for example, in Veysey Well 1 (49.41 $m^3/(h \cdot MPa)$ to 12.52 $m^3/(h \cdot MPa)$) in the Imperial Valley (Messer *et al.*, 1978), California, in Melleray doublet (21.25 $m^3/(h \cdot MPa)$ to 6 $m^3/(h \cdot MPa)$) (Boisdet *et al.*, 1989), France, and in Well Gt NG 2/89 (220 $m^3/(h \cdot MPa)$ to 124 $m^3/(h \cdot MPa)$) (Birner *et al.*, 2015), Neustadt-Glewe, Germany, where all the reservoirs are sandstone and the flow is dominated by matrix flow (as opposed to fracture flow). In the Netherlands, matrix-permeability dominated sandstone reservoirs are the main geothermal plays, including Delft Sandstone and Slochteren Sandstone plays (Mijnlieff, 2020), providing heating to surrounding greenhouses and buildings. However, injectivity problems are often observed and have been reported in several doublets in the Netherlands, of which the micro-biological activities and scaling are believed to be the main driven mechanisms (Water Research Institute (KWR), 2015;

Croese *et al.*, 2019). Increases of injectivity have also been observed, which have been apportioned to both dissolution processes and thermal cracking.

Although preventative measurements have been suggested and implemented in practice, e.g. using filters and adding chemical inhibitors (Kindle *et al.*, 1984; Kalvani *et al.*, 2021), injectivity decline still can be encountered. Therefore, restoration technology is often needed to recover and/or improve injectivity. For example, strong acids, alcohols or certain ketones can be used to mitigate clay swelling (Kindle *et al.*, 1984), and chemical treatment is the preferred method to remove or reduce scaling (Messer *et al.*, 1978; Jarrahian *et al.*, 2024). However, chemical additives are expensive and are strictly regulated (Jarrahian *et al.*, 2024). Moreover, the high temperature environment in geothermal wells poses additional challenges for the chemical removal method. Stimulation technology, e.g. hydraulic stimulation (or fracking), is an alternative. However, this is often not allowed due to concerns about the high pressures used inducing seismicity (Pluymakers *et al.*, 2023). This has led to the proposal of 'soft stimulation' methods, which are a suite of methods that aim to improve the injectivity with lower pumping pressures in combination with other processes. Among the soft stimulation technologies, thermal stimulation and cyclic stimulation are popular choices.

Thermal stimulation involves injecting cold water into the reservoir at a pressure below the breakdown pressure (defined as the pressure required to fracture the rock mass), as opposed to the higher pressures typically used in hydraulic fracturing. This approach has been successfully implemented in numerous geothermal projects, including the Wells H40 & H41 at the Los Humeros field in Mexico (Luviano *et al.*, 2015) and HE-8 at Hellisheidi in Iceland (Gunnarsson, 2011), where it improved injection performance by reducing pump pressure. Reactivation of pre-existing fractures and the creation of new fractures induced by thermal stresses are considered the primary mechanisms behind the effectiveness of thermal stimulation (Horne, 1982).

Cyclic stimulation requires alternating phases of high and low flow rate to induce fatigue damage and has been demonstrated to lower down injection pressure in both laboratory, mine-scale experiments and field tests (Hofmann *et al.*, 2019). For example, laboratory tests on sandstone and granite samples have shown significant reductions in breakdown pressure following cyclic injection (up to 20% for Pocheon granite cores (Zhuang *et al.*, 2019b), 7.18% - 18.9% for Xujiahe sandstone (Kang *et al.*, 2020) and 16% for dry Tennessee sandstone (Patel *et al.*, 2017)). Additionally, cyclic injection has been observed to lead to the formation of more complex fracture networks, as opposed to the simple fractures typically induced by conventional hydraulic stimulation (Patel *et al.*, 2017; Wei *et al.*, 2023). A field-scale test performed on well PX-1 at the Pohang enhanced geothermal system (EGS) project site in South Korea demonstrated that cyclic injection was able to improve the injectivity from 0.5 L/(s·MPa) to 2.6 L/(s·MPa) while managing seismic activity to remain below the target threshold of M_w 2.0 (Hofmann *et al.*, 2019; Zang *et al.*, 2021). A challenge in inducing cyclic fatigue is that a fatigue limit exists for rocks, resulting in a minimum injection pressure which is required to induce fatigue , typically between 0.75 and 0.9 of the breakdown pressure in monotonic hydraulic fracturing (Cerfontaine & Collin, 2018; Schijve, 2009).

Combining thermal and cyclic stimulation has been proposed to improve the stimulation performance of heavy oil reservoirs (cyclically injecting hot water or steam), taking

advantage of the cyclic effect of hot water on oil viscosity (Hou *et al.*, 2016). In contrast, cyclic thermo-hydraulic stimulation (cyclically injecting cold water) to geothermal reservoirs based on the mechanism of cooling-induced thermal stress and fatigue damage is rarely reported and studied. Therefore, a combination of both soft stimulation technologies is proposed and compared with other stimulation scenarios, e.g. monotonic and stepwise stimulation, in this thesis. Yet, investigating the mechanisms behind different stimulation requires thorough understanding of the near-borehole thermo-hydro-mechanical (THM) processes.

Coupled THM processes happen during both standard operations and stimulation operations, inducing large stress changes in the near-borehole area. Cyclic injection can induce fatigue damage in rocks, which, together with the cooling-induced stress, can result in near-borehole cracking events. The formation of near-borehole fractures can largely improve the flow condition around the wellbore, therefore improving the well performance. However, due to the complex coupled THM processes and discontinuous nature of the problem, understanding the near-borehole cracking events is a non-trivial task, which therefore poses challenges in designing a stimulation strategy. This thesis, therefore, aims to provide tools to understand the near-borehole cracking events as a result of monotonic, stepwise, or cyclic coupled THM processes. The tools include a geo-mechanical model and a micro-seismic monitoring proposal. The geo-mechanical model is used to study the different stimulation scenarios for a synthetic reservoir with near-borehole clogging, inspired by the Geothermie Delft project and nearby geothermal projects. In addition, the feasibility of using a new distributed acoustic sensing (DAS) configuration to locate and characterise near-borehole cracking events will be explored.

1.3. MODELLING CYCLIC THERMO-HYDRO-MECHANICAL PROCESSES

1.3.1. NEAR-BOREHOLE COUPLED THM PROCESSES

The injectivity changes mentioned in the previous section are a result of coupled processes in the subsurface, particularly in the near-borehole region where there is the largest temperature and pressure gradients. The focus of this thesis is on the coupled thermo-hydro-mechanical processes. Chemical processes, while important, are broadly beyond the scope of this thesis, although are included in the review contained in Chapter 2.

Coupled processes indicate that two or more processes interact with each other, with the independent solution of any one process being impossible without simultaneous solution of the others (Vardon, 2009; Jacquey, 2017; De Simone, 2017). During the re-injection of cooled water back to geothermal reservoirs, coupled THM processes happen and can partly control the well performance. The cooling effect can induce volumetric strain in rock mass which is restrained by surrounding media, leading to thermal stresses. This is the thermal-to-mechanical effect, which can induce new fractures or re-activate natural fractures. Conversely, the mechanical deformation may result in energy loss, thus leading to changes in temperature. However, this mechanical-to-thermal effect is usually small and thus can be ignored in geo-mechanical analyses (Zimmerman, 2000; De Simone *et al.*, 2013). In addition, fluid properties, e.g. viscosity and density (Veldkamp *et al.*, 2016b), are influenced by the temperature and may therefore induce fluid flow

due to changing temperature gradient. This is the thermal-to-hydraulic effect, which, during cold water injection, inevitably leads to injectivity decline. In contrast, any change in fluid pressure distribution will influence heat transfer, thus temperature distribution. This hydraulic-to-thermal effect largely controls the efficiency of heat extraction from subsurface. Moreover, as the thermal-to-mechanical effect, the deformation of the rock was shown to be a function of the stress and pore-water pressure and can be described by effective stress theory (Terzaghi, 1943). On the other hand, deformation in rock mass or creation of new fluid paths (i.e. new fractures or re-activated natural fractures) can change the fluid flow behaviour.

Fig. 1.3 summarises the main couplings among thermal, hydraulic and mechanical processes in subsurface. These coupled THM processes control the near-borehole flow and heat transfer conditions. The resulting stress changes can create new fluid paths through the formation of new fractures or re-activation of natural fractures, which, in turn, will largely change the near-borehole fluid flow and heat transfer. These complex coupled THM processes are the mechanisms behind any geothermal operations, including re-injection and stimulation. A thorough understanding of the non-linear coupled processes and discontinuous problems is therefore crucial for designing injection or stimulation plans.

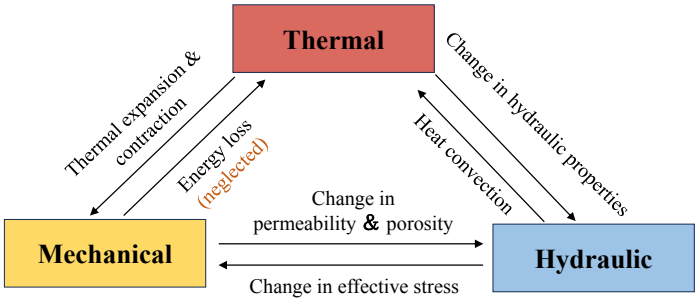


Figure 1.3: Illustration of the interactions between thermal, hydraulic and mechanical processes in the porous media (after Rühaak *et al.* (2017)).

1.3.2. NUMERICAL METHODS FOR MODELLING DISCONTINUITY PROBLEMS

Understanding how the fracturing processes are influenced by the coupled THM processes resulting from cyclic re-injection, and how the injection performance is influenced by the fracture characteristics and behaviour, is crucial for designing and managing operations, yet is a non-trivial task. Analytical studies are generally restricted to simple 1D problems in an idealised geometry, e.g., studies on optimising heat extraction from enhanced geothermal systems (EGS) (Akdas & Onur, 2022; Fox *et al.*, 2016), or combined with field data to derive empirical relationships between injection temperature and injectivity (Grant *et al.*, 2013).

Thanks to the rapid development of high-performance computation, more complex and coupled processes can be studied with a more realistic description of the subsurface and its evolution. Multiple advanced codes have been developed to study coupled thermo-

hydraulic and thermo-hydro-mechanical processes and transport phenomena in complex subsurface structures, such as TOUGH2 (Doughty, 2013), MRST-AD (Krogstad *et al.*, 2015), FEHM (Zyvoloski, 2007), AD-GPRS (Garipov *et al.*, 2018), and DARTS (Voskov, 2017), OpenGeoSys (Kolditz *et al.*, 2012), GEOX (Settgast *et al.*, 2017), MOOSE-based codes (Dudani *et al.*, 2014; Podgorney *et al.*, 2021; Jacquey, 2017), UDEC (Israelsson, 1996), DRAC (Pérez Carreras, 2018), and LAGAMINE (Charlier, 1987; Collin *et al.*, 2002). Some of these codes are able to simulate fully coupled thermo-hydro-mechanical processes in the subsurface where pre-existing or new fractures play a key role, each employing various approaches to tackle simulations involving discontinuities.

Two main categories of numerical approaches have been proposed and developed to solve problems which include discontinuities, namely continuous and discrete numerical methods (Aliabadi & Rooke, 1991; Lanru & Ove, 2007). The former category includes methods like the Finite Difference Method (FDM), Finite Element Method (FEM) and Boundary Element Method (BEM), and treats the rock as an equivalent continuum with the discontinuities being either implicitly or explicitly represented. In contrast, the Discrete Element Method (DEM, including Distinct Element Method, Discontinuous Deformation Analysis and Bounded Particle Method) treats the rock as an assemblage of particles or blocks, so that discontinuities are explicitly considered. Although DEM allows larger displacements and rotations of discrete elements, it is not easily able to solve flow and heat transfer problems by its own. in addition, it is computationally expensive to calculate the interactions between particles or blocks, which limits the application to small-scale problems. In addition, significant uncertainties can be introduced as it is challenging to model realistic particle geometries and to determine the material parameters required to define the mechanical relationships between the particles (Min, 2013). Therefore, continuous numerical methods, typically FEM (which has advantages over FDM and BEM in terms of efficiency in handling non-linear processes and capability of describing complex boundary geometries (Min, 2013)), remain the most popular numerical methods to simulate multi-physics problems including discontinuities, despite challenges in incorporating them into meshes.

1.3.3. COHESIVE ZONE MODEL WITH FATIGUE DAMAGE VARIABLE

The simulation of discontinuous problems can be performed with different techniques based on FEM, such as Element Deletion Method (Livermore Software Technology, 2007), Adaptive Element Method (Schrefler *et al.*, 2006)), Extended Finite Element Method (XFEM) (Jafari *et al.*, 2023), cohesive interface elements (Settgast *et al.*, 2017; Lequesne *et al.*, 2006; Dieudonné *et al.*, 2015; Cerfontaine *et al.*, 2015; Liaudat *et al.*, 2023), and Phase Field Method (PFM) (Lepillier *et al.*, 2020). Among the proposed approaches, the cohesive interface element, combined with the cohesive zone model (CZM), is the dominant choice in modelling fracturing processes using FEM (Nguyen *et al.*, 2017), due to its mitigation of the need to calculate the stress singularity at the fracture tips that is commonly challenging in methods based on linear elastic fracture mechanics (e.g., XFEM) (Min, 2013; Nguyen *et al.*, 2017) and its clear physical meaning. In addition, unlike XFEM (Min, 2013; Wu *et al.*, 2020), cohesive interface elements are capable of modelling fracture nucleation and initiation (Nguyen *et al.*, 2017). Although the phase-field method can also avoid the challenges in stress singularities, finer meshes with dimensions smaller

than the so-called length-scale parameter are required, resulting in a high computational cost (Dally *et al.*, 2020).

The cohesive zone model was first proposed by Dugdale (1960) and Barenblatt (1962) to circumvent the unrealistic infinite stresses at the fracture tip obtained for a linear elastic material, assuming a cohesive-law-governed zone in front of the fracture tip (shown in Fig. 1.4). Later, Hillerborg *et al.* (1976) introduced CZM into FEM to simulate crack initiation and growth in concrete. When discretising the material domain, the material separation and thus damage of the structure can be described by interface elements in-between continuum elements (Scheider, 2001), governed by the cohesive law that relates traction and separation of the two surfaces of the interface element. Due to the advantages mentioned earlier, the cohesive interface elements have been widely applied to modelling hydraulic fracturing (Nguyen *et al.*, 2017), fault slip (Van Den Bogert, 2015), the behaviour of soil–structure interfaces (Cerfontaine *et al.*, 2015) and gas fracturing in clay barriers (Liaudat *et al.*, 2023). However, most of the previous research only considered hydro-mechanical or pneumo-hydro-mechanical couplings (Liaudat *et al.*, 2023; Dieudonné, 2016; Nguyen *et al.*, 2017; Lu *et al.*, 2013; Carrier & Granet, 2012). As heat transfer and thermal stresses play a key role in extracting geothermal energy, fully coupled THM processes are necessary to be considered in the model. A limited number of previous works considered heat transfer in interface elements, for example, Alonso *et al.* (2013), Pérez Carreras (2018) and Cui *et al.* (2019) considered heat transfer in interface elements, but with a double node scheme, which does not allow the consideration of the temperature and fluid pressure inside the discontinuity independently from the adjacent continuum elements, although has a simpler formulation. The temperature and pressure at the middle of the interface requires assumptions, e.g., taking the average value between the bottom and top faces of the interface. It has been demonstrated that in certain circumstances the double-node scheme can introduce errors that depend on the longitudinal temperature/pressure profile, hydraulic/diffusion coefficients and thus on mechanical processes (Liaudat *et al.*, 2023). In contrast, the triple-node scheme allows a more “flexible” representation of the transversal fluid and heat flow between the interface element and the surrounding continuum elements. Therefore, such interface elements can be used for applications where an explicit representation of the mid-plane pressure and temperature is convenient, such as the interfaces between permeable and impermeable materials. In addition, the mechanical laws implemented in the interface elements of previous works reflect the targeted physical process, with for example, the work of Cui *et al.* (2019) and Ranjbar *et al.* (2020) not including damage processes and Alonso *et al.* (2013) not updating stiffness with damage. Since the problems considered in their work were always in compression and mode I fractures are not considered, the thermo-mechanical and hydro-mechanical couplings were moderate. Furthermore, in their modelling exercises, the shearing path was prescribed along a pre-defined line and the cases where the fractures can choose the most efficient fracturing paths were not discussed.

The mechanical response of the cohesive interface element is governed by a traction-separation law (specifically referred to a bilinear elasto-damage law in this work). Traditionally, the law can only describe damage due to static loading beyond a strength threshold. If loading remains below the strength, the behaviour is elastic, with no additional da-

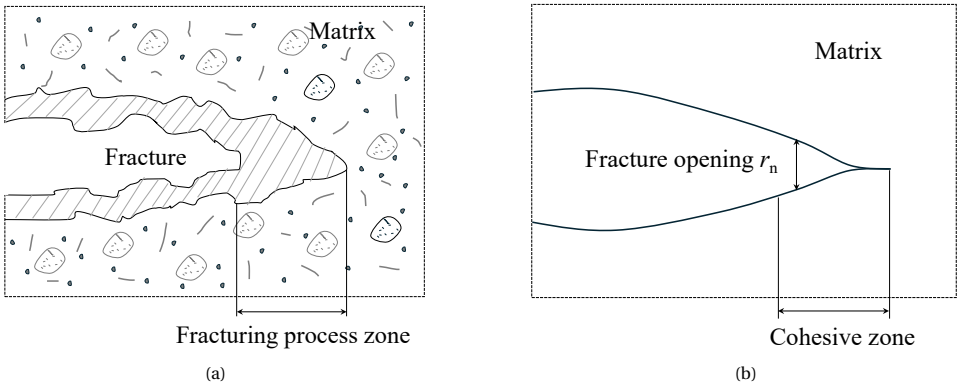


Figure 1.4: Schematic description of: (a) fracturing process zone at the fracture tip, and (b)conceptualised cohesive zone which is used to represent the fracturing process zone (after Elices *et al.* (2002))

mage, regardless of the number of loading cycles. Although efforts have been made to incorporate fatigue damage due to cyclic loading into the elasto-damage law, some limitations still remain. Xi *et al.* (2021) and Wei *et al.* (2023) both introduced a fatigue damage variable into constitutive laws to model the degradation of tensile strength. However, these models do not account for thermal effects, rendering their method unsuitable for cyclic thermal stimulation. In addition, both models assume constant stiffness in the elastic stage, which fails to capture the observed degradation of rock stiffness and the accumulation of deformation (Cerfontaine & Collin, 2018; Xiao *et al.*, 2010). Wei *et al.* (2023) also formulated the fatigue damage variable as a function of the number of cycles under constant-amplitude loading, which does not consider varying-amplitude cyclic loading.

Therefore, this thesis aims to fill the mentioned gaps by: a) developing a fully-coupled THM model using zero-thickness and triple-node interface elements, which can be inserted in-between continuum elements to represent pre-existing fractures or provide arbitrary potential cracking paths; b) developing a new traction-separation law incorporating a fatigue damage variable to account for fatigue effects during the simulation of fracturing processes under cyclic thermo-hydro-mechanical loadings with varying amplitude.

1.4. MICRO-SEISMIC MONITORING USING DISTRIBUTED ACOUSTIC SENSING

1.4.1. MICRO-SEISMIC MONITORING METHODS

Micro-seismic monitoring entails the detection of small-scale rock-failure events with magnitude less than 0 on the Richter scale and frequency ranging roughly from 0.1 Hz - 10 kHz (Meng *et al.*, 2018; Wu *et al.*, 2016)). It has been widely used in geothermal and/or underground storage projects since its inception in the 1970s (Warpinski, 2009). Its most notable application is mapping stimulation operations to provide information on the stimulated volume, fracture geometry and complexity and geo-mechanical responses

(Le Calvez *et al.*, 2007; Martyushev *et al.*, 2024). This gives information of the subsurface stimulation processes in 3D continuously, allowing the improvement of operations and to react to unexpected issues in real time, e.g. induced seismicity (Li *et al.*, 2019). For example, micro-seismic monitoring of six hydraulic fracturing tests at the M-site field, a fluvial sandstone reservoir in the Piceance basin of Colorado, from multilevel and triaxial seismic receivers in two wells were used to image the fracture height, length and azimuth and to correlate the geometry with the injection volume and type (Warpinski *et al.*, 1999). The imaged fractures were also compared with a fracture model, showing good agreement while also indicating a lack of downward growth in the model, suggesting other constraints on the fracture maybe missing, or less likely, incorrect stress data (Warpinski *et al.*, 1999). Shapiro *et al.* (2006) interpreted micro-seismic data of two hydraulic fracturing experiments in the Carthage Cotton Valley tight gas field, in eastern Texas, using the well-known analytical hydraulic fracturing model, i.e. the so-called PKN model that describes the propagation of a straight planar height-fixed vertical fracture due to injection of fracturing fluid (Valkó & Economides, 1995). Their results suggested the fracture growth during a dominant part of the injection duration could be mainly controlled by the fluid loss effects and they demonstrated the estimation of the permeability of the fracture and of the reservoir based on the triggering front and back front curves of the induced micro-seismic events on the spatial-temporal plots (Shapiro *et al.*, 2006). Cornet & Jianmin (1995) reported that a network of 15 subsurface 3D seismic stations was employed to monitor the injection tests conducted at the granite test side at Le Mayet De Montagne, central France, and the inversion of the micro-seismic data, together with measurements from hydraulic tests on pre-existing fractures with known orientations, led to the determination of the regional stress field and the identification of the fault plane for each of the focal mechanisms. Analysis of the recorded micro-seismic events during hydraulic fracturing tests in the context of enhanced geothermal system (EGS) at the Sanford Underground Research Facility, South Dakota, confirmed a complex mixed-mode fracture network comprised of multi-strand hydraulic fractures and shear-reactivated pre-existing weak planes (Schoenball *et al.*, 2020). In short, microseismic monitoring is an essential tool to ensure efficiency and safety of operations in the subsurface.

Conventionally, 1-component (1C) or 3-component (3C) geophones can be buried on the surface, installed in shallow boreholes, or in deep downhole of treatment or offset wells to monitor micro-seismicity. Although the (near-)surface monitoring can provide a wide coverage, which yields a well-constrained horizontal location (Eisner *et al.*, 2011), it suffers from large uncertainty in depth and low signal-to-noise ratio (S/N) due to signal attenuation and noises from surface human activities (Eisner *et al.*, 2011; Diller & Gardner, 2012). Therefore, downhole monitoring (commonly in offset wells) is more popular due to its closer monitoring position to the stimulated zone, leading to a higher S/N. Unlike the surface monitoring, downhole monitoring can provide a robust depth constraint. Yet, the accuracy in azimuth progressively degrades with the increasing distance between monitoring and treatment wells (Eisner *et al.*, 2011). In addition, the downhole monitoring fails to provide good coverage due to its restricted geometry in the borehole. Consequently, multiple offset wells, which may not be available, especially for new fields, are generally required to deduce the source mechanisms (Eaton & Forouhideh, 2011). However, drilling offset wells generally incur substantial additional costs (Lellouch

et al., 2020) and is not common, especially at the onset of large projects (Peyret *et al.*, 2012). It is also challenging for geophones to safely, efficiently and permanently perform in harsh downhole environment where high temperature, high pressure and aggressive chemicals are often encountered.

Recently, distributed acoustic sensing (DAS), sometimes also known as distributed dynamic strain sensing, via optical fibres (Fig. 1.5a) is attracting increasing attention for micro-seismic monitoring, as an alternative to traditional point sensors like geophones. DAS relies on elastic Rayleigh scattering (Fig/ 1.5b) from inhomogeneities in an optical fibre as encountered by a pulse of light. The optical fibre itself acts as densely distributed sensors that sense the strain or strain rate over a defined length, the so-called gauge length (Hartog, 2017; Hasani, 2024), as shown in Fig. 1.5a. It is a unique feature of DAS that it can provide continuous measurements over an entire well with high spatial and temporal resolution (Lellouch *et al.*, 2020; Mad Zahir *et al.*, 2023). Moreover, compared to conventional sensors such as geophones, DAS can be deployed in extremely harsh environments, such as geothermal wells, because the optical fibre is protected by primary polymer coating. Fibre-optic cables can be permanently installed behind well casings, thereby increasing the signal-to-noise ratio (S/N) (Lellouch *et al.*, 2020) and allowing regular operations to continue unimpeded. This eliminates the need to drill offset monitoring boreholes, thus saving costs. Yet, limitations exist and need to be considered when designing a DAS installation. Optical fibres sense the axial strain or strain rate along its trajectory, therefore only providing a one-component (1C) signal and leading to broadside insensitivity, i.e. no sensing of wave motion perpendicular to the cable orientation. The 1C nature of DAS has limited its capability of fully locating the micro-seismic events, particularly in polarity analysis (Lellouch *et al.*, 2020) and source-mechanism inversion.

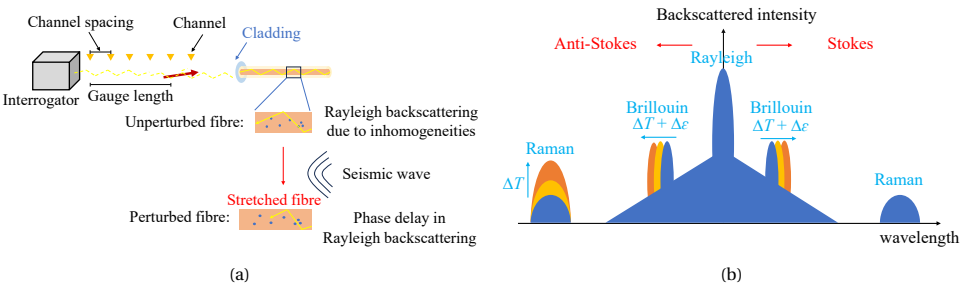


Figure 1.5: Illustration of the (a) DAS principle, and (b) different backscattered light in the fibre (after Li *et al.* (2022); EGU Seismology ECS Team (2023); Hasani (2024)).

1.4.2. SOURCE LOCALISATION AND MECHANISMS

Fully localising cracking events is important for tracking the stimulated volume, understanding in-situ stress states and stress rotation during stimulation. Some approaches have been proposed to fully localise a micro-seismic source. One of the possible solutions is to install optical fibres in multiple wells, e.g. the multi-well installation at the Hydraulic Fracturing Test Site 2 R & D program in the Permian Delaware Basin (Ciezobka, 2021) and the multi-well DAS micro-seismic monitoring program conducted in Northern Nevada

(Dadi *et al.*, 2024). Alternatively, optical fibres can be installed all the way along vertical and horizontal/over-deviated borehole sections, such as in the field case reported in Webster *et al.* (2013) and Verdon *et al.* (2020), and the field test implemented during hydraulic stimulation in the Meramec formation (Karrenbach *et al.*, 2019). However, drilling offset wells or horizontal wells is often costly and is not always possible due to restricted surface and geological conditions. Other methods have been proposed to localise the source but with requirements on the geological conditions. For instance, Lellouch *et al.* (2022) proposed to locate micro-seismic events based on recorded signals from a single horizontal fibre-optic cable, but their method requires conditions where the reservoir can act as a waveguide. Baird *et al.* (2020) takes advantage of the anisotropy (vertical transverse isotropic) of the media, where the vertical and horizontal shear-wave velocities differ, to fully constrain the location via a single horizontal fibre-optic cable. Although both methods show promising results, they need a-priori information and therefore limit their approach to a more general situation.

Determining the source mechanism of near-field micro-seismicity is essential to understand the physics of the stimulation processes, thus identifying the contributions from hydraulic fractures and natural fractures (or weak planes) (Nolen-Hoeksema & Ruff, 2001; Schoenball *et al.*, 2020). The seismic moment tensor can provide an estimate of the source mechanism and can be determined from the inversion of the observed seismic waveforms (Wu *et al.*, 2023). The moment tensor is a symmetric and second-order tensor which has six independent components. It is generally decomposed into three elementary parts: including isotropic (ISO), double-couple (DC) and compensated linear vector dipole (CLVD) parts, corresponding to volumetric changes (explosion or implosion), pure shear failure and tensile failure without volumetric change respectively (Vavryčuk, 2015). Therefore, the moment tensor is a direct representation of the stresses (or strains) in the vicinity of the source, and allows the estimation of orthogonal strain axes for each event and identification of the stress state at the front of stimulated area and the potential failure planes (Baig & Urbancic, 2010). For example, moment tensor inversion was performed by Ohtsu (1991) based on P-wave amplitude from eight micro-seismic events recorded during small-scale hydro-fracturing test in siliceous sandstone at the Imaichi underground power plant. Their results suggested tensile cracks occurred in the outer boundary with crack-opening motions perpendicular to pre-existing joints, while shear cracks occurred mainly near the treatment borehole with motions parallel to the joint plane. Studies on induced micro-seismicity from hydro-fracturing tests at the Hijiori (Japan) hot dry dock geothermal facility (Sasaki, 1998) and at the KTB borehole in North-East Bavaria (Germany) Jost *et al.* (1998) suggested best-fit DC focal mechanisms without significant volumetric component, indicating shear failures. Sasaki (1998) has shown that seismic energy radiated from a tensile failure is small as compared with that of a shear failure, resulting in less detectability of tensile cracking events. In contrast, non-DC components, corresponding to tensile failures, have been reported in the results of moment tensor inversion of singals recorded during hydraulic fracturing tests at the M-site field, Colorado (Nolen-Hoeksema & Ruff, 2001), at the European Hot Dry Rock (HDR) site of Soultz-sous-Forets, France (Cuenot *et al.*, 2006), at the Coso geothermal field, California (Julian *et al.*, 2007), and in the Carthage Cotton Valley, Texas (Šílený *et al.*, 2009). Yet, the non-DC components cannot be reliably resolved from a single vertical

array of receivers, thus leading to simplified assumptions on only deviatoric mechanisms (Nolen-Hoeksema & Ruff, 2001; Šílený *et al.*, 2009).

Before the non-trivial moment-tensor inversion, resolvability analysis is valuable to assess whether the unknowns can be accurately retrieved from an inversion (Vera Rodriguez *et al.*, 2011). Resolvability of the full moment tensor based on synthetic data has been investigated for three-component (3C) geophones (particle velocities) (Nolen-Hoeksema & Ruff, 2001; Vavryčuk, 2007; Vera Rodriguez *et al.*, 2011) and for DAS (1C strain/strain rate) (Vera Rodriguez & Wuestefeld, 2020; Bader *et al.*, 2023; Wu *et al.*, 2023) in single and multiple vertical wells. For example, Vera Rodriguez & Wuestefeld (2020) analytically examined the resolvability from two vertical fibre-optic cables, separated at least 50 m from each other and aligned with the coordinate axes, with the source at the origin. This configuration ensures enough focal coverage to have a robust resolution of five components. And if one of the cables is moved away from the coordinate axes, the full moment tensor can be resolved (Vera Rodriguez & Wuestefeld, 2020). However, this configuration indicates that an additional well needs to be drilled, which is expensive.

1.5. EASYGO PROJECT

Given the challenges in geothermal operations and the ambitious expansion plans for geothermal energy in many countries, there is an urgent need for experts with a broad understanding of geothermal systems. The European-Commission-funded Marie Skłodowska-Curie Innovative Training Networks project EASYGO, which stands for Efficiency And SafetY in Geothermal Operations, created such an opportunity to train 13 next-generation geothermal experts. EASYGO brought together four of the IDEA League partners (TU Delft, ETH Zurich, RWTH Aachen and Politecnico di Milano) and ten industry partners. All the 13 PhD candidates were trained in two of the four universities and at least one of the industry partners. The ambition of EASYGO was to contribute to making Europe a world leader in geothermal science, operational technology and education, thereby accelerating the energy transition.

The individual research projects of this research programme covered the whole chain of geothermal operations. Specific research topics were: optimised representation of reservoir heterogeneity, reservoir management including upscaling of laboratory-scale measurements to reservoir scale, near-borehole coupled processes, power-plant component optimisation, optimised injection strategies including alternative fluid, e.g. CO_2, and geophysical-geochemical monitoring during operations. Different methods were used in the sub-projects, including on-site field measurements, laboratory experiments and novel simulation techniques. All sub-projects were aligned with two key research questions: "How do we run geothermal systems efficiently?" and "How do we run geothermal systems safely?"

This PhD project was one of the 13 sub-projects of EASYGO, aiming to investigate the near-borehole coupled thermo-hydro-mechanical (THM) processes and evaluate their impact on well performance. The research was conducted at TU Delft and RWTH Aachen, with an industry secondment at Aardyn to gain practical field experience.

1.6. MOTIVATION AND RESEARCH OBJECTIVES

A comprehensive understanding of coupled THM processes is essential for designing optimal injection/stimulation strategies that prevent injectivity impairment or facilitate its remediation when it occurs. However, understanding the subsurface processes is a non-trivial task.

Numerical simulation can help us understand the near-borehole coupled THM processes. Yet, it is challenging to model these processes when discontinuities exist. Simulating fracture initiation and propagation in permeable intact rock requires special techniques. Moreover, there is a need to incorporate the fatigue damage into existing constitutive law to investigate fatigue damage under cyclic coupled THM loadings, allowing the study of the combination of thermal and cyclic stimulation scenarios.

In addition to geo-mechanical simulation, micro-seismic monitoring is essential to observe if stimulation is to be effectively deployed, and as an effective method to understand and monitor operational near-borehole cracking events. DAS using optical fibres is gaining popularity in monitoring geothermal operations. Nevertheless, current geometry of the optical fibres requires an additional horizontal section or new offset wells to fully locate and characterise micro-seismic sources, largely increasing the cost. A more cost-efficient way is to install two fibre-optic cables separately in one vertical well, but its feasibility is unclear.

This thesis therefore aims to fill these gaps by:

(1) developing a fully coupled THM cohesive interface element that can be, combined with continuum finite element, used to model pre-existing fractures or potential cracking paths in intact rock;

(2) developing a new traction-separation law that incorporates fatigue damage under varying-amplitude and coupled THM loading;

(3) demonstrating modelling methods to simulate fracture initiation and propagation in highly permeable sandstone reservoir under cyclic THM processes;

(4) with the developed tool, evaluating different injection/stimulation scenarios, including monotonic, stepwise, cyclic, combined stepwise and cyclic stimulation, all with cooling effects considered;

(5) evaluating the feasibility of the dual-cable DAS in one vertical well for source localisation and source mechanism inversion.

1.7. OUTLINE OF THE THESIS

This thesis consists of 7 chapters, and is organised as follows.

Chapter 2 presents a comprehensive literature review on the injectivity issues encountered in geothermal projects. The history and motivation of re-injection is first introduced, followed by an explanation of the mechanisms behind injectivity decline and injectivity enhancement respectively.

Chapter 3 describes the development of a zero-thickness and triple-nodded interface element, which, combined with cohesive zone model, can be used to simulate fracture

initiation and propagation. The mathematical formulations for the continuum finite element and interface element are presented, together with the modelling approach to represent potential cracking paths in intact rock. In addition, substantial verification and validation are discussed to demonstrate the performance of the proposed model.

Chapter 4 further extends the work in Chapter 3 by developing a new elasto-damage constitutive law that incorporates a fatigue damage variable into the tensile branch, allowing the simulation of cyclic thermal stimulation scenarios. Extensive validations against cyclic Brazilian test, cyclic hydraulic test, and cyclic thermal stimulation test are performed to demonstrate the capability of the proposed model to capture fatigue damage under cyclic coupled THM loading, including varying-amplitude loading.

Chapter 5 presents the simulations of different stimulation scenarios using the developed tool. Fully coupled THM simulations are first performed on a normal injection scenario to a synthetic reservoir, inspired by the Geothermie Delft project. In addition, simulation of different stimulation scenarios to the synthetic reservoir with assumed near-borehole clogging are investigated. The stimulation performance of monotonic, stepwise and cyclic stimulation and combined stepwise and cyclic stimulation is evaluated and discussed.

Chapter 6 discusses the feasibility of using a dual-cable DAS in a single vertical borehole to locate and characterise the micro-seismic sources. The localisation process is first introduced with a base example. Localisation accuracy sensitivity to source parameters and noise levels is conducted. In addition, the resolvability of the moment tensor components is discussed on the basis of resolution matrix. Based on the previous geo-mechanical simulation, how the near-borehole tensile fractures can be understood is also discussed.

Chapter 7 summarises the main conclusions of this thesis, and recommendations for future research on the geo-mechanical modelling and micro-seismic monitoring are presented.

2

LITERATURE REVIEW ON THE MECHANISMS CAUSING INJECTIVITY CHANGES IN GEOTHERMAL PROJECTS

In geothermal projects, injectivity can be influenced during reinjection, both positively and negatively. A comprehensive review is conducted in this chapter to understand the mechanisms behind the increasing and decreasing injectivity. Interconnected physical, chemical and biological clogging contributes to injectivity decline, and the decreasing reservoir temperature plays a major role in triggering these processes. In contrast, re-opening/shearing of pre-existing fractures and thermal cracking are the main contributors for injectivity enhancement during reinjection. Detailed data showing worldwide examples of injectivity changes have been collected and presented.

This chapter has been published in Luo *et al.* (2023), to which Wen Luo and Anna Kottsova equally contributed as joint first author. Credit for the figures in this chapter go to Anna Kottsova.

2.1. INTRODUCTION

In geothermal projects, re-injection of produced water has been widely applied for disposing wastewater, supplying heat exchange media and maintaining reservoir pressure. Accordingly, it is a key process for environmental and well performance assessment, which partly controls the success of projects. However, the injectivity, a measure of how easily fluids can be reinjected into reservoirs, is influenced by various processes throughout installation and operation, as is summarised in Fig .2.1. Both injectivity decline and enhancement have been reported during re-injection operations, while most current studies tend to only focus on one aspect. This chapter aims to provide a comprehensive discussion on how the injectivity can be influenced during re-injection, both positively and negatively. This includes a detailed overview of the different clogging mechanisms, in which decreasing reservoir temperature plays a major role, leading to injectivity decline. Strategies to avoid and recover from injectivity reduction are also introduced. Followed is an overview of mechanisms underlying injectivity enhancement during re-injection, wherein re-opening/shearing of pre-existing fractures and thermal cracking have been identified as the main contributors. In practice, nevertheless, mixed-mechanism processes play a key role during re-injection.

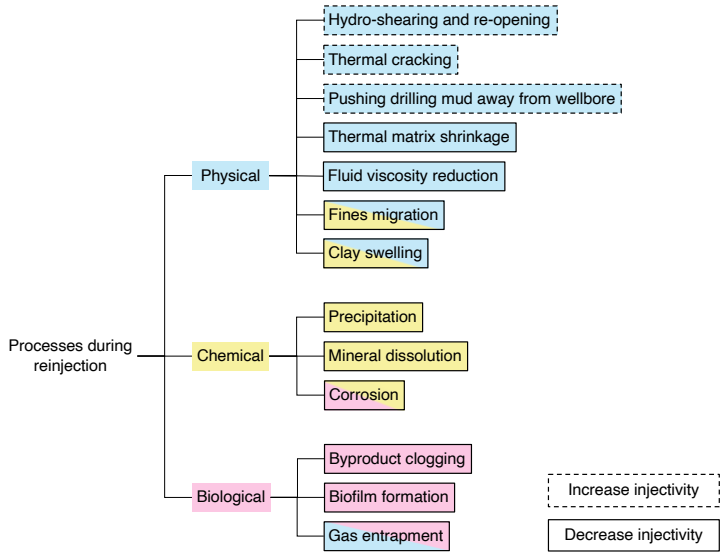


Figure 2.1: Overview of mechanisms underlying injectivity decline and enhancement during re-injection. Mechanics are color-coded by type, i.e. whether they are physical, chemical or biological. Mechanisms in two colours include two processes (i.e. physico-chemical, physico-biological, chemo-biological processes).

2.2. HISTORY AND REGULATION OF RE-INJECTION OF GEOTHERMAL FLUIDS

Re-injection techniques started to be applied in the late 1960s in Ahuachapan (El Salvador) (Stefansson, 1997) when low-temperature water was injected back into a high-

temperature reservoir for environmental reasons. From the 1970s, the number of re-injection wells has been continuously growing. The initial purpose of re-injection was the disposal of steam condensate. However, a positive influence on extraction well productivity was noticed. In 1987, wastewater was re-injected in the Geysers geothermal field in California when the production declined rapidly, and an improved production was noticed immediately (Goyal & Conant, 2010). Consequently, re-injection started to be applied also for reservoir performance improvement. Even though this method originated in high-enthalpy fields, it soon was also applied in low-enthalpy reservoirs. In low-temperature reservoirs, the amount of produced water which needs to be disposed of is substantially higher.

The discharge/disposal of geothermal fluids is an important issue, which is addressed by various national regulations, including in the USA and many countries of the EU. An overview of regulations on both reinjection and water discharge is summarized in Tab. . Even though regulations vary between countries, some similarities can be seen.

According to the EU Water Framework Directive (European Parliament and Council, 2000), no uniform obligation on re-injection of geothermal brine exists. National governments can decide individually whether geothermal fluid re-injection is required in their countries. In the Netherlands, permits are needed for discharge into surface water system or sewer system, which are only granted under strict environmental conditions (Dutch Government, 2024, 2025) and would not usually be met with geothermal waste water. Therefore, re-injection, allowed with a permit which specifies safe conditions (Staatstoezicht op de Mijnen, 2020), is the only viable option.

Table 2.1: Overview of worldwide regulations on re-injection and produced water discharge

Country	Obligatory re-injection?	Regulations on discharge of produced water
Belgium (Manzella *et al.*, 2021)	No	1) Discharge into natural surface systems is allowed after comprehensive quality-quantity check and treatment procedures. 2) Radioactivity control of fluids (NORM waste) before discharge is imposed.
France (Rybach, 2003)	No	1) Discharge into surface water needs to be authorised and requires control of radionuclides, total suspended solids (TSS), chemical oxygen demand (COD), temperature. 2) Radioactivity control of fluids (NORM waste) before discharge is imposed.
Germany (Rybach, 2003)	No	Water used for balneology cannot be reinjected.
Hungary (Rybach, 2003; German Environment Agency (UBA), 2011; Skog, 2019)	Yes	1) Water produced for greenhouse and space heating has to be reinjected. Reinjection of water used for balneology is prohibited. 2) Discharge into natural surface system is allowed after comprehensive quality-quantity check and treatment procedures. 3) Increased fees for the discharge of thermal water into surface water exist to promote reinjection.
Iceland (Kallesøe *et al.*, 2021)	No	1) In high-enthalpy reservoirs, reinjection is mostly used for the resource and environmental preservation. 2) Regulations on environmentally hazardous content exist. 3) Water from low-enthalpy reservoirs can be freely discharged into surface waters. 4) Due to low chemical content, water does not pose an environmental threat. 5) Limits on drawdown are established.
Italy (Manzella *et al.*, 2021)	Yes	Discharge to surface/shallow ground water is not allowed in Tuscany. Geothermal fluid is reinjected into the reservoir.

Continued on next page

(Continued from previous page)

Country	Obligatory re-injection?	Regulations on discharge of produced water
Netherlands (Dutch Government, 2024, 2025)	Implied	1) Permits are needed for discharge into surface water system or sewer system, which are only granted under strict environmental conditions, which would not usually be met with geothermal waste water, usually meaning that reinjection is the only viable option. 2) Reinjection is allowed with a permit which specifies safe conditions.
Philippines (Skog, 2019)	No	Reinjection is an operational requirement for geothermal fields due to environmental protection of agricultural areas.
Switzerland (Rybach, 2003)	No	Water management laws are determined individually by cantons.
USA (Skog, 2019)	Yes	Framework is defined individually by the states. For example, in California reinjection is obligatory to get full property rights.

Field experience has shown that re-injection does not only satisfy the environmental regulations, but also has a positive influence on extraction well productivity. Today, re-injection is widely applied for the following reasons (Kaya *et al.*, 2011):

(1) Produced water disposal due to environmental reasons and regulations.

(2) Recharge of the reservoir/aquifer.

(3) Pressure compensation to account for fluid extraction and to prevent subsidence.

(4) Enhancement of thermal extraction from over- and underlying formations.

(5) Thermal storage.

2.3. INJECTIVITY DECLINE DURING RE-INJECTION

One key issue that determines the success of re-injection, thus of the whole geothermal project, is to achieve and maintain injectivity, generally represented by injectivity index (the ratio of mass injection rate to pressure change, which can be represented by the wellhead pressure), at acceptable level. However, ensuring long-term good injection performance is non-trivial. In many geothermal fields where re-injection has been applied, continuous decreases in injectivity have been recorded. For example, significant injectivity decline were reported in Veysey Well 1 (49.41 $m^3/(h \cdot MPa)$ to 12.52 $m^3/(h \cdot MPa)$) in the Imperial Valley (Messer *et al.*, 1978), California, in Melleray doublet (21.25 $m^3/(h \cdot MPa)$ to 6 $m^3/(h \cdot MPa)$) (Boisdet *et al.*, 1989), France, and in Well Gt NG 2/89 (220 $m^3/(h \cdot MPa)$ to 124 $m^3/(h \cdot MPa)$) (Birner *et al.*, 2015), Neustadt-Glewe, Germany, where all the reservoirs are sandstone formation and the flow is dominated by matrix. In some extreme cases, poor injectivity performance has led to the abandonment of the wells (Ungemach, 2003; Markó *et al.*, 2024), or even the shutdown of the whole geothermal project, such as the Klaipeda geothermal plant in Lithuania, of which the operating company declared bankruptcy in 2017 (Guinot & Marnat, 2021). Tab. 2.2 collects geothermal field examples where decreasing injectivity was observed.

In the Netherlands, injectivity problems are often noticed and reported in, for example, several doublets in the western basin of the Netherlands, of which the micro-biological activities and precipitation of carbonates due to degassing of CO_2 in the systems are believed to be the main driven mechanisms (Water Research Institute (KWR), 2015; Croese *et al.*, 2019).

Table 2.2: Field examples of changes in injectivity index (II) during reinjection into geothermal reservoirs.

Field example	Reservoir temp.	Re-injection temp.	Injection period	Initial II	Ending II	Injectivity decline mechanisms
TR-14, Berlin (LDS), El Salvador (Castro *et al.*, 2006)	~290 °C	175 °C	Jul. 1998 - Oct. 1999	40 kg/s	10 kg/s	Silica precipitation in the reservoir
BR34, Broadlands, New Zealand (Boisdet *et al.*, 1989)	> 260 °C	94 °C	Nov. 1978 - Jan. 1979	4.35 kg/(s·bar)	3.48 kg/(s·bar)	Silica precipitation in the reservoir
KD-1A, Kizildere, Turkey (Yeltekin & Parlaktuna, 2006)	195 °C	(20 - 42) °C	Nov. 1975 - Dec. 1975	3.30 kg/(s·bar)	1.90 kg/(s·bar)	Silica scaling
KD-7, Kizildere, Turkey (Yeltekin & Parlaktuna, 2006)	205 °C	(97 - 98) °C	Jun. 1995 - Aug. 1995	0.73 kg/(s·bar)	0.19 kg/(s·bar)	Calcite scaling and consequent fines migration
R1, Otake, Japan (Itoi *et al.*, 1989)	(120 - 162) °C	(50 - 80) °C	Oct. 1983 - Jan. 1986	148.62 kg/(s·bar)	1.39 kg/(s·bar)	Silica scaling in the well
R2, Otake, Japan (Itoi *et al.*, 1989)	(120 - 162) °C	(50 - 80) °C	Jul. 1984 - Sep. 1986	91.39 kg/(s·bar)	27.20 kg/(s·bar)	Silica scaling in the well
Nag-67, Tiwi, Philippines (Ontoy *et al.*, 2003)	260 °C	(152 - 171) °C	1989 - 1999	9.13 kg/(s·bar)	1.30 kg/(s·bar)	Silica scaling in the well
Veysey, North Brawley, U.S. (Messer *et al.*, 1978)	(149 - 204) °C	-	Nov. 1975 - Dec. 1976	1.00 kg/(s·bar)	0.35 kg/(s·bar)	Silica scaling and consequent fines migration

Continued on next page

(Continued from previous page)

Field example	Reservoir temp.	Re-injection temp.	Injection period	Initial II	Ending II	Injectivity decline mechanisms
Gt-NG 2/89, Neustadt-Glewe, Germany (Dieudonné *et al.*, 2015)	99 °C	30 °C	2007 - 2012	6.11 kg/(s·bar)	3.44 kg/(s·bar)	Sulphate scaling and consequent fines migration
KGDP-1I, Klaipeda, Lithuania	36 °C	11 °C	2002 -2015	1.58 kg/(s·bar)	0.36 kg/(s·bar)	Gypsum precipitation and migration of corrosion products
KGDP-4I, Klaipeda, Lithuania	36 °C	11 °C	2002 -2015	8.58 kg/(s·bar)	0.31 kg/(s·bar)	
N/A (Triassic sediments), the Netherlands (Croese *et al.*, 2019; Kottsova *et al.*, 2022)	(80 - 84) °C	(30 -40) °C	2017 -2019	2.4 kg/(s·bar)	1.1 kg/(s·bar)	Corrosion + biological clogging of the well

Injectivity decline results in one or more of several possibilities: (i) less water injected with the same amount of produced water, (ii) a lower production and injection rate, or (iii) increased injection pressures to allow the same amount of water to be injected. For the first item, there would be less fluid pressure in the reservoir, with a potential consequence of land subsidence. For example, significant subsidence due to lowered reservoir pressure have been reported in Wairakei, Broadlands and Kaweru fields, New Zealand, among which the most serious subsidence (>14 m) has been observed in the Wairakei field since its operations (Allis, 2000). Another risk related to lowered reservoir pressure is the possibility of invasion of colder ground water, leading to early thermal breakthrough (Skog, 2019). Additionally, lower re-injection rates directly impact production rate, especially for hot dry rock reservoirs which lack both in-situ fluids and rock permeability and thus cannot be efficiently exploited without sustainable re-injection. Both imbalanced re-injection or higher injection pressures can also increase the potential for micro-seismicity. Of course, reducing both production and injection, has significant effects on the economic performance of a geothermal project.

There is a typical reduction of injectivity with a decrease of the temperature of injected water due to the impact of the increase in viscosity (in some cases, e.g. in the 2012 injection test in Groß Schönebeck (Blöcher *et al.*, 2016), viscosity decreased due to a reduced salt concentration despite the decreased temperature) and thermal shrinkage of the matrix. This is an unavoidable part of a geothermal project where fluid with a reduced temperature is injected. These processes are, in principle, reversible with a subsequent increase in temperature. However, the main process for a permanent reduction in injectivity is clogging. Several studies investigated specific aspects of clogging mechanisms during geothermal operations (Song *et al.*, 2020; Kamila *et al.*, 2021).

Primary clogging mechanisms can be divided into three groups based on the nature of the responsible processes (Fig. 2.1): a) physical processes, related to the migration of particles; b) chemical processes, caused by chemical reactions; c) biological processes as a result of bacterial activities. There are, however, processes which could be caused by different mechanisms or a combination of those, such as corrosion, they are therefore highlighted separately. Clogging processes occur at different stages of geothermal system operation, shown in Fig. 2.2, and will be described in detail in the following sections. While it is mostly clear, where each type of clogging occurs, the time scale can rarely be stated uniformly due to inability to track processes inside the porous media. Physical clogging by external fines has been reported to usually be the first one observed, while clogging due to chemical reactions may take a longer time (Rinck-Pfeiffer *et al.*, 2000).

2.3.1. PHYSICAL PROCESSES

Physical clogging has been identified as one of the primary mechanisms and also most common mechanism of injectivity decline in geothermal reservoirs for some decades (Song *et al.*, 2020). It was first observed in the early 1980s in the Paris basin, where severe clogging problems led to abandonment of several injection wells (Ungemach, 2003). Several different processes can be distinguished within physical clogging, such as migration of injected fines, internal particles transport (due to changes in pH and salinity and due to high flow rate) and clay swelling, shown in Fig. 2.3 (Bennion, 2002). It is important to mention, that the last two occur as a combination between physical and

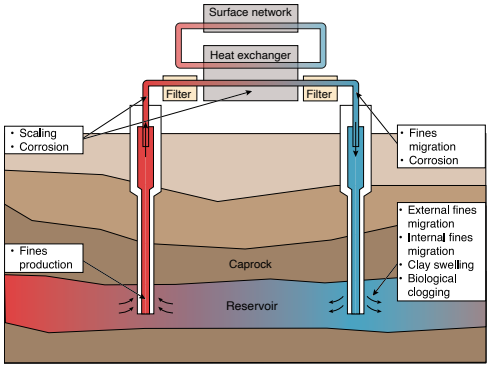


Figure 2.2: Schematic diagram of clogging at different stages of re-injection.

chemical processes. Two other mechanisms, excluded in the figure, are water viscosity decrease and thermal shrinkage of the matrix due to lower temperature of reinjected fluid.

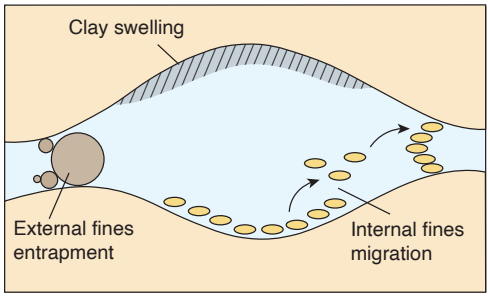


Figure 2.3: Schematic diagram of physical clogging processes.

The most common and first observed among the mentioned physical processes is external particle entrapment (Rinck-Pfeiffer *et al.*, 2000). Generally, suspended particles exist in produced water despite complex filtration systems and are, therefore, reinjected into the reservoir (Moghadasi *et al.*, 2004). Migrating particles can have different shapes, densities and sizes, which also influences their entrapment. Such entrapment could happen at different locations in the formation. Primarily, they can accumulate at the wellbore face, forming a filter cake or narrowing the wellbore (Ungemach, 2003). Similarly, fines may block the perforations. Finally, as particles migrate with fluid flow inside the porous media, they could induce permeability impairment inside the reservoir.

It has been traditionally accepted that at a ratio of particle size to pore diameter smaller than 1/7, no clogging occurs at smaller injection volumes. However, at large injected volumes this rule of thumb may not be satisfied [90]. Particles with smaller size distribution (starting from 5% to 7% of pore throat diameter) can also contribute to clogging if they form bridges due to electrostatic and van-der-Waals interaction (Bennion, 2002). Larger injected particles block the pores due to the size exclusion mechanism. Size distribution also influences the penetration depth of such particles. Wang *et al.* (2012)

in experiments with a seepage column of plexiglas identified 1 cm penetration depth for particles with sizes in the range of 0.075 to 0.0385 mm and 2 cm depth for fines smaller than 0.0385 mm. In most cases the depth of damage by external particles does not exceed 1–2 cm (Bennion, 2002).

Besides external particle entrapment, interaction of internal particles with injected fluids could also damage the injectivity as a result of particles detachment, migration and precipitation(Yuan & Wood, 2018). Detachment and adsorption of internal fines is controlled mainly by the equilibrium between electrostatic force and drag and lifting forces.

Electrostatic forces acting on particles can be influenced by pH and salinity variations. Mineralogical composition of most sandstone aquifers includes various types of clays. Clay minerals are very sensitive to the ionic strength and pH of injected fluids, as they may deflocculate or, on the contrary, form aggregates inside the porous media (Rosenbrand *et al.*, 2015). This problem is less common for the reinjection processes in geothermal operations, as the primary chemical composition remains unchanged. However, when fluids from external sources are injected, e.g. at Broadlands in New Zealand where cold river water was used (Horne, 1982), permeability could be damaged due to the incompatibility between injected and in-situ fluids. In addition, surface processes of scaling or gas dissolution might decrease the salt concentration, and bacterial activity can lead to changes in pH. These fluctuations can cause destabilisation of clay systems and, consequently, fines migration and pore blockage.

Furthermore, drag forces acting on internal particles can be influenced by injection parameters, such as rate of fluid circulation or dynamic viscosity (Song *et al.*, 2020; Ungemach, 2003). It was identified that an individual critical flow rate exists for each formation, which, if exceeded, can lead to internal fines detachment and migration (Nguyen *et al.*, 2021). For sandstones, critical flow rates in the order of 0.01 m/s have been reported, however, the rates are reservoir-specific (Nguyen *et al.*, 2021; Ochi & Vernoux, 1998). Consequently, optimal flow rate is expected to avoid fines detachment and migration and, at the same time ensure efficiency of geothermal production.

Similar processes also influence the swelling of clays, a phenomenon of significant increase in clay volume due to water invasion into layered structure of clay minerals, especially for the montmorillonite group. Up to 6 times increase in clay volume could be induced as a result of water penetration, causing severe permeability impairment (Shirazi *et al.*, 2010). Similarly to fines migration, if the composition of the reinjected water remains the same, clay minerals might not be affected. However, scaling during production could lower the salinity of reinjected fluid, thus leading to clay swelling.

Physical clogging can also be a result of gas entrapment. This can occur due to poor isolation in surface equipment and consequent air leaks, or biological activity in the reservoir (Bouwer, 2002). Gas clogging is highly influenced by pressure and temperature, although these are typically associated with production. For example, pressure drop or temperature increase can lead to gas exsolution from the infiltrated fluid inside the porous media (Bouwer, 2002), and pressure fluctuations during production can also lead to gas bubbles formation, reduce rock permeability and disturb the fluid flow (Boeije *et al.*, 2022). Furthermore, gas exsolution in the production casing can disturb the thermodynamic equilibrium of the geothermal fluid and consequently induce mineral scaling (Köhl *et al.*,

2020).

2.3.2. CHEMICAL PROCESSES

The problem of scaling and precipitation is quite common for geothermal fields. It was first recognised in the 1980s when serious scaling in the production equipment was noticed at geothermal sites (Portier *et al.*, 2009). Around the same time, wellhead injection pressure rise was linked to fluid-reservoir incompatibility which resulted in precipitation and blockage (Ochi & Vernoux, 1998). Even though previous studies mostly concentrated on the scaling problems in production lines and power plants, precipitation can also occur in the reservoir pore space during reinjection processes (Brehme *et al.*, 2018; Köhl *et al.*, 2020). Many field studies report scaling in production and power plant equipment (Pambudi *et al.*, 2015; Haklıdır & Balaban, 2019). The basic reason for chemical clogging processes is thermo-dynamic equilibrium shift due to changes of external parameters (Markó *et al.*, 2021). Precipitation and dissolution are the main chemical processes influencing injectivity, as shown in Fig. 2.4.

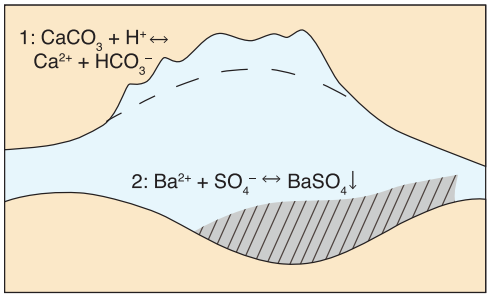


Figure 2.4: Schematic diagram of chemical clogging processes: 1 - dissolution (e.g. of calcite) increases pore space, 2- precipitation (e.g. of barite) decreases pore space.

Scaling can significantly decrease well injectivity and reduce operation efficiency (Haklıdır & Balaban, 2019). The most common natural mineral that could form scales is silica, followed by carbonates and sulfates (Dempsey *et al.*, 2012; Qazvini *et al.*, 2021). Stability of these minerals can be assessed by the saturation index (SI). It shows if a mineral tends to be dissolved or precipitated in water under certain conditions and is influenced by ionic concentration, temperature and pressure (Qazvini *et al.*, 2021). At SI < 0 a mineral is dissolved (under-saturation), at SI > 0 a mineral precipitates (super-saturation), while at SI = 0 water and minerals are in equilibrium.

SI is strongly temperature- and pH-dependent. Due to temperature changes during production, gas and vapor are released and the brine composition changes, which can lead to brine super-saturation (Setiawan *et al.*, 2019). The injection temperature optimal for scaling prevention is highly dependent on the reservoir conditions and may significantly vary between 130 °C – 170 °C for hot reinjection systems and 30 °C – 80 °C for cool injection in case of silica scaling (Kamila *et al.*, 2021).

Haklıdır & Balaban (2019) studied precipitation tendency for high-temperature geothermal fields. They calculated saturation indices for different minerals at a temperature range from 50 °C –250 °C. The curves for amorphous silica show that sampled fluids are

generally supersaturated at temperatures lower than 100 °C – 150 °C. Calcite, on the other hand, showed a high scaling risk, as fluids are supersaturated in the whole temperature range studied. Fluids with anhydrite and gypsum showed low risk for operations at temperatures >50 °C. Massive gypsum precipitation, however, has been reported at lower temperatures at a power plant in Lithuania operating at 11 °C – 40 °C (Brehme *et al.*, 2019).

The influence of pH on silica precipitation kinetics has been reviewed by Cornet & Jianmin (1995). They showed that the rate of silica polymerization and, consequently, precipitation also increases as a result of ionization of silica with pH, especially at high pH from 7.8 to 9.8 (Cornet & Jianmin, 1995). Therefore, operating with a pH 7 or lower is generally considered to mitigate silica polymerization kinetics.

Apart from natural mineral deposition, metal precipitation from geothermal brine can also occur. For example, lead scaling has been reported in several cases with high concentration of lead ions in formation water (Bressers & Wilschut, 2014; Holl *et al.*, 2003). This scaling is caused by redox reactions, where lead ions oxidized metallic iron, resulting in deposition of metallic lead (Bressers & Wilschut, 2014).

Another major chemical process is mineral dissolution due to rock-fluid interactions (Fig. 2.4), e.g. dissolution of calcite or muscovite near the wellbore zone (Chen *et al.*, 2020). The dissolution of minerals leads to an increase in ionic concentration of the flowing brine, which along with the reduced temperature of the injected fluid can result in secondary precipitation further inside the reservoir (Rinck-Pfeiffer *et al.*, 2000). Chen *et al.* (2020) modelled the balance between dissolution and precipitation in a granitic reservoir with SO_4·Cl–Na reservoir fluid type and showed that the balance can be achieved at 35 °C, thus minimising porosity and permeability variations.

Moreover, corrosion also influences the efficiency of geothermal operations. Corrosion refers to metal deterioration as a result of reactions between metals within engineered systems (e.g. tubulars) and geothermal brines. Various types of corrosion can be defined based on the agents causing chemical reactions: oxygen, hydrogen, chloride and others (Corsi, 1986). One of the major reasons for corrosion is saturation of brine with oxygen at different stages of geothermal operations, e.g. in the reinjection line, which further oxidizes Fe^{2+} to Fe^{3+} and leads to precipitation. It has been observed that the concentration of Fe^{3+} ions increases from the production to the injection site (Brehme *et al.*, 2018). The presence of chloride ions also enhances corrosion, even at temperatures less than 50 °C. Moreover, increase in concentration of hydrogen ions, i.e. decrease of pH level may also promote corrosion. Production of hydrogen sulphide (H_2S), due to bacterial activity, is a common example of this process (Veldkamp *et al.*, 2016a).

If the corrosion products are not filtered completely in the power plant, they could further migrate with the fluid flow into the reservoir and become a source of clogging as external fines. Some studies show that corrosion products make up to 60% of the external fines (Brehme *et al.*, 2018).

2.3.3. BIOLOGICAL PROCESSES

Bacterial clogging has been reported widely at geothermal sites, sometimes quite severe with permeability impairment up to 4 orders of magnitude (Thullner, 2010; Newcomer *et al.*, 2016; Brehme *et al.*, 2018; Burté *et al.*, 2019). Such clogging primarily occurs in

the near-wellbore zone but it has also been reported in the surface equipment, and thus can further be transferred into the reservoir during reinjection (Rinck-Pfeiffer *et al.*, 2000; Feng *et al.*, 2021). Several mechanisms of bacterial clogging have been observed (Baveye *et al.*, 1998; Song *et al.*, 2020; Bennion, 2002), as is illustrated in Fig. 2.5. Bacterial cells can accumulate in porous media: an increased concentration of organic matter on the rock surface leads to biofilm formation and impedes fluid flow. In addition, accumulated bacteria secrete high amounts of viscous polymer by-product as they grow (Rezaeizadeh *et al.*, 2021). This polymer increases the viscosity of moving fluids with decreased temperature due to reinjection and thus can decrease permeability (Song *et al.*, 2020). Furthermore, bacterial activity could promote scaling, e.g. iron oxide, and gas entrapment, e.g. H_2S, which could also reduce permeability.

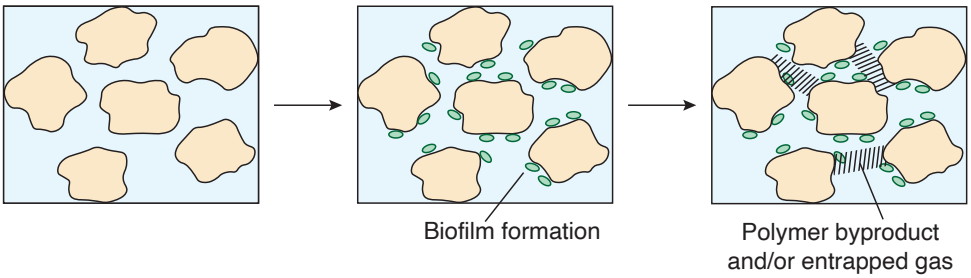


Figure 2.5: Illustration of biological clogging processes.

Generally, two different sources of bacteria can be defined. Primarily, groundwater may already contain anaerobic bacteria. Sulphate-reducing bacteria (SRB) are the most common anaerobic bacteria in the subsurface, they can produce H_2S, which leads to further problems (Baveye *et al.*, 1998): a) it decreases the pH and shifts thermodynamic equilibria of geothermal fluids; b) the produced gas can accumulate in bubbles, which, if large enough, can block porous channels; c) H_2S promotes oxidation of iron and magnesium irons, which can cause severe corrosion and produce dispersed scaling in the system (Brehme *et al.*, 2018). Burté *et al.* (2019) also reported that deposits produced during these reactions promote further microbial activity on the surface, thus aggravating the clogging process. Secondly, external aerobic bacterial cells can be accumulated during production, separation and reinjection processes. Their growth is mainly promoted due to contact with oxygen, e.g. during pumping (Gino *et al.*, 2010).

Bacterial activity is greatly influenced by the temperature variations. Generally, this activity is observed at temperatures lower than 90 °C (Bennion, 2002). SRB's activity has been reported for temperatures up to 80 °C (Rosnes *et al.*, 1991). Even thermophilic bacteria are active at temperatures of 85 °C–93 °C (Rosnes *et al.*, 1991). It can therefore be assumed that these bacteria are not active in high-enthalpy reservoirs, but might start their activity in the power plant and reinjection systems. In middle- or low-enthalpy geothermal systems, these bacteria are common and often cause clogging problems. Ma *et al.* (2021) investigated SRB in hot springs and identified their peak activity at temperatures between 30 °C–80 °C, depending on the population. Brehme *et al.* (2018) reported increase in bacteria population by a factor of 2.7 as a result of optimal growth

environment over several years in the low-enthalpy Klaipeda reservoir. However, the main bacterial activity was related to the surface infrastructure of the power plant, rather than the reservoir. The growth of bacteria in the power plant infrastructure, in combination with viscosity increase due to lowering of the temperature could cause obstructions of flow paths and injectivity problems.

Different types of clogging can occur in the geothermal reservoir, and many of them are coupled processes, occurring simultaneously or consequently. Ma *et al.* (2017) made a comparison between different types of clogging at the same temperature of 70 °C. It showed highest permeability reduction by chemical clogging, being 15.3%, followed by clogging by suspended particles at 12.6% and microbial clogging with 11.2% damage. Studying the combination of these effects and the prediction of total damage to the reservoir is a comprehensive task still to be solved.

2.3.4. STRATEGY TO AVOID AND RECOVER INJECTIVITY DECLINE

As discussed above, physical, chemical and biological clogging occurs as a result of incompatibility between injected fluids and targeted reservoirs, leading to injectivity decline. A thorough investigation of the characteristics of injected fluids (pH, compositions, solid contents, temperature, etc.) and targeted reservoirs (porosity/permeability distribution, in-situ temperature and pressure, brine compositions, mineralogy, etc.) is therefore necessary before operations. Based on the detailed understanding of the speciality and characteristics of injected fluids and targeted formations, actions can be taken before reinjection operations to avoid injectivity decline and during reinjection to recover injectivity if it has been damaged already. Several studies have provided comprehensive reviews of the clogging prevention and control measures throughout the reinjection cycle (Jeong *et al.*, 2018; Yoshitaka *et al.*, 2021; Wang *et al.*, 2023). Here the most common methods applied as well as some new proposed techniques are discussed.

As shown above, particle entrapment is one of the most common causes of damaged injectivity. Primarily, filtration systems allow the removal of most particles in the reinjection water. Additionally, monitoring the particles at key locations allows knowledge of where the particles are produced and thus prevents particle entrapment in the wellbore, perforation holes or near-field formation (Kindle *et al.*, 1984). Kindle *et al.* (1984) provided a general guideline for preventing particle entrapment, i.e. particles with a diameter between 0.45 μm and 10 μm should be removed from the injected water. Depending on the solid contents and particle size, different technologies can be used to remove the particles, including gravity separation, centrifugation and filtration.

The 'backwashing method' can also be used to remove an external filter cake if it has formed with a reversed flow in the well, while acid treatment can be used to clean the near-wellbore zone (Diaz *et al.*, 2016; Ungemach, 2003). However, interaction of different reservoir minerals with acid might lead to scaling and further clogging (Portier *et al.*, 2009), thus care should be taken. This can be eliminated with the use of suitable chemical additives, aimed at preventing chemical reactions in the reservoir. Clogging due to clay swelling can be avoided by adding clay swelling inhibitors, such as potassium chloride (KCl) if the formation is proven to be clay-rich. If clay swelling already occurs, strong acids, alcohols or certain ketones can be added to mitigate the effects (Kindle *et al.*, 1984). Prevention of scaling and precipitation can be performed with different

strategies, depending on the type of scaling. To prevent the migration of scales into the reinjection system, cooling ponds or precipitation basins can be installed and scaling inhibitors can be added (Kamila *et al.*, 2021), typically in high-enthalpy reservoirs due to larger temperature gradient and changes in chemical composition of in-situ brines (Setiawan *et al.*, 2019; Yanaze *et al.*, 2019). Controlling the injection temperature above a certain value to keep silica concentration below the amorphous silica saturation level is another widely-used approach to avoid silica scaling (Kindle *et al.*, 1984).

Pressure control is an effective method to avoid carbonate scaling by keeping CO_2 in solution, thus maintaining mineral solubility (Finster *et al.*, 2015). Additional injection of CO_2 can not only be used to control the pressure but also to shift the chemical equilibrium of carbonate, thus avoiding or mitigating the carbonate scaling. Modification of the pH level is another approach, particularly common for silica scaling prevention (Finster *et al.*, 2015), as it strongly influences the rate of scale formation. However, acid-related corrosion is a major concern of this technique.

Corrosion prevention is commonly done with the use of different chemical inhibitors. However, various temperature and pressure conditions in geothermal reservoirs challenge the selection of working chemicals. New methods aimed at removing iron from the geothermal fluid are also being developed, such as oxidation and filtration (Kalvani *et al.*, 2021), ultrafiltration or usage of bioadsorbents (Tang *et al.*, 2021; Fujita *et al.*, 2022).

Control of biological clogging can be challenging. One of the main challenges is the need for a detailed classification and characterization of bacteria in specific geothermal fluids (Feng *et al.*, 2021). Where there is a potential identified for biological clogging, minimization of such clogging is usually achieved by addition of bactericides, which requires extensive laboratory pre-testing, e.g. on fluid compatibility. Reduction of aerobic bacterial activity can be achieved by operating in closed surface loops without oxygen contact with water at the surface. Another way is sterilization of injected water, with chemicals or ultraviolet ray. Ma *et al.* (2017) observed the positive effect of that method, as sterilization decreased the microbial clogging rate from 15.3% to 4.1%.

In general, controlling reinjected fluid composition can help eliminate the negative effects of fluids incompatibility or thermodynamic effects. This can require comprehensive expensive laboratory testing, individually for each geothermal reservoir. In the case of bio-clogging detailed fluid analysis and time-consuming tests to identify bacteria origin can be required as well as experiments at the field conditions.

To the best of authors' knowledge, despite the development of advanced reservoir properties evolution models, no uniform system exists for prediction of the effect of different clogging mechanisms during well operation. Both experimental and numerical research, combined with field testing are required to approach this challenging task, aiming to predict and prevent injectivity decline in geothermal wells.

2.4. INJECTIVITY ENHANCEMENT DURING RE-INJECTION

Previous discussions have shown that injectivity is strongly temperature-dependent, mostly because chemical clogging and biological activities can be triggered at lower temperatures, as well as increasing viscosity of colder injected fluids can largely increase flow resistance. However, some field experiences have illustrated the positive effects of lower injection temperatures on injectivity, such as the injectivity increases observed during

cold water injection into well Th2 in the central Molasse basin (Germany) (Baumann *et al.*, 2017), HN-09 in Hellisheiði field (Iceland) (Gunnarsson, 2011) and MK-20 in Mokai field (New Zealand) (Grant *et al.*, 2013)]. Tab. 2.3 summarises field examples where unintentional injectivity enhancement has been observed as a result of re-injection of cold water. Such an unintentional increase in injectivity is helpful for energy saving, as lower injection pressures are then possible.

Although the potentially positive consequences of cold water injection have been well recognised and applied in thermal stimulation in deep geothermal reservoirs, it is often not easy to identify the predominant mechanisms for each specific reservoir during regular injection, as the mechanisms depend on the reservoir characteristics, e.g. fracture or non-fracture, in-situ temperatures and rock types.

Table 2.3: Field examples where unintentional increasing injectivity was observed during reinjection

Field example	Reservoir temp.	Re-injection temp.	Injection period	Initial II	Ending II
Th2, Molasse, Germany (Baumann *et al.*, 2017)	105 °C	60 °C	Jan. 2006 - Jan. 2012	0.8 kg/(s·bar)	1.3 kg/(s·bar)
BR7/BR23/BR28, Broadlands, New Zealand (Clotworthy, 1989)	272 °C	98 °C	June 1979	-	Increase in II reported
KD-1A, Kizildere, Turkey (Yeltekin & Parlaktuna, 2006)	195 °C	(20 - 42) °C	Nov. 1975 - Dec. 1975	3.30 kg/(s·bar)	1.90 kg/(s·bar)
HN-09, Hellisheiði, Iceland (Gunnarsson, 2011)	~250 °C	(15/90/120) °C	Feb. 2009	4.50 kg/(s·bar)	5.20 kg/(s·bar)
OK-2, Southern Negros, Philippines (Dobbie *et al.*, 1982)	257 °C	-	Apri. 1981 - Dec. 1981	1.3 kg/(s·bar)	2.5 kg/(s·bar)
4R1, Tongonan, Philippines (Horne, 1982; Dobbie *et al.*, 1982)	324 °C	170 °C	Feb. 1978 - Dec. 1981	2.3 kg/(s·bar)	13 kg/(s·bar)

2.4.1. INDIVIDUAL MECHANISMS

There are four main possible physical mechanisms for thermal enhancement of permeability, as is shown in Fig. 2.6: a) re-opening of pre-existing fractures, b) shear dilation of pre-existing fractures, c) new thermal fractures, d) secondary thermal fractures perpendicular to main fractures. In addition, the condensate of steam in high enthalpy reservoirs containing two-phases of water, increases water saturation thus increasing relative permeability of water can contribute to increasing injectivity. This has been observed through decreasing injection pressure while re-injection into BR7 in the Broadlands field already in 1981 (Horne, 1982). In addition, although cleaning of debris or mineral precipitation from near-field fractures is also believed to contribute to injectivity enhancement during re-injection, it occurs most likely when injection/stimulation tests are carried out immediately after drilling, e.g. stimulation operations at the Reykir geothermal field in Iceland in 1970s (Axelsson *et al.*, 2006).

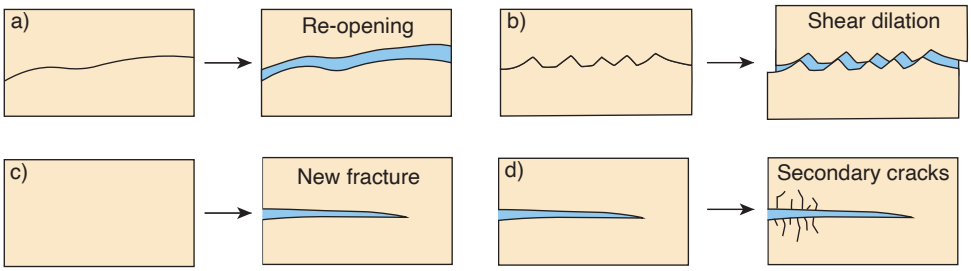


Figure 2.6: Four mechanisms of thermally induced permeability increase during reinjection.

The re-opening of pre-existing fractures is a result of cooling thus contraction of the rock matrix (Grant *et al.*, 2013), as well as the increase in fluid pressure in fractures, which is confirmed by various numerical simulations (Ghassemi, 2012; Koh *et al.*, 2011). In subsurface, rocks are laterally constrained. Thus, once the rock matrix is cooled down, thermal stress increments occurs in the tensile direction, pulling the fracture faces apart. The thermally-induced tensile stress increments reduce the stresses at the contacting asperities of pre-existing fractures, increasing permeability. High stresses at contacting asperities has been shown experimentally to cause pressure dissolution creep that can lead to further decreasing fracture permeability (Yasuhara *et al.*, 2011; Faoro *et al.*, 2016). The re-opening of pre-existing fractures is considered to be underlying the increase in injectivity of wells BR13 and BR23 from the Broadland field, New Zealand, during the reinjection in 1980 (Grant *et al.*, 2013), as well as the success of thermal stimulation of the KJ-14 well in 1980 (Krafla, Iceland) (Siratovich *et al.*, 2011). The increase in injectivity caused by re-opening pre-existing fractures is often reversible (e.g. BR23 showing reversible injectivity changes) (Grant *et al.*, 2013), which means injectivity will decrease if reinjection stops and increase again if reinjection re-starts. However, during cyclic injection, irreversible injectivity changes may be caused by frictional and mating effects on fracture surfaces (Lima *et al.*, 2019).

In contrast, increase in injectivity caused by shear dilation is irreversible as observed during an injection test in GPK1 at Soultz Hot Dry Rock (HDR) site (Evans *et al.*, 2005), and a low-pressure stimulation in NWG-55-29 at Newberry Volcano EGS site (Cladouhos *et al.*,

2016). The fracture aperture increases as a result of self-propping of fracture asperities(Fig. 2.6). The irreversible increase in permeability is also confirmed in laboratory tests on granite rocks (Vogler *et al.*, 2016; Ye & Ghassemi, 2018). However, no change or even decrease in permeability has been observed during shearing tests on low-porosity sandstone samples, likely due to fault core compaction (Kluge *et al.*, 2021). When stimulating fractured reservoirs, shear dilation is increasingly thought to be the dominant mechanism (Bijay & Ghazanfari, 2021). Consequently, hydro-shearing now is becoming a popular stimulation technology with the injection of cold fluids at pressures far below fracture pressure to shear natural fractures. Although increasing pore pressure is considered as the primary reason for shear slip of pre-existing fractures, thermal stresses are attracting more attention as re-injection pressure is generally insufficient to shear natural fractures (Ghassemi *et al.*, 2007). For instance, modeling results by Jeanne *et al.* (2014) have shown that shear failures of pre-existing fractures were induced by thermal contraction around the wellbore, where strong cooling effects occur during cold water injection into well P32 at Geyser geothermal field, California. Thermal stresses have also been believed to partly contribute to post-injection micro-seismic events caused by shear slip of fractures/faults, such as post-injection seismic events at Soultz-Sous-Forêts (Evans *et al.*, 2005) and at Basel (Häring *et al.*, 2008), since heat transfer in subsurface is much slower than fluid flow that can induce micro-seismic events right after reinjection.

Thermal fractures are believed to be a result of nucleation, growth, interaction and coalescence of micro-cracks, which include inter-granular and intra-granular micro-cracks, resulting from mismatches of thermal expansion between adjacent mineral particles and from the temperature gradient in the rock (Wang *et al.*, 1989). New thermal fractures are most likely induced around a wellbore, where there the highest temperature gradient occurs. However, secondary thermal cracks that are perpendicular to the main fractures, shown in Fig. 2.6 (d), can also occur in the deeper reservoir, and have been believed to be of great importance for increasing injectivity, particularly in EGS (Zhou *et al.*, 2010). For instance, tracer, micro-seismic and geochemical measurements indicated that thermally-induced secondary crack growth contributed to the observed reservoir growth during stress-unlocking experiments at well EE-1 at the Fenton Hill site, New Mexico, where hydraulic fracturing and sidetracking from the GT-2 well created the primary reservoir (Tester *et al.*, 1989). However, thermal energy production was only increased by 25%–30% by means of non-interacting secondary fractures. Numerical simulations by Zhou *et al.* (2010) indicate that continuously-growing and interacting secondary fractures, that can be induced deeply into the reservoir, contribute largely to the increase of injectivity and energy extraction efficiency.

In summary, injectivity could be influenced by various processes during operations and the injectivity decline, which is often reported, can endanger geothermal projects. Disturbances in temperature, pressure, stress field and chemical composition in geothermal reservoirs due to re-injection could trigger complex coupled processes (physical, chemical, biological or a combination of them) that influence injectivity. Fig. 2.1 summarises the processes that can either deteriorate or enhance injectivity during re-injection. Those processes affecting the near-wellbore area largely control the overall injectivity, and should be considered prior to any operations.

2.4.2. COMBINED MECHANISMS

Each main mechanism that explains injectivity enhancement during reinjection was introduced separately in the last section. However, in practice, these processes generally happen at the same time and are difficult to distinguish from each other. For instance, the successful stimulation test at KJ-14 at Krafla, Iceland, was attributed to both re-opening of pre-existing fractures and initiation of new thermal fractures (Siratovich *et al.*, 2011). Also at the COSO EGS site, evidence for both mode I and mode II fractures have been reported during stimulation experiments (Ghassemi, 2012). One particular example of mixed mechanisms is wing cracks, as is shown in Fig. 2.7, an out-of-plane growth of pre-existing fractures occurring meanwhile shear slip happens. These wing cracks indeed fail in tension, in the orientation of the most compressive stress (Johnson, 2014). The mixed-mechanism shear slip and tensile wing cracks have been studied in forward models to explain the micro-seismic signals during water injection into well P32 at the Geysers field (Johnson, 2014). Wing cracks were also observed in experimental works by Ye & Ghassemi (2018), in which the equivalent permeability of the sample was enhanced by 17–35 times as a result of initiation and coalescence of wing cracks.

Inspired by the fact of the mixed mechanisms behind reinjection and stimulation, mixed-mechanism stimulation (MMS) has been proposed(McClure & Horne, 2014; Norbeck *et al.*, 2018), to stress the difference from pure fracturing/shearing stimulation. Norbeck *et al.* (2018) believed that the stimulation to Pohang EGS, South Korea, where operations caused shear stimulation in one well while hydraulic fracturing in another well located in close proximity and at same depth (Park *et al.*, 2017), rovides possible evidence for potential MMS success. The idea of MMS is that MMS guarantees interaction and coalescence of new and pre-existing fractures and the formation of large-scale fracture networks, which can largely increase flow surface and heat transfer efficiency. Pioneering modelers have worked on MMS to shale reservoirs, but application to geothermal reservoirs still need to attract attention (Norbeck *et al.*, 2018).

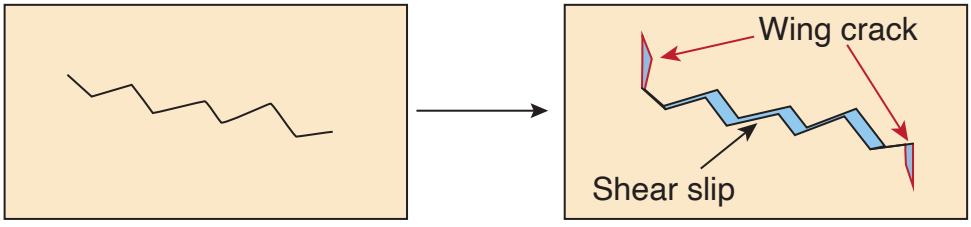


Figure 2.7: Schematic drawing of a shear slip of a pre-existing fracture with wing cracks initiated.

In addition, cyclic stimulation is also gaining popularity due to its management of the breakdown pressure. Field-scale tests performed on Well PX-1 at the Pohang EGS site in South Korea has demonstrated that cyclic stimulation scheme was able to improve the injectivity while managing the largest seismic below the targeted threshold of M_w 2.0 (Hofmann *et al.*, 2019; Zang *et al.*, 2021). Experimental tests have also shown fatigue damage effects due to cyclic injection to sandstone and granite samples (Patel *et al.*, 2017; Zhuang *et al.*, 2019b; Kang *et al.*, 2020).

2.5. CONCLUSION

Reinjection is a key process for geothermal projects that is critical for environmental and project performance. The injectivity is, however, influenced by various processes throughout installation and operation. This review provides a comprehensive discussion on how injection can cause both positive and negative effects. Both effects should be carefully considered when planning the reinjection strategy. Typically, the injection temperature is of great importance for both sides, either triggering clogging, which can reduce injectivity or inducing thermal cracking that may significantly enhance injectivity.

Injectivity can be significantly affected by different clogging processes, which result in pore blockage and permeability decrease. Three major groups of physical, chemical and biological processes are distinguished, of which all can be interconnected. Injectivity impairment reasons are unique to every geothermal field due to different reservoir types and properties, as well as fluid and rock composition. Different parameters affect individual mechanisms, the most common being decreased temperature due to the principle of geothermal energy extraction. Due to the systems complexity and uniqueness, the prediction of clogging processes is not a trivial task, especially taking into account the interconnection between different processes. Even though a variety of preventive measures for maintaining rock permeability has been developed and applied in the geothermal industry, the problem of clogging is still relevant and requires individual comprehensive analysis for every case.

Although lowering the injection temperature can trigger various clogging problems and increase fluid viscosity, leading to increasing flow resistance, injectivity enhancement during reinjection has been widely reported in such cases. Thermally-induced re-activation of pre-existing fractures and thermal cracking are believed to be the main reason. While reversible changes in injectivity have been ascribed to re-opening of pre-existing fractures, irreversible changes are generally owing to shear dilation of pre-existing fractures and formation of new fractures. However, it is not easy to identify exact stimulation mechanisms for each specific reservoir, as the mechanisms are reservoir-specific and depending on the reservoir characteristics, e.g. fracture or non-fracture, in-situ temperatures and rock types, and operating conditions. In practice, various processes related to thermal stresses occur at the same time during reinjection, and it is difficult to distinguish one from another.

Inspired by the mechanisms behind injectivity enhancement during re-injection of cold water, mixed mechanism stimulation and soft stimulation have been proposed to improve the injection performance and/or manage the high injection pressure, which could potentially induce micro-seismicity. Although thermal stimulation and cyclic stimulation have been gaining popularity and been performed in laboratory and fields, a combination of both has rarely been reported and studied. Therefore, this thesis aims to study the cyclic thermal stimulation strategy to fill this gap.

3

COUPLED THM COHESIVE INTERFACE ELEMENT: THEORY, VERIFICATION AND QUALITATIVE VALIDATION

A method is presented in this chapter to simulate coupled thermo-hydro-mechanical processes, including the re-activation of existing fractures and fracturing of the rock matrix. The model is based on the finite element method, and utilises a newly developed cohesive interface element to represent discontinuities. The interface element belongs to the family of zero-thickness elements and is triple-nodded. It is developed to allow the simulation of longitudinal and transversal fluid/heat flow. The method is successfully verified against analytical solutions for hydraulic fracturing (KGD model) and for the thermo-hydraulic response of a single fracture (Lauwerier's problem). Qualitative validation is achieved against experimental data of cold water injection in granite samples.

This chapter has been published in Luo *et al.* (2025d).

3.1. INTRODUCTION

In this chapter, a fully coupled THM model using zero-thickness and triple-noded interface elements is developed, on the basis of existing literature (Collin *et al.*, 2002; Lequesne *et al.*, 2006; Liaudat *et al.*, 2023), to allow the simulation of fracture initiation and propagation under coupled THM loading. Heat conduction and convection are allowed in both longitudinal and transversal directions of the interface element, with stabilisation used for cases with high Péclet number. An elasto-damage law is used to characterise the mechanical response of the discontinuity, allowing the opening of the interface elements. This, in turn, leads to strong coupling, as the longitudinal hydraulic conductivity of the interface elements evolves with the opening. In addition, a node-to-node contact approach is used to pre-determine the contact faces of the interface elements, thus assuring that the contact faces are pre-determined and accelerating computation, particularly when interface elements are inserted in between all the continuum elements, as discussed in the validation example. Compared to the previous work by Liaudat *et al.* (2023), the current work expands the application of the proposed method for geothermal reservoirs and other cases where coupled THM processes in discontinuities play a key role. In addition, the substantial verification and validation implemented in this work demonstrates the performance of the developed method.

The structure of this chapter is as follows: first, a brief introduction to the modelling approach is presented, followed by the mathematical formulations for both continuous and discontinuous media. Subsequently, the code is verified against coupled thermo-hydraulic and hydro-mechanical analytical solutions to demonstrate its accuracy, after which the proposed method is validated against experimental results from a near-borehole thermal fracturing experiment conducted by Zhang *et al.* (2019)

3.2. NUMERICAL MODEL

3.2.1. MODELLING APPROACH

Modelling fracture behaviour in continuous porous media (e.g., rock) is a non-trivial task, as discontinuities break displacement compatibility of standard FEM formulations and pose strong singularities in the solutions. To mitigate these difficulties, zero-thickness interface elements, a conceptually simple technique, are used to represent the discontinuities in this work. Interface elements are inserted in between continuum elements to represent pre-existing or potential fractures, as is shown in Fig. 3.1. A 2D modelling approach is used, with each interface element having in total 9 nodes, equally distributed on top, mid, and bottom planes (Fig. 3.1b). For an unloaded interface element, these three planes coincide in the same position. That means, for instance, that nodes 1^{t}, 1^{m}, and 1^{b} have initially the same coordinates. This is why this element is called a zero-thickness and triple-nodded interface element.

The bottom and top faces of the interface element share nodes with the continuum element with four degrees of freedom corresponding to coordinates x, and y, water pressure p_{w}, and temperature T, while the mid-plane nodes have only degrees of freedom of water pressure p_{w} and temperature T. In this way, different constitutive laws can be used for the continuum and the discontinuities, allowing for a more realistic representation of the heat and fluid flows along and across the fracture. The nodes of the bottom and top

faces of the interface which are in contact with each other are pre-determined to both improve robustness and decrease computation. This, however, reduces the amount of shear displacement possible.

In a previous work, Liaudat *et al.* (2023) developed a Pneumo-Hydro-Mechanical Interface (PHMI) element to simulate gas fracturing in saturated clay samples under isothermal conditions. In this work, theinterface element is further developed to take into account thermal processes under the assumptions that the material is always water saturated (i.e., without considering a gas phase). Additionally, the water properties (e.g., density and thermal conductivity) are assumed to be linearly proportional to temperature change. In the following section, the mathematical formulations for both the continuum and discontinuities are described. The newly developed formulations have been implemented into the FEM code LAGAMINE (Charlier, 1987), in which the formulation of continuum was implemented by Collin *et al.* (2002). The finite element procedure of the interface element, as an example, is presented in Appendix A

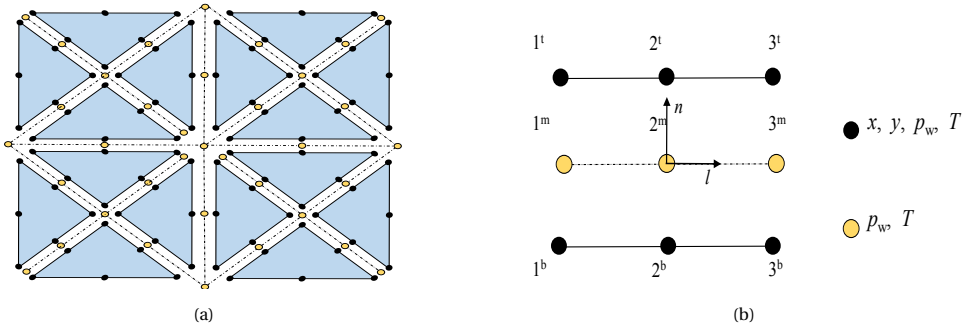


Figure 3.1: Finite elements used. (a) Interface elements in between continuum elements to represent pre-existing or potential cracking paths, and (b) Element node numbering, nodal degrees of freedom and local basis

3.2.2. GOVERNING EQUATIONS FOR THE CONTINUUM POROUS MEDIUM

The governing equations follow the formulation proposed by Collin *et al.* (2002) Here the equations with corresponding constitutive laws are briefly introduced.

HYDRAULIC PROBLEM

The water mass balance equation without any internal source or sink reads as follows::

$$\frac{\partial(\phi\rho_w)}{\partial t} + \nabla\cdot(\rho_w \mathbf{v}_w) = 0 \tag{3.1}$$

where ρ_w [kg/m^3] is the water density, ϕ the porosity, and $\mathbf{v}_w$ [m/s] the Darcy velocity vector. The latter is in turn defined as:

$$\mathbf{v}_w = -\frac{\mathbf{K}}{\mu_w}\nabla p_w \tag{3.2}$$

where $\mathbf{K}$ [m^2] is the intrinsic permeability tensor, μ_w [Pa · s] is the water dynamic viscosity, and $\mu_w = 0.6612(T-229)^{-1.562}$, where T [K] is the temperature (Collin *et al.*, 2002). p_w [Pa] is the water pressure.

MECHANICAL PROBLEM

If equilibrium state is assumed and if gravity is neglected, the equation of momentum conservation reads as follows:

$$\nabla \cdot \boldsymbol{\sigma} = \mathbf{0} \tag{3.3}$$

where $\boldsymbol{\sigma}$ [Pa] is the Cauchy's total stress tensor.

The considered mechanical constitutive law for the bulk rock is the classical law (Jaeger *et al.*, 2009). If compressive stress and strain are defined as negative, the thermo-poro-elastic constitutive law reads as follows:

$$\Delta\boldsymbol{\sigma} = \mathbb{C} : \Delta\boldsymbol{\epsilon} - \alpha\Delta p_{\mathrm{w}}\boldsymbol{I} - \beta_{\mathrm{b}} K_{\mathrm{b}} \Delta T \boldsymbol{I} \tag{3.4}$$

where $\mathbb{C}$ is the 4th-order elastic stiffness tensor, $\boldsymbol{\epsilon}$ is the strain tensor, α is the Biot coefficient, $\boldsymbol{I}$ is the 2nd-order identity tensor, β_{b} is the bulk volumetric thermal expansion coefficient, and K_{b} [Pa] is the drained bulk modulus.

THERMAL PROBLEM

Under the assumption of local thermal equilibrium, with no internal source or sink, the equation of energy conservation reads:

$$\frac{\partial[(\rho c)_{\mathrm{b}} T]}{\partial t} + \nabla \cdot q_{\mathrm{T}} = 0 \tag{3.5}$$

where, $(\rho c_{\mathrm{p}})_{\mathrm{b}} = (1-\phi)(\rho c_{\mathrm{p}})_{\mathrm{s}} + \phi(\rho c_{\mathrm{p}})_{\mathrm{w}}$ is the bulk volumetric heat capacity (with c_{p} [J/(kg·K)] being the phase specific heat capacity, ρ the phase density, and the subscripts s and w referring to the solid and the water phases, respectively), and q_{T} [J/(m^2· s)] is the heat flux vector. The latter is obtained from the following expression:

$$q_{\mathrm{T}} = -\lambda_{\mathrm{b}} \nabla T + \rho_{\mathrm{w}} c_{\mathrm{pw}} \boldsymbol{q}_{\mathrm{D}} T \tag{3.6}$$

where the first term corresponds to Fourier's law with the bulk thermal conductivity given by λ_{b} [J/(m· s · K)] $= (1-\phi)\lambda_{\mathrm{s}} + \phi\lambda_{\mathrm{w}}$, and the second term corresponds to the heat advection due to water flow.

3.2.3. GOVERNING EQUATIONS FOR THE DISCONTINUITIES

The mechanical and hydraulic governing equations for the interface elements are inherited from Liaudat *et al.* (2023) with the gas phase being neglected. Additionally, the governing equations for thermal processes are included here. Note that the following equations are tailored for 2D problems.

HYDRAULIC PROBLEM

The mass balance for water in a differential volume of discontinuity wdl reads:

$$\frac{\partial}{\partial t}(w\rho_{\mathrm{w}}) + \frac{\partial q_{\mathrm{w}}^{\mathrm{l}}}{\partial l} - q_{\mathrm{w}}^{\mathrm{b}} - q_{\mathrm{w}}^{\mathrm{t}} = 0 \tag{3.7}$$

where w [m] is the width of the discontinuity, $q_{\mathrm{w}}^{\mathrm{l}}$ [kg/(m·s)] is the longitudinal water mass flow, and $q_{\mathrm{w}}^{\mathrm{b}}$ [kg/(m^2·s)] and $q_{\mathrm{w}}^{\mathrm{t}}$ [kg/(m^2·s)] are the transversal water mass flows incoming to the discontinuity from surrounding continuum medium (Liaudat *et al.*, 2023).

The mass flows in Eq. (3.7) can be expanded as:

$$q_{\mathrm{w}}^{\mathrm{l}} = \rho_{\mathrm{w}} v_{\mathrm{w}}^{\mathrm{l}}; \quad q_{\mathrm{w}}^{\mathrm{b}} = \rho_{\mathrm{w}} v_{\mathrm{w}}^{\mathrm{b}}; \quad q_{\mathrm{w}}^{\mathrm{t}} = \rho_{\mathrm{w}} v_{\mathrm{w}}^{\mathrm{t}} \tag{3.8}$$

where $v_{\mathrm{w}}^{\mathrm{l}}$ [m^2/s], $v_{\mathrm{w}}^{\mathrm{b}}$ [m/s] and $v_{\mathrm{w}}^{\mathrm{t}}$ [m/s] are the longitudinal and transversal (top and bottom) volumetric flows. These flows obtained from the following generalised Darcy's law:

$$v_{\mathrm{w}}^{\mathrm{l}} = -\frac{t^{\mathrm{l}}}{\mu_{\mathrm{w}}} \frac{\partial p_{\mathrm{w}}^{\mathrm{m}}}{\partial l}; \quad v_{\mathrm{w}}^{\mathrm{b}} = -\frac{k^{\mathrm{b}}}{\mu_{\mathrm{w}}} \check{p}_{\mathrm{w}}^{\mathrm{b}}; \quad v_{\mathrm{w}}^{\mathrm{t}} = -\frac{k^{\mathrm{t}}}{\mu_{\mathrm{w}}} \check{p}_{\mathrm{w}}^{\mathrm{t}} \tag{3.9}$$

where t^{l} [m^3] is the longitudinal hydraulic coefficient, k^{b} [m^2] and k^{t} [m^2] are the transversal permeability of the interface, $p_{\mathrm{w}}^{\mathrm{m}}$ [Pa] is the water pressure at the middle plane, and $\check{p}_{\mathrm{w}}^{\mathrm{b}}$ [Pa] and $\check{p}_{\mathrm{w}}^{\mathrm{t}}$ [Pa] are the transversal pressure jumps between the bottom and top face and the mid-plane, respectively. The transversal pressure drops are defined as follows:

$$\check{p}_{\mathrm{w}}^{\mathrm{b}} = (p_{\mathrm{w}}^{\mathrm{m}} - p_{\mathrm{w}}^{\mathrm{b}}); \quad \check{p}_{\mathrm{w}}^{\mathrm{t}} = (p_{\mathrm{w}}^{\mathrm{m}} - p_{\mathrm{w}}^{\mathrm{t}}) \tag{3.10}$$

where $p_{\mathrm{w}}^{\mathrm{b}}$ and $p_{\mathrm{w}}^{\mathrm{t}}$ are the water pressures at the bottom and top sides of the discontinuity.

The longitudinal hydraulic coefficient t^{l} is estimated using the Reynolds lubrication equation, which describes the laminar flow of an incompressible and Newtonian fluid flowing between two parallel plates (Zimmerman & Yeo, 2000). It reads:

$$t^{\mathrm{l}} = \frac{r_{\mathrm{n}}^3}{12} + t_0^{\mathrm{l}} \tag{3.11}$$

where r_{n} [m] is the normal separation of the interface, and t_0^{l} [m^3] is the initial longitudinal hydraulic coefficient, which makes it possible to assign an initial longitudinal transmissivity to the discontinuity even if it is closed from the mechanical point of view. The longitudinal hydraulic coefficient t^{l}, defined in Eq. 3.11, plays the same role in the hydraulic governing equations of the discontinuity as the intrinsic permeability $\mathbf{K}$ in the hydraulic governing equations of the continuum. Both parameters account only for the geometrical characteristics of the medium through which the liquid flows, i.e., they are independent of the fluid properties. The fluid properties (as well as the time dimension) are introduced via the water dynamic viscosity μ_w in Eqs. 3.2 and 3.9, for the continuum and discontinuities, respectively.

The width w will evolve with the normal separation of interface r_{n}:

$$w = r_{\mathrm{n}} + w_0 \tag{3.12}$$

where w_0 [m] can be set to be non-zero to assign an initial storage volume to the discontinuity even if it is mechanically closed (Liaudat *et al.*, 2023).

MECHANICAL PROBLEM

The equation of momentum conservation for the interface element reads as follows:

$$\frac{\partial \boldsymbol{\sigma}_{\mathrm{c}}}{\partial l} = \mathbf{0} \tag{3.13}$$

where l is the longitudinal axis of the interface element, and $\boldsymbol{\sigma}_c = [\sigma_n, \sigma_l]$ [Pa] is the total stress on the interface mid-plane, with σ_n and σ_l being the normal and shear stress components on that plane.

For the mechanical constitutive behaviour of the discontinuity, the bilinear traction-separation law schematically depicted in Fig. 3.2 is used (Mi *et al.*, 1998; Liaudat *et al.*, 2023). More advanced constitutive laws can be incorporated easily into the code. This bilinear law can describe fracture initiation and propagation characterised by six parameters: the maximum tension and shear strength σ_{n0} [Pa], σ_{l0} [Pa], the normal and shear "cracking"separation r_{n0} [m], r_{l0} [m], the normal and shear debonding separation r_{nc} [m], r_{nc} [m]. The dashed lines in Fig. 3.2 represents the unloading-reloading path when reaching the relative displacement r_n^* or r_l^*.

In the loading condition, the normal and shear stresses are given by the following expressions:

$$\sigma'_n = \begin{cases} (1-D)K_{n0}r_n & \text{if } r_n \geq 0 \\ K_{n0}r_n & \text{if } r_n \leq 0 \end{cases} \tag{3.14}$$

$$\sigma_l = (1-D)K_{l0}r_0 \tag{3.15}$$

where σ'_n [Pa] represents Terzaghi's effective normal, defined as $\sigma'_n = \sigma_n + p_w^m$. $K_{n0} = \sigma_{n0}/r_{n0}$ [Pa/m] and $K_{l0} = \sigma_{l0}/r_{l0}$ [Pa/m] are the initial normal and shear slope respectively. When an interface element is used to represent natural fractures, the normal slope can have a physical meaning, interpreted as fracture stiffness, for instance, as a result of interpenetration of fracture surfaces due to presence of asperities (Cerfontaine *et al.*, 2015; Lei & Barton, 2022). In the context of this chapter, K_{n0} is interpreted as penalty coefficients, thus allowing negligible interpenetration of fracture surfaces regardless of their roughness (Cerfontaine *et al.*, 2015). To enforce the contact constraints, the slope should be set high enough to reduce artificial compliance (Liaudat *et al.*, 2023). However, the choice of their values is a trade-off between having artificial compliance and having numerical convergence problems. Additionally, D is the damage variable ranging from 0 (intact rock) to 1 (fully separated fracture). This damage variable evolves as follows:

$$D = \min\left(\frac{\bar{\omega}}{1+\bar{\omega}}\frac{1}{\eta}, 1\right) \tag{3.16}$$

$$\bar{\omega} = \max(\omega) \tag{3.17}$$

$$\omega = \left\langle \left(\frac{\langle r_n \rangle}{r_{n0}}\right)^{\beta} + \left(\frac{|r_l|}{r_{l0}}\right)^{1/\beta} - 1 \right\rangle \tag{3.18}$$

$$\eta = 1 - \frac{r_{n0}}{r_{nc}} = 1 - \frac{r_{l0}}{r_{lc}} \tag{3.19}$$

where ω is a positive scalar that defines the mechanical degradation of the interface element for a given normal and shear separations, $\bar{\omega}$ is a history variable that stores the maximum value reached by ω during the loading history, and $\langle\cdot\rangle = (\cdot + |\cdot|)/2$ is the Macaulay bracket (Liaudat *et al.*, 2023). β is a material parameter that characterise the mixed mode damage and is assumed to be 1 in this work (Liaudat *et al.*, 2023). The above

equations state that if the separation r_n (or r_l) is less than the normal crack separation r_{n0} (or r_{l0}), the damage variable D is then zero. If $r_{n0} < r_n < r_{nc}$ (or $r_{l0} < r_l < r_{lc}$), D is between 0 and 1, determined by the ratio of $(r_n - r_{n0})/(r_{nc} - r_{n0})$ and $(r_l - r_{l0})/(r_{lc} - r_{l0})$. Otherwise if r_n (or r_l) is beyond the debonding separation r_{nc} (or r_{lc}), D is forced to be 1, indicating a completely separation of the interface element.

Moreover, mechanical viscosity is added to the contact stress to resolve the solution jump that can result in numerical divergence (Lequesne, 2009; Liaudat *et al.*, 2023) :

$$\sigma'_n = \sigma_n + p_w^m + \sigma_v \qquad \text{with} \quad \sigma_v = \zeta \frac{\partial r_n}{\partial t} \tag{3.20}$$

where ζ [Pa · s/m] is the viscosity added to resolve large fast changes in the solution, which occur faster than the time discretisation, and can cause numerical divergence. The added viscosity ζ slows down the strain rate and thus stabilised the solution. Detailed discussion on the solution jumps and how the added viscosity helps mitigate this issue can be found in other works (Lequesne, 2009; Liaudat *et al.*, 2023).

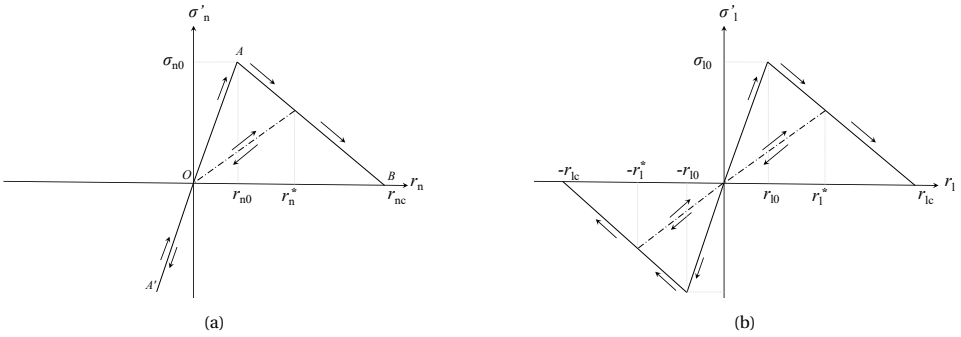


Figure 3.2: The elasto-damage law (following Liaudat *et al.* (2023)). (a) normal branch; (b) shear branch. The dashed line indicating the un-loading/re-loading path after reaching relative displacements r_n^* or r_l^*.

THERMAL PROBLEM

The conservation of energy, in terms of temperature, applied to a differential volume of discontinuity $w\mathrm{d}l$ reads:

$$\frac{\partial}{\partial t}(w\rho_w c_{pw} T^m) + \frac{\partial q_T^l}{\partial l} - q_T^b - q_T^t = 0 \tag{3.21}$$

where q_T^s [J/(m^2· s)] is the rate of change of the heat stored in the discontinuity, q_T^l [J/(m · s)] is the longitudinal heat flow, q_T^b [J/(m^2· s)] and q_T^t [J/(m^2· s)] are the normal heat flows incoming from the surrounding continuum medium via bottom and top faces to the discontinuity, respectively.

The terms in Eq. (3.21) can be expanded as:

$$q_T^l = -w\lambda_w \frac{\partial T^m}{\partial l} + c_{pw} q_w^l T^m \tag{3.22}$$

$$q_{\mathrm{T}}^{\mathrm{b}} = -\lambda_{\mathrm{w}} \frac{2\check{T}^{\mathrm{b}}}{\max(w, \bar{w})} + c_{\mathrm{pw}} q_{\mathrm{w}}^{\mathrm{b}} \check{T}^{\mathrm{b}} \tag{3.23}$$

$$q_{\mathrm{T}}^{\mathrm{t}} = -\lambda_{\mathrm{w}} \frac{2\check{T}^{\mathrm{t}}}{\max(w, \bar{w})} + c_{\mathrm{pw}} q_{\mathrm{w}}^{\mathrm{t}} \check{T}^{\mathrm{t}} \tag{3.24}$$

where $\check{T}^{\mathrm{b}} = T^{\mathrm{m}} - T^{\mathrm{b}}$ and $\check{T}^{\mathrm{t}} = T^{\mathrm{m}} - T^{\mathrm{t}}$ are the temperature jumps between the bottom or top face and the mid-plane, with T^{m}, T^{b} and T^{t} being the temperatures at the mid-plane, bottom and top face of interface element, respectively, and λ_{w} is the thermal conductivity of the water. $\bar{w}$ is a penalty coefficient to avoid singularity when interface elements are used to provide potential cracking paths in intact rock. The penalty coefficient should be as small as possible to reduce the artificial compliance.

3.3. VERIFICATION AGAINST ANALYTICAL SOLUTIONS

Verification is undertaken against analytical benchmarks to verify the reliability of the proposed model in simulating coupled thermo-hydraulic process in the interface element, as well as simulating fracturing processes with hydro-mechanical coupling.

3.3.1. THERMO-HYDRAULIC COUPLING IN A SINGLE FRACTURE

VERIFICATION AGAINST LAUWERIER'S PROBLEM

The first example considers heat advection along a single fracture combined with heat conduction into the surrounding continuum medium. Lauwerier (1955) and Barends (2010) provided the analytical solution to this problem. In their concept, a homogeneous fracture with a width w is overburdened and under-burdened by two impermeable rock matrices with a uniform initial temperature T_{ini}, as schematically depicted in Fig. 3.3a. Water with a temperature T_{inj} is injected into the fracture at a constant volume rate. The upper and lower faces of the fracture are impermeable to water, but heat conduction into the surrounding matrix is allowed (Barends, 2010). Other assumptions to derive the analytical solution are listed below:

(1) Temperature across the vertical profile of the fracture is uniform, i.e. no vertical temperature gradient in the fracture.

(2) Darcy velocity along the fracture is constant.

(3) Density, specific heat capacity, and thermal conductivity of water are constant.

(4) Thermal diffusion and dispersion are neglected in the longitudinal direction;

(5) The domain size is semi-infinite.

(6) The surrounding matrix are homogeneous and isotropic.

With the above concept and assumptions, the analytical solution for the time evolution of the temperature profile along the fracture is as follows (Lauwerier, 1955; Barends, 2010):

$$T(x,t) = T_{\mathrm{ini}} + (T_{\mathrm{inj}} - T_{\mathrm{ini}}) \mathrm{erfc}\left(\frac{\lambda' x}{\rho_{\mathrm{w}} c_{\mathrm{pw}} w \sqrt{\lambda' \nu_{\mathrm{w}} (\nu_{\mathrm{w}} t - x)/(\rho' c_{\mathrm{p}}')}} \right) H\left(t - \frac{x}{t}\right) \tag{3.25}$$

where, T_{ini} and T_{inj} are the initial and injection temperature, respectively, $\rho^{'}$, $\lambda^{'}$ and $c_p^{'}$ are the density, the thermal conductivity, and the specific heat capacity of the surrounding matrix, respectively, ρ_w and c_{pw} are the density and specific heat capacity of water, respectively, v_w [m/s] is the Darcy velocity along the fracture, erfc() is the complementary error function, and $H()$ is the Heaviside function.

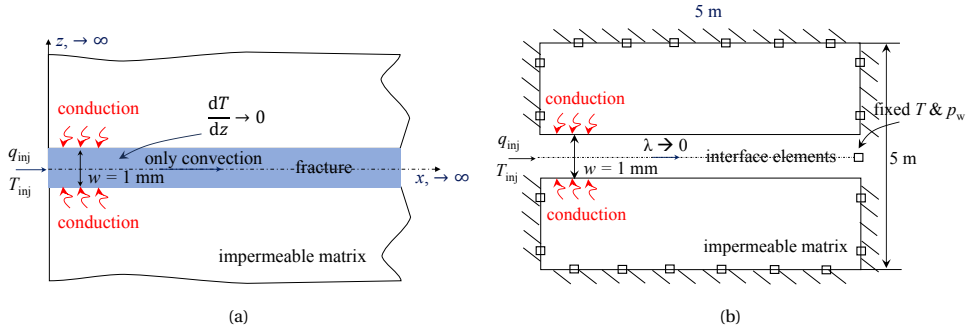


Figure 3.3: Description of the problem for (a) analytical and (b) numerical solutions.

To verify the numerical model, the Lauwerier's problem is considered with the parameters indicated in Table 3.1. The considered numerical boundary conditions are indicated in Fig. 3.3a. For simulated times of less than 30,000 s, the domain size of 5×5 m^2 was found large enough to neglect boundary effects in the heat transport, thus matching the semi-infinite domain assumption of the analytical solution. The interface elements, used to represent the fracture, is placed at the centre of the domain, shown in Fig. 3.3b. Fluid flow and heat advection are assumed to be unidirectional along the fracture. The transversal hydraulic coefficients are set to zero to match the assumption of null transversal heat convection. Since the longitudinal heat conduction in the fracture is neglected in the analytical solution, a very low thermal conductivity of 0.001 W/(m·K) is adopted for water in the numerical model. The vertical temperature profile in the fracture is assumed to be uniform (i.e. zero vertical temperature gradient) in the analytical solution, therefore, in the numerical model following the approach of Barends (2010) a high thermal conductivity of $\lambda_w = 10$ W/(m·K) for transversal heat flow is used in Equations (3.24) and (3.23). Additionally, the surrounding matrix is set as impermeable, with heat conduction allowed. The initial temperature of the domain is T_{inj}. All input parameters are listed in Table 3.1. The domain is discretised into 2600 elements, including quadratic continuum elements and interface elements.

The numerical and analytical results are then compared in terms of the temperature profile along the fracture at different times(Fig. 3.4a) and the temperature evolution at positions $x = 1$ m, 1.5 m, 2m, and 3 m away from the injection point (Fig. 3.4b). These plots show an excellent agreement between the numerical and analytical solutions.

STABILISING NUMERICAL INSTABILITIES FOR HIGH PÉCLET NUMBER

It is well known that in convection-dominated transport problems, a high ratio between advective and conductive heat transport can lead to numerical instabilities, i.e., oscillations (Pérez Carreras, 2018; Diersch, 2014). Therefore, further consideration and treatment

Table 3.1: Input parameters for modelling thermo-hydraulic processes in a single fracture

Parameter	Symbol	Value	Unit
Fracture width	w	0.001	m
Longitudinal hydraulic coefficient	t_0^{l}	10^{-11}	m^3
Transversal permeability	$k_{\mathrm{b}}, k_{\mathrm{t}}$	0	m^2
Injection flow rate	q_{inj}	0.00001	m^3/s
Injection temperature	T_{inj}	303	K
Initial temperature	T_{ini}	373	K
Water density	ρ_{w}	1000	kg/m^3
Water viscosity	μ_{w}	0.001	Pa·s
Thermal conductivity of water	λ_{w}	0.001	W/(m·K)
Water specific heat capacity	c_{pw}	4184	J/(kg·K)
Matrix density	$\rho^{'}$	2800	kg/m^3
Matrix thermal conductivity	$\lambda^{'}$	7.7	W/(m·K)
Matrix specific heat capacity	$c_{\mathrm{p}}^{'}$	850	J/(kg·K)

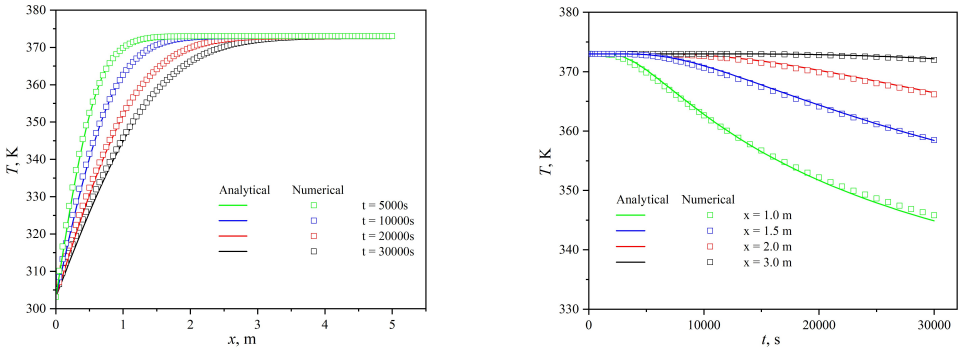


Figure 3.4: Comparison of numerical and analytical solutions of Lauwerier's problem. (a) Temperature distribution along the fracture; (b) Temperature evolution at different positions.

are needed to stabilise the numerical solution. In this section, stabilisation of the the numerical instability is presented, with the results illustrated with the numerical model in Fig. 3.3b.

The Péclet number for heat transport in a fracture in the longitudinal direction, Pe, defines the ratio between advective to conductive heat transport:

$$Pe = \frac{\rho_w c_{pw} h v_w^l / w}{2\lambda_w} \tag{3.26}$$

where w [m] and h [m] are the width and the longitudinal size of the interface element, respectively.

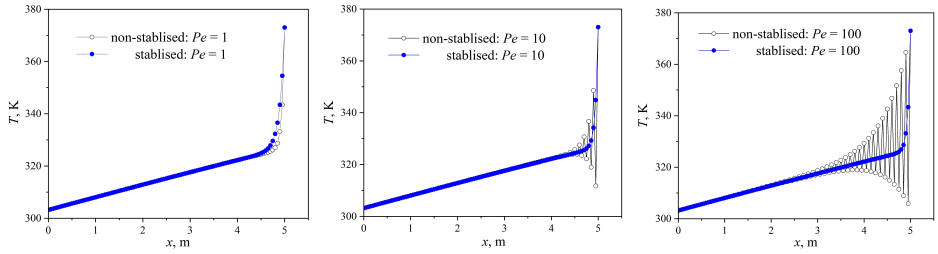
In the numerical solution to the heat transfer problem presented in Fig. 3.3b, if the flow velocity is increased or heat conductivity is reduced, numerical instability can be observed and found to be related to Péclet number, as shown in Fig. 3.5. If no stabilisation method is implemented, oscillations will occur once the Péclet number is greater than 1, and the numerical solution will deteriorate with increasing Péclet number. Multiple methods have been proposed to stabilise the numerical solution, such as upwind Petrov-Galerkin method and Bubble Functions method (Heinrich *et al.*, 1977; Baiocchi *et al.*, 1993). However, introducing the weighting function (as in the Petrov-Galerkin method) or bubble function into the finite element formulation increases computational cost and can be non-trivial. In addition, implementing these approaches in the current code would require significant modifications. A simpler method is to add an artificial diffusion coefficient (λ_a) to the physical diffusion coefficient (λ_w), called the Balance Equation Method (Owen, 1984; Pérez Carreras, 2018). The artificial diffusion coefficient is defined as:

$$\lambda_a = \delta \rho_w c_{pw} h |v_w^l| / w \tag{3.27}$$

where δ is a tuning parameter. To stabilise the solution, the Péclet number must always be smaller than 1, therefore a tuning parameter equal to around 0.5 ensures stability. The Péclet number after stabilisation is then:

$$Pe = \frac{\rho_w c_{pw} h v_w^l / w}{2(\lambda_w + \lambda_a)} \tag{3.28}$$

This method is only valid for cases without internal energy sources (or sinks), i.e., the right-hand side of Eq. (3.21) is 0. Because in our research, generally no internal energy sources/sinks exist, the balance equation method is implemented here to stabilise the solution. Temperature profile along the fracture under different Péclet number is shown in Fig. 3.5, The stabilised solution shows no oscillation even when the original Péclet number is 100, and meanwhile shows good agreement with non-stabilised solution when Péclet number is 1. It should be noted that, as is shown in Fig. 3.5a, the added artificial diffusion can result in slight deviation from the exact solution, due to the added conduction to achieve stabilisation. Yet, conduction accounts for only small part of the heat transfer along the fracture and conduction in the matrix is more important. Consequently, the results remain accepted accuracy.



(a) $Pe = 1$ (b) $Pe = 10$ (c) $Pe = 100$

Figure 3.5: Temperature profile along the fracture at time step 5000 s, with and without stabilisation. A tinning parameter of 0.5 is used to stabilise the numerical solution due to high Péclet number in longitudinal heat flow in a fracture.

3.3.2. HYDRO-MECHANICAL PROCESSES - KGD MODEL

In this example, fracture propagation as a result of localised water injection in an infinite, homogeneous and impermeable medium without leak-off is considered under plane-strain conditions. The KGD model (Fig. 3.6a), proposed by Khristianovic & Zheltov (1955) and Geertsma & De Klerk (1969) has been widely used to verify numerical solutions to hydraulic fracturing, and is used here to provide analytical solution to the considered problem. The KGD model assumes a fracture with a rectangular shape in the vertical plane with an elliptical shape in the horizontal plane, as is shown in Fig. 3.6a. The rectangular vertical cross section extends from the injection face with the maximum aperture to the fracture tip with a null width (Geertsma & De Klerk, 1969). Initially, the fracture is assumed to be without any appreciable opening. At $t_0 = 0$ s, water with a constant volumetric injection rate Q_0 is injected. The injected fluid flows through the fracture without leak-off into the surrounding medium. The fracture opens and propagates as the fluid pressure diffuses along the fracture. Other assumptions of the KGD model are (Valkó & Economides, 1995; Spence & Sharp, 1985; Adachi & Detournay, 2002):

(1) The rock matrix is linear elastic.

(2) The fracture has a constant height in the vertical direction.

(3) The fracture aperture at the fracture tip is zero.

(4) Zero-toughness condition is assumed, i.e., no mechanical energy spent on fracture propagation;

(5) Zero-lag condition is assumed, i.e., no lag between fluid and the fracture tip;

(6) The flow rate along the fracture is everywhere equal to the injection.

(7) Fluid flow is solved based on lubrication theory.

With the above basic assumptions, Adachi & Detournay (2002) have proposed the following analytical solutions to obtain the evolution of the half length of the fracture L,

the aperture at the fracture mouth (at the injection point) r_{nw}, and the net pressure at the fracture mouth $p_{\mathrm{n,w}}$:

$$L(t) = 0.466\left(\frac{E'Q_0^3}{\mu}\right)^{1/6} t^{1/3} \tag{3.29}$$

$$r_{\mathrm{nw}}(t) = 0.924\left(\frac{\mu Q_0^3}{E'}\right)^{1/6} t^{1/3} \tag{3.30}$$

$$p_{\mathrm{n,w}}(t) = 2.28(E'^2\mu)^{1/3} t^{-1/3} \tag{3.31}$$

where $E' = \frac{E}{1-\nu^2}$ [Pa] is the plane strain modulus, with E [Pa] and ν being the the Young's modulus and the Poisson's ratio of the rock matrix, Q_0 [m^3/s] is the constant volumetric injection rate, and μ [Pa · s] is the fluid viscosity.

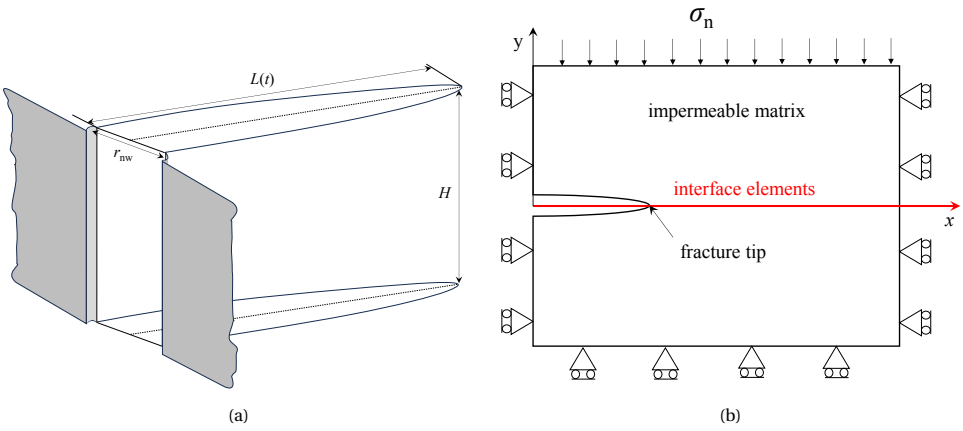


Figure 3.6: Description of KGD model in (a) 3D and (b) 2D (Valkó & Economides, 1995).

To numerically solve the viscosity-dominated KGD problem, a 5 m ×10 m (X × Y, X is the size in the direction of fracture propagation while Y the size in the direction perpendicular to fracture propagation) domain with interface elements inserted at the middle is considered, shown in Fig. 3.6b. The domain size is chosen so that the conditions Y ≥ $10L(t_{\mathrm{f}})$ and X ≥ $2L(t_{\mathrm{f}})$, where t_{f} is duration of the water injection, are met. This condition was proved sufficient to avoid effects from boundary conditions (Settgast *et al.*, 2017). Considering only half-wing of the KGD fracture is modelled, the injection rate in the simulation is $Q_0\rho_{\mathrm{w}}/2$. To simulate the viscosity dominated condition, the fluid viscosity is set to 1 mPa · s, while the tensile strength is set to 1000 Pa (Settgast *et al.*, 2017). Other parameters are presented in Table 3.2.

The simulation results are compared with the analytical solution in Fig. 3.7a to 3.7c. A good general agreement between the numerical and analytical solutions is appreciated. The initial increase phase of the simulated $p_{\mathrm{n,w}}$ at the beginning of injection observed in Fig. 3.7a is because in the model the flow rate is linearly increased from 0 to $Q_0\rho_{\mathrm{w}}/2$ in a very short time (0.1s). In addition, the deviation observed in all comparisons can be explained as a result of the assumed fracture shape in the analytical solution and the ability of the numerical solution to respond to the mechanical perturbation. As stated earlier,

the analytical solution assumes an elliptic shape along the fracture ($r_n = r_{nw}\sqrt{1-\frac{x}{L(t)}}$ (Garolera Vinent, 2017)). However, the numerical model does not give exactly the same shape, due to the intrinsically imposed geometric restriction at the fracture tip ($\frac{dr_n}{dx} = 0$), which results in a sigmoid close to the tip (Fig. 3.7d) (Garolera Vinent, 2017).

Table 3.2: Material parameters for KGD numerical model

Parameters	Symbols	Values	Units
Young's modulus	E	20	GPa
Poisson's ratio	ν	0.20	-
Tensile strength	σ_{n0}	1000	Pa
Cracking separation	r_{n0}	1×10^{-12}	m
Debonding separation	r_{nc}	1^{-10}	m
Fluid density	ρ_w	1000	kg/m^3
Fluid viscosity	μ	0.001	Pa·s
Injection rate	$Q_0\rho_w/2$	5×10^{-4}	kg/s

3.4. VALIDATION

To validate the numerical model, simulations of the thermal fracturing experiments conducted by Zhang *et al.* (2019) are carried out. A brief recap of the experimental procedure is given below, followed by the introduction to the numerical model and the comparison of simulation and experiment results. Finally, a sensitivity analysis is performed to show how the key parameters can influence the model performance. A 2D approach to the modelling is taken in order to reduce the computational load. This is considered to be sufficient to simulate the general processes and especially as in 3D material hetrogeneities will play a further role in the specific fracture evolution. The evaluation of the performance will focus general on the qualitative behaviour, with a lower focus on the quantitative performance.

3.4.1. RECAP OF THE EXPERIMENT

The aim of the experiments conducted by Zhang *et al.* (2019) was to study the influence of cold water injection on the hydraulic fracturing processes. Granite samples (properties listed in Table 3.3) with dimensions of 0.1 m × 0.1 m × 0.12 m were used. A hole was drilled in each sample, and a pipe with perforated holes was placed into the drilled hole with the dimensions shown in Fig. 3.8. The annulus between the wellbore and the wall of the drilled hole was sealed.

The samples were then slowly heated to 323 K, 373 K and 473 K with the temperature maintained for 12 hours to ensure uniform and complete heating. Subsequently, an anisotropic stress was applied to the samples, with $\sigma_v = 10$ MPa, $\sigma_H = 7.5$ MPa and $\sigma_h = 5$ MPa (Fig. 3.8a). Distilled water with a temperature of 293 K was injected into the wellbore under controlled-rate condition to induce fractures. In the description of the experiments (Zhang *et al.*, 2019), the controlled-rate condition was not presented. However, it can be back-calculated from the water pressure response curve, as it is discussed below.

The injection pressure response was monitored and presented in Fig. 3.9. After the

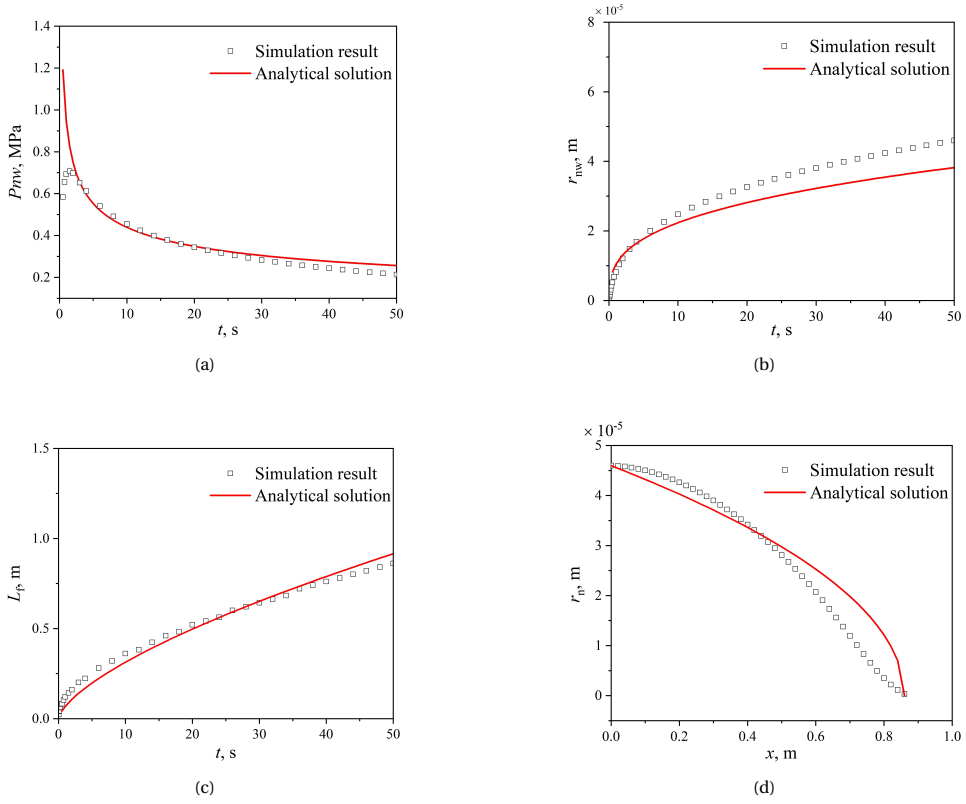


Figure 3.7: Comparison of simulation results and analytical solutions of the KGD problem. (a) $p_{\mathrm{n,w}}$ at injection point; (b) $r_{\mathrm{nw}}(t)$ at injection point; (c) $L(t)$; (d) Opening along the fracture (t = 50s)

Table 3.3: Properties of granite samples used in the experiment, data from Zhang *et al.* (2019)

Parameter	Symbol	Value	Unit
Porosity	ϕ	0.14	-
Permeability	k	6×10^{-19}	m^2
Young's modulus	E	32	GPa
Poisson's ratio	ν	0.2	-
Tensile strength	σ_{t}	20.5	MPa
Density	ρ_{s}	2590	$\mathrm{kg/m}^3$
Volumetric thermal expansion coefficient	β_{s}	6.2×10^{-6}	1/K
Specific heat capacity	c_{ps}	950	$\mathrm{J/(kg^{-1}{\cdot}K^{-1})}$
Thermal conductivity	λ_{s}	4	$\mathrm{W/(m^{-1}{\cdot}K^{-1})}$

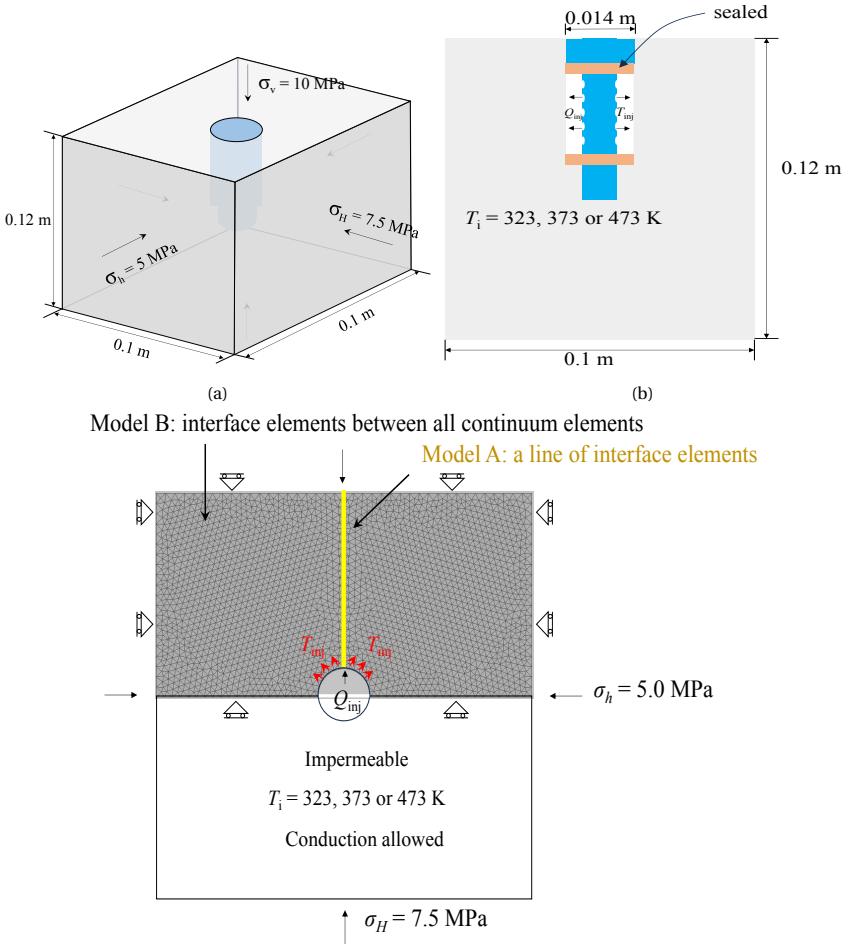


Figure 3.8: Schematic description of the experiment (modified from Zhang *et al.* (2019)) and numerical model. (a) 3D schematic of the initial conditions of the rock samples; (b) Vertical cross section; (c) Horizontal cross section (numerical model)

fracturing experiment, red ink was injected to visualise the fractures. The results show red ink diffused in the direction perpendicular to the minimum in-situ stress when the rock temperature was 373 K, indicating a single fracture formed in that direction (Fig. 3.11a). In contrast, red ink diffused in all directions when the rock temperature was 473 K, indicating fracture branching (Fig. 3.11b).

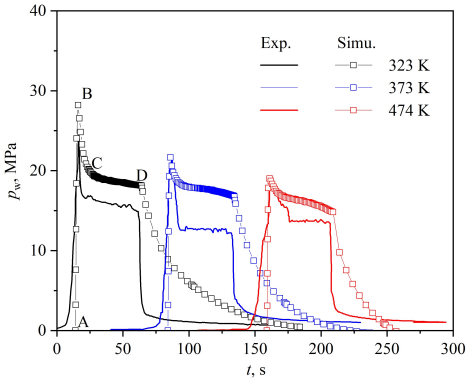


Figure 3.9: Comparison of pressure response curves from simulations (Model A) and experiments by Zhang *et al.* (2019).

3.4.2. NUMERICAL MODEL

A 2D symmetric numerical model with a size of 0.1 m × 0.05 m (upper half domain) is built to simulate the experiments (Fig. 3.8c). A horizontal plane strain condition is chosen because the maximum stress is σ_v, which means vertical fractures are expected to be induced (and were observed in the experiments) (Zhang *et al.*, 2019). A hole with a radius of 0.007 m is placed at the center. The boundary conditions are shown in Fig. 3.8c. Initial stresses σ_H and σ_h are set for the elements. Due to symmetry, only half of the domain is considered. Two models were considered to represent possible fractures. Firstly, Model A, which had a single line of interface elements in the direction of maximum horizontal stress, was used to validate against the experimental results with rock temperature of 323 K and 373 K. In these two cases, only a single main fracture was observed so that a pre-defined cracking path in the model is possible. Secondly, Model B, which had interface elements in between all continuum elements, was used to investigate fracture branching, as was observed when the rock was heated to 473 K.

As the permeability of the intact rock is extremely low (6×10^{-19} m^2), the continuum elements that represent the intact rock are set to be impermeable, while thermal conduction is allowed. This is done by setting k^b and k^t to zero. Injection rate is imposed only at the mouth of the interface element that is at the wellbore in the direction of the maximum horizontal stress, while the temperature boundary condition is imposed around the wellbore. To simulate the behaviour of the intact rock yet allowing only fluid flow in the interface elements, we set the initial aperture and hydraulic coefficient of interface elements to give behaviour equivalent to the rock sample, based on the rock sample's porosity and permeability, given by the following equations:

$$t_0^{\mathrm{l}} = kL^* \quad , \qquad w_0^{\mathrm{l}} = \phi L^* \tag{3.32}$$

where k[m^2] and ϕ are the rock permeability and porosity, respectively, L^*[m] is the characteristic element length, defined as the dominant size of the continuum elements in the mesh, which can be obtained via mesh quality analysis. For this study $L^* = 0.00163$ m.

In the simulation, the injection rate is fixed at the mid-plane node of the first interface element at the borehole in the direction of the maximum stress, indicated by the blue rectangle in Fig. 3.8c. Since the injection rate was not disclosed in the original paper (Zhang *et al.*, 2019), it is back-calculated from the experimental pressure response curve by running a model without interface to reach the breakdown pressure and selecting the corresponding injection rate. Note that the injection rate q_{inj} here is 2D, and can be approximately linked to 3D by multiplying the height of the open-hole section, through which the fluid was injected. Since the highest Péclet number reached in this exercise is around 0.017, stabilisation technique is not needed. Therefore the tuning parameter λ_{a} in Eq.3.27 is 0 in this case. Except for rock properties listed in Table 3.3, other input parameters of the simulation are presented in Table 3.4. The simulation results are then compared to experimental pressure curve to show the agreement between the simulation and experiments under each temperature setting, i.e., 323 K, 373 K and 473 K. After that, a sensitivity analysis on injection rate (q_{inj}, kg/(m · s)), tensile strength (σ_{t}) and debonding separation (r_{n}^*) is performed.

Table 3.4: Input parameters for the simulation, data partly from Zhang *et al.* (2019)

Parameter	Symbol	Value	Unit
Rock temperature	T_{i}	323, 373, or 473	K
Injection temperature	T_{inj}	293	K
Injection rate	q_{inj}	3×10^{-6}	kg/(m·s)
Water density	ρ_{w}	1000	kg/m^3
Water viscosity	μ_{w}	0.001	Pa · s
Water specific heat capacity	c_{pw}	4184	J/(kg^{-1}·K^{-1})
Water thermal conductivity	λ_{w}	0.598	W/(m^{-1}·K^{-1})
Initial hydraulic conductivity	t_0^l	1E-21	m^3
Initial aperture	w_0	2E-4	m
Tensile strength	σ_{t}	20.5	MPa
Cracking separation	r_{n0}	3×10^{-8}	m
Debonding separation	r_{n}^*	2×10^{-6}	m

3.4.3. COMPARISON BETWEEN SIMULATION AND EXPERIMENTAL RESULTS

The pressure response curves (offset in time for visualisation) from Model A and experiments are compared in Fig. 3.9. The pressure is monitored at the mouth (the blue rectangle shown in Fig. 3.8c, mid-plane node) of the line of the interface elements, at which the fluid was injected with a fixed flow rate. It is shown in Fig. 3.9 that Model A successfully simulates the pressure response during the whole fracturing processes. Both experimental and numerical results show after a linear pressure increase (Stage A-B in Fig. 3.9), a peak stress at point B, followed by a non-linear pressure drop (Stage B-C) that

corresponds to unstable fracture propagation stage and a nearly constant pressure response (Stage C-D) that corresponds to a stable fracture propagation stage. After injection stops at Point D, pressure drops to zero both in the experiment and numerical simulation, yet at a different rate.

A decrease in peak pressure (the pressure that is required to fracture the rock) with increasing rock temperature is observed both in simulation and experiment consistently. This is because a greater reduction in confining stress due to stronger cooling effect makes fracturing more likely. Fig. 3.10 illustrates the simulated evolution of fracture aperture in Model A. It shows that with increasing initial rock temperature, i.e. stronger cooling shock, the fracture aperture is significantly larger. In addition, fracture closing can be observed in Fig. 3.10 at t=90 s, which occurs after the injection stops, i.e., after point D in Fig. 3.9.

Figure 3.9 illustrates that in the initial linear pressure response (Stage A-B), the numerical solution shows a more steep curve compared to that of the experimental result. This can be attributed to the fact that the fluid used in the experiment was not de-aired and thus had a higher compressibility, as well as to the storage effect of the experimental equipment. In addition, the simulated fracture propagation pressures (i.e., the nearly constant pressure response in Fig. 3.9) are higher than those from experiment for all three cases. This could be because the model assumes a fixed-displacement in X direction at both left and right boundary (see Fig. 3.8c), which constrains the opening of the fracture. Moreover, the gradual decrease after point D in the simulated injection pressure is a result of boundary conditions (fixed zero flow rate at injection point while fixed pressure at the ending point of the interface elements after injection stops). The details of the pressure in the injection system after injection was stopped is not presented, so this is likely to be due to differences in the boundary conditions in the experiment and the numerical model.

Figure 3.12 compares the first principal stresses in Model A with different initial rock temperatures. High tensile stresses of up to 68 MPa, much higher than rock tensile strength, are observed around the wellbore when initial rock temperature is 473 K. This indicates tensile failures should occur not only in the initial direction of maximum stress, but also around the wellbore when initial rock temperature is 473 K. In contrast, when initial rock temperature is 373 K or 323 K, the stress around the borehole remains lower than rock tensile strength, indicating no tensile failures occur except in the direction of the maximum stress. This is consistent with the experimental results (Fig. 3.11), which show that the red ink diffused in all direction when rock temperature was 473 K, indicating fracture branching, while only diffused in the direction of maximum in-situ stress at 373 K, indicating a single fracture in that direction. This is to say, our model with interface elements inserted in the direction of maximum stress can qualitatively match the experimental results for the cases with initial rock temperatures of 323 K and 373 K, but it is not able to capture the fracture branching observed when initial rock temperature is 473 K.

To show the capability of the proposed model to simulate fracture branching, interface elements are inserted in between all the continuum elements in Model B to provide potential cracking paths in other directions, at the expense of increasing the computational cost. Figure 3.13 shows the simulated fracture opening with the first principal stress

[1] Reprinted from Zhang *et al.* (2019) with permission from Elsevier. License No.: 5764200568636

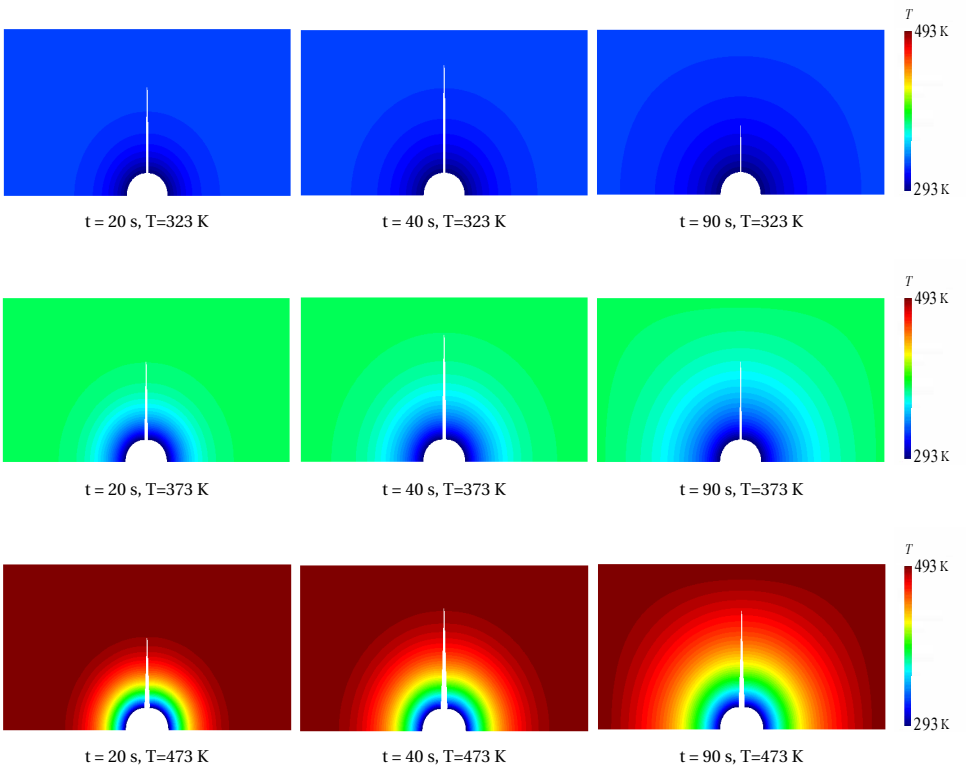
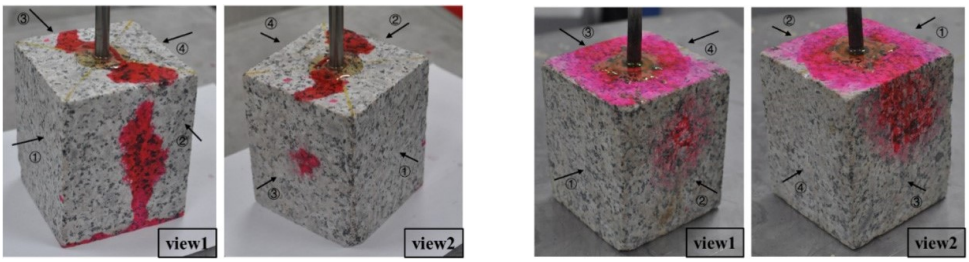


Figure 3.10: Fracture aperture evolution under different in-situ temperatures (fracture opening is scaled up 300 times). For all cases, the injection starts at 0 s and ends at 50 s, while the simulation ends at 168 s.



(a) (b)

Figure 3.11: Experimental results from Zhang *et al.* (2019) showing red ink diffusion in rock with an initial temperature of (a) 373 K and (b) 474 K[1]

plotted from Model B. It can be clearly seen fractures are also induced in other directions except for the direction of the maximum stress when the rock temperature is 473 K. In contrast, only a single fracture is formed when the rock temperature is 323 K or 373 K, though fracturing is allowed to happen in other directions. This shows a good agreement with the experimental results.

This validation exercise further demonstrates the advantage of using the triple-node scheme, rather than double-node one, for interface elements. In double-node elements, the mid-plane water pressure, which is used to compute the longitudinal flux and is considered for H-M coupling, is obtained as the average of the pressures on both sides of the interface. Accordingly, an increase of fluid pressure at the mid-plane can only occur at the expense of increasing the water pressure at the side nodes, which are shared with the surrounding continuum elements. However, any increase in water pressure at these nodes automatically raises the water pressure at the integration points of the surrounding continuum elements through the interpolation functions. This occurs even if the continuum medium is considered impervious and the transversal hydraulic coefficient of the interface is set to zero. Consequently, water is transferred from the interface elements into the pores of the surrounding continuum, effectively increasing the storage capacity of the modelled fracture. Moreover, this increase in storage capacity depends on the size of the surrounding continuum elements, introducing another source of mesh dependency. In contrast, in triple-node elements, the mid-plane pressure is evaluated independently of the side pressure. By setting k^{b} and k^{t} to zero , the mid-plane nodes become completely independent of the side nodes for the hydraulic problem. Consequently, an increase in water pressure at the mid-plane nodes (i.e., inside the fracture) does not change the amount of water stored in the continuum. Note, however, that for the mechanical problem, the effect of the fluid pressure inside the fracture is maintained, as the H-M coupling is established through the mid-plane pressure.

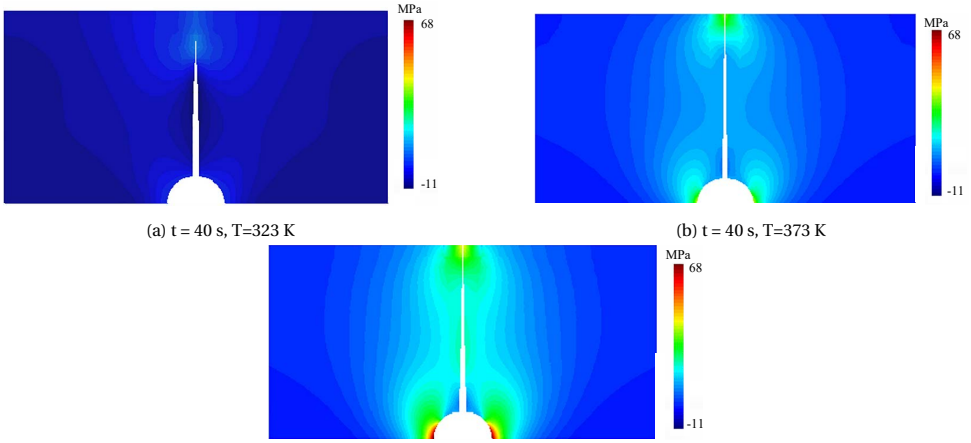
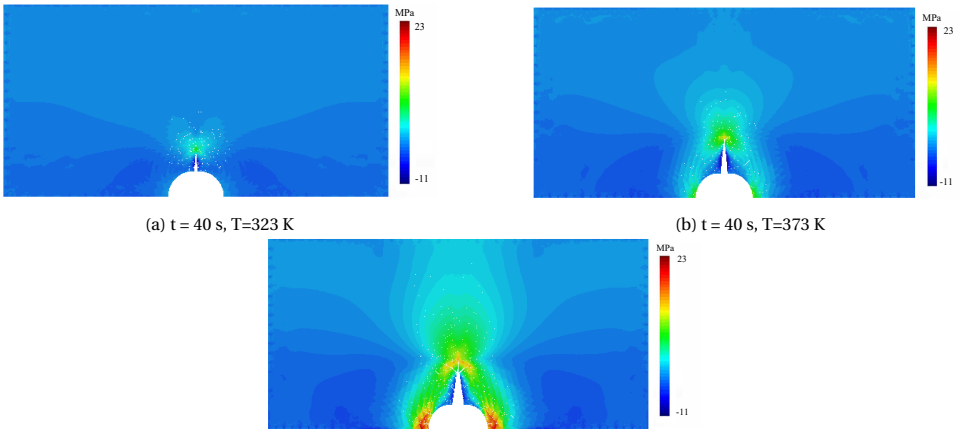


Figure 3.12: First principal stress field (σ_1) for different initial temperatures in Model A. When the temperature is initially 473 K, tensile stress significantly greater than the tensile strength (20.5 MPa) is observed at the wellbore (fracture opening is scaled up 1000 times).



(a) t = 40 s, T=323 K

(b) t = 40 s, T=373 K

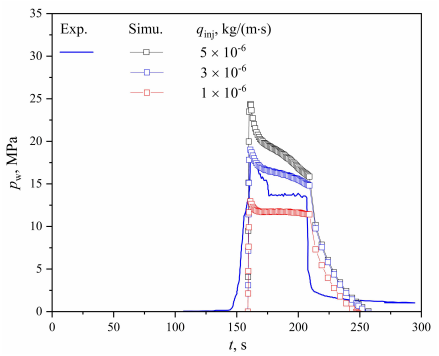
(c) t = 40 s, T=473 K

Figure 3.13: First principal stress field σ_1 under different initial temperatures in Model B. When temperature was initially 473 K, induced fractures are also observed in other directions, while for other two cases, only a single fracture is induced as it is in the model with only a single line of interface elements inserted in the direction of σ_{yy}. (Fracture opening is scaled up 1000 times).

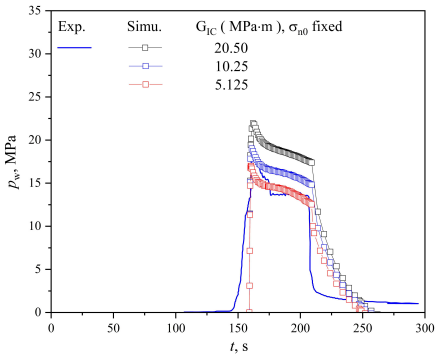
3.4.4. SENSITIVITY ANALYSIS

Sensitivity analysis is performed on the injection rate (q_{inj}), longitudinal hydraulic conductivity t_0^l and specific fracture energy in Mode I ($G_{IC} = \frac{1}{2}\sigma_{n0} \cdot r_{nc}$) for both Model A and Model B, respectively. When performed against varying G_{IC}, σ_{n0} is fixed while r_{nc} is changed, and vice versa.

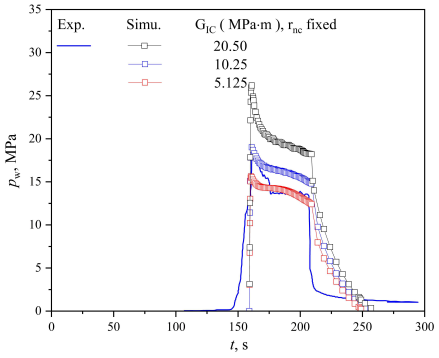
Results in Figs. 3.14a and 3.15a show that, as expected, for both models, higher injection rate leads to a higher pressure response, including the peak pressure and propagation pressure (which is not necessarily stable). This injection rate dependency of the pressure response is consistent with other laboratory experiments and numerical simulations in the literature (Zhuang *et al.*, 2019a; Cheng *et al.*, 2021; Fallahzadeh *et al.*, 2017), and it is well accepted by engineers (Guo *et al.*, 1993). In addition, higher specific fracture energy (both fixed σ_{n0} and fixed r_{nc}) leads to higher pressure response for both models, due to the increasing resistance. But the peak pressure in the pressure response curve shows less sensitivity to the case with σ_{n0} fixed in Fig. 3.14b and 3.15b, compared to Fig. 3.14c and 3.15c. As for the hydraulic conductivity, an increase in t_0^l leads to an increase in the pressure response for Model A, while for model B only an increase in the breakdown pressure is significant.



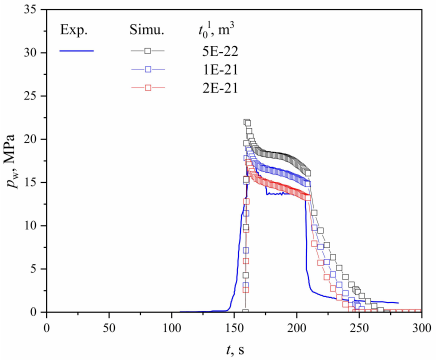
(a) Sensitivity to q_{inj}



(b) Sensitivity to G_{IC} with σ_{n0} fixed

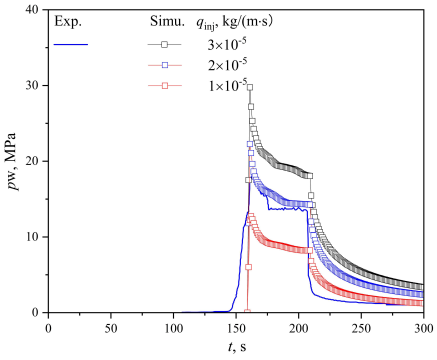


(c) Sensitivity to G_{IC} with r_{nc} fixed

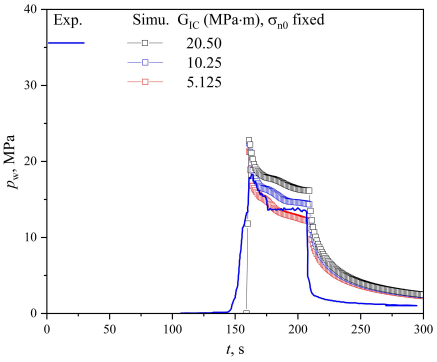


(d) Sensitivity to t_0^1

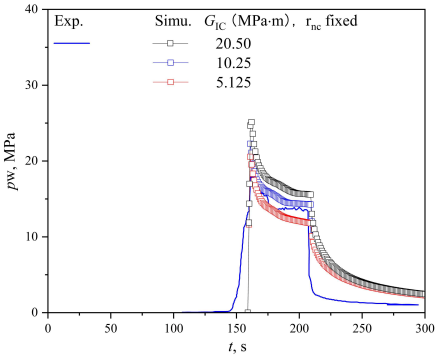
Figure 3.14: Sensitivity analysis Model A: the influence of injection rate Q_{inj} and specific fracture energy G_{IC} on pressure response.



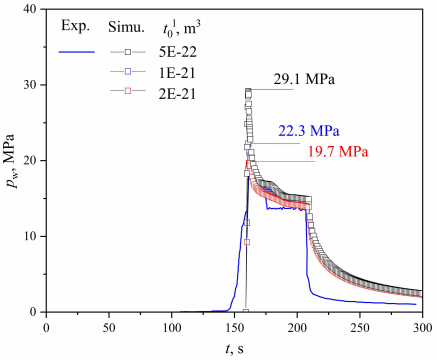
(a) Sensitivity to q_{inj}



(b) Sensitivity to G_{IC} with σ_{n0} fixed



(c) Sensitivity to G_{IC} with r_{nc} fixed



(d) Sensitivity to t_0^1

Figure 3.15: Sensitivity analysis Model B: the influence of injection rate Q_{inj} and specific fracture energy G_{IC} on pressure response.

3.5. CONCLUSIONS

In this chapter, a method is developed to simulate fracturing processes using the cohesive zone model considering fully THM couplings, with specific applications considered of under geothermal energy extraction. Possible discontinuities are represented by zero-thickness triple-nodded interface elements, which allow solid elements to separate with mechanical damage and the simulation of longitudinal and transversal fluid/heat flow in the discontinuity. The cubic law is used to update the fracture transmissivity as a function of its aperture, while a elasto-damage law to characterise the mechanical response of the discontinuity. To simulate pre-existing fractures or fracture initiation/propagation in an intact rock, interface elements can be inserted in between continuum elements surrounding pre-existing fractures or in between all continuum elements to provide potential crack paths, respectively.

The method is verified against analytical benchmarks and validated against experimental data on cold water injection into rock samples. The verification shows that the numerical solutions match well with the analytical solutions, illustrating the correctness of the numerical scheme. The validation shows a good agreement between the numerical and experimental results, demonstrating that the model is able to simulate THM processes and, in particular, cracking around a wellbore impacting the inflow ability during and after cold water injection. The proposed method has several potential applications beyond geothermal reservoirs. It can be used to optimise oil and gas recovery via hydraulic fracturing and soft stimulation techniques, such as thermal stimulation and cyclic stimulation, where the opening of the fractures leads to strong thermo-mechanical and hydro-mechanical couplings. In addition, its flexible representation of transversal fluid and heat flows allows simulation of the interface between permeable and impermeable materials (e.g., artificial fractures in enhanced geothermal systems or steel casing-cement interface), existing discontinuities with filling material, or fractures where the pore space at both sides is progressively clogged by chemical or mechanical processes.

4

SIMULATION OF FATIGUE DAMAGE UNDER CYCLIC COUPLED THERMO-HYDRO-MECHANICAL PROCESSES

A tool for the simulation of cyclic thermal stimulation of geothermal reservoirs is developed. A new elasto-damage law is developed by incorporating a fatigue damage variable into the tensile branch. The fatigue damage variable is calibrated using the number of loading cycles and fatigue life at different load intensities (i.e. a stress-number of cycles or S-N curve). With this formulation, the tensile strength and stiffness of the interface element degrade with increasing cycle number. In addition, Palmgren-Miner's rule is used to account for varying-amplitude cyclic loading. While the mechanical constitutive laws are temperature-independent, the thermal expansion and contraction lead to stress changes, which can generate cyclic stress paths under temperature cycles. The proposed method is validated against three laboratory tests from the literature, including the cyclic Brazilian test, the cyclic hydraulic fracturing test and the cyclic thermal stimulation test to demonstrate its ability to capture fatigue damage under cyclic coupled THM processes, including varying amplitude loading.

This chapter has been submitted for publication as Luo *et al.* (2025a)

4.1. INTRODUCTION

Rock fatigue failure is a common phenomenon in subsurface engineering projects, and can be either beneficial (e.g., fatigue cracks near geothermal or hydrocarbon wells (Hofmann *et al.*, 2019, 2021; Zang *et al.*, 2025)) or detrimental (e.g., fatigue damage of dams (Meng *et al.*, 2023)). The fatigue damage of rocks subjected to cyclic mechanical, hydraulic or thermal loading has been extensively studied, demonstrating that rock strength can be reduced and that fracture patterns can become more complex under cyclic loading (Cerfontaine & Collin, 2018; Zang *et al.*, 2021; Jung *et al.*, 2021; Niu *et al.*, 2023). For example, cyclic Brazilian tests conducted by Erarslan & Williams (2012) and Liu *et al.* (2018) have shown that rock samples fail under lower ultimate loads and exhibit different fracturing mechanism compared to those under monotonic loading.

In addition to pure mechanical loading, coupled hydro-mechanical and thermo-mechanical loadings have also been used to induce fatigue damage in rocks. Laboratory cyclic hydraulic fracturing tests on sandstone and granite samples have shown significant reductions in breakdown pressure (up to 20% for Pocheon granite cores (Zhuang *et al.*, 2019b), 7.18% - 18.9% for Xujiahe sandstone (Kang *et al.*, 2020), and 16% for dry Tennessee sandstone) (Patel *et al.*, 2017). Laboratory tests have also shown that cyclic hydraulic stimulation can lead to the formation of more complex fracture networks, as opposed to the simpler fractures typically induced by conventional hydraulic stimulation (Patel *et al.*, 2017; Wei *et al.*, 2023). Moreover, the effectiveness of cyclic hydraulic fracturing has also been demonstrated in field-scale tests, such as the cyclic hydraulic stimulation of well PX-1 at the Pohang enhanced geothermal system (EGS) project site, South Korea, which demonstrated that cyclic injection was able to improve well performance while ensuring that seismic activity remains below the target threshold of M_w 2.0 (Hofmann *et al.*, 2019; Zang *et al.*, 2021). In addition, cyclic heating-cooling treatment on rocks can also reduce their strength, which has been demonstrated in experiments (Gasc-Barbier *et al.*, 2014; Zhu *et al.*, 2020). However, study of rock fatigue damage under cyclic fully coupled thermo-hydro-mechanical (THM) loadings is rarely reported. Cyclic THM processes can happen in, for example, nuclear waste repository or stimulation to geothermal reservoirs. A combination of thermal stress and fatigue damage may further accelerate the rock failures. Therefore, the investigation of the rock fatigue damage under cyclic THM loadings is necessary and meaningful, while existing literature mainly focuses on individual loadings and simple hydro-mechanical or thermo-mechanical loadings.

Numerical simulation provides an essential tool for understanding fatigue damage of rocks. Incorporating fatigue damage into the cohesive zone model is a common method to predict the onset and propagation of fatigue fractures. The cohesive zone model was first proposed by Dugdale (1960) and Barenblatt (1962) to circumvent the unrealistic infinite stresses at the fracture tip obtained for a linear elastic material, assuming a cohesive-law governed zone in front of the fracture tip. Later, Hillerborg *et al.* (1976) introduced CZM into FEM to simulate crack initiation and growth in concrete. When discretising the material domain, the material separation and thus damage of the structure can be described by interface elements in-between continuum elements (Scheider, 2001), governed by the cohesive law that relates traction and separation of the two surfaces of the interface element. It has the advantages of the capability to simulate fracture initiation, intuitive physical meaning and its mitigation of the need to calculate the stress

singularity at the fracture tip over other approaches like extended finite element method. The traction-separation law, consisting of an elastic and an elastic-softening curves, is controlled by two material parameters, i.e. the critical fracture energy G_{I} (for mode-I fracture) and the tensile strength σ_{n0}, shown in Fig.4.1a. The damage of the rock, after the tensile strength is reached, is described by the elastic-softening curve.

Traditionally, the law can only describe damage due to monotonic loading beyond a strength threshold. If loading remains below the strength, the behaviour is elastic, with no additional damage, regardless of the number of loading cycles. Previous efforts have been made to incorporate fatigue damage due to cyclic loading into the cohesive law (Roe & Siegmund, 2003; Maiti & Geubelle, 2005; Robinson *et al.*, 2005; Turon *et al.*, 2007; Khoramishad *et al.*, 2010; De Moura & Gonçalves, 2015; Choi *et al.*, 2020; Xi *et al.*, 2021; Wei *et al.*, 2023). For example, Robinson *et al.* (2005) incorporated a fatigue damage variable into the cohesive law based on a modified Paris power law equation, which relates the fatigue crack growth rate ($\mathrm{d}a/\mathrm{d}N$, a is the fatigue crack length and N the number of cycles) to the amplitude of the applied stress intensity factor ($\Delta K = K_{\max} - K_{\min}$, $K_{\max}$ is the maximum stress intensity factor while $K_{\min}$ the minimum). The model was used to simulate delamination growth in composite material and their numerical results showed that the model can reproduce the characteristics of the Paris power law that is commonly observed in experiments, though the model considers only the maximum load. Munoz *et al.* (2006) further extended the work of Robinson *et al.* (2005) to consider the cyclic loads with non-zero minimum value. Turon *et al.* (2007) developed a cohesive zone model with a single damage variable and related the damage state with the number of cycles and the loading conditions. Khoramishad *et al.* (2010) integrated a strain-based fatigue damage with the cohesive law to simulate the impact of cyclic loading on the bonded joints. Unlike most of the previous model, the degradation of the cohesive strength is possible and dependent on the fatigue damage, making it possible to accumulate fatigue damage before the cohesive separation stage is reached. Xi *et al.* (2021) and Wei *et al.* (2023) followed the same concept but formulated the fatigue damage variable as a function of the number of cycles. One limitation is that the cohesive stiffness remains unchanged in the elastic stage. In contrast, some other literatures, e.g. Nojavan *et al.* (2016a); Choi *et al.* (2020), presented the computation of the damage evolution during cyclic loading is in conjunction with an unloading–reloading relation in the cohesive zone model, while allowing the degradation of the reloading stiffness.

While existing models have advantages and limitations in incorporating and computing fatigue damage, none address fully coupled thermo-hydro-mechanical loading, which requires the consideration of the thermal processes in the cohesive interface element. In addition, a specific cracking path was prescribed along a pre-defined line in most of the modelling exercises in the previously mentioned literature, while the cases where fracture can initiate and propagate in the most efficient fracturing paths are not mentioned. These limitations render the models unsuitable for simulating fatigue failure in, e.g. nuclear waste repository and geothermal reservoirs, where fractures can propagate in arbitrary but most efficient direction. In addition, the re-loading stiffness is unchanged if the traction-separation path is in the elastic stage in previous models (Khoramishad *et al.*, 2010; Xi *et al.*, 2021; Wei *et al.*, 2023), which fails to capture the observed degradation of rock stiffness and the accumulation of deformation (Cerfontaine & Collin, 2018; Xiao

et al., 2010). Wei *et al.* (2023) also formulated the fatigue damage variable as a function of the number of cycles under constant-amplitude loading, which does not consider varying-amplitude cyclic loading.

In this chapter, we introduce a fatigue damage variable into the cohesive zone model, which, together with cohesive interface elements and continuum elements that consider fully coupled THM processes, can simulate fatigue failures under cyclic THM loading. The fatigue damage variable is calibrated using the number of loading cycles and fatigue life at different load intensities (S-N curve, or stress-number of cycles curve). With this formulation, the tensile strength and stiffness of the interface element both degrade with increasing cycle number. Palmgren-Miner's rule is used to account for varying-amplitude cyclic loading. While the traction-separation law is temperature-invariant, the thermal expansion and contraction of the continuum elements lead to stress changes, which can generate cyclic stresses under varying temperature cycles, and therefore includes the impact of thermally-induced stresses. The proposed method is validated against three laboratory tests from the literature, including cyclic Brazilian test, cyclic hydraulic fracturing test and cyclic thermal stimulation test to demonstrate its ability to capture fatigue damage under cyclic coupled THM processes, including varying amplitude loading. The proposed model can be used to simulate cyclic thermo-hdyraulic stimulation in subsurface projects, e.g. geothermal projects, and rock failures in subsurface infrastructure projects, e.g. the damaged zone under cyclic THM loading around radioactive waste repositories.

4.2. NEW ELASTO-DAMAGE LAW

As introduced in previous chapter, continuum finite elements are used to model intact rock while zero-thickness three-node interface elements are used to model discontinuities, as shown in Fig. 3.1. The interface elements can be inserted in-between continuum elements surrounding a pre-defined path to model pre-existing fractures or weak planes, or can be inserted in-between all the continuum elements to provide arbitrary potential cracking paths. Conventionally, the mechanical response of the interface elements is governed by the bi-linear elasto-damage law presented in Figure 3.2.3, which can only describe damage evolution when loading reaches the strength. For loading below the tensile strength, the stress-displacement path will remain unchanged in the elastic stage with no resulting damage no matter how many times the loading is repeated. However, fatigue damage of rock under cyclic loading below the strength have been observed in experiments and field examples, e.g. (Patel *et al.*, 2017; Zhuang *et al.*, 2019b; Hofmann *et al.*, 2019; Kang *et al.*, 2020). Therefore, there is a need to incorporate fatigue damage into the conventional elasto-damage law to allow degradation of strength and stiffness in the elastic stage.

In this chapter, a fatigue damage variable D_{f} is introduced to degrade the tensile strength as follows:

$$\sigma_{\mathrm{nm}} = (1 - D_{\mathrm{f}})\sigma_{\mathrm{n0}} \tag{4.1}$$

where D_{f} is the fatigue damage variable. σ_{nm} [Pa] is the degraded tensile strength after m cycles, and σ_{n0} [Pa] is the initial tensile strength of the rock as in the conventional law.

σ_{nMf} is the degraded tensile strength after M_{f} cycles, with M_{f} the fatigue life corresponding to an applied loading σ_{A}. This degraded tensile strength is then used to calculate the stiffness of the interface element with a fixed cracking separation r_{n0}, as shown in Fig. 4.1b, thus allowing also degradation of the stiffness in the elastic stage:

$$K_{\mathrm{nm}} = \frac{\sigma_{\mathrm{nm}}}{r_{\mathrm{n0}}} \tag{4.2}$$

where K_{nm} [Pa/m] is the stiffness after m cycles. Then the modified elasto-damage law can be described as:

$$\sigma'_{\mathrm{n}} = \begin{cases} (1-D)K_{\mathrm{nm}} r_{\mathrm{n}} & \text{if } r_{\mathrm{n}} > 0 \\ K_{\mathrm{n0}} r_{\mathrm{n}} & \text{if } r_{\mathrm{n}} \leq 0 \end{cases} \tag{4.3}$$

Note the degraded stiffness K_{nm} is only used in tension ($r_{\mathrm{n}} > 0$), so that the stiffness in compression is still kept as K_{n0}, which is interpreted as a penalty coefficient to limit the penetration of the fracture surfaces.

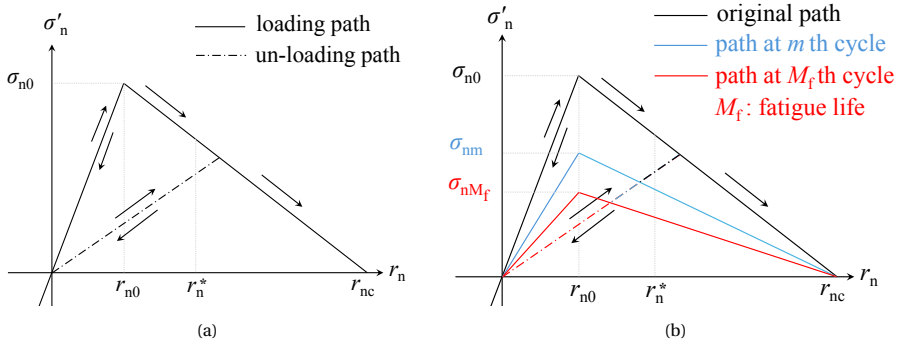


Figure 4.1: Comparison of the (a) conventional and (b) modified elasto-damage law.

To determine the fatigue damage variable, a linear strength degradation is assumed (Xi *et al.*, 2021; Nojavan *et al.*, 2016b). Thus, when subjected to a constant-amplitude cyclic loading (Fig. 4.2a), it can be defined as:

$$D_{\mathrm{f}} = \left(1 - \frac{\sigma_{\mathrm{A}}}{\sigma_{\mathrm{n0}}}\right) \frac{m}{M_{\mathrm{f}}} \tag{4.4}$$

where σ_{A} [Pa] is the amplitude of the cyclic loading, as is shown in Fig. 4.2a. M_{f} is the fatigue life (maximum number of cycles until failure) under a specific constant-amplitude cyclic loading.

When subjected to varying-amplitude cyclic loading, shown in Fig. 4.2b, Equation 4.4 can be further developed based on the Palmgren-Miner's rule, which reads:

$$D_{\mathrm{f}} = \sum_i \left(1 - \frac{\sigma_{\mathrm{A}i}}{\sigma_{\mathrm{n0}}}\right) \frac{1}{M_{\mathrm{f}i}} \tag{4.5}$$

where, i indicates the ith cyclic loading that has a maximum amplitude of $\sigma_{\mathrm{A}i}$, as is shown in Fig. 4.2b. $M_{\mathrm{f}i}$ is the fatigue life corresponding to the applied loading level $\sigma_{\mathrm{A}i}$.

An empirical S-N relationship is used as a criteria to determine the fatigue life M_{fi}, which relates the maximum value of the cyclic loading (σ_{Ai}) to the fatigue life M_{fi} of the rock. This relationship has been widely used in metals, concrete and rocks (Nojavan *et al.*, 2016b; Chen *et al.*, 2017; Cerfontaine & Collin, 2018; Xi *et al.*, 2021). It reads (Cerfontaine & Collin, 2018; Xi *et al.*, 2021) :

$$\frac{\sigma_{Ai}}{\sigma_{n0}} = a \log_{10} M_{fi} + b \tag{4.6}$$

where a and b are the two model parameters that can be obtained from experimental data.

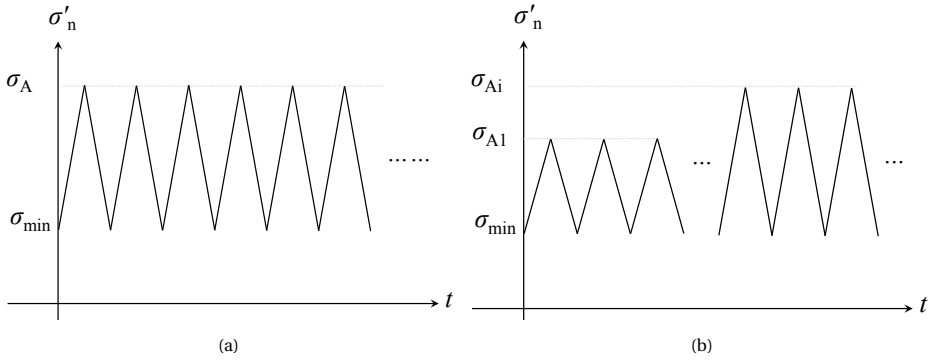


Figure 4.2: Cyclic loading with (a) constant amplitude; and (b) varying amplitude.

4.3. VALIDATION AGAINST CYCLIC BRAZILIAN TEST

In this section, the proposed method is validated against cyclic Brazilian tests conducted by Erarslan & Williams (2012).

4.3.1. DESCRIPTION OF THE EXPERIMENT

The Brazilian test, also known as the splitting tensile strength test, is a common method to estimate the tensile strength of brittle rocks. In this test, a thin circular disc is placed in between loading platens or curved loading jaws, and diametrically loaded until failure (Fig. 4.3a). Upon loading, a line of equally-distributed tensile stress will be induced in the centre of the specimen, shown in Fig. 4.3b. The compressive force applied at failure (defined as the maximum force the sample can sustain) F_{max} [N] is used to calculate the tensile strength σ_{n0} [Pa] according to:

$$\sigma_{n0} = -\frac{2F_{max}}{\pi d h_0 \alpha}\left(\sin\alpha - \frac{\alpha}{2}\right) \tag{4.7}$$

where d [m] and h_0 [m] are the radius and the thickness of the disc, respectively, and α is the contact angle (Navidtehrani *et al.*, 2022).

In the work of Erarslan & Williams (2012), Brisbane tuff was used to produce the specimens with a diameter of 52 mm and a thickness of 26 mm. The material properties

are presented in Tab. 4.1. The specimens were used to conduct monotonic and cyclic Brazilian tests in a setup, whose two jaws were designed to make contact with the specimen at diametrically opposed surfaces over an arc of contact of (α =) 10° (Erarslan & Williams, 2012). The specimen was loaded with monotonic or cyclic loading perpendicular to the contact arc at a rate of 200 N/s. In the monotonic loading case (in this chapter sample BR-3 is taken as an example), the sample failed when the loading reached 20.98 kN. This case will be simulated first to explore the mesh sensitivity. In the cyclic Brazilian tests, a series of cyclic tests with constant amplitude at 95%, 90%, 80% and 70% of $F_{\max}$ (the load at failure under monotonic loading) were performed to determine the fatigue life, with the experimental S-N relation and fitted relationship presented in Fig. 4.4. The cases of cyclic tests with constant amplitude at 95% and 90% of $F_{\max}$ are then simulated to validate against experimental results, i.e. experimental fatigue life and fracture patterns.

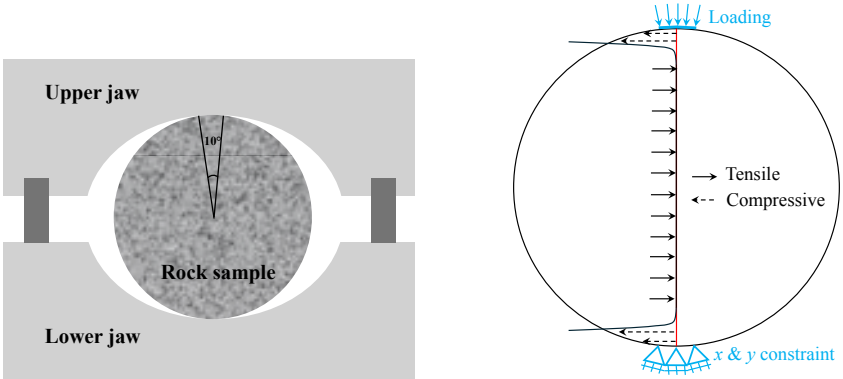
Table 4.1: Material properties and model parameters (Erarslan & Williams, 2012).

Parameter	Symbol	Value	Unit
Material properties			
Young's modulus	E	2.6E10	Pa
Poisson's ratio	ν	0.26	-
Mode-I fracture toughness	K_{IC}	1.18E6	Pa$\cdot$ m$^{0.5}$
Tensile strength (BR-3, used for static loading)	σ_{n0}	9.87E6	Pa
Tensile strength (used for cyclic loading)	σ_{n0}	10.82E6	Pa
Model parameters			
Cracking separation	r_{n0}	1E-7	m
Debonding separation	r_{nc}	1E-5	m
Stiffness of interface elements	K_{n0}	9.87E14 or 10.82E14	Pa
Mechanical viscosity	ζ	1E9	Pa $\cdot$ s/m
Parameter a in Eq. 4.6	a	-0.051085	-
Parameter b in Eq. 4.6	b	0.9929	-

In the cyclic Brazilian tests, other samples were then used (Erarslan & Williams, 2012). The maximum loading at failure ($F_{\max}$) under static loading was measured at 23 kN. Then, a series of cyclic tests with constant amplitude at 95%, 90%, 80% and 70% of $F_{\max}$ were performed to determine the fatigue life, with the experimental S-N relation and fitted relationship presented in Fig. 4.4.

4.3.2. NUMERICAL MODEL

A 2D model is constructed to simulate the monotonic and cyclic Brazilian tests (Fig. 4.3b). The bottom arc with a contact angle of 10° is fixed in both x and y directions, while the top arc is imposed by monotonic or cyclic loading. The domain is meshed with second-order triangular elements, and interface elements are inserted in between all the triangle elements to allow fractures to occur in arbitrary directions. Three different meshes are constructed to investigate the mesh sensitivity of the model, as is shown in Fig. 4.5a to 4.5c. Fig. 4.5a presents a coarse mesh (1770 continuum elements) with a straight line imposed along the central axis of the circle, since a straight fracture is predicted to be induced



(a) (b)

Figure 4.3: (a) Schematic description of Brazilian test; (b) Tensile stress distribution along the centre of the disc.

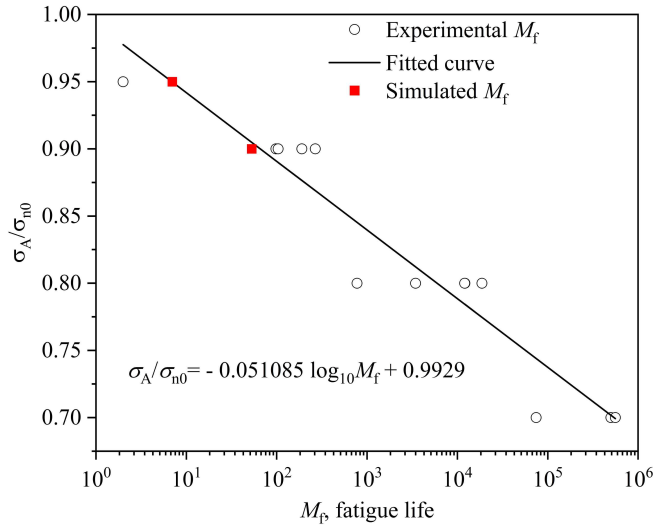


Figure 4.4: Experiment and simulation results of fatigue life M_f under different maximum loading σ_A. Experimental data is from Erarslan & Williams (2012).

along the central axis according to analytical solutions (International Society for Rock Mechanics, 1978; Navidtehrani *et al.*, 2022). Interface elements were inserted between all continuum elements. Yet due to the likely highest tension values along this straight line, it provides a preferential cracking path. In contrast, Fig. 4.5b and 4.5c presents a coarse (1484 continuum elements) and a finer mesh (12268 continuum elements), respectively, without the imposed straight line along the central axis and interface elements inserted between all continuum elements. Consequently, no cracking path along the central axis is prescribed in the meshes of Fig. 4.5b and 4.5c. The model parameters are shown in Tab. 4.1. The tensile strength and the debonding separation are determined from material tensile strength and mode-I fracture toughness. The stiffness of the interface element is set to a high value to reduce artificial compliance while managing numerical convergence.

4.3.3. NUMERICAL SIMULATION OF THE STATIC BRAZILIAN TEST

Simulation results of the monotonic Brazilian test on sample BR-3 is discussed here. The loading was applied at a rate of 200 N/S until a maximum loading at 20.98 KN, as was in the experiment. A sensitivity analysis on the mesh is first conducted, with the results shown in Fig. 4.5d to 4.5i. In Fig. 4.5d to 4.5f, the damage variable D is shown to highlight the simulated fracture patterns at maximum loading for the three meshes. Fig. 4.5d shows that a straight fracture along the central axis can be simulated with the mesh shown in Fig. 4.5a, where a straight line (of interface elements) is imposed along the central axis. This is consistent with the experimental fracture pattern shown in Fig. 4.7a and the theoretical solution. A maximum force of 20.98 kN is applied, which corresponds to a tensile strength of 9.87 MPa, corresponding well to the input tensile strength. However, no damage is seen in Fig. 4.5e, in which no straight line is imposed along the central axis and the mesh is coarse. In contrast, if the mesh in the central part of the model is made to be fine enough (to automatically generate some straight mesh edges in the central part), as is shown in Fig. 4.5c, the central fracture can be simulated (Fig. 4.5f), though the fracture has to follow the element edges. In addition, Fig. 4.5g to 4.5i presents the distribution of the horizontal stress σ_x. The horizontal stresses in Fig. 4.5g have a maximum tension of around 7.25 MPa, indicating a relaxation of stress after the tensile fracture occurs. In Fig. 4.5h tension is seen of approximately 10 MPa (exceeding the tensile strength) along the central axis, thus should induce fractures, however cannot due to the orientation of the mesh. Instead, the fracture can only be induced if the load is increased to 29.12 KN in the simulation using the coarse mesh in Fig. 4.5b, almost 40% higher than the 20.98 KN in the experiment. In Fig. 4.5i, σ_x is again relaxed along the central axis with a distribution similar to that of Fig. 4.5g as a result of the formation of the fracture(s). Due to the less structured alignment of the mesh, the fracture distribution is less even and results is a less uniform stress distribution immediately around the fracture zone, and results in a calculated tensile strength of 8.85 MPa. The mesh sensitivity analysis highlights the influence of the mesh orientation and mesh density on the simulation results, although the stresses prior to fracturing are almost identical. A priori knowledge of the position and direction of the fracture initiation and propagation is therefore helpful to allow the use of coarse mesh, which demonstrates the importance of the analytical solutions. Otherwise, several different meshes may be used to capture the correct fracture propagation.

Based on the model with mesh presented in Fig. 4.5a, a comparison of simulated and

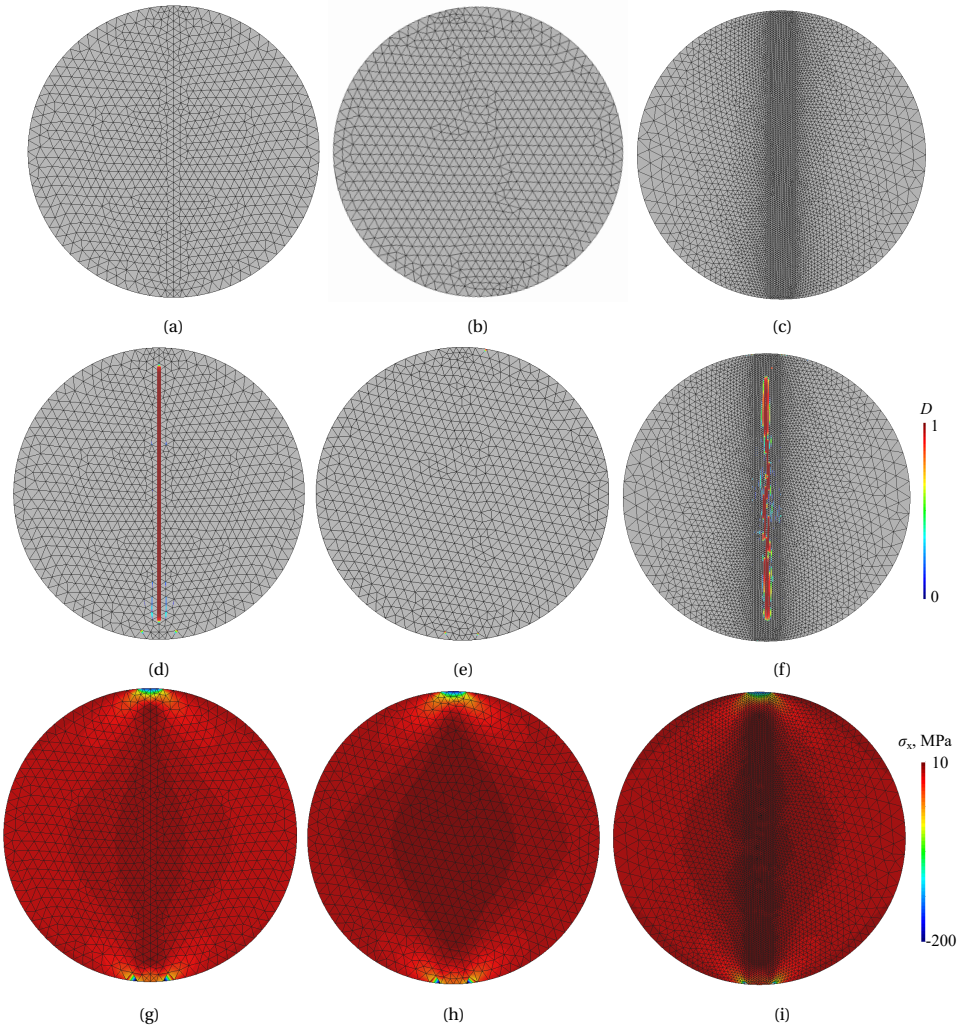


Figure 4.5: Mesh sensitivity analysis. (a) - (c): three different meshes consisting of second-order triangle continuum elements and interface elements that are inserted between all the continuum elements to provide arbitrary potential cracking paths. (a) coarse mesh (1770 continuum elements) with a straight line imposed along the central axis of the circle; (b) coarse mesh (1484 continuum elements) without the imposed straight line along the central axis; (c) finer mesh (12268 continuum elements) without the imposed straight line along the central axis. (d) - (f): corresponding simulated damage variable at failure, indicating the fracture patterns. (g) - (i): distribution of σ_x at failure.

experimental axial and lateral strains is presented in Fig. 4.6, showing generally good agreement with a slight deviation, which is from the artificial compliance as a result of insertion of interface elements. In addition, failure can be clearly seen at the turning point on the simulated curve when loading reaches 20.98 kN, shown in Fig. 4.6, indicating increasing strain since the specimen failed and could not sustain the controlled loading. The peak loading is reached at time step 104.9 s.

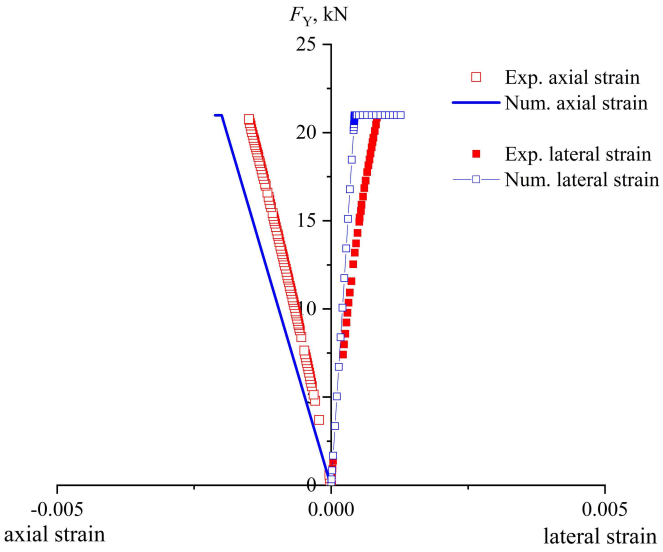


Figure 4.6: Comparison of experimental and numerical results of axial and laterial strain in the static Brazilian test on sample BR-3.

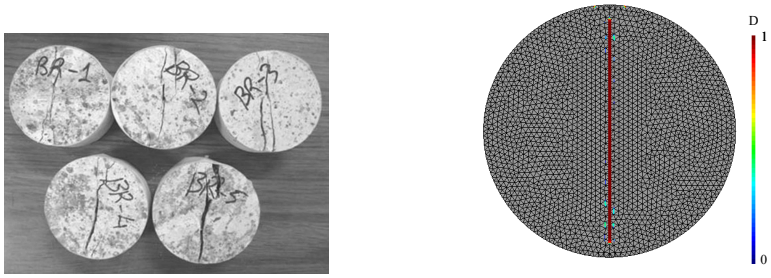


Figure 4.7: Comparison of experimental and simulated damage in the specimens. (a) BR-3 after failure under static loading in the experiment (figure from Erarslan & Williams (2012)); (b) Damage variable at t = 125 s in the simulation.

4.3.4. NUMERICAL SIMULATION OF THE CYCLIC BRAZILIAN TEST

After initial validation against the static loading experimental data from sample BR-3, the model can then be validated against cyclic Brazilian tests. As mentioned earlier, a series of cyclic experimental tests with maximum loading at 95%, 90%, 80% and 70% of $F_{\max}$ (23 kN) was performed to determine the corresponding fatigue life (Erarslan & Williams, 2012). Based on the element test data shown in Fig. 4.4, both parameters a and b of the empirical relationship (Eq. 4.6) can be determined. In addition, the tensile strength is chosen as 10.87 MPa, as derived from the maximum force applied $F_{\max}$ (23 KN). Other material properties and model parameters are kept the same as shown in Tab. 4.1. We select the cases where the maximum loading during cyclic loading are 95% and 90% of $F_{\max}$ (23kN) as examples to demonstrate the capability of the proposed model.

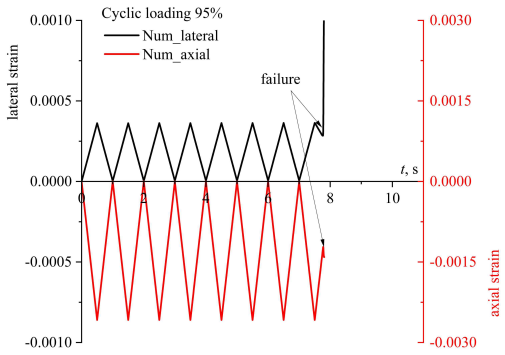
Figs. 4.8a and 4.8c show the lateral and axial strain evolution with time. It is clearly shown that a sudden sharp increase in lateral strain is observed in the 8th and 54th cycles in the cases of 95% and 90% $\sigma_{\max 0}$, respectively. As opposed to the single failure observed in static tests, a complex fracture pattern is seen in the experimental results, resulting in an overall failure of the sample (Fig. 4.9), with the numerical results also indicating a network of fractures. The number of cycles to achieve failure at a corresponding loading amplitude is presented in Fig. 4.4, showing a good agreement with the S-N curve fitted from the experimental data, thereby demonstrating the capability of the proposed method to capture the fatigue damage due to cyclic loading at different loading amplitudes.

To further demonstrate the capability of the proposed model to handle varying-amplitude cyclic loading, two synthetic loading cases (not performed experimentally) with varying-amplitude cyclic loading are simulated. In Case A, the applied maximum load is equal to 90% $\sigma_{\max 0}$ for the first 10 cycles, before increasing to to 95% $\sigma_{\max 0}$ in the later cycles (Fig. 4.10a). The corresponding results (Fig. 4.10b) show that failure of the sample happens at the 15th cycle, less than the fatigue life (54 cycles) under cyclic loading with constant maximum loading at 90% $\sigma_{\max 0}$ but more than that (8 cycles) under cyclic loading with constant maximum loading at 95%$\sigma_{\max 0}$. Inspired by the results from Case A, the applied maximum load in Case B is set to 95% $\sigma_{\max 0}$ in the first 5 cycles, before decreasing to 90%$\sigma_{\max 0}$ in later cycles (Fig. 4.10c). Interestingly, unlike Case A where failure happens after 14 cycles (first 10 lower-amplitude cyclic loading + later 4 higher-amplitude cyclic loading), failure is seen in the 31st cycle in Case B (Fig. 4.10d).

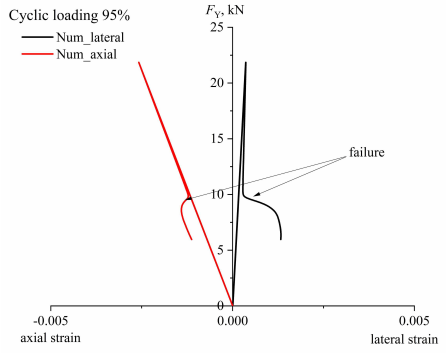
4.4. VALIDATION AGAINST CYCLIC HYDRAULIC FRACTURING TEST

4.4.1. DESCRIPTION OF THE EXPERIMENT

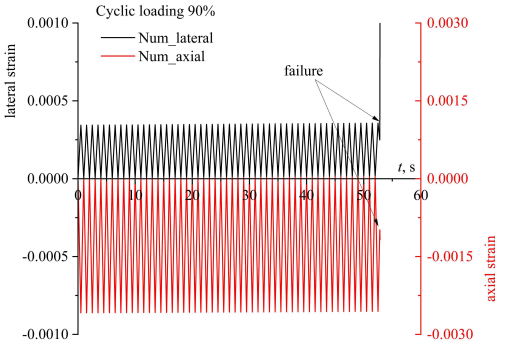
The hydraulic fracturing test is widely used to determine the tensile strength of rocks and/or the magnitude of the in situ stresses. Zhang et al. conducted laboratory (cyclic) hydraulic fracturing tests on granite samples cored from the Pocheon geothermal field to demonstrate the concept of cyclic stimulation (Zhuang *et al.*, 2019b). The targeted Pocheon granite contained three orthogonal cleavage planes, namely the rift (R), graine (G) and hardway (H) planes. Specimens used in the experiments were cored perpendicular to each of the R, G and H planes, and thus are labelled as R, G and H groups, respectively. The rift plane was seen to have the weakest strength, with an average measured Brazilian



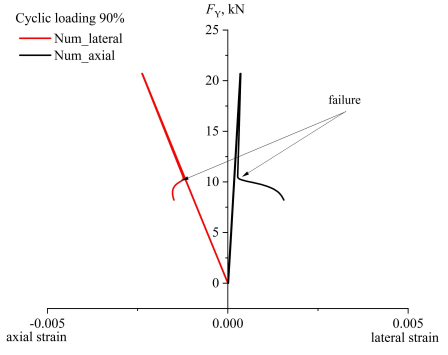
(a) Strain vs. time under 95% σ_{max0}.



(b) Load vs. strain under 95% σ_{max0}.

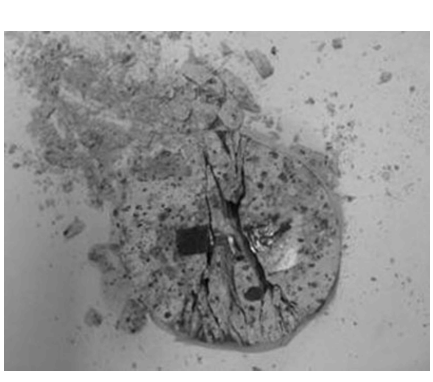


(c) Strain vs. time under 90% σ_{max0}.

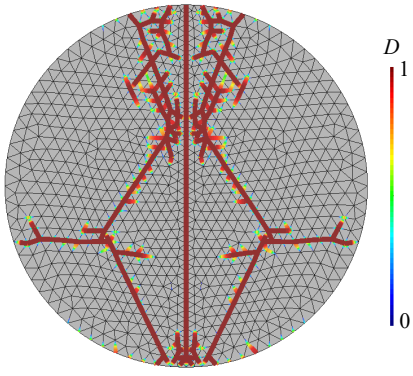


(d) Load vs. strain under 90% σ_{max0}.

Figure 4.8: Lateral (positive) and axial (negative) strain evolution with time and loading under different cyclic loadings.

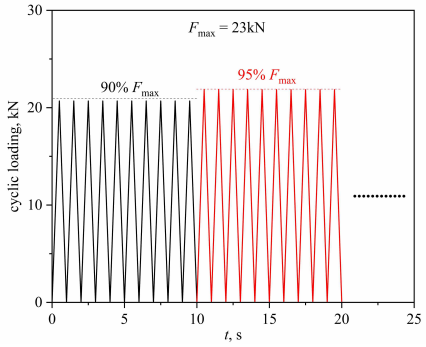


(a)

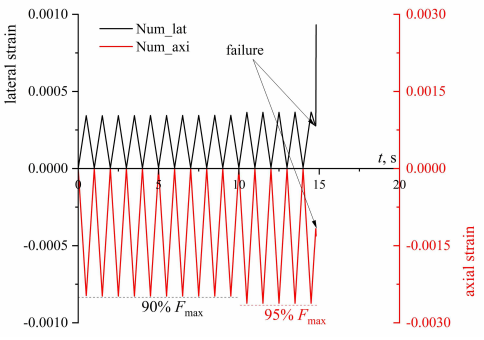


(b)

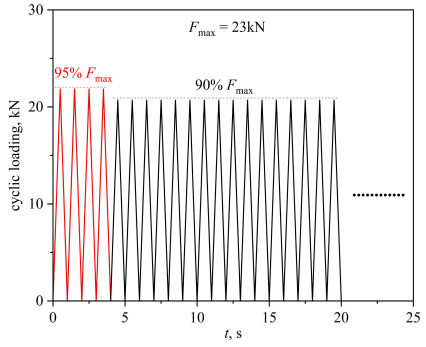
Figure 4.9: Comparison of the failed sample under cyclic loading (a) in the experiment (figure reproduced from Erarslan & Williams (2012)); and (b) in the simulation (95% σ_{max0}).



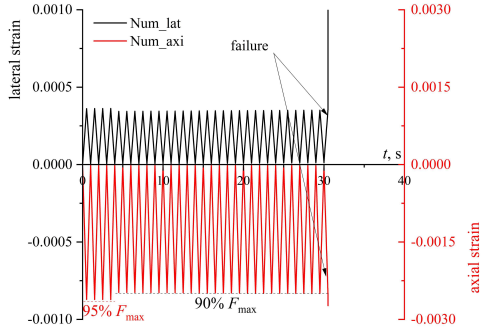
(a) Applied varying-amplitude cyclic loading in case A.



(b) Strain evolution in case A.



(c) Applied varying-amplitude cyclic loading in case B.



(d) Strain evolution in case B.

Figure 4.10: Simulation results of varying-amplitude cyclic loading and corresponding lateral and axial strain evolution cases.

tensile strength equal to 6.1 MPa. Hydraulic fracturing tests on specimens in Group G and H were seen to induce fractures in the weakest rift plane. In this chapter, we focus only on the fracturing tests on specimens from group H, with the orientation of the sample and the cleavage planes shown in Fig. 4.11a. Other properties of the specimens in group H are presented in Tab. 4.2.

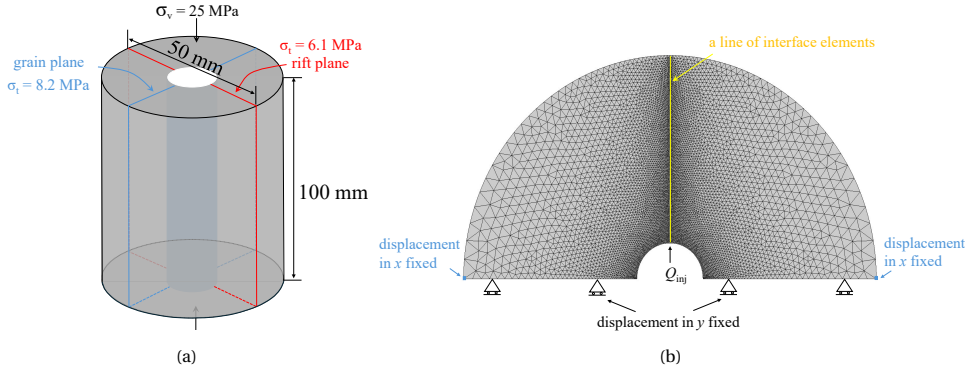


Figure 4.11: Description of (a) the Pocheon granite specimen in group H and (b) the corresponding numerical model. A line of interface elements is used in the model to represent the weakest rift plane, on which fracture can be induced by injection of fluid.

Table 4.2: Properties of the Pocheon granite specimens in group H and model parameters.

Material properties			
Parameter	Symbol	Value	Unit
Young's modulus	E	5.8E10	Pa
Poisson's ratio	ν	0.30	-
Density	ρ_s	3000	kg/m^3
Tensile strength (rift plane)	σ_{n0}	6.1E6	Pa
Model parameters			
Cracking separation	r_{n0}	1E-7	m
Debonding separation	r_{nc}	2E-7	m
Mechanical viscosity	ζ	1E12	Pa·s/m
Parameter a in Eq. 4.6	a	-0.021129	-
Parameter b in Eq. 4.6	b	0.90437	-

A borehole with a diameter of 8 mm was drilled through the center axis of the specimens to allow the injection of fluid, as is shown in Fig. 4.11a. Two sets of tests were conducted, one using a controlled pressurisation rate and the other with a controlled injection rate. Here, we focus on the tests of controlled injection rate (100 mm^3/s), in which the horizontal confining pressure is zero while the vertical stress was 25 MPa to prevent fluid leakage from the top and bottom surfaces. Monotonic fracturing was first implemented using 12 specimens to determine an average monotonic breakdown pressure, which was 6.9 MPa. Cyclic fracturing tests then followed with a maximum injection

pressure ranging from 74% to 95% of the monotonic breakdown pressure, using another 34 samples. Since injection rate was controlled, the injection time was therefore adjusted to achieve the desired injection pressure. Fig. 4.12 presents the number of cycles needed to fail the specimens under different maximum injection pressure in the experiments.

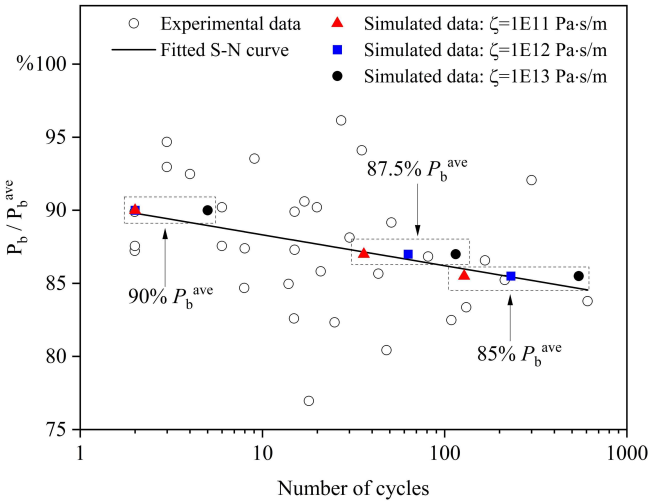


Figure 4.12: Experiment and simulation results of fatigue life M_f under different maximum injection pressure p_{inj}.

4.4.2. NUMERICAL MODEL

A 2D model is constructed to simulate both the monotonic and cyclic fracturing tests (Fig. 4.11b). Only half of the horizontal section of the specimen is considered due to symmetric condition. A line of interface elements is inserted along the symmetry axis to represent the weakest rift plane, along which fracture can be induced upon fluid injection. The solid elements represent the rock matrix, which is assumed to be impermeable due to its extremely low permeability. The bottom boundaries of the model are fixed along the y direction, with two nodes at the left and right sides fixed along the x direction to provide reaction to the whole system. No confining stress is applied matching the experimental conditions. Other model input parameters for the interface elements are summarised in Tab. 4.2.

4.4.3. NUMERICAL SIMULATION OF THE MONOTONIC INJECTION TESTS

Monotonic fracturing is first simulated to demonstrate the capability of the model and determine the simulated monotonic breakdown pressure. A ramped injection rate, shown in Fig. 4.13a, is used to simulate the borehole storage effect. Fig. 4.13 compares the simulation and experimental results of the monotonic hydraulic fracturing test. It shows that the numerical model can successfully capture the pressure response with a peak pressure at 6.48 MPa (compared to 6.9 MPa in the experiment). Additionally, the damage variable of the all of the interface elements is recorded in the simulation and averaged

and compared with the AE records of the experiment. Both values represent the damage process of the rock sample in different ways. When the averaged damage variable reaches 1, it indicates the whole line of interface elements is fully opened. The time period over which the damage variable increases from zero to 1 is the same time period with the AE events with the highest amplitude and most densely recorded events.

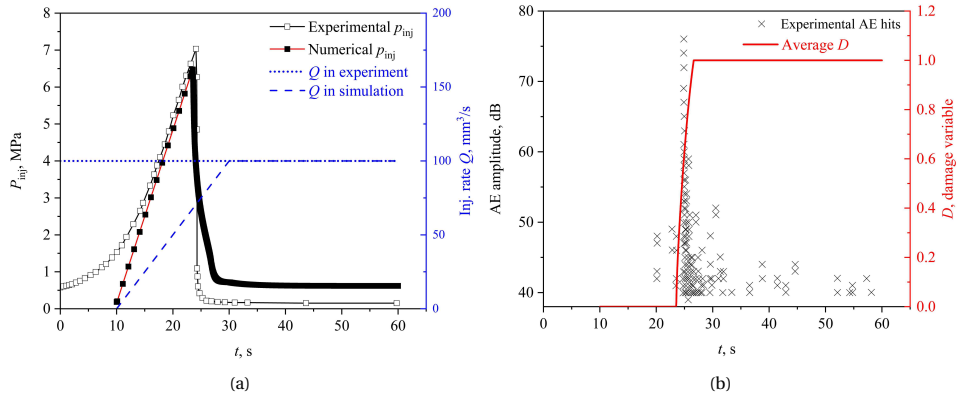


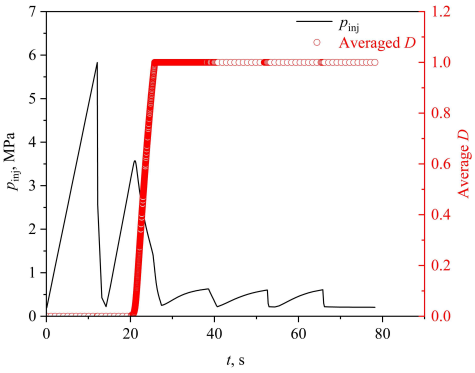
Figure 4.13: Comparison of experiment and simulation results of (a) pressure response and (b) experimental AE hits and simulated damage variable D during monotonic hydraulic fracturing test.

4.4.4. SIMULATION RESULTS OF THE CYCLIC INJECTION TESTS

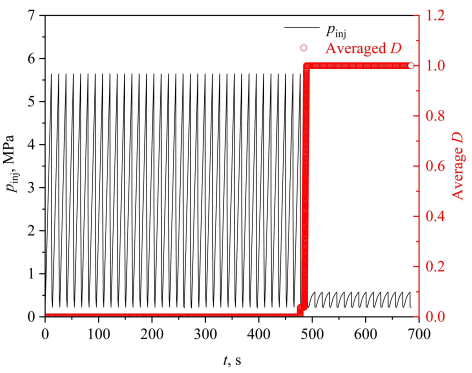
The model then is used to simulate the cyclic fracturing tests, with the maximum injection pressure reaching 90%, 87% and 85% of the simulated p_b^{ave} (6.48 MPa) in each cycle. Each cycle has the same injection rate and time period, so in cases where damage (partially) occurs, the achieved pressure is lower than the initial pressure. The same domain and input parameters are used as in the monotonic simulations.

The simulated pressure response and averaged damage variable under different cyclic injection pressure are presented in Fig. 4.14. Fig. 4.14 shows the granite sample fails in the 2nd cycle, 63rd cycle and 231st cycle under a cyclic injection pressure of 90% p_b^{mono}, 87% p_b^{mono} and 85% p_b^{mono} respectively. The relationship between the fatigue life and the cyclic injection pressure is plotted as blue rectangles in Fig. 4.12, showing a good agreement with the S-N curve fitted from experimental data. Therefore, the proposed model can successfully reproduce the fatigue damage due to cyclic hydraulic stimulation.

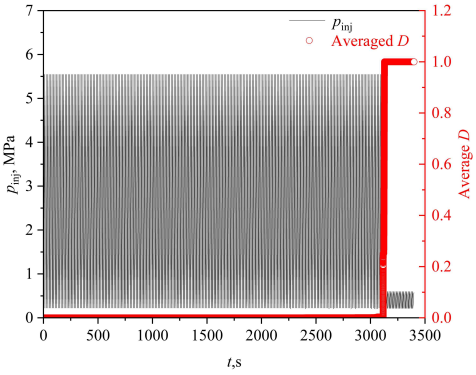
Viscous stress is added in Eq. 3.20 to resolve large fast changes in the solution, which occur faster than the time discretisation, and can cause numerical divergence. The added viscosity ζ slows down the strain rate and thus stabilised the solution, however it could also have an impact on the predicted behaviour including the fatigue life. To investigate the impact of the added viscosity, simulations of the cyclic hydraulic fracturing test are run with four different viscosities, i.e., ζ = 0 Pa·s/m, 1E11 Pa·s/m, 1E12 Pa·s/m and 1E13 Pa·s/m. The predicted fatigue life for different injection pressures with the different viscosities is presented in Fig. 4.12. It is seen that by increasing the viscosity, the fatigue life also increases. Here, the impact of the viscosity on the results are discussed in detail for the case under p_{inj} = 90% p_b^{mono}. The simulated injection pressures are shown in



(a) Pressure response under $p_{inj} = 90\% p_b^{mono}$.



(b) Pressure response under $p_{inj} = 87\% p_b^{mono}$.



(c) Pressure response under $p_{inj} = 85\% p_b^{mono}$.

Figure 4.14: Simulated pressure response and evolution of the average damage variable under different p_{inj}.

Fig. 4.15. When the mechanical viscosity is 0Pa · s/m, the simulation cannot converge when interface elements reach the cracking separation r_{n0}. If a 1E11Pa · s/m viscosity is added, the problem of lack of convergence reduces slightly, but the simulation still stops after 1.5 cycles. If more viscosity is added, i.e. ζ = 1E12Pa · s/m, the simulation is able to run continuously, with fatigue life matching the point when the other simulations stop. However, when adding a larger viscosity, in this case ζ = 1E13Pa · s/m, damage occurs gradually and increases per cycle, with the fatigue life being significantly increased, see Fig. 4.12. With a further reduction in injection pressure, the differences become larger, however, these are still in fitting with the experimental behaviour and are therefore considered to be reasonable.

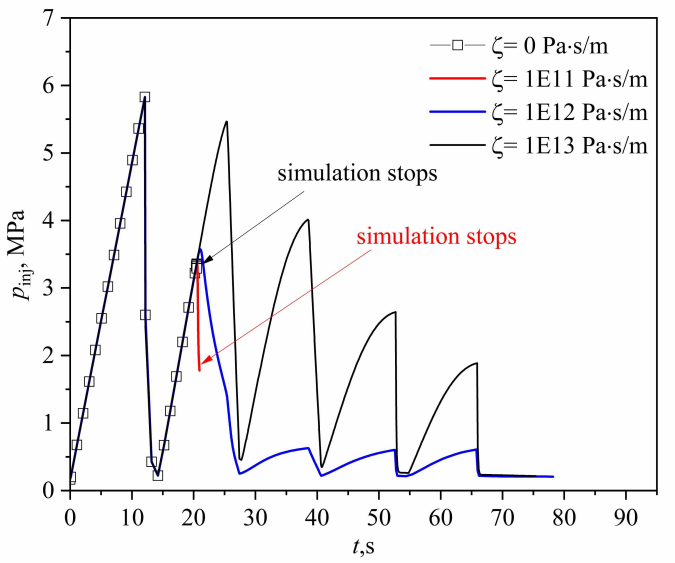


Figure 4.15: Influence of mechanical viscosity of the fatigue simulation.

4.5. VALIDATION AGAINST CYCLIC THERMO-HYDRAULIC FRACTURING TEST

4.5.1. DESCRIPTION OF THE EXPERIMENT

Thermal stimulation, which takes advantages of both thermal stress and hydraulic pressurisation, has been proposed and utilised in geothermal reservoirs. This aims to reduce the breakdown pressure during hydraulic fracturing, therefore reducing environmental impacts. Hong et al. experimentally studied the monotonic and cyclic injection of cold liquid nitrogen and water into granite samples (Hong *et al.*, 2023). In this chapter, we focus on both monotonic and cyclic injection of cold water conducted by Hong et al., against which the proposed method is validated (Hong *et al.*, 2023).

The samples are formed from granite cored from the province of Shangdong, China, (properties of the granite are presented in Tab. 4.3) and were manufactured to be cubes

with the size of 100 mm × 100 mm × 100 mm, schematically shown in Fig. 4.16a. A hole 60 mm deep and 16 mm in diameter was drilled in the centre of the samples. A steel tube 40 mm deep and 14 mm in diameter was cemented in the hole, leaving a 20 mm deep 'open hole' section. The temperature at the open hole section was monitored by a thermocouple attached to the wall of the open hole.

Table 4.3: Properties of the granite samples and parameters used for the interface elements (Hong *et al.*, 2023).

Parameter	Symbol	Value	Unit
Properties of the granite samples			
Density	ρ_s	2630	kg/m^3
Young's modulus	E	39.41	GPa
Poisson's ratio	ν	0.28	-
Tensile strength	σ_{n0}	10.02	MPa
Permeability	k	1.1E-3	mD
Porosity	ϕ	0.0045	-
Linear thermal expansion coefficient*	α	4.8E-6	K^{-1}
Thermal conductivity	λ	3.1	W/(m · K)
Parameters of the interface elements			
Cracking separation	r_{n0}	1E-8	m
Debonding separation	r_{nc}	1E-5	m
Mechanical viscosity	ζ	1E12	Pa·s/m
Parameter a in Eq. 4.6	a	-1.0	-
Parameter b in Eq. 4.6	b	0.99	-

The experiments consisted of two phases: (1) cooling-heating cycles; (2) fracturing test via injection of cold water. Fig. 4.17 shows the evolution of the borehole temperature and injection pressure during one single cooling-heating cycle and during the fracturing test respectively. The samples were firstly pre-heated to 473 K in a muffle furnace. Then, the samples were loaded with initial stresses of σ_v = 15 MPa, σ_H = 10 MPa and σ_h = 7 MPa in a true triaxial fracturing equipment (Hong *et al.*, 2023), which is designed to insulate the sample and allows the injection of fluid. In both phases, a 600-second natural cooling down of the samples happened first before any injection of cold water (Stage I in Figs. 4.17a and 4.17b).

In the cooling-heating cycle, shown in Fig. 4.17a, water with temperature of 323 K was injected into the borehole with a constant low injection pressure of 2 MPa, lasting for 180 seconds (Stage II in Fig. 4.17a). After injection stopped, the open hole naturally re-heated and then cooled (Stage III in Fig. 4.17a). The samples were then removed from the triaxial equipment and re-heated to 473 K in the muffle furnace (Stage IV in Fig. 4.17a) before the next cooling-heating cycle. After the required cooling-heating cycles, the samples were then subjected to high-pressure injection of cold water to determine the (reduced) breakdown pressure, shown in Fig. 4.17b. In contrast to the cooling-heating cycle, water with temperature of 323 K was injected into the borehole with a constant

0*: The thermal expansion coefficient is calculated from the thermal expansion coefficient of the dominant minerals' (30% K-feldspar and 47% oligoclase). Data from Hong *et al.* (2023).

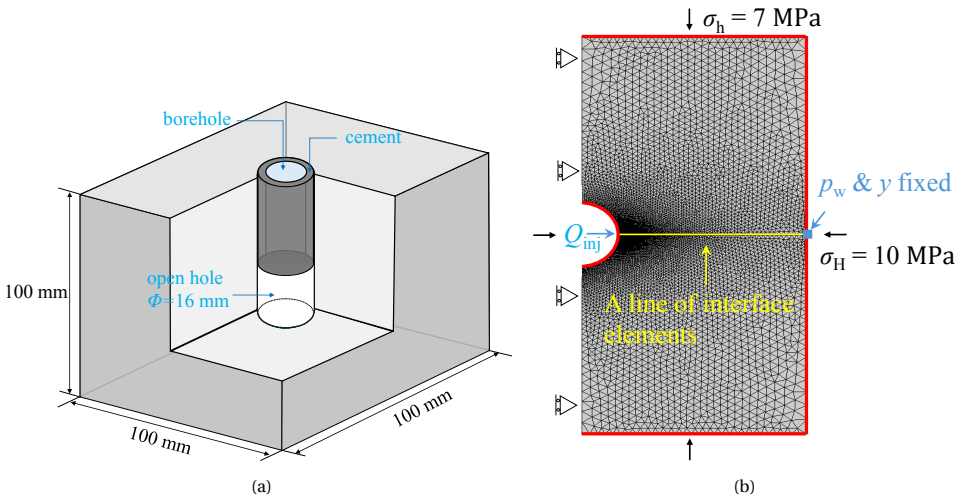


Figure 4.16: Description of (a) the granite samples used in the experiment and (b) the corresponding 2D numerical model. A line of interface elements is used in the model to represent the potential fracture path, on which fracture can be induced by injection of fluid.

injection rate of 30 mm^3/min, leading to an average pressurisation rate of 0.386 MPa/s until the breakdown pressure. Four cases were performed by Hong *et al.* (2023), including monotonic fracturing test without cooling-heating cycle, 1 cycles, 3 cycles and 5 cycles of such cooling and heating, which were labelled as W7, W8, W2 and W9 repsectively (Hong *et al.*, 2023). Experimental results show that a decreased breakdown pressure was observed with the number of cooling-heating cycles increasing, as presented in Fig. 4.18.

4.5.2. NUMERICAL MODEL

A 2D symmetric model, shown in Fig. 4.16b, is constructed. Since a single fracture wing was observed in the direction of σ_H after fracturing tests in the experiments, only a single line of interface elements are inserted the direction of σ_H in the model to represent the potential fracture path, which also aids to reduce the computational burden. Initial stresses of σ_H = 10 MPa and σ_h = 7 MPa are applied. The continuum elements are set to be impermeable due to the extremely low permeability of the granite, but heat conduction is allowed. Water is injected into the interface elements from the mid-node of the interface element at the borehole wall. In Stage II of the cooling-heating cycles, the injection pressure is kept constant at 2 MPa. In contrast, during the fracturing stage, the injection rate is ramped to 30 mm^3/min in 60 seconds and then kept constant. This simulated the storage effect, where in the experiment the pressure build-up rate was an average of 0.386 MPa/s. The temperature at the borehole is controlled based on its evolution shown in Fig. 4.17.

The key parameters for the interface element are presented in the Tab. 4.3. Tensile strength was determined via Brazilian test in original paper (Hong *et al.*, 2023). The cracking separation is set high to reduce artificial compliance, while the de-bonding separation is determined from granite toughness. Since no element tests are available

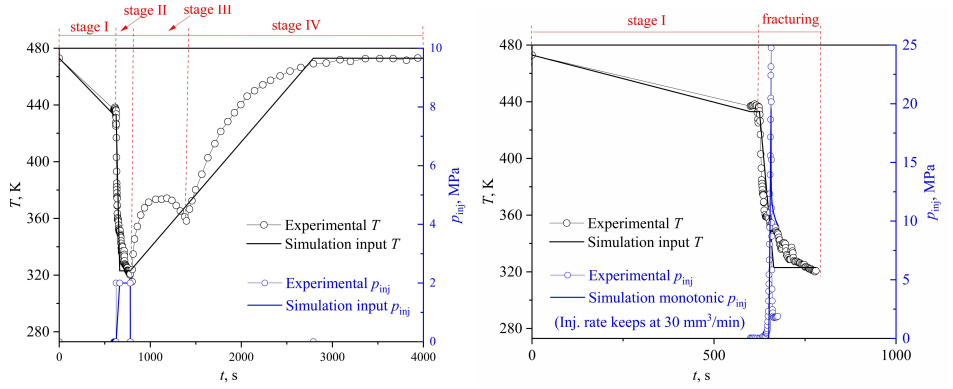


Figure 4.17: Changes of borehole temperature and injection pressure in (a) one signle cooling-heating cycle; and (b) monotonic fracturing test.

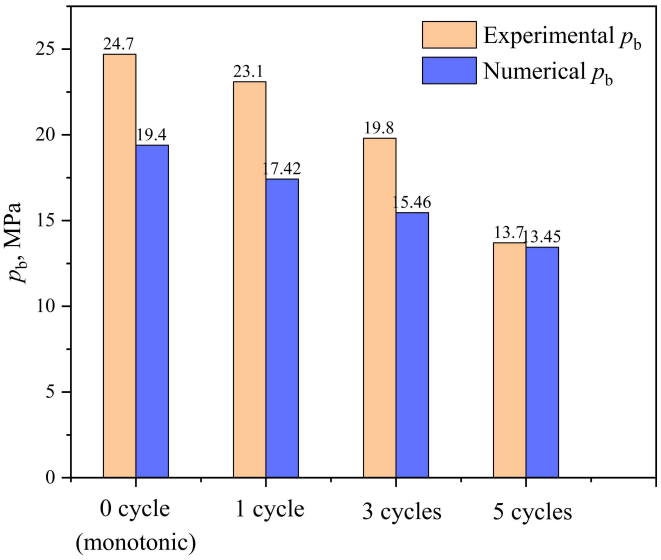


Figure 4.18: Breakdown pressure in the fracturing tests against the number of cooling-heating cycles and simulations (Hong *et al.*, 2023).

for the samples used in this experiment, the S-N relationship is determined based on the results of the breakdown pressure, shown in Fig. 4.18. However, since this is a fully THM coupled problem, the actual applied normal stress (σ_A) on the first interface element at the borehole during cooling-heating cycles and the degraded tensile strength (σ_{nm}) after cycles cannot be obtained directly. First, to determine σ_A in the Equation 4.6, a coupled THM simulation of the cooling stage is performed to determine the largest tangential stress $\sigma_t^{cooling}$ (at the wellbore in the direction of σ_H) reached during cooling, which is σ_A. To determine the degraded tensile strength σ_{nm}, a coupled THM simulation of the fracturing stage with high-pressure injection is performed to determine the tangential stress σ_t^{frac} (at the wellbore in the direction of σ_H). We simulate the monotonic fracturing test, and pick the tangential stresses σ_t^{frac} at which the normalised injection pressure (defined as the ratio of the injection pressure to the monotonic breakdown pressure, p/p_b^{mono}) reaches the corresponding normalised breakdown pressures (p_b/p_b^{mono}) under different cycles in the experiments. These picked tangential stresses σ_t^{frac} are viewed as the degraded tensile strengths σ_{nm} after different cooling cycles, as is shown in Tab. 4.4.

Now we have three data points of different cycles with corresponding degraded tensile strengths under a given normal stress σ_A (σ_A here is constant since in stage 1 the injection pressure and temperature were not changed.) Based on Equations. 4.1, 4.4 and 4.6, we can determine the corresponding fatigue life M_f of these three cases. Then the parameter a and b can be obtained by best-fitting the three data points.

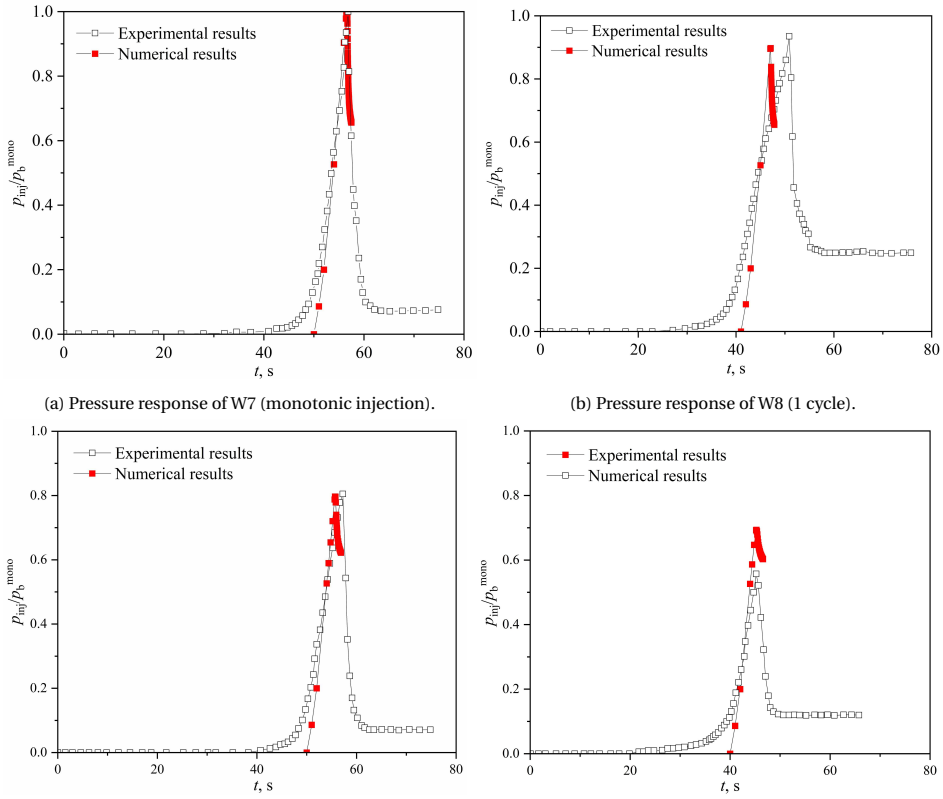
Table 4.4: Degraded tensile strengths from the the experimental data (obtained by simulating the fracturing test under monotonic injection) and from the simulation considering fatigue damage.

No. of cycles	Exp. p_b/p_b^{mono}	Exp. σ_{nm}/σ_{n0}	Simu. D_f	Simu. σ_{nm}/σ_{n0}
0	1	1	0	1
1	0.94	0.95	0.228	0.77
3	0.80	0.68	0.452	0.55
5	0.55	0.17	0.675	0.33

4.5.3. RESULTS AND DISCUSSION

Fig. 4.19a presents the normalised injection pressure response during the monotonic fracturing test (i.e. without a cooling-heating cycle) while Fig. 4.18 compares the exact injection pressure during monotonic fracturing in the experiment and simulation. The simulated monotonic breakdown pressure p_b is 19.5 MPa, around 20 % lower than that (24.7 MPa) observed in the experiment. The working hypothesis is that the tensile strength used in the model was taken from the strength measured at room temperature via the Brazilian test (Hong *et al.*, 2023), while the sample was heated to 473 K before conducting the fracturing test. Other possible factors include the chosen values of the linear thermal expansion coefficient α and the thermal conductivity λ. In the simulation, α is estimated based on the thermal expansion coefficients of the dominant minerals (30% K-feldspar and 47% oligoclase) of the granite used in the experiment (Hong *et al.*, 2023). However, the overall linear thermal expansion coefficient of the rock sample could be different from the one calculated from mineral components. In addition, the thermal conductivity is not mentioned in their paper, and is estimated here. Moreover, due to the limited number of samples tested, sample heterogeneity could play a significant role.

Figs. 4.19b, 4.19c and 4.19d shows the normalised pressure response during the fracturing tests after 1, 3 and 5 cooling-heating cycles, respectively. A clear trend of decreasing p_b with increasing number of cycles that was observed in the experiment is well reproduced in the simulation, as is demonstrated in also Fig. 4.18. The decreased p_b is a result of the fatigue damage accumulated during the cooling-heating cycles, in which both the thermal stress and the 2 MPa injection pressure have an impact. The accumulated fatigue damage and corresponding simulated σ_{nm}/σ_{n0} are listed in Tab. 4.4. The fatigue damage variable D_f increases with increasing number of cooling cycles, contributing to the reduced breakdown pressure. One thing worth explaining is that the values of σ_{nm}/σ_{n0} after 1 and 3 cycles are lower than their counterparts determined from experimental data, while the value after 5 cycles is higher. This is because the S-N curve is determined by best-fitting for the three data points, leading to an overall least distance to these three points while different differences between the simulated and experimental σ_{nm}/σ_{n0}.



(a) Pressure response of W7 (monotonic injection).

(b) Pressure response of W8 (1 cycle).

(c) Pressure response of W2 (3 cycles).

(d) Pressure response of W9 (5 cycles).

Figure 4.19: Normalised pressure (p_b/p_b^{mono}) response during the fracturing tests of the selected cases W7 (monotonic injection without cooling-heating cycle), W8 (1 cycle), W2 (3 cycles) and W9 (5 cycles) in the experiment and simulation. Note that the simulation is stopped after the breakdown pressure is overcome.

4.6. CONCLUSIONS

To enable the simulation of cyclic thermal stimulation to geothermal reservoir a cohesive interface element has been improved, adding a fatigue damage variable into the elasto-damage constitutive law that characterises the mechanical response of the interface element. The interface element can be used to model pre-existing or new fractures. The fatigue damage variable is determined by the number and magnitude of the cycles.

The proposed method is validated against three experiments from literature with different thermo-hydro-mechanical coupling, including the cyclic Brazilian test, the cyclic hydraulic fracturing test and the cyclic thermal stimulation test. All three validation results show the fatigue damage due to cyclic loading or reduced breakdown pressure due to cyclic injection/cyclic cooling-heating treatment can be well reproduced by the proposed method. In addition, the ability of the method to handle varying-amplitude cyclic loading is also demonstrated by the simulation of a synthetic cyclic loading based on the Brazilian test, in which the results show different patterns of the varying amplitude can lead to a different fatigue life. The method can be used in simulations to support the design of cyclic thermal stimulation strategy for geo-energy projects, such as geothermal energy production. Extensive experimentation may be needed to determine the fatigue damage variable evolution, and further efforts could be made to determine this more efficiently, e.g. from data collected during field tests.

5

NUMERICAL STUDY OF THE SOFT STIMULATION SCENARIOS

In this chapter, the previously developed tool is used to study the mechanisms underlying rock damage, and analyse the performance of different stimulation scenarios of a synthetic clogged reservoir. The properties of this synthetic reservoir are inspired by the geothermal project installed on the TU Delft campus and surrounding geothermal projects. First, the data collection and the synthetic reservoir are introduced. The simulation results are then presented to assess the effectiveness of different stimulation scenarios, including monotonic, stepwise, and cyclic stimulation (varying injection temperature or injection rate), as well as stepwise cyclic stimulation. Simulation results show that stepwise stimulation yields the most favourable outcomes, followed by stepwise cyclic stimulation. Fatigue effects are seen to play only a negligible role in the improved performance since the tensile stress at the fracture tip is relaxed with the continuous fracture growth. In addition, cyclic-injection-temperature stimulation is seen to be generally neither better or worse than monotonic stimulation, but has slightly different characteristics, creating more local damage controlled by the period of cyclic injection, with almost identical injection pressures to achieve the same injection rate.

This chapter has been submitted for publication as Luo *et al.* (2025b)

5.1. INTRODUCTION

The geothermal project on the TU Delft campus comprises a doublet installed in a sedimentary system. It was drilled in 2023 and is designed for both research and commercial thermal energy supply (Vardon *et al.*, 2024). The two wells target the early Cretaceous Delft sandstone formation, which is a matrix-dominated reservoir located at approximately 2 km beneath the Delft campus. The reservoir permeability in the high-permeability zones is up to 1.6 Darcy (1.6×10^{-12} m^2) according to logging data (Voskov *et al.*, 2024) and well testing results. Therefore, initial stimulation is not anticipated to be needed. Hot water is predicted to be produced at around 353 K, with an initial maximum production rate of 350 m^3/h, and the cooled-down water will be re-injected to the same reservoir at a temperature that can be as low as 293 K, which would result in a 25 MW supply of thermal energy at peak conditions in an environmental-friendly way (Vardon *et al.*, 2024).

The longevity of such projects is critical for achieving economic performance and maximising their contribution to low-carbon energy supply. Several geothermal doublets in the Netherlands and beyond have reported a decline in injectivity, which is believed to be the result of microbiological activity and chemical scaling (Water Research Institute (KWR), 2015; Croese *et al.*, 2019). Generally, fine migrations (Ochi & Vernoux, 1998), clay swelling (Priisholm *et al.*, 1987), scaling (Tranter *et al.*, 2020) and microbial activity can play a key role in impairing injectivity in sandstone reservoirs. Experimental studies (see Ochi & Vernoux, 1998; Fadili *et al.*, 2022; Chai *et al.*, 2022, among others) have shown that the mobilisation of particles due to either low salinity of the injected water or hydrodynamic effects can reduce the injectivity of sandstone. Priisholm *et al.* (1987) and Krishna Mohan *et al.* (1999), among others, have shown irreversible permeability loss of sandstone samples following the injection of brines due to clay swelling. Field studies and subsequent analyses have demonstrated that occurrence of scaling due to changes in the thermodynamic equilibrium resulting from the injection of cooled water (Tut Haklidir & Özen Balaban, 2019; Markó *et al.*, 2021; Luo *et al.*, 2023).

Flooding experiments on sandstone samples conducted by Yu *et al.* (2018) showed an 80% reduction in permeability due to fine migration, while pore-scale studies by Tang *et al.* (2020) and He *et al.* (2025) reported a 2 to 3 orders of magnitude reduction in permeability. The penetration depth of the clogging can be in different scales, from millimetres to metres. For example, Timmer *et al.* (2003) reported that the clogging material was concentrated as pore-reducing coatings around and between sand grains in the first 100 mm outside the wall of the shallow boreholes used to extract groundwater in South Holland. Experimental works by Messer *et al.* (1978) and Abrams (1977) suggested significant clogging up to 0.6 m from the borehole (due to fines migration), and 1.2 m (due to silica scaling) from the borehole wall in the Veysey Well 1, in Imperial Valley. A similar penetration depth is also reported in Franco *et al.* (2006), in which sonic investigation was conducted to determine the clogged zone extent in a case in the North Sea. Analysis of drill stem test data via dimensionless pressure transient equation suggested an impaired permeability of 48.3 milliDarcy (mD) was likely to have occurred in the near-borehole zone up to a distance of 3.6 m from the borehole wall for a well called Prz-2 (Szpunar & Budak, 2012), where the initial reservoir permeability was 140.6 mD).

There are a number of potential techniques to recover from injectivity decline (see Chapter 2), the effectiveness of which largely depends on the cause of the decline. Thermal

effects on injectivity have been observed (see Chapter 2), and thermal stimulation has been proposed. Yet, limited laboratory and field tests have been carried out (Grant *et al.*, 2013; Luviano *et al.*, 2015). In addition, cyclic stimulation has been suggested and tested in the laboratory and field to achieve stimulation performance with reduced risk of induced seismicity (Hofmann *et al.*, 2019; Jung *et al.*, 2021; Zang *et al.*, 2025), as fatigue effects are believed to play a role. Combining thermal and cyclic stimulation could further improve the stimulation performance while further reducing the required injection pressure. However, studies on cyclic thermal stimulation have rarely been reported. Therefore, in this chapter, the previously developed geo-mechanical tool is used to understand the underlying mechanisms and compare the stimulation performance of different stimulation scenarios of a synthetic reservoir, which is assumed to be partially clogged. The scenario is inspired by the geothermal project installed on the TU Delft campus and nearby geothermal projects. In the following, the synthetic reservoir is first described, after which the modelling method is presented. After introducing the investigated stimulation scenarios, the results are presented and discussed. The main conclusion is then summarised.

5.2. SYNTHETIC RESERVOIR WITH CLOGGED NEAR-BOREHOLE ZONE

The potential of stimulation is analysed on a synthetic case of a sandstone reservoir with clogged near-borehole zone.

The synthetic reservoir is assumed to be a non-fractured sandstone reservoir, inspired by the Delft Sandstone Formation. A borehole with a radius of 0.2 m is located at the centre of a circular domain with a radius of 500 m and a thickness of 100 m. A near-borehole zone with a radius of 5 m is assumed to be clogged, with impaired permeability decreasing to 1% of the initial reservoir permeability k_0. Clogging with a (much) smaller distance from the borehole wall could exist, but in this case, either chemical or mechanical means could probably be used to rehabilitate the well. Therefore, a reasonably extreme case has been selected.

Representative reservoir data is collected from the TU Delft campus geothermal project. Comprehensive data has been collected during the drilling of the doublet (Vardon *et al.*, 2024), including from cores and a large suite of open-hole well logs in the reservoir section of both wells. With regional knowledge, the data from the doublet and surrounding wells, a normal faulting regime can be assumed. Logging data and regional knowledge allows an estimation of the pore pressure to be around 21 MPa and in-situ stresses to be σ_v = 48 MPa, σ_H = 42 MPa and σ_h = 38 MPa, at depth of 2000 m. According to regional studies, the azimuth of the σ_H is between N130°E and N150°E. After drilling, the well DEL-GT-01 has been tested by means of a gas-lift, providing valuable information of the reservoir quality, such as permeability and temperature. In addition, previous oil and gas explorations and other nearby geothermal projects provide a large dataset including hydraulic, thermal and mechanical properties (Aramburo Velez, 2017; Soustelle *et al.*, 2022). The properties used in exploratory analysis are summarised in Tab. 5.1.

Table 5.1: Reservoir data for the explorartory analyses, based on the Delft Sandstone Formation (Aramburo Velez, 2017; Soustelle *et al.*, 2022; Vardon *et al.*, 2024; Voskov *et al.*, 2024)

Parameter	Symbol	Value	Unit
Reservoir thickness	H_r	100	m
Total vertical stress	σ_v	48	MPa
Total maximum horizontal stress	σ_H	42	MPa
Total minimum horizontal stress	σ_h	38	MPa
Initial reservoir pressure	p_{wi}	21	MPa
Initial reservoir temperature	T_i	353	K
Reservoir porosity	ϕ	0.17	-
Solid density	ρ_s	2650	kg/m^3
Reservoir permeability	k_0	1.6×10^{-12}	m^2
Impaired permeability	k_0'	1.6×10^{-14}	m^2
Young's modulus	E	11.5	GPa
Poisson's ratio	ν	0.15	-
Unconfined compressive strength	σ_c	48	MPa
Tensile strength*	σ_t	4.8	MPa
Internal friction coefficient	μ	0.75	-
Volumetric thermal expansion coefficient	β	6.5E-5	1/K
Thermal conductivity	λ	3	W/(m·K)
Specific heat capacity	c_{ps}	2450	kJ/(m^3·K)

*: σ_t is assumed to be 1/10 of σ_c, which is derived from logging data.

5.3. METHOD

5.3.1. NUMERICAL MODEL

Geometry and mesh. To simulate the near-borehole coupled processes under thermo-hydraulic stimulation in the synthetic reservoir, a symmetric plane strain 2D horizontal model with a domain radius of 500 m is constructed, shown in Fig. 5.1a. The domain is composed of 3 material groups with radius from (0.2 m - 5 m), (5 m - 10 m) and (10 m - 500 m) respectively, in order to assign different properties to the clogged zone and unclogged zone, and to insert interface elements only in the near-borehole domain (0.2 m - 10 m). A borehole with radius of 0.2 m is placed at the centre.

The model is meshed with 2nd-order triangular continuum elements, with interface elements inserted in between all the continuum elements within the inner region from 0.2 m - 10 m radius to enable arbitrary fracture initiation and propagation near the borehole (see Fig. 5.1b). This approach ensures reasonable reservoir performance taking into account the far-field behaviour while minimising computational and memory demands by avoiding interface elements throughout the entire domain. As shown in Chapter 4, insertion of interface elements in between continuum elements to provide potential cracking paths in intact rock will introduce artificial compliance that have an impact on thermo-hydro-mechanical response (although this is not an issue when interface elements are used to represent pre-existing discontinuities.). To reduce the mechanical artificial compliance, the stiffness of the interface elements is set as high as possible

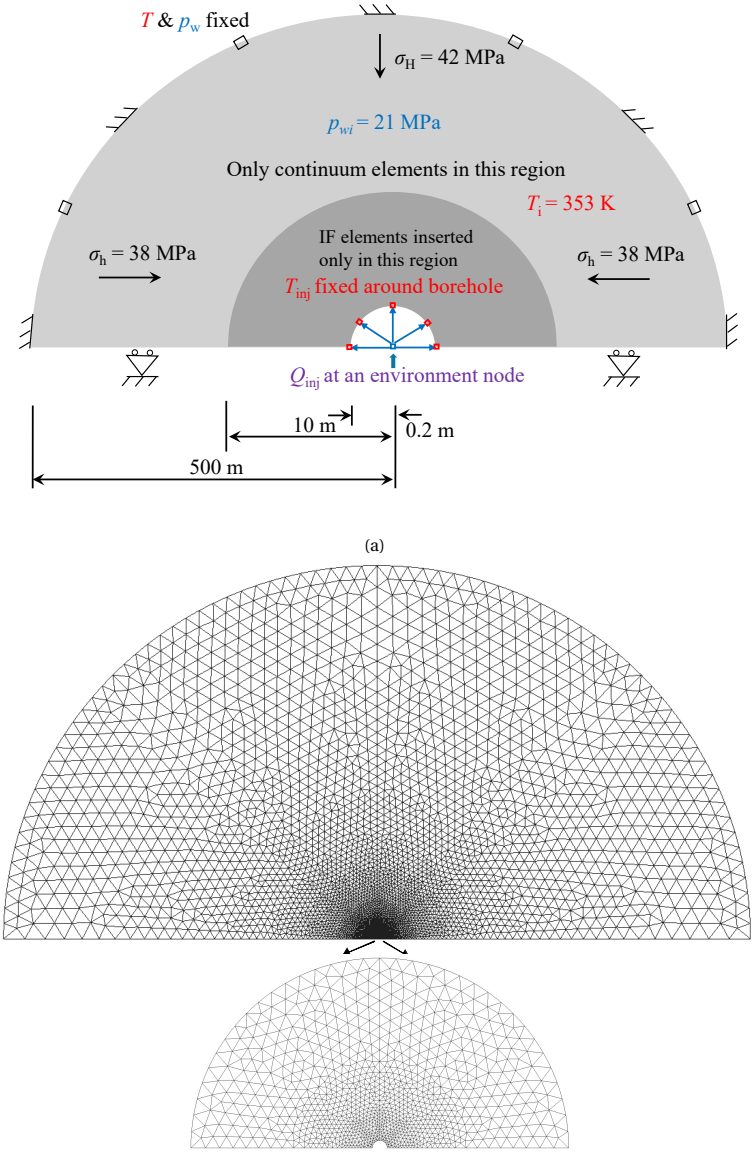


Figure 5.1: Schematic of the (a) Numerical model domain with boundary conditions. Not to scale. An environment node is used to mimic the wellbore, on which the injection rate is applied. The environment node is connected with the borehole nodes without flow resistance. Interface elements are inserted in bewteen all the continuum elements within the inner region from 0.2 m - 10 m radius (the dark gray region). Outside this region, only continuum elements are used; and (b) meshing of the domain.

without causing numerical difficulties, i.e. a lack of convergence, as discussed in Chapter 4. The hydraulic and thermal artificial compliances can be reduced in a similar way, by assigning a high transversal transmissivity of the interface element to reduce the flow resistance. The detail of reducing the hydraulic and thermal artificial compliances is presented in Appendix B.

Initial and boundary conditions. In the numerical model, the initial stresses are σ_H = 42 MPa in y direction while σ_h = 38 MPa in x direction. The displacement at the line of symmetry boundary (bottom as shown in Fig. 5.1a) is fixed in y direction due to symmetry, while at the far-field boundary the displacement is fixed in both x and y directions. A uniform normal load, which is equal to the steady-state injection pressure, is distributed around the borehole throughout the simulation time, leading to a zero effective stress around the borehole. In addition to the mechanical boundary conditions, temperature and fluid pressure are fixed at initial values at the far-field boundary. A constant injection rate q_{2D} (kg/(m·s)), leading to a total injection rate Q_{inj} (m^3/h, = 2 × ×3600 × H_r × ρ_w × q_{2D}) for the open-hole section with thickness of H_r, is applied on an environment node, which is connected to the borehole nodes without resistance to mimic the wellbore. The temperature at the borehole wall is fixed at the injection temperature T_{inj}.

Constitutive models and parameters. The elastic model is used for the continuum elements, while the previously developed elasto-damage law (see Fig. 5.2) that incorporates the fatigue damage into the tensile branch is used for the interface elements. In the loading condition, the normal and tangential (to the mid-plane of the interface element) stresses are given by the following expressions:

$$\sigma'_n = \begin{cases} (1-D)K_{nm}r_n & \text{if } r_n \geq 0 \\ K_{n0}r_n & \text{if } r_n \leq 0 \end{cases} \tag{5.1}$$

$$\sigma_l = (1-D)K_{l0}r_l \tag{5.2}$$

where σ'_n [Pa] represents Terzaghi's effective normal stress, defined as $\sigma'_n = \sigma_n + p_w^m$, and $K_{n0} = \sigma_{n0}/r_{n0}$ [Pa/m] is the initial normal stiffness while $K_{nm} = \sigma_{nm}/r_{n0}$ is the normal stiffness after mth cycles and $\sigma_{nm} = (1-D_f)\sigma_{n0}$. σ_l and r_l are the tangential stress and separation respectively, and $K_{l0} = \sigma_{l0}/r_{l0}$ is the tangential stiffness. Note that in the context of this paper, the slopes K_{n0} is interpreted as penalty coefficients, thus allowing negligible interpenetration of fracture surfaces regardless of their roughness (Cerfontaine *et al.*, 2015). To enforce the contact constraints, the slope should be set high enough to reduce artificial compliance (Liaudat *et al.*, 2023). However, the choice of their values is a trade-off between having artificial compliance and having numerical convergence problems.

Additionally, D is the damage variable ranging from 0 (intact rock) to 1 (fully separated fracture). This damage variable evolves as follows:

$$D = \min\left(\frac{\bar{\omega}}{1+\bar{\omega}}\frac{1}{\eta}, 1\right) \tag{5.3}$$

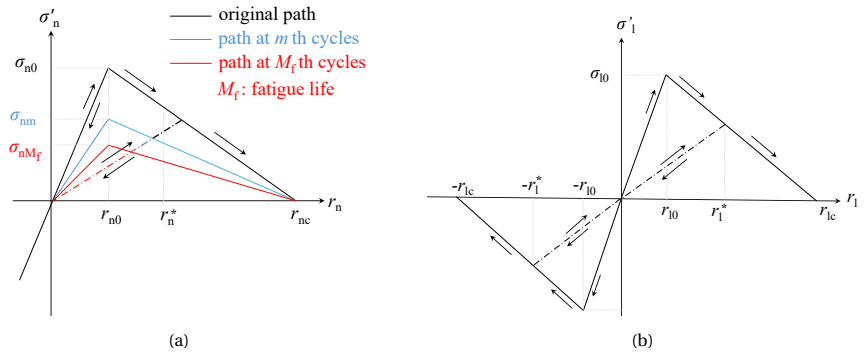


Figure 5.2: The elasto-damage law. (a) Tensile branch incorporating the fatigue damage; (b) Shear branch

$$\bar{\omega} = \max(\omega) \tag{5.4}$$

$$\omega = \langle (\frac{\langle r_n \rangle}{r_{n0}})^{\beta} + (\frac{|r_l|}{r_{l0}})^{1/\beta} - 1 \rangle \tag{5.5}$$

$$\eta = 1 - \frac{r_{n0}}{r_{nc}} = 1 - \frac{r_{l0}}{r_{lc}} \tag{5.6}$$

where ω is a positive scalar that defines the mechanical degradation of the interface element for a given normal separations, $\bar{\omega}$ is a history variable that stores the maximum value reached by ω during the loading history, and $\langle \cdot \rangle = (\cdot + |\cdot|)/2$ is the Macaulay bracket (Liaudat *et al.*, 2023). β is a material parameter that characterise the mixed mode damage and is assumed to be 1 in this work (Liaudat *et al.*, 2023). The above equations state that if the separation r_n (or r_l) is less than the normal crack separation r_{n0} (or r_{l0}), the damage variable D is then zero. If $r_{n0} < r_n < r_{nc}$ (or $r_{l0} < r_l < r_{lc}$), D is between 0 and 1, determined by the ratio of $(r_n - r_{n0})/(r_{nc} - r_{n0})$ and $(r_l - r_{l0})/(r_{lc} - r_{l0})$. Otherwise if r_n (or r_l) is beyond the debonding separation r_{nc} (or r_{lc}), D is forced to be 1, indicating a completely separation of the interface element.

The fatigue damage is defined as:

$$D_f = \sum_i \left(1 - \frac{\sigma_{Ai}}{\sigma_{n0}}\right) \frac{1}{M_{fi}} \tag{5.7}$$

where i indicates the ith cyclic loading that has a maximum amplitude of σ_{Ai}. M_{fi} is the fatigue life corresponding to the applied loading level σ_{Ai}.

An empirical S-N relationship is used as a criterion to determine the fatigue life M_{fi}, which relates the maximum value of the cyclic loading (σ_{Ai}) to the fatigue life M_{fi} of the rock. It reads (Cerfontaine & Collin, 2018; Xi *et al.*, 2021):

$$\frac{\sigma_{Ai}}{\sigma_{n0}} = a \log_{10} M_{fi} + b \tag{5.8}$$

where a and b are model parameters that can be determined from experimental data.

The parameters assigned to the continuum elements are presented in Tab. 5.1, while the parameters for the interface elements are summarised below in the Tab. 5.2. Note that the initial longitudinal transmissivity of the interface element is determined as equivalence to the impaired permeability of the continuum element via Equation 3.32 in Chapter 3, while the transversal transmissivity is set to a high value to reduce artificial compliance, as discussed in Appendix B.

The parameters a and b that describe the S-N relationship are determined by fitting the experimental data collected from literature. All the strength used was measured using sandstone rock samples. The fitting curve is shown in Fig. 5.3.

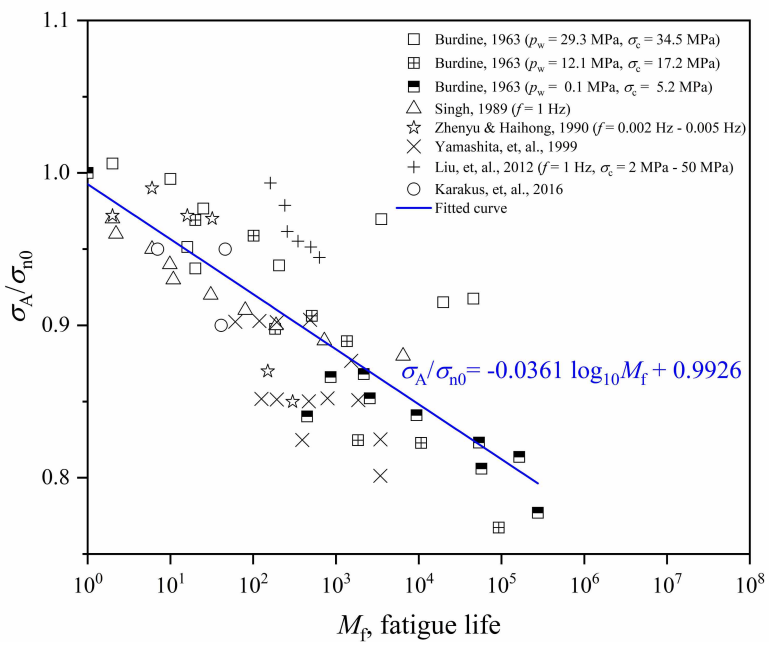


Figure 5.3: S-N relationship determined by fitting the experimental data collected from the literature.

q

Table 5.2: Input parameters for the interface elements used in the model

Parameter	Symbol	Value	Unit
Tensile strength	σ_{n0}	4.8	MPa
Tensile cracking separation	r_{n0}	1E-7	m
Tensile debonding separation	r_{nc}	1E-6	m
Shear strength	σ_{l0}	32	MPa
Shear cracking separation	r_{l0}	1E-7	m
Shear debonding separation	r_{lc}	1E-6	m
Mechanical viscosity	ζ	1E14	Pa·s/m
Parameter a	a	-0.0361	-
Parameter b	b	0.9926	-
Initial aperture	w_0	1E-5	m
Initial longitudinal transmissivity (non-clogged)	t_0^l	1.6E-17	m^3
Initial longitudinal transmissivity (clogged)	t_0^l	1.6E-19	m^3
Initial transversal transmissivity (in both cases)	$t_0^{b/t}$	1E-10	m^2
Stabilisation coefficient*	$\delta \cdot h$	10	m

*: δ is a tuning parameter and h is the element length (see details in Appendix B), which are used in both longitudinal and transversal heat transfer in the interface elements to stabilise the numerical solution.

5.3.2. INVESTIGATED SCENARIOS

The model including interface elements (with stabilisation and interface element parameters selected for accuracy) will be used to study various synthetic injection and stimulation scenarios with fully coupled THM processes and fatigue damage considered, allowing fracture initiation and propagation. The normal scenario, i.e. cold water injection into the reservoir without any clogging, is presented and discussed in Appendix C. In this chapter, the focus is on the different stimulation scenarios, including monotonic, stepwise, cyclic stimulation and combined stepwise and cyclic stimulation, based on the reservoir with clogged near-borehole zone (assuming a clogged radius of 5 m where the permeability is reduced to 0.01 k_0) to evaluate the stimulation performance of different stimulation strategies. Considering the large computational burden and the soft stimulation practice performed in Pohang geothermal field (Hofmann *et al.*, 2019), the total operation period is restricted in 5 days. Tab. 5.3 summarises the investigated scenarios, which are further detailed below.

The simulation of different stimulation scenarios for a synthetic reservoir with clogged near-borehole zone are then carried out. First, monotonic (increased to the designed flow rate in 1 s and then kept constant) injection of cold water with different injection rates, labelled as $M1$ (Q_{inj} = 360 m^3/h), $M2$ (Q_{inj} = 288 m^3/h), $M3$ (Q_{inj} = 216 m^3/h) and $M4$ (Q_{inj} = 54 m^3/h), are first simulated. Based on scenario $M1$, the simulations of coupled hydro-mechanical (H-M), thermo-hydraulic (T-H) and fully coupled THM processes are compared to highlight the influence of the temperature and the initiation and propagation of fractures. In addition, the effects of different injection temperatures (ΔT = 35 K, 40 K, 45 K) are further discussed, with simulations based on $M2$.

Secondly, two stepwise stimulations, as is shown in Fig. 5.4a (labelled as $S1$) and Fig.

Table 5.3: Synthetic injection scenarios. The total injection time is 120 h. In each cycle of the scenario $C1$, the ΔT is kept at 40 K for Δt, which can be 5 hours or 10 hours, and then kept at 0 K for another 0.9 Δt. In each cycle of scenario $C2$ and $C3$, the Q_{inj} is kept at $Q_{\text{inj}}^{\max}$ for $\Delta t^{'}$, which can be 6 min or 12 min, and then kept at $Q_{\text{inj}}^{\min}$ for another $0.5\Delta t^{'}$.

Inj. scheme	Label	Inj. rate, Q_{inj} (m^3/h)	$\Delta T(K) = T_{\text{inj}} - T_{\text{i}}$
Clogged reservoir ($k = 0.01k_0$ within $r_{\text{c}} = 5$ m)			
Monotonic	$M1$	360	0/40
	$M2$	288	35/40/ 45
	$M3$	216	40
	$M4$	54	40
Stepwise	$S1$	216 → 216 (each 60 h)	40
	$S2$	108 → 216 → 216 (each 40 h)	40
Cyclic T_{inj}	$C1$	216	40 (Δt) ↔ 0 ($0.9\Delta t$)
Cyclic Q_{inj}	$C2$	5.4 ($0.5\Delta t^{'}$) ↔ 54 ($\Delta t^{'}$)	40
	$C3$	28.8 ($0.5\Delta t^{'}$) ↔ 216 ($\Delta t^{'}$)	40
Cyclic + stepwise	$CS1$	(5.4 ↔ 54) → (54 ↔ 216)	40
	$CS2$	(5.4 ↔ 54) → (54 ↔ 108) → (108 ↔ 216)	40

5.4b (labelled as $S2$), are investigated with ΔT fixed at 40 K.

Thirdly, different cyclic stimulations, as is shown in Fig. 5.4c (labelled as $C1$) and Fig. 5.4d (labelled as $C2$ or $C3$), are investigated. Scenario $C1$ represents the injection temperature is cycled with fixed injection rate, while scenarios $C2$ and $C3$ represent the injection rate is cycled with fixed injection temperature. For scenario $C1$, the ΔT is cycled between 0 K and 40 K, with injection rate fixed at 216 m^3/h. In one complete cycle, the ΔT is first kept at 40 K for a period of Δt, which can be 5 hours or 10 hours, and then changed to 0 K for $0.9\Delta t$, which is chosen to avoid numerical divergence (happens if keeping $\Delta T = 0$ K for Δt) while keeping enough time for the reservoir to warm up. In contrast, for scenarios $C2$ and $C3$, the maximum injection rate is either 54 m^3/h or 216 m^3/h respectively, while the minimum injection rate is $Q_{\text{inj}}^{\max}/10$ instead of shut in (for numerical convergence and practical reasons, e.g. to avoid the largest seismic events which have been observed during shut-in (Baisch *et al.*, 2010; Park *et al.*, 2017; Hofmann *et al.*, 2019)), with the ΔT fixed at 40 K. In one complete cycle, the injection rate is first kept at its maximum $Q_{\text{inj}}^{\max}$ (= 216 m^3/h or 54 m^3/h) for a period of $\Delta t^{'}$, which can be 6 min or 12 min, and then the injection rate decreases to $Q_{\text{inj}}^{\min}$ (= $Q_{\text{inj}}^{\max}/10$), which is kept for $\Delta t^{'}/2$. Note that the Δt is much larger than $\Delta t^{'}$ since the heat transfer is much slower than hydraulic process.

Fourthly, a combination of cyclic and stepwise stimulation strategy is investigated, as is shown in Fig. 5.4e (labelled as $CS1$) and Fig. 5.4f (labelled as $CS2$). Scenario $CS1$ is a combination of cyclic injection rate and the stepwise scenario $S1$, while scenarios $CS2$ is a combination of cyclic injection rate and the stepwise scenario $S2$. The injection temperature is fixed in both scenarios.

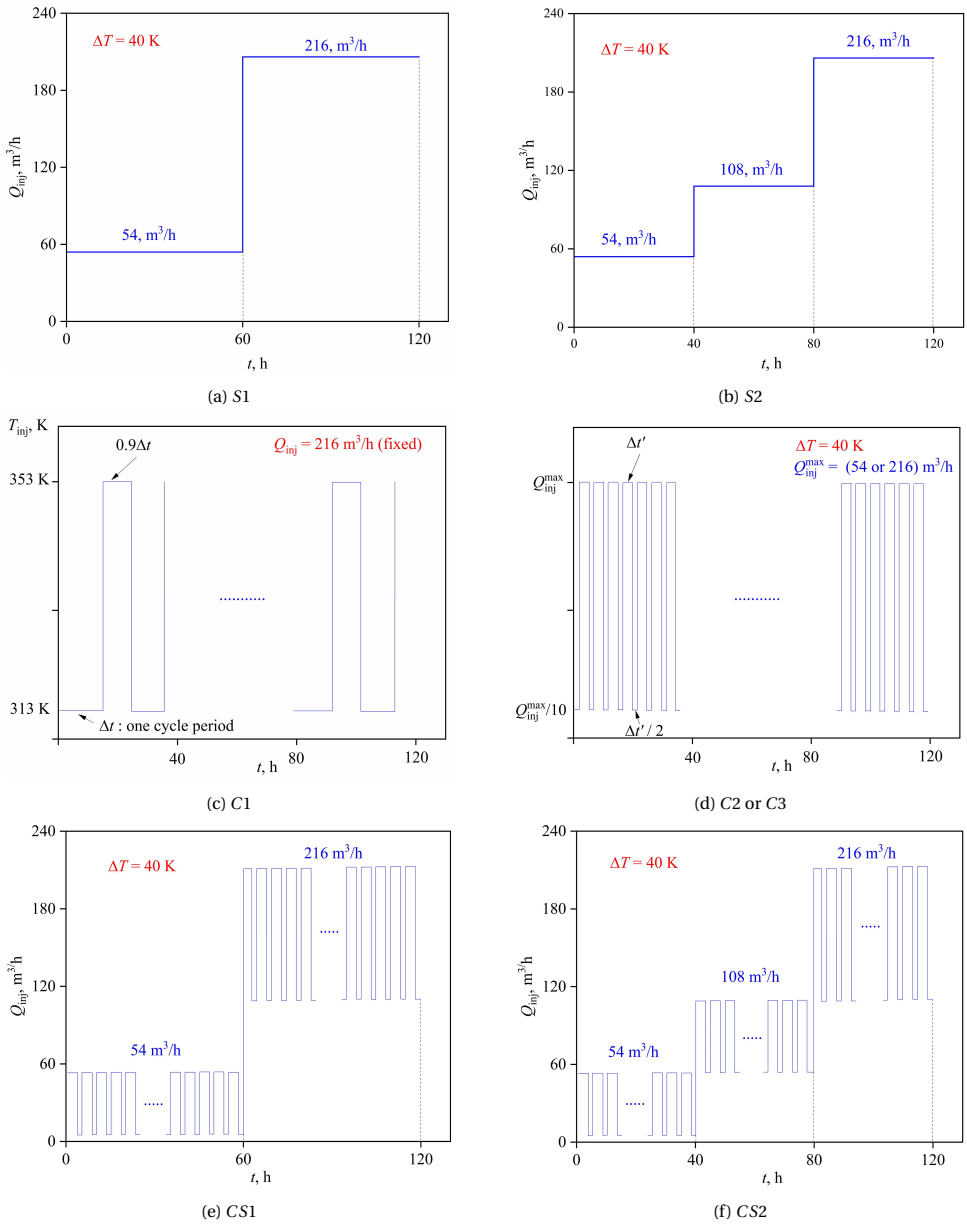


Figure 5.4: Visualisation of the investigated scenarios. (a) - (b): Stepwise stimulation scenarios. Injection temperature is fixed at 313 K. (c): The cyclic injection temperature scenario $C1$, where Δt is the cycle period, which is either 5 hours or 10 hours. (d): The cyclic injection rate scenario $C2$ or $C3$, where $\Delta t^{'}$ is the cycle period, which is 6 min or 12 min. Maximum injection rate is 54 m^3/h or 216 m^3/h, while the minimum injection rate is $Q_{inj}^{max}/10$, with injection temperature fixed at 313 K. (e) - (f): Combined cyclic and stepwise stimulation scenarios $CS1$ and $CS2$.

5.4. RESULTS AND DISCUSSION

5.4.1. MONOTONIC STIMULATION (*M*1 - *M*3)

This section considers the response of the reservoir with near-borehole clogging to monotonic injection with different rates and temperatures. To compare results, an average damage variable ($\bar{D}$) is defined as the average value of damage variables over the interface elements along a line through the 5 m radius clogged zone in the direction of the maximum initial stress σ_H, i.e. the location where the main fracture is expected to be induced and propagate. $\bar{D}$ can be used to indicate the length of the main fracture and therefore indicate if the main fracture breaks through the clogged zone. An average damage variable ($\bar{D}$) of 1 along this line indicates the main fracture breaks through the 5 m clogged area, thus connecting the wellbore and the un-clogged zone.

Fig. 5.5 compares the pressure response under fixed Q_{inj} = 360 m^3/h with consideration of coupled THM (with ΔT = 40 K), T-H (with ΔT = 40 K) and H-M (with ΔT = 0 K) processes in the simulations. Results show that the injection pressure reaches a constant value at 32.5 MPa quickly for the case of H-M simulation, indicating that steady state is reached quickly due to the fast pressure diffusion. In contrast, for the case of T-H simulation, the injection pressure keeps increasing to 39.5 MPa, at which the pressure remains approximately constant, as a result of the propagation of the cooling front, which increases the viscosity therefore flow resistance. If the fully coupled THM processes are considered, the injection pressure increases to 34.1 MPa, and then sharply and continuously decreases as a result of the initiation and propagation of near-borehole fractures. At approximately t = 65 h, there is a sudden and significant drop in the pressure, indicating that fracture(s) breaks through the clogged zone, and connects the wellbore and the un-clogged zone. The comparison highlights the importance of the consideration of the fully coupled THM processes and the initiation and propagation of fractures.

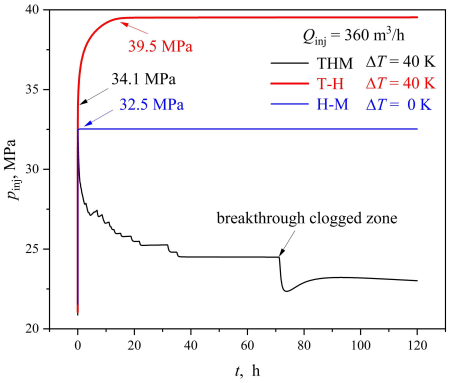
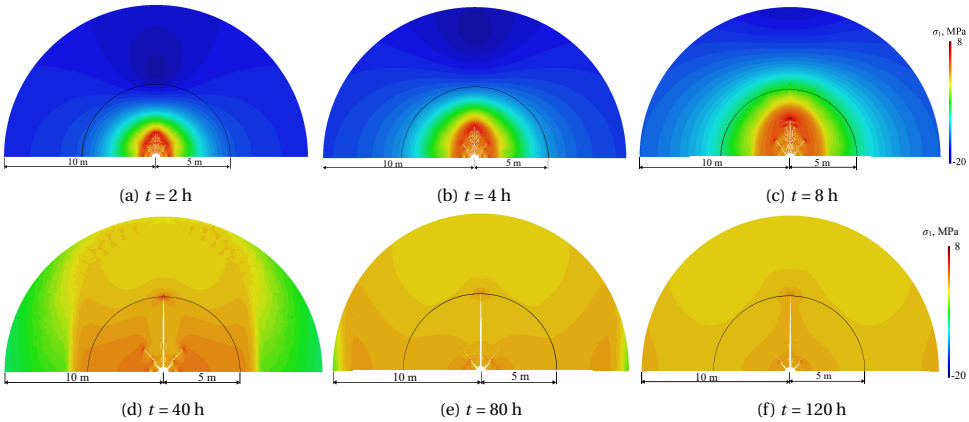


Figure 5.5: Comparison of injection response under coupled THM, T-H, H-M simulations with Q_{inj} fixed at 360 m^3/h (*M*1 scenario).

As shown in Fig. 5.6, in the *M*1 scenario (the fully coupled THM case), there is a main fracture propagating in the direction of the major principal stress and two symmetric fracture branches induced which are oriented around 45° and -45 ° (0° is defined to be in

the North). To explain this phenomenon, Fig. 5.6 presents the fractures evolution with the distribution of the major principal stress σ_1 in the near-borehole zone, taking the case of Q_{inj} = 360 m^3/h and ΔT = 40 K as an example. In the first few hours, as is shown in Fig. 5.6a - 5.6c, small fractures are induced around the borehole due to the thermal stress and hydraulic pressure. Although pore pressure and temperature changes act as isotropic scalar loads, the initial stresses and applied stresses lead to the strongest tensile stress to be in the direction of σ_{H} (i.e. y direction). Therefore, the main fracture opens first, pushing the side fractures to close. On the other hand, the stress concentration at the borehole wall due to both cold fluid injection causes further tensile stresses which remain lowest in the direction of σ_{h} and highest at the tip of the already opened fracture. In addition, the mesh also plays a role. The edges of the elements are radially intersecting the borehole in the direction of 45°, 90° and 135°, as shown in Fig. 5.1b, in which the mesh is presented. In contrast, in other directions, the edges of the elements intersect with the borehole with an angle deviated from the radial direction. Therefore, the normal stress applied on these interface elements (edges) is lower than the first principal stress, and are unable to open the interface elements. Consequently, fracture branches find its easiest way to propagate in the direction of 45° and 135 °, while fracture branches in other directions are closed.



(a) t = 2 h (b) t = 4 h (c) t = 8 h

(d) t = 40 h (e) t = 80 h (f) t = 120 h

Figure 5.6: Distribution of the first principal stress σ_1 at different time steps with deformed mesh under Q_{inj} = 360 m^3/h and ΔT = 40 K ($M1$ scenario). The legend range is -20 MPa (compressive) to 10 MPa (tensile). The deformation is 50 times enlarged, and only the domain within a radius of 10 m is shown.

Fig. 5.7a compares the injection pressure and evolution of the averaged damage variable $\bar{D}$ for scenarios $M1$ to $M4$ with fully coupled THM processes under different injection rate Q_{inj} at fixed ΔT = 40 K. As is shown in Fig. 5.7a, all simulations show substantial damage, with $\bar{D}$ reaching values well above 0.8 when the injection rate is 216m^3/h, 288 m^3/h, and 360 m^3/h. The sudden drop in injection pressure at approximately t = 118h and t = 70h is observed for the cases of Q_{inj} is 288 m^3/h and 360 m^3/h respectively, with the corresponding $\bar{D}$ at 1, indicates a fracture fully penetrating the clogged area. If the injection rate is largely reduced to 54 m^3/h, the length of the fracture(s) is limited, although damage is seen to continuously occur.

In addition, the pressure around the tip of the main fracture is relaxed in the clogged area as a result of breaking through the damage area, as is shown in Fig. 5.8c, while for the case of $Q_{\text{inj}} = 360$ m^3/h, the injection pressure is recovering as the cold front moves further, though the main fracture breakthroughs the clogged area. For the other two cases ($Q = 54$ m^3/h and 216 m^3/h), no pressure relaxation happens since fracture is shorter and does not breakthrough the clogged area. A high peak of injection pressure at 28.9 MPa - 34.1 MPa is observed when Q_{inj} is equal to or higher than 216 m^3/h, which is significantly higher than the injection pressure (21.5 MPa) for the unclogged reservoir, and could potentially increase the risk of induced seismicity and equipment failure.

Fig. 5.7b compares stimulation performance with different injection temperatures with the same injection rate ($M2$ scenario). The results show no significant difference in peak pressure, all at around 31.5 MPa, while a larger temperature difference of $\Delta T =$ 45 K and 40 K can result in earlier breakthrough of the clogged zone and lower injection pressure after reaching the peak pressure. This is because, as shown in Fig. 5.9c, the large thermal stress leads to a more damage around the borehole, even complete separation of some continuum elements, which results in the early stop of simulations due to lack of convergence (for the case of $\Delta T = 45$ K), as shown in Fig. 5.7b. In contrast, $\Delta T = 35$ K does not results in a breakthrough of the clogged zone, with the injection pressure reducing by the least, reducing only to 26 MPa at $t = 120$ h, with pressure accumulation around the main fracture, shown in Fig. 5.9a.

Comparing Fig. 5.7a and 5.7b, it demonstrates that both increasing the injection rate Q_{inj} and the temperature difference ΔT can improve the stimulation performance. Yet, increasing the injection rate comes with increasing peak pressure, which could lead to higher risk of inducing seismicity. In contrast, increasing the temperature difference seems to be a more safe and efficient method to improve the simulation performance, with the same peak pressure but significantly more damage and lower injection pressure. However, increasing the temperature difference should be always implemented with care to meet environment regulations and avoid temperature-sensitive clogging processes.

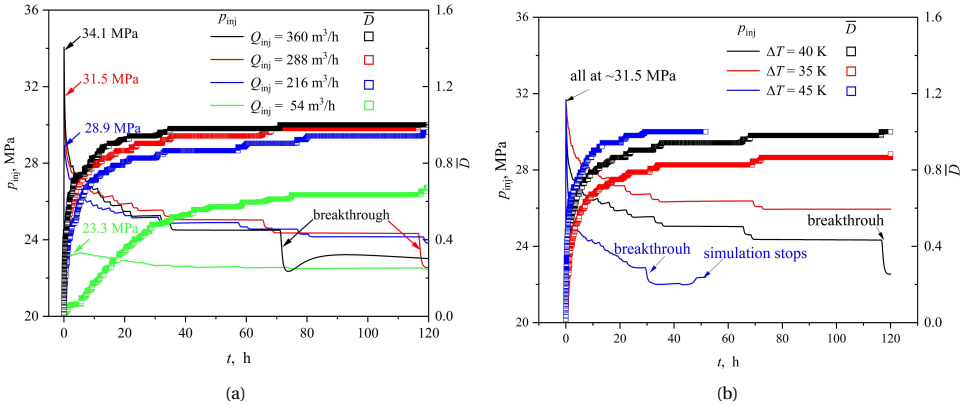


Figure 5.7: Injection pressure and averaged damage variable evolution under (a) $M1$ to $M4$ scenarios, different injection rate with fixed ΔT = 40 K; and (b) $M2$ scenario different ΔT with fixed Q_{inj} = 288 m^3/h. The damage variable is averaged over the interface elements along a line through the 5 m clogged area from the borehole to the outer radius in the direction of the maximum initial stress σ_H.

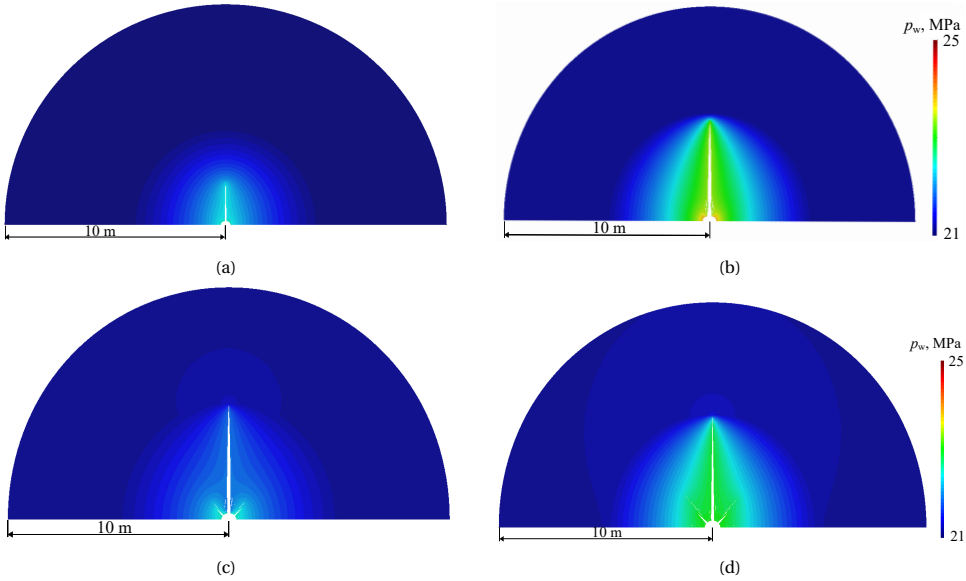


Figure 5.8: Pressure distribution at t = 120 h with deformed mesh under different injection rate (ΔT is fixed at 40 K) - $M1$ to $M4$ scenarios. (a) Q_{inj} = 54 m^3/h; (b) Q_{inj} = 216 m^3/h; (c) Q_{inj} = 288 m^3/h; (d) Q_{inj} = 360 m^3/h. The deformation is 50 times enlarged, and only the domain within a radius of 10 m is shown.

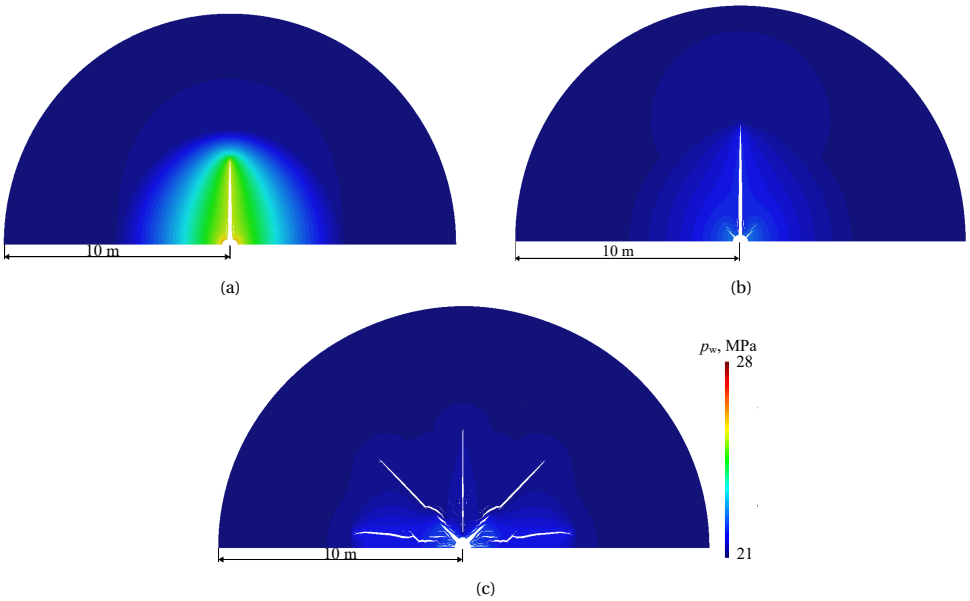


Figure 5.9: Pressure distribution at t = 120 h with deformed mesh under different temperature difference (Q_{inj} is fixed at 288 m^3/h) - $M2$ scenario. (a) ΔT = 35 K; (b) ΔT = 40 K; (c) ΔT = 45 K. The deformation is 50 times enlarged, and only the domain within a radius of 10 m is shown.

5.4.2. STEPWISE STIMULATION ($S1$ - $S2$)

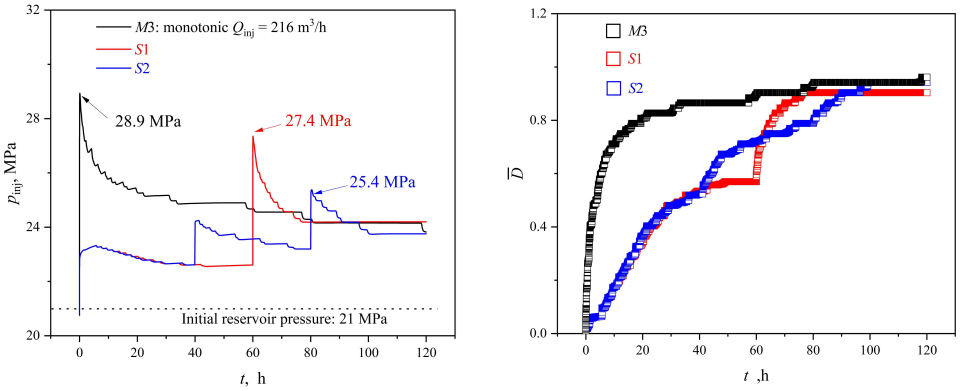
In this section, the stepwise and cyclic stimulation strategies are evaluated, assuming the maximum injection rate Q_{inj}^{max} is 216 m^3/h and the maximum temperature difference ΔT^{max} is 40 K.

Fig. 5.10 compares the injection pressure (p_{inj}) and averaged damage variable ($\bar{D}$) under monotonic stimulation scenario $M2$ and stepwise stimulation scenario $S1$ and $S2$. It is shown that with stepwise stimulation, compared with monotonic stimulation, a lower maximum injection pressure is achieved with more gradual damage. The three-step scheme ($S2$) leads to better stimulation performance (i.e. a lower maximum injection pressure) than the two-step scheme ($S1$). The highest pressure under monotonic stimulation, shown in Fig. 5.10a, is about 28.9 MPa, while that under stepwise stimulation $S1$ is about 27.4 MPa and that under $S2$ is 25.4 MPa, shown in Fig. 5.10a. The decreasing maximum injection pressure is because damage is accumulated in the previous steps, in which the injection rate is low.

In the stepwise simulations, the main fracture is shown to be shorter than that under monotonic stimulation, though the main fracture grows to a slightly smaller length in the end of the stimulation (see Fig. 5.10b). At the final time step, the main fracture under scenario $S2$ is longer than that under scenario $S1$, leading to a lower pressure at the borehole and around the main fracture, as shown in Fig. 5.11. In all scenarios, no high-way connection is made between the borehole and the un-clogged zone, thus relatively high pressure remains around the main fracture - which could be addressed by

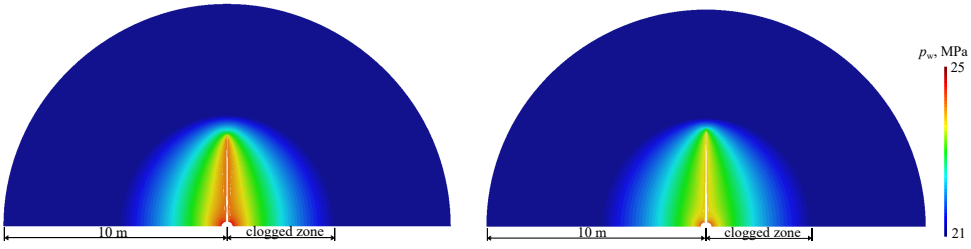
further increasing the injection rate. In addition, the reservoir has few fractures outside the main fracture, so it is unlikely to have subsequent problems such as sand production.

It can be concluded that the stepwise stimulation strategy has better stimulation performance than monotonic stimulation, as it reduces the required peak injection pressure (substantially), reduces long-term injection pressures (slightly) and slightly decreases overall reservoir damage.



(a) (b)

Figure 5.10: Comparison of the (a) injection pressure (p_{inj}); and (b) averaged damage variable ($\bar{D}$) evolution under monotonic stimulation scenario $M2$ and stepwise stimulation scenarios $S1$ and $S2$. The temperature difference ΔT is fixed at 40 K.



(a) Scenario $S1$ (b) Scenario $S2$

Figure 5.11: Pressure distribution with deformed mesh at t = 120 h (deformation enlarged 100 times), and only the domain within a radius of 10 m is shown.

5.4.3. CYCLIC STIMULATION ($C1$ - $C3$)

SCENARIO $C1$: CYCLIC INJECTION TEMPERATURE

Fig. 5.12a compares the injection pressure response under monotonic and cyclic-temperature injection. It can be seen that the highest injection pressure during cyclic-temperature injection is slightly higher than that under monotonic stimulation. In addition, the main fracture does not breakthrough the clogged zone in either scenario, as is indicated in Fig. 5.12b. In Fig. 5.13, the main fracture and the fracture branching are

longer and larger under monotonic stimulation (the results of pressure are shown in Fig. 5.8b, which highlight the fracture extend better) than those under cyclic-temperature stimulation, though there are more secondary fractures induced during cyclic-temperature stimulation. However, the resulting long-term injection pressure is similar in all cases. The extent of the secondary fractures are seen to be controlled by the time period of the injection of cold water, as is shown in Fig. 5.13.

It is therefore concluded that cyclic-temperature stimulation (within the bounds of the scenarios considered here) is generally neither better or worse than monotonic stimulation, but has slightly different characteristics. Monotonic injection creates a larger single fracture which breaks through the clogged zone, whereas thermal cycles create more local damage controlled by the period of the cyclic injection.

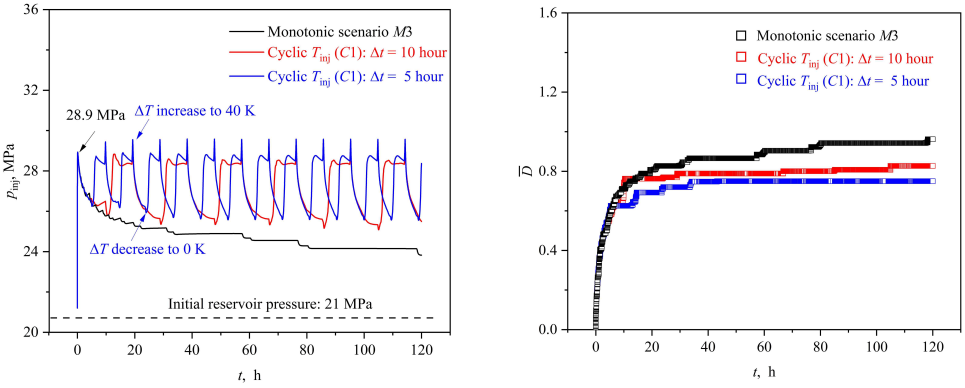


Figure 5.12: (a) Injection pressure evolution; and (b) corresponding averaged damage variable evolution under monotonic and cyclic-temperature stimulation with $Q_{\text{inj}} = 216$ m^3/h - scenario $C1$. Cyclic period is 5 hours and 10 hours.

SCENARIO $C2$ & $C3$: CYCLIC INJECTION RATE

In Scenario $C2$, cyclic stimulation with a lower maximum injection rate (54 m^3/h) is investigated. Fig. 5.14a compares the pressure response and averaged damage variable under monotonic stimulation $M4$ and 12 min cyclic stimulation with and without the fatigue damage. It shows that the peak pressure under monotonic stimulation is slightly higher than cyclic stimulation. This is because the cyclic injection scheme slows down the pressure build up and at the same time, near-borehole damage is accumulated, resulting lower peak pressure. In the 5-day stimulation, the monotonic scheme shows the best stimulation performance, with a lower maximum injection pressure and longer main fracture (indicated by the averaged damage variable) after the first 20 hours. In addition, a comparison of the injection pressure under cyclic stimulation with and without fatigue damage included, demonstrates that fatigue damage makes a minor difference, only causing slightly earlier fracture growth, as can be seen in the enlarged part in Fig. 5.14a. Even if the cyclic frequency is increased, as is shown in Fig. 5.14b, the fatigue effect makes little difference. The reason is likely that the growing fractures make the pressure difficult

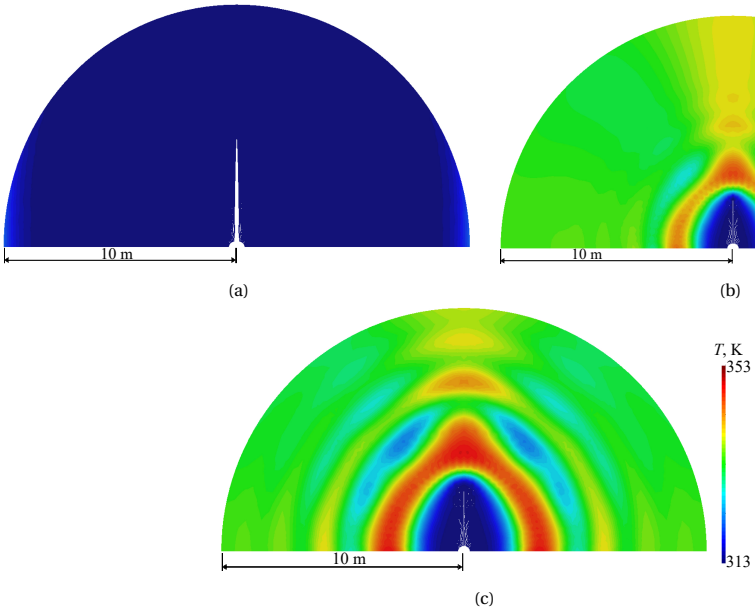


Figure 5.13: Temperature distribution at t = 120 h with deformed mesh under (a) monotonic ($Q_{\text{inj}}^{\text{max}}$ = 216 m^3/h), (b) 5-hour and (c) 10-hour cyclic-temperature stimulation (ΔT = 40 K $\leftrightarrow$ 0 K) - scenario $C1$. The deformation is 100 times enlarged.

to maintain at a level that can induce fatigue damage within a reasonable number of cycles. This can be seen in Fig. 5.15a and 5.15c, in which the first principal stress σ_1 at the fracture tip is shown to be around 3 MPa at t = 120 h, smaller than the tensile strength (4.8 MPa) due to stress relaxation after fracture growth, indicated by the increased averaged damage variable at t = 120 h shown in Fig. 5.14a. The continuous increase in the averaged damage variable demonstrates the continuous fracture growth, therefore continuous stress relaxation. In contrast, during the period when the averaged damage variable keeps the constant (i.e. no fracture growth), the fatigue effect still does not make significant difference. This is because the stress applied on the interface element at the fracture tip is too small to induce effective fatigue damage within the cycles before fracture growing. This can be seen for the case of cyclic stimulation without damage variable, shown in Fig. 5.15b, the σ_1 at the fracture tip is around 4 MPa, leading to the ratio $\sigma_{\text{A}}/\sigma_{\text{n0}}$ (i.e. 4/4.8) equal to 83%, which leads to a fatigue life of around 30 000 cycles (see Fig. 5.3). Consequently, significant fatigue damage cannot be achieved with the current cyclic scheme. In addition, since the matrix, even though is assumed to be partly clogged, is still relatively permeable. Pressure in the main fracture diffuses towards the surrounding matrix, thus not easy to build up in the interface elements at the fracture tip.

In scenario $C3$, cyclic stimulation with higher maximum injection rate (216 m^3/h) is investigated. Fig. 5.16 compares the pressure response and averaged damage variable under monotonic stimulation $M3$ and cyclic stimulation $C3$ with and without fatigue damage variable included. It shows the injection pressure under cyclic stimulation

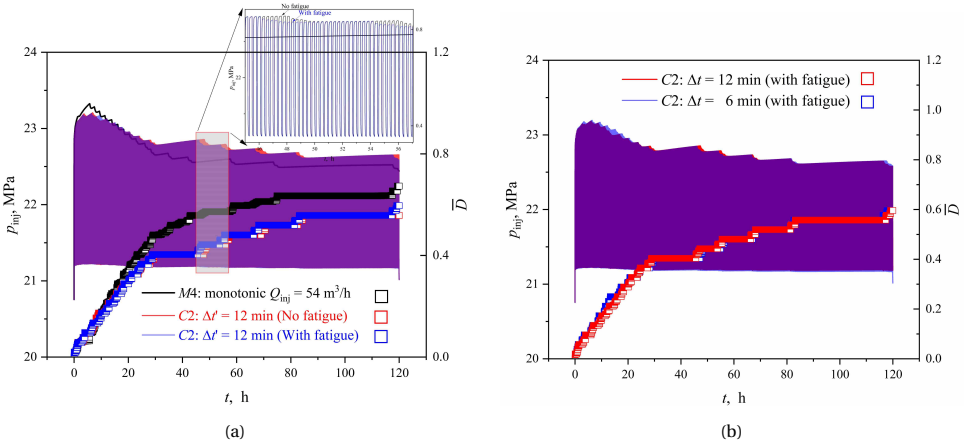


Figure 5.14: Injection pressure response and averaged damage variable evolution for scenario *C*2 (a) under 12-min cyclic stimulation (Q_{inj} = 54 m^3/h) with and without fatigue damage variable included in the traction-separation law; and (b) under 12-min and 6-min cyclic stimulation with fatigue damage included.

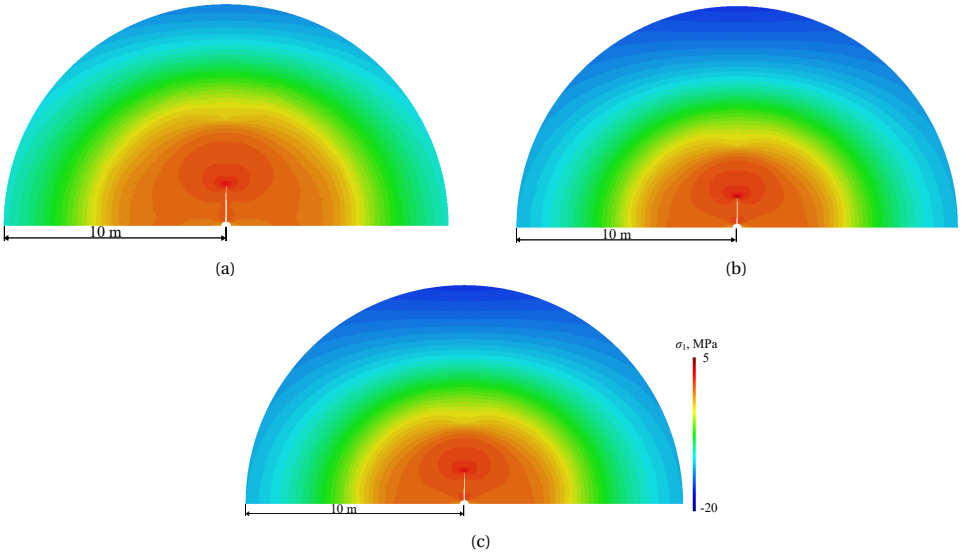


Figure 5.15: Horizontal stress (σ_x) distribution at t = 120 h with deformed mesh under (a) monotonic stimulation (scenario *M*4); (b) cyclic stimulation without fatigue damage (scenario *C*2); (c) cyclic stimulation with fatigue damage (scenario *C*2). The deformation is 100 times enlarged, and only the domain within a radius of 10 m is shown.

is always slightly higher than the monotonic stimulation, except for the initial stage where the cyclic stimulation outperforms the monotonic stimulation, as also observed in scenario *C*2. This is because the higher injection rate leads to quick fracture growth, while cyclic reduction in injection rate slows down the fracture growth. In addition, the underlying mechanism why the fatigue dmage does not make a difference is the same with that explained earlier, therefore not repeated here.

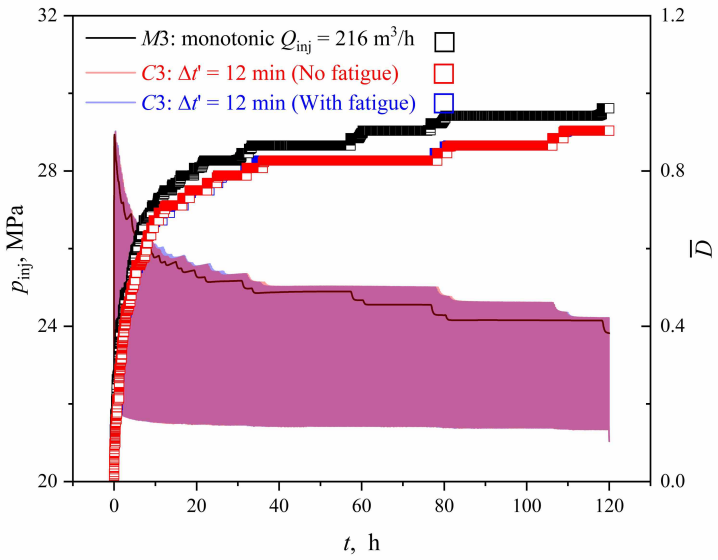


Figure 5.16: Injection pressure response and averaged damage variable evolution under 12-min cyclic stimulation (Q_{inj} = 216 m^3/h) with and without fatigue damage variable included in the traction-separation law - scenario *C*3.

5.4.4. COMBINED CYCLIC AND STEPWISE STIMULATION (*CS*1 - *CS*2)

In scenarios *CS*1 and *CS*2, the combined cyclic and stepwise stimulation strategy is investigated. Fig. 5.17a compares the pressure response under monotonic stimulation and stimulation scenarios *CS*1 and *CS*2. It shows that the highest spike under monotonic stimulation (28.9 MPa) is significantly reduced to 28 MPa and 25.8 MPa by changing the stimulation scenario to *CS*1 and *CS*2 respectively. Yet, the highest spike is higher than that under only stepwise stimulations, especially the three-step stimulation *S*2. This is because the continuous injection in each step causes longer fracture (as can be seen in Fig. 5.17b) at the end of each step. When the injection rate is increased, the longer fracture leads to lower peak pressure than that under *CS*1 and *CS*2 scenarios. In addition, at t = 80 h - 120 h, the injection pressure under *S*1 and *S*2 is significantly lower than that under *CS*1 and *CS*2 respectively. It therefore can be concluded that stepwise combined with cyclic stimulation is better than monotonic stimulation, but is inferior than only stepwise stimulation.

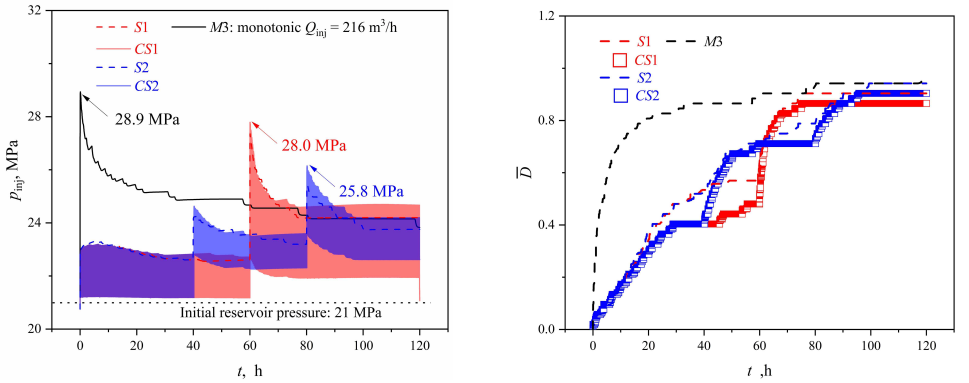


Figure 5.17: (a) Injection pressure response under combined cyclic and stepwise stimulation (Scenario *CS*1 and *CS*2); and (b) Corresponding averaged damage variable $\bar{D}$.

5

5.5. CONCLUSION

Thermo-hydro-mechanical (THM) simulations of cold-water injection into a reservoir are undertaken to investigate the potential thermo-hydraulic stimulation of clogged reservoirs. To enable potential fracture development, interface elements are inserted between all continuum elements, providing potential paths for crack initiation. Simulation results from models with and without interface elements (presented in Appendix B) show excellent agreement, validating the robustness of the approach.

For a clogged reservoir, THM simulations of various stimulation strategies - monotonic, stepwise, cyclic, and stepwise combined with cyclic - demonstrate that stepwise stimulation yields generally the most favourable outcomes. Specifically, it enables the lowest peak injection pressure of 4.4 MPa above the initial reservoir pressure compare to 7.9 MPa above initial pressures in the monotonic case (with the maximum injection rate at $Q_{\text{inj}} = 216$ m^3/h and $\Delta T = 40$ K). The long-term injection pressures after stepwise stimulation is also seen to be slightly lower than those observed in the monotonic, cyclic or stepwise combined with cases. Cyclic-temperature stimulation (within the bounds of the scenarios considered here) is observed to be neither better or worse than monotonic stimulation, but has slightly different characteristics. Monotonic injection creates a larger single fracture which breaks through the clogged zone, whereas thermal cycles create more local damage controlled by the period of the cyclic injection. Conversely, cyclic-injection-rate stimulation slightly underperform (under higher injection rate) or slightly outperforms (under lower injection rate) the monotonic stimulation, with fatigue effect playing a negligible role. A combined approach incorporating both cyclic and stepwise strategies may offer enhanced stimulation performance compared to monotonic stimulation, but is observed to be inferior than stepwise stimulation alone in the conditions considered here.

6

FEASIBILITY STUDY OF THE APPLICATION OF A DUAL-CABLE DAS TO MICRO-SEISMIC MONITORING

This chapter proposes a single-well dual-cable DAS configuration to reduce the need for drilling additional wells or sections, where two DAS cables are assumed to be positioned within a single vertical well at opposite sides of the well. Synthetic DAS signals are generated by an open-source code to study the feasibility of the dual-cable DAS for localising a seismic source and resolving its moment tensor. Results suggest the source location can be fully determined, yet low signal-to-noise ratio and azimuth close to 0° (North, aligned with the two cables) lead to a decrease in accuracy. The full moment tensor can be resolved only if the epicentral distance is 5 meters or less, while non-Double-Couple components can be reliably resolved with an epicentral distance up to 20 meters, showing improvement compared to installations with a single cable. Consequently, near-borehole failures, regardless of the source mechanisms, can be characterised within an epicentral distance of 5 m. With epicentral distance increasing, resolvability of the mix-mode failures is reduced first, followed by the resolvability of the pure shear or tensile failures, which depends on the azimuth. Overall, the results demonstrate that a single-well dual-cable configuration has the potential for monitoring and understanding near-borehole micro-seismic events induced during geothermal reinjection and stimulation operations.

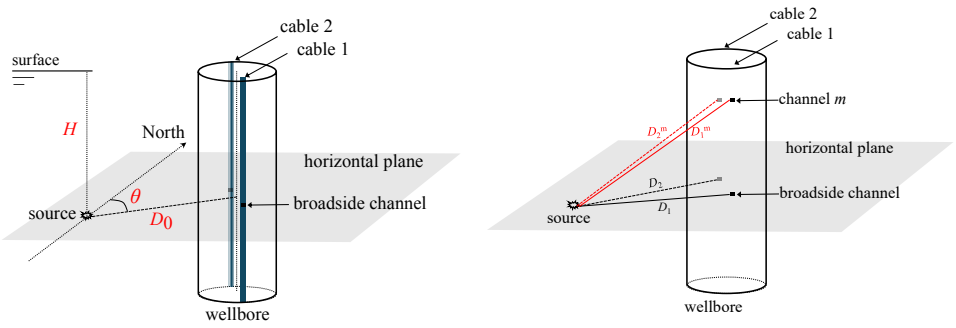
This chapter has been published in Luo *et al.* (2025c)

6.1. INTRODUCTION

Monitoring of near-borehole cracking events can also be characterised and understood via micro-seismic monitoring. Distributed acoustic sensing (DAS) that uses optical fibres as sensing units, is attracting increasing interest in micro-seismic monitoring in geothermal projects. Standard optical fibres provide one-component measurements along the fibre and this poses challenges in determining certain characteristics of the source, such as its azimuth and its full moment tensor. Full source characteristics can be obtained via offset wells and/or horizontal sections but comes with substantial extra costs.

This chapter proposes a single-well dual-cable DAS configuration to reduce the need for drilling additional wells or sections, where two DAS cables are assumed to be positioned at opposite sides within a single vertical well, as is shown in Fig. 6.1a. Synthetic DAS signals are generated by an open-source code that assumes plane layered media, and used to study the feasibility of the dual-cable DAS for localising a seismic source and resolving its moment tensor. A localisation procedure is presented, and a sensitivity analysis of localization accuracy is conducted with respect to source parameters and noise levels. Also, an analysis is performed to assess the resolvability of the moment-tensor components from the dual-cable DAS configuration. The key questions that will be addressed in this chapter, with regard to the single-well dual-cables DAS are: (1) can the micro-seismic sources be fully localised? (2) is the localisation accuracy sensitive to source frequency, noise, source azimuth and mechanism? (3) is the moment tensor fully resolvable? (4) how can it be used to understand stimulation operations?

In this chapter, the generation of synthetic DAS signals is presented in Section 6.2. The demonstration of the localisation method to determine the source depth (H), source-to-wellbore epicentral distance (D_0) and source to wellbore azimuth (θ), defined in Fig.6.1a, is presented in Section 6.3, including a sensitivity analysis. In Section 6.4, the resolvability of the moment tensor via one- and dual-cable DAS array in one single vertical wellbore is compared and discussed. In Section 6.5,the application of this dual-cable DAS to monitor stimulation operations is discussed based on a geo-mechanical simulation of stimulation operation to a synthetic reservoir, and the whole is finalised by a conclusion section.



(a) Description of dual-cable DAS configuration

(b) Definition of parameters used in locating

Figure 6.1: Description of the geometry of the dual-cable DAS configuration

6.2. GENERATING DAS SIGNALS

To generate synthetic DAS signals, a model using the so-called reflectivity method is used. The reflectivity method assumes plane-layered media and inhomogeneities occur only in the vertical direction. Analytical solutions are obtained in the frequency–horizontal-wavenumber domain, and the time-space domain responses are obtained by a numerical evaluation of the horizontal-wavenumber integral. This all is implemented in the open-source code Computer Program in Seismology (CPS) (Jost & Herrmann, 1989; Herrmann, 2013). First, we define the coordinate system with North being along x with unit vector $\mathbf{e}_x$, East being along y with unit vector $\mathbf{e}_y$, and the downward being z with unit vector $\mathbf{e}_z$. The model domain is depicted in Fig. 6.2. A 1000-meter thick layer is constructed with two half-spaces on top and at the bottom. The layer is isotropic and homogeneous. A borehole with diameter of 0.36 m is placed vertically through the layer. Two DAS cables are installed at opposite sides of the borehole, one at the North and the other at the South, from a depth of 445 m to 555 m. A point-force source is excited at a depth of 500 m, with its distribution in time given by a Ricker wavelet, a second-derivative of a Gaussian. The source-to-borehole azimuth is 45° (North is 0° while East is 90°). The DAS has a gauge length (L_G) of 2.5 m, over which the strain is averaged (over three channels) with a channel spacing (L_C, the distance between two adjacent channels or say points) of 1.25 m. With this configuration, there is therefore 87 channels on a each DAS cable. Other parameters used in the model are presented in Tab. 6.1, with the parameters selected to be realistic, but otherwise have no specific significance. For example, the P- and S-wave velocities are selected in the range of wave velocities of common sandstone reservoirs. The borehole diameter of 0.36 m is selected as a reasonable value for geothermal wells. In the following, the discussion is restricted to the frequencies from 20 Hz to 200 Hz, which is a typical frequency range of field micro-seismicity during hydraulic fracturing operations (Maxwell & Cipolla, 2011; Van der Baan *et al.*, 2013; Grechka *et al.*, 2021), with epicentral distance from 5 to 100 m and source force magnitude $F_0 = 2{\cdot}10^5$ N. The source excitation is assumed to occur directly next to the cable and within the depth range of the cable.

The output used from the model is the point strain at the defined DAS channels. However, DAS measures averaged strain over gauge length, which therefore dominates the spatial resolution (Hasani, 2024). The following equation is then performed to get the averaged strain:

$$\bar{\epsilon}^m_{zz} = \frac{1}{L_G}\int_{z_m - L_G/2}^{z_m + L_G/2} \epsilon^m_{zz} dz \tag{6.1}$$

where $\bar{\epsilon}^m_{zz}$ and ϵ^m_{zz} are the averaged and point strain at the mth channel respectively, z_m is the depth of the mth channel. Since the gauge length is 2.5 m while channel spacing is 1.25 m, there are three channels over which the strain is averaged for a single channel.

6.3. LOCALISATION METHOD

6.3.1. INTRODUCTION TO THE LOCALISATION METHOD

For optical fibres installed along the borehole (either behind casing or somehow coupled to the inner part of the casing) to monitor micro-seismic activity during stimulation operations, the depth of the micro-sesimic events is likely to be within the range of the

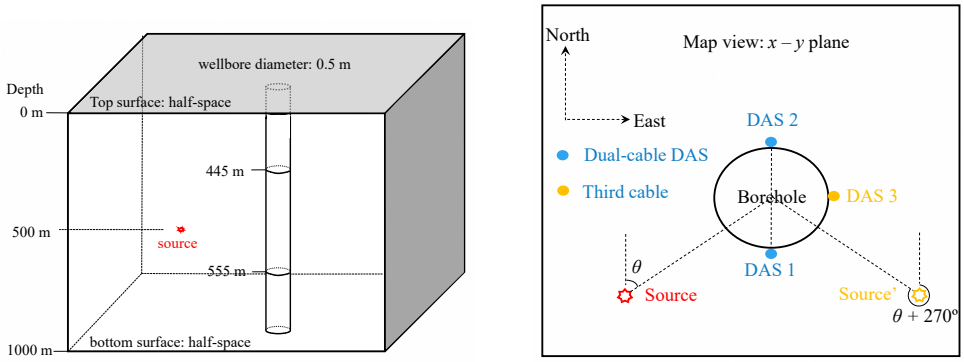


Figure 6.2: Schematic illustration of the numerical model with the dual-cable DAS configuration. (a) The model in 3D; (b) Map view on x - y plane. In (b), blue dots indicate the dual-cable DAS in a vertical well while the orange dot indicate a third cable. As discussed in Section 6.3.1, the dual-cable DAS can only determine two possible azimuths, leading to a non-unique location, i.e. the red star and the orange star in (b). In addition, results in Section 6.3.3 show that when the azimuth θ is approaching 0° or 360°, the accuracy in determining the azimuth via the dual-cable DAS decreases largely. A third cable can help both to determine uniquely the azimuth and improve the localisation accuracy when the azimuth θ is approaching 0° or 360°.

Table 6.1: Input parameters for model to generate synthetic DAS signals

Parameter	Symbol	Value	Unit
borehole diameter	d_0	0.36	m
P-wave velocity	V_p	3200	m/s
S-wave velocity	V_s	1847	m/s
sampling interval	dt	0.16	ms
source mechanism	$\mathbf{F} = F_0\mathbf{e}_z$	2×10^5	N
source function	Ricker wavelet		
source frequency	f_0	200	Hz
source epicentral distance	D_0	40	m
source depth	H	500	m
source azimuth	θ	45	°

DAS cable's length. In this case, the source depth H is the easiest to determine from DAS signals, namely picking the apex of the P- and S-wave arrivals along the fibres. In addition, the epicentral distance D_0 can be determined by comparing the actual curvature of the arrivals to the theoretical curvatures and selecting the one which best matches it, with the assumption that the wave velocity is known a priori, e.g. from logs.

When it comes to determining the source azimuth θ, we take advantage of the time difference Δt^m between arrivals on the mth channels on DAS cable 1 and cable 2, due to them being on opposite sides of the borehole. The time difference multiplied by the known wave velocity can give us the distance difference ($\Delta L^m = D_1^m - D_2^m$, defined in Fig. 6.1b) from the source to the mth channels on cables 1 and 2, which is a function of the source azimuth. For example, this distance difference for the channel at the same depth with the source is shown in Fig. 6.3. One possible method to get the time difference is by simply picking the arrival times at the different cables. However, this method is highly dependent on the picking accuracy and restricted by the sampling rate. We therefore use a signal-difference approach which is very sensitive to small time differences. The signal difference is based on the signal attribute known as the Normalised Root-Mean-Square (NRMS) difference that is independent of the sampling rate, which will be clarified below.

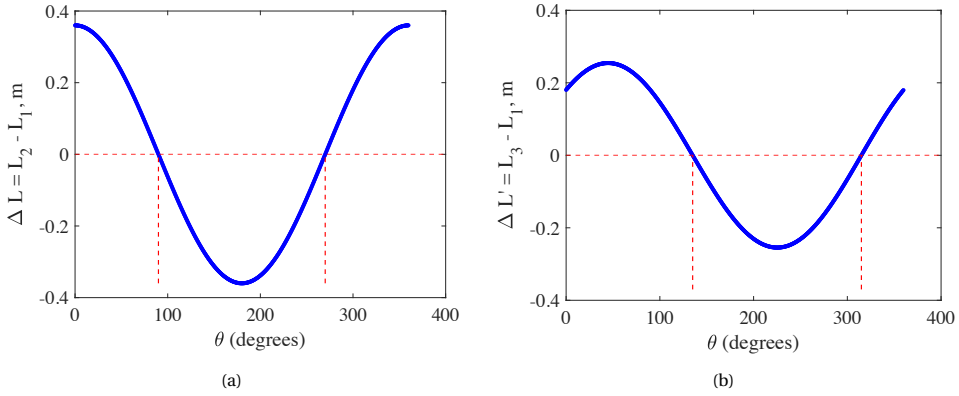


Figure 6.3: Distance difference (a) ΔL (= $L_2 - L_1$) between cables 1 and 2, and (b) $\Delta L'$ (= $L_3 - L_1$) between cables 1 and 3, as a function of source azimuth at channel at same depth of the source. The red dotted lines indicate that one ΔL (or $\Delta L'$) gives two solutions to the azimuth θ. Installing a third cable can help determine the unique azimuth by simply comparing the arrival times on cable 1 and 3. In addition, in (a), when the azimuth θ is approaching 0°, 180° or 360°, the slope of the curve is approaching zero leading to insensitivity of ΔL to the changes in azimuth θ, thus large error in the retrieved azimuth, as discussed later in Section 6.3.3. Installing a third cable can help to improve the accuracy, as shown in (b), where the slope of the curve is reasonably high when the azimuth θ is approaching 0°, 180° or 360°.

The Normalised Root-Mean-Square difference, is defined as:

$$\Delta_{NRMS}(a(t), b(t)) = \frac{2\mathscr{A}_{RMS}(|a(t)| - |b(t)|)}{\mathscr{A}_{RMS}(a(t)) + \mathscr{A}_{RMS}(b(t))} \tag{6.2}$$

where $a(t)$ and $b(t)$ are the two sets of DAS signals. Non-standard absolute values are used in this definition since they are useful when the two signals show opposite signs, for

example when the azimuth is 90° and the source is a F_x, generating two opposite-sign signals on the two DAS cables.

$\mathscr{A}_{RMS}$ is the Root-Mean-Square amplitude, defined as:

$$\mathscr{A}_{RMS}(x(t)) = \sqrt{\frac{\int_{t_1}^{t_2} x^2(t)\mathrm{d}t}{t_2 - t_1}} = \sqrt{\frac{\sum_{N1}^{N2} x_i^2}{N_2 - N_1}} \tag{6.3}$$

where N_1 and N_2 are the starting and ending time samples within the specific time window t_1 - t_2.

With this definition, the Δ_{NRMS} between the mth channel on cable 1 and the mth channel on cable 2 can be obtained, represented by the "observed"Δ^m_{NRMS}. To determine the time difference Δt^m, this observed Δ^m_{NRMS} is compared against a series of pre-computed Δ_{NRMS} to identify the best-fit Δ_{NRMS}. Once identified, the time difference associated with the best-fit Δ_{NRMS} and its neighbouring values are interpolated to get the accurate Δt^m. More details of the pre-computed Δ_{NRMS} can be found in C

Once the time difference Δt^m is determined, the corresponding difference in distance (ΔL^m) can be obtained, which is used to back-calculate the azimuth θ^m from the relation, for example as shown in Fig. 6.3. The final azimuth θ is obtained by averaging the θ^m of all the channels along the cable. Note that, as shown in Fig. 6.3, one ΔL gives two possible azimuths. Yet, this can be resolved by installing a third cable in the well (as shown in Fig. 6.2b) or by utilising the signal attenuation due to the fluid in the borehole. Here the determination of the unique azimuth using a third cable is elaborated. As shown in Fig. 6.2b and Fig. 6.3, two possible source locations are determined by the dual-cable DAS, symmetrically positioned with respect to the line defined by cables 1 and 2 on the $x-y$ plane. If a third cable is installed, for example at the side as indicated by the orange circle in Fig. 6.2b, a unique source location can be determined by comparing the arrival times on DAS cable 1 and cable 3. In addition, the installation of the third cable can also help improve the accuracy in determining the azimuth when the azimuth is approaching 0°, 180° or 360°, which will be discussed in detail in the following Section 6.3.3.

6.3.2. BASE EXAMPLE

In this section, we demonstrate the localisation method based on a base example. The DAS configuration is the same as before, i.e., as shown in Fig. 6.2 with the parameters as given in Tab. 6.1. Fig. 6.4a presents the strain signal on DAS cable 1.

The depth of the source can quite easily be picked via the apex of the hyperbola in Fig. 6.4a, i.e. at 500 m. The epicentral distance can be obtained via a comparison of the curvature of the observed arrivals on DAS cable 1 to the theoretical curvature (Fig. 6.4b); in this case the S-wave arrival is taken since it is the strongest arrival. A best fit of 42 m is obtained, while the true distance is 40 m. The error in the determined epicentral distance is partly from the time interval used to calculate the theoretical curvatures and partly from the accuracy of the picking (in this case the S-wave using short-time average / long-time average method). Yet, the result remains in an acceptable range (defined as that the relative error is less than 5%).

Next we show how to determine the azimuth. Since the time difference in the signals is symmetric with respect to the channel at the source depth, only channels on the first half

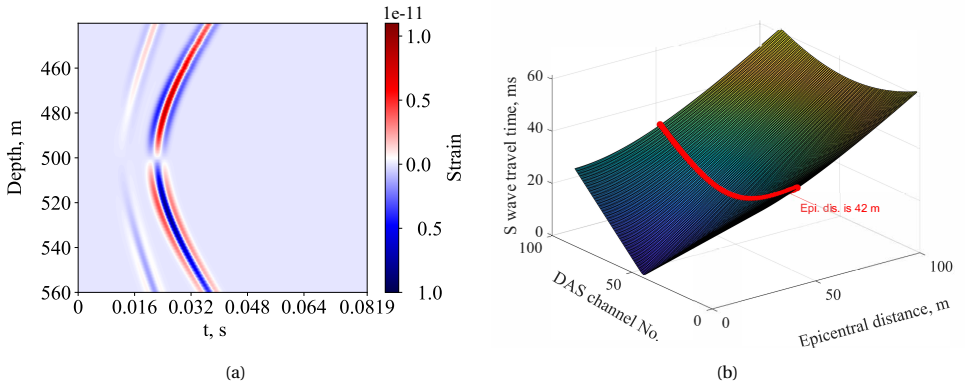


Figure 6.4: (a) Strain signals on DAS cable 1 due to a vertical point force; and (b) method to determine epicentral distance.

of (above the source depth) the DAS cable are considered where the channel numbering goes from top to bottom. Fig. 6.5 shows the observed $\Delta^{\text{DAS}}_{NRMS}$ and the determined azimuth at each channel. The result shows that the averaged azimuth is 46.8°, demonstrating a satisfactory accuracy (defined as that the absolution azimuth error $\Delta\theta$ is less than 5°) when compared to the real azimuth (45°).

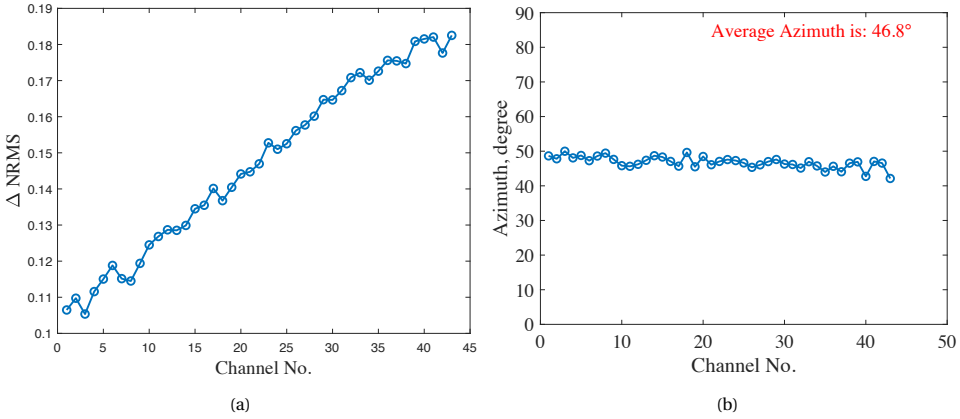


Figure 6.5: (a) The observed Δ^{m}_{NRMS} of each channel; (b) Determination of averaged azimuth by comparing the observed Δ^{m}_{NRMS} with the pre-computed Δ_{NRMS} library. Channel number 1 indicates the top channel at the depth of 445 m, while channel number 44 indicates the channel at the source depth of 500 m. Due to symmetry, the channels from 500 m to 555 m are not shown here.

6.3.3. SENSITIVITY ANALYSIS

In this section, the sensitivity to frequency content, noise level, source mechanism and azimuth is investigated to evaluate their influence on the accuracy of the localisation. Since the advantage of the dual-cable DAS configuration mainly lies in its improvement

in determination of the azimuth, we focus on that only and will not show the sensitivity of the depth and epicentral distance to the above mentioned parameters.

SENSITIVITY TO SOURCE FREQUENCY

The frequency of the micro-seismic events induced during hydraulic stimulation is commonly in the range of tens to hundreds of Hz (Maxwell & Cipolla, 2011; Van der Baan *et al.*, 2013; Grechka *et al.*, 2021). Therefore, the influence of the central source frequency from 20 Hz to 200 Hz on the accuracy is compared. Fig. 6.6 compares the DAS signals for source frequencies of 50 Hz and 100 Hz, as well as their determined azimuths. Together with Fig. 6.5b, which shows the case for the frequency of 200 Hz, the results suggest that the accuracy to predict the azimuth is not sensitive to frequency of 50 Hz, 100 Hz and 200 Hz. A more continuous sensitivity analysis, as shown in Fig. 6.7, demonstrates that the location error ($\Delta\theta$, the difference between the true and determined azimuth) remains within 3° for frequencies in the range from 20 to 200 Hz. However, for low-frequency events (< 20 Hz), the large wavelengths may result in negligible differences between signals positioned on opposite sides of a 0.36 m diameter borehole. The trend of the decreasing $\Delta^{\text{DAS}}_{NRMS}$ with reduced frequency can be seen in Fig. 6.6, of which the right axis shows the corresponding $\Delta^{\text{DAS}}_{NRMS}$, demonstrating a higher $\Delta^{\text{DAS}}_{NRMS}$ for the case of f = 100 Hz than that of f = 50 Hz.

SENSITIVITY TO NOISE

Although one of the advantages of downhole monitoring is the improvement in the signal-to-noise ratio (S/N), noise still needs to be considered especially during operations and especially since DAS recordings are generally noisier than standard geophone signals. Therefore, the influence of noise on the localisation accuracy is evaluated. Gaussian noise is added to the DAS signals using a normal distribution $\mathcal{N} = \mu + \sigma^2\mathcal{Z}$, where $\mathcal{Z}$ is the standard normal variable, $\mu = 0$ and σ is chosen from 1×10^{-13}, 4×10^{-13} and 10×10^{-13}, leading to a S/N of 18.8 dB, 7.7 dB and 2.5 dB, respectively.

Fig. 6.8 shows the signals with the different noise levels and the determined azimuth on each channel. Results suggest that when the noise level is at S/N = 18.8 dB, the accuracy of the determined average azimuth is acceptable, with an error of 2.9%. With an increasing noise level, the accuracy decreases significantly, with errors of 7.1% and 16.2% for the other two cases. The noise has a dramatic influence on the accuracy for channels close to the source depth (i.e. 500 m or say channel 44), the reason being that the strain at these channels becomes very small due to the wave motion being as-good-as perpendicular to the fibre, and then the noise dominates the localisation accuracy. One possible solution is to exclude these channels; however, as shown in Fig. 6.8f, the accuracy from the remaining channels also declines towards the source depth, albeit more gradually. Fig. 6.9 presents the azimuth error ($\Delta\theta$) versus noise levels (represented by σ) from $\sigma = 1{\cdot}10^{-13}$ to $20{\cdot}10^{-13}$. It shows that when the noise level increases to $13{\cdot}10^{-13}$ or higher, the azimuth error dramatically increases to 45°. This highlights the importance of improving S/N via, for example, signal processing or installation of the fibre outside the casing.

SENSITIVITY TO AZIMUTH

So far, the source to borehole azimuth was chosen as 45°. Since one of the main motivations to consider a single-well dual-cable DAS is to determine azimuth, it is necessary

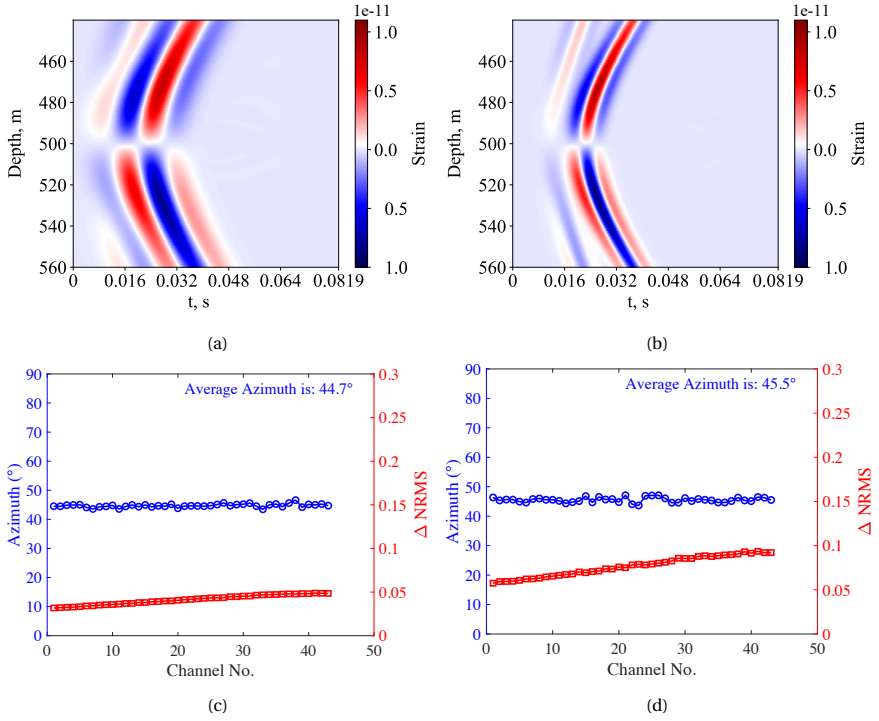


Figure 6.6: DAS signals for central source frequencies of (a) 50 Hz and (b) 100 Hz, and corresponding determined azimuth (c) and (d) on channel 1 (top channel, at depth 443.75 m) to 44 (source-depth channel, at depth 500 m). Other source parameters are the same with the base example.

to examine the dependence of the localisation accuracy on this parameter. The source mechanism is assumed to be a vertical point force $\mathbf{F}_z$ and therefore signals on the DAS cable will remain the same with changing azimuth. However, when the *difference* in the signals between DAS cable 1 and cable 2 is taken, it will vary with azimuth, as is illustrated in Fig. 6.10, which shows that the location error increases with the decrease in azimuth. When the azimuth is smaller than approximately 15°, $\Delta\theta$ becomes larger than 5°. More specifically, the azimuth of 15°, 45° and 75° is compared in Figs. 6.11a - 6.11c. 6.3 The best accuracy of the localised azimuth is achieved at 75°, while the lowest accuracy at 15°, with errors of 45%, 4%, 0.8% for azimuths of 15°, 45° and 75° respectively, though larger $\Delta_N RMS$ is seen for smaller azimuth.

The reason that $\Delta\theta$ increases with decreasing azimuth is that, as shown in Fig. 6.3, the slope of the curve of the relation between ΔL and θ decreases when θ approaches 0°, leading to an insensitivity to the change in azimuth. In contrast, the slope reaches its maximum value when $\theta = 90°$, therefore having the highest accuracy in the localisation. Additional constraints from a third DAS cable (as indicated by the orange dot in Fig. 6.2b) in the borehole can well resolve the low accuracy in locating the azimuth close to 0°. As is shown in Fig. 6.3b, unlike the insensitivity of ΔL ($= L_2 - L_1$) to the azimuth θ when θ is

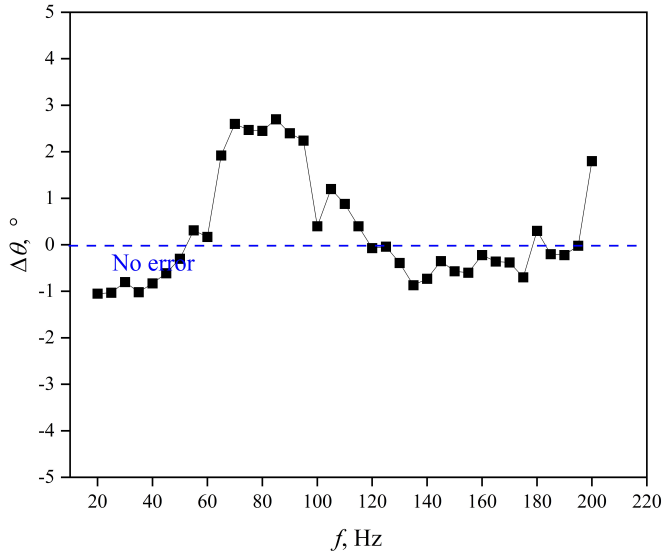


Figure 6.7: Sensitivity analysis to source frequency

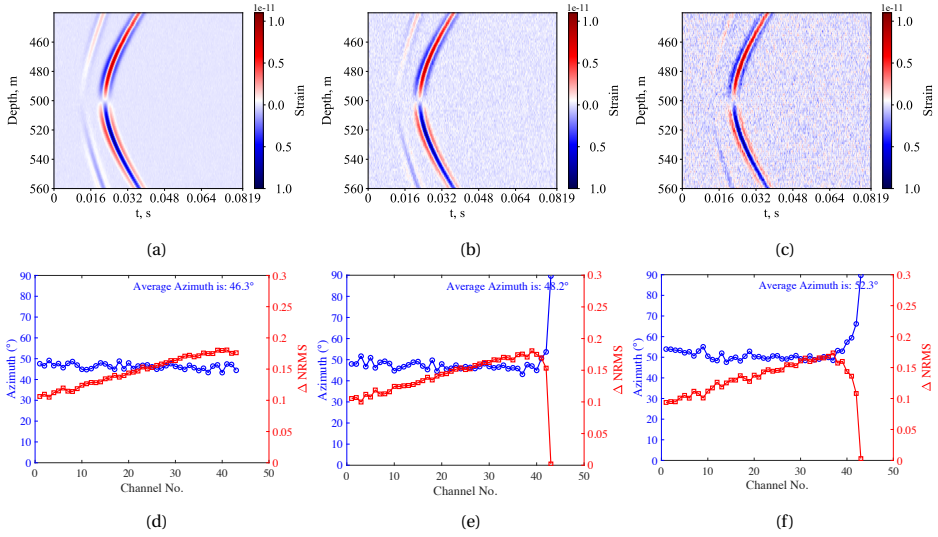


Figure 6.8: DAS (strain) signals with noise levels of (a) S/N = 18.8 dB, (b) 7.7 dB and (c) S/N = 2.5 dB, and corresponding determined azimuth (d) - (f) on channel 1 (top channel, at depth 443.75 m) to 44 (source-depth channel, at depth 500 m). Source parameters are same as in base example.

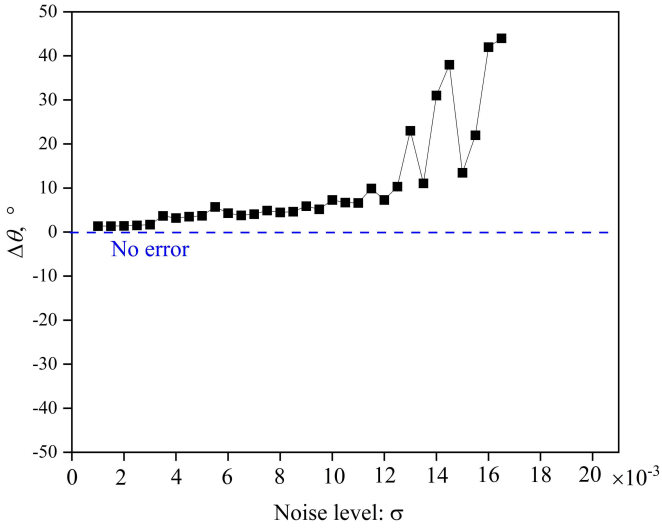


Figure 6.9: Sensitivity analysis to noise level

approaching 0°, 180° or 360°, $\Delta L'$ (= $L_3 - L_1$) shows reasonably good sensitivity to θ, since the slope of the curve is significantly higher than zero when θ is approaching 0°, 180° or 360°. Fig. 6.12 compares the azimuth determined from $\Delta L \sim \theta$ and from $\Delta L' \sim \theta$ when the azimuth is 0° and 15°. It shows that there is a large error when using the relationship $\Delta L \sim \theta$. For example, for the actual $\theta = 0°$, the determined θ is 13.1°, significantly deviating from the true azimuth. In contrast, the determined θ is very close to the actual value when using the relationship $\Delta L' \sim \theta$. For the actual $\theta = 0°$, the determined θ is 1.1°, showing a significant improvement in the accuracy.

SENSITIVITY TO FORCE-SOURCE MECHANISM

In the above when the observed $\Delta NRMS^m$ is matched with the theoretical Δ_{NRMS}, the source mechanism was assumed to be $\mathbf{F} = \mathrm{F}_0\mathbf{e}_z$, consistent with the source mechanism of the observed Δ^m_{NRMS}. However, source mechanisms vary, and therefore it is necessary to evaluate how the localisation accuracy responds to different source mechanisms. Here we only consider other force-source mechanisms, and we exclude forces in the y-direction since source with force in the x direction shows the same nature.

Here, we let the source mechanisms vary from $\mathbf{F} = \mathrm{F}_0\mathbf{e}_z$ (Fig. 6.4a), $\mathbf{F} = \mathrm{F}_0\mathbf{e}_x$ (Fig. 6.13a) and $\mathbf{F} = \mathrm{F}_0(\mathbf{e}_x + \mathbf{e}_z)$ (Fig. 6.13b). The corresponding determined azimuths are shown in Fig. 6.5b, 6.13c and 6.13d respectively. The results indicate that the highest localization accuracy is achieved when the source mechanism of the observed Δ^m_{NRMS} and the theoretical Δ_{NRMS} match (both being $\mathrm{F}_0\mathbf{e}_z$, Fig. 6.5b). The worst match is when the source mechanism is $\mathrm{F}_0\mathbf{e}_x$ (Fig. 6.13c) with an error of 11.3%. Fig. 6.13d shows a better localization accuracy for the case of $\mathbf{F} = \mathrm{F}_0\mathbf{e}_x + \mathrm{F}_0\mathbf{e}_z$ than the case of $\mathbf{F} = \mathrm{F}_0\mathbf{e}_z$, because of the presence of the $\mathrm{F}_0\mathbf{e}_z$ component in the source, which helps to maintain accuracy.

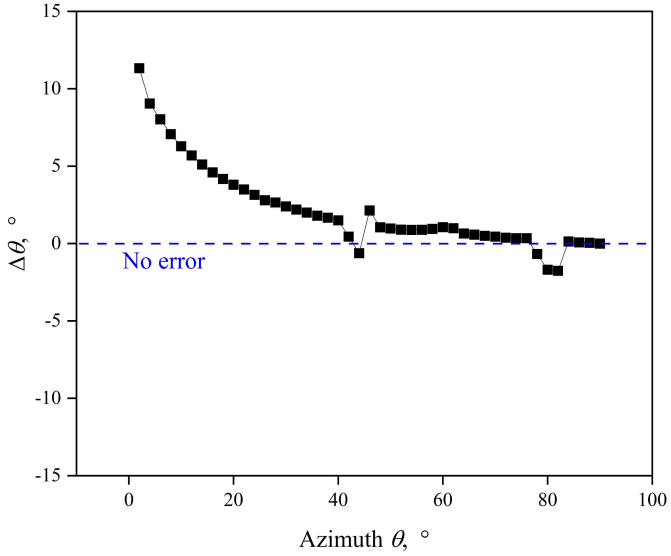


Figure 6.10: Sensitivity analysis to azimuth

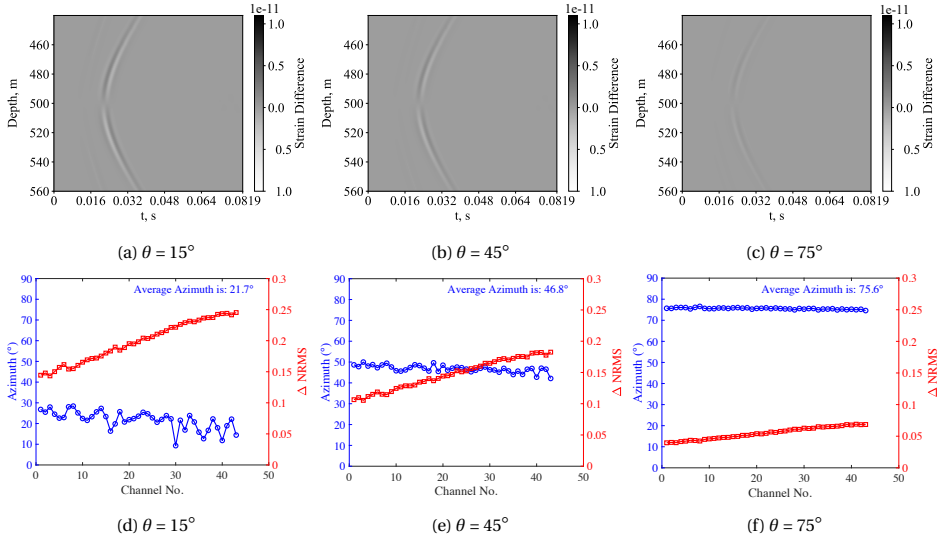
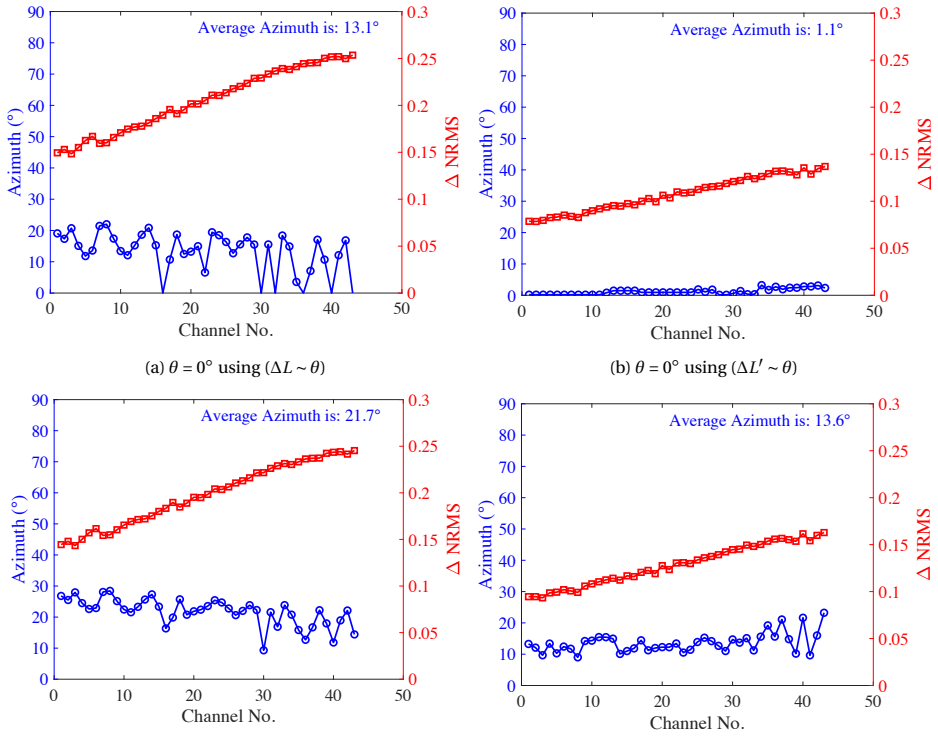


Figure 6.11: Difference in DAS signals between DAS cable 1 and cable 2 with a source-to-borehole azimuth of (a) 15°, (b) 45° and (c) 75°, and (d) - (f) corresponding $\Delta NRMS$ and determined azimuth on channel 1 (top channel, at depth 443.75 m) to 44 (source-depth channel, at depth 500 m). Other source parameters are the same with the base example.



(a) $\theta = 0°$ using $(\Delta L \sim \theta)$

(b) $\theta = 0°$ using $(\Delta L' \sim \theta)$

(c) $\theta = 15°$ using $(\Delta L \sim \theta)$

(d) $\theta = 15°$ using $(\Delta L' \sim \theta)$

Figure 6.12: Comparison of the determined azimuth using the relationship $\Delta L \sim \theta$ and $\Delta L' \sim \theta$ respectively for the case of (a) - (b) $\theta = 0°$ and (c) - (d) 15°

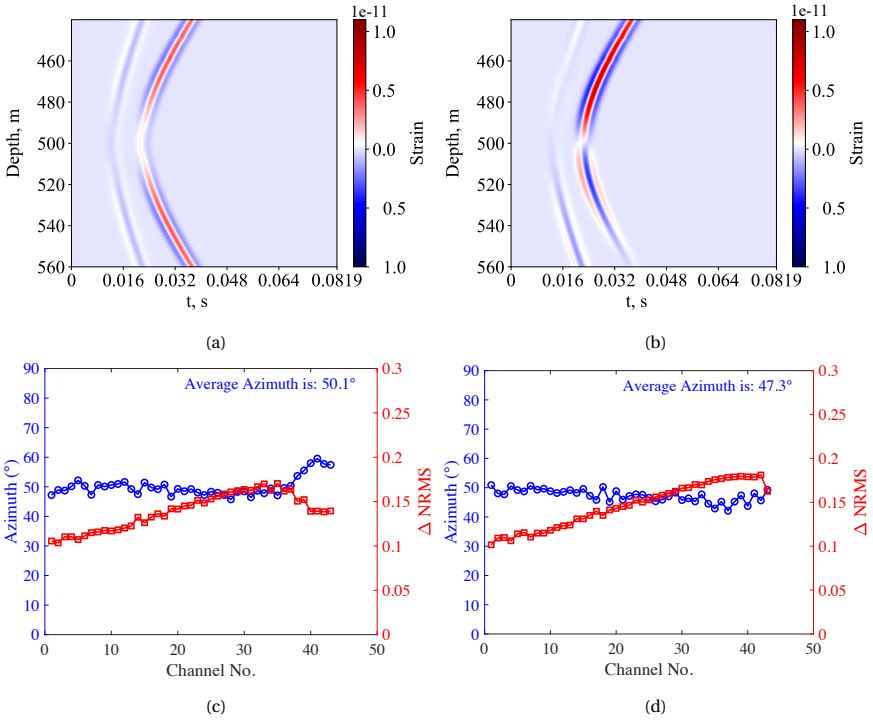


Figure 6.13: DAS (strain) signals with source mechanism of (a) $\mathbf{F} = F_0\mathbf{e}_x$ and (b) $\mathbf{F} = F_0\mathbf{e}_x + F_0\mathbf{e}_z$, and corresponding determined azimuth (c) and (d) on channel 1 (top channel, at depth 443.75 m) to 44 (broadside channel at depth 500 m). Other source parameters are the same with the base example.

SENSITIVITY TO EPICENTRAL DISTANCE

Fig. 6.14 demonstrates the sensitivity of the azimuth error to the epicentral distance from 4 m - 100 m. It shows that the absolute value of $\Delta\theta$ is within 3°, though relatively larger error is seen when the epicentral distance is less than around 30 m or more than 70 m. The reason for the slightly decreased accuracy with small epicentral distance is likely that P- and S-wave signals overlapped with such close distance. In addition, for the larger distance, at which the accuracy also slightly decrease, the reason could be the weakened signals and that the numerical noise therefore plays a role. Overall, the investigated epicentral distance reasonably has little impact on the azimuth accuracy.

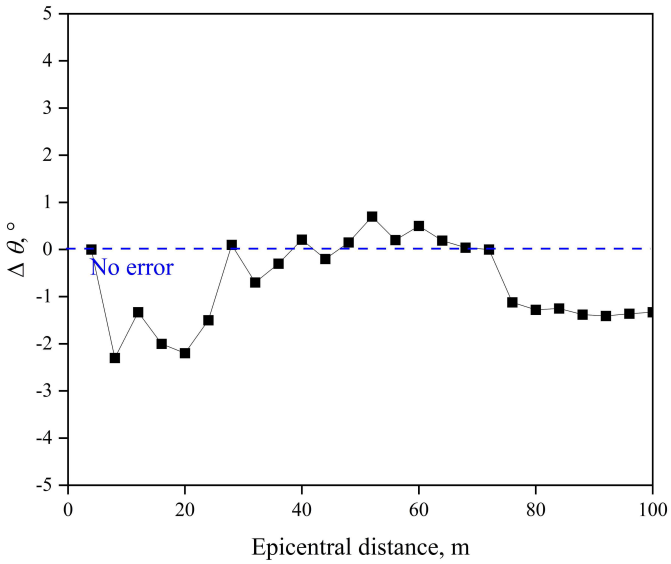


Figure 6.14: Sensitivity analysis to epicentral distance

6.4. MOMENT TENSOR RESOLVABILITY

In a previous study by Vera Rodriguez & Wuestefeld (2020), the resolvability of the moment tensor was investigated with two well-separated boreholes. Here, we investigate what happens when the two DAS cables are within one borehole, with the results from Vera Rodriguez & Wuestefeld (2020) used as a reference case. In this section, we show how to construct the resolution matrix from semi-analytical solutions (via the code CPS). Although the discussion in this feasibility study is limited to homogeneous and isotropic media for simplicity, the proposed method to construct the resolution matrix can be used to study inhomogeneous and anisotropic media. In addition, it was shown in the previous discussion that the source location can be fully determined with reasonable accuracy (with the aid of a third cable); in the following discussion, the location of the source is assumed to be known a-priori. A sensitivity analysis is performed on the localisation uncertainty to evaluate the influence of this uncertainty on the resolvability.

6.4.1. CONSTRUCTION OF THE RESOLUTION MATRIX

Source mechanism inversion includes retrieving the source time function and moment tensor. Since the primary goal of this work is to evaluate the resolvability of the time-independent moment tensor only, the time dependence of the source process is not considered (Vavryčuk & Kühn, 2012; Chapman & Leaney, 2012), thus simplifying the problem to linear moment-tensor inversion. The moment-tensor components can be linearly related with the observed data by (Vavryčuk & Kühn, 2012; Vera Rodriguez & Wuestefeld, 2020):

$$\boldsymbol{G}\boldsymbol{m} = \boldsymbol{d} \tag{6.4}$$

where $\boldsymbol{M} = [M_{xx}, M_{xy}, M_{xz}, M_{yy}, M_{yz}, M_{zz}]$ is the model vector composed of six unknown independent moment tensor components to be retrieved. The x is in the direction of North while y is in the direction of East. $\boldsymbol{d} = [d_1, d_2, \cdots, d_N]$ is the data vector consisting of the observed strain amplitude on DAS (in this work, z component of strain), and N is the number of channels. $\boldsymbol{G}$ is the geometry matrix, and can be expanded as:

$$G = \begin{bmatrix} G_{11} & G_{12} & G_{13} & G_{14} & G_{15} & G_{16} \\ G_{21} & G_{22} & G_{23} & G_{24} & G_{25} & G_{26} \\ & & \cdots & \cdots & & \\ G_{N1} & G_{N2} & G_{N3} & G_{N4} & G_{N5} & G_{N6} \end{bmatrix} \tag{6.5}$$

In this work, $\boldsymbol{G}$ is constructed from semi-analytical solution calculated from CPS (Herrmann, 2013) that gives the complete solution. Taking the ith channel as an example, the elements can be described as:

$$\begin{aligned}
G_{i1} &= \frac{\partial}{\partial z}\left[\frac{Z_{SS}}{2}\cos(2\phi) - \frac{Z_{DD}}{6} + \frac{Z_{EX}}{3}\right]_i \\
G_{i2} &= \frac{\partial}{\partial z}\left[Z_{SS}\sin(2\phi)\right]_i \\
G_{i3} &= \frac{\partial}{\partial z}\left[Z_{DS}\cos\phi\right]_i \\
G_{i4} &= \frac{\partial}{\partial z}\left[-\frac{Z_{SS}}{2}\cos(2\phi) - \frac{Z_{DD}}{6} + \frac{Z_{EX}}{3}\right]_i \\
G_{i5} &= \frac{\partial}{\partial z}\left[Z_{DS}\sin\phi\right]_i \\
G_{i6} &= \frac{\partial}{\partial z}\left[\frac{Z_{DD}}{3} + \frac{Z_{EX}}{3}\right]_i
\end{aligned} \tag{6.6}$$

where ϕ is the azimuth angle. Z_{SS} is the function of the response to a strike-slip source, Z_{DS} represents the response to a vertical dip-slip source, Z_{DD} can be understood as part of a vertical or radial displacements for a 45 ° dip-slip source observed at an azimuth of 45 °, and Z_{EX} represents the response to an explosive source (Jost & Herrmann, 1989; Herrmann, 2013).

When the data contain noise (e.g. numerical noise) or other signal not covered by the modelling, then Eq. 6.4 can be solved by the least-squares solution, as was done in

Vera Rodriguez & Wuestefeld (2020), so:

$$\boldsymbol{M} = \left[\boldsymbol{G}^T \boldsymbol{G}\right]^{-1} \boldsymbol{G}^T \boldsymbol{d} = \boldsymbol{A}^{-1} \boldsymbol{G}^{\mathrm{T}} \boldsymbol{d} \tag{6.7}$$

with $\boldsymbol{A} = \boldsymbol{G}^T \boldsymbol{G}$. And the so-called resolution matrix $\boldsymbol{R}$ is accordingly constructed as:

$$\boldsymbol{R} = \boldsymbol{A}^{\dagger} \boldsymbol{A}, \tag{6.8}$$

where $\boldsymbol{A}^{\dagger}$ is the pseudoinverse of matrix $\boldsymbol{A}$, which is equal to $\boldsymbol{A}$ when all the elements in the model vector $\boldsymbol{m}$ are linearly independent and resolvable (Vera Rodriguez & Wuestefeld, 2020). Thus, the resolution matrix $\boldsymbol{R}$ indicates the resolvability of the moment tensor components. When $\boldsymbol{R}$ is not the identity, its diagonal elements with value of 1 indicate that the corresponding moment tensor components are fully resolvable, while its diagonal elements with value of 0 indicate that the corresponding moment tensor components are completely not resolvable. In addition, non-zero off-diagonal values indicate linear dependence between two components.

Some of the diagonal elements with a value of 1 can correspond to extremely small values (less than 0.001, for example, due to noise), indicating that the related moment-tensor component cannot be resolved robustly. It is reported in Nolen-Hoeksema & Ruff (2001) that satisfactory inversion results can be obtained when the condition number (ratio of the largest singular value to the smallest, in our case of square symmetric matrices the largest eigenvalue to the smallest) of $\boldsymbol{A}^{\dagger}$ is smaller than 500. Thus, each non-zero eigenvalue is evaluated by computing the ratio of the largest eigenvalue to it. If this ratio exceeds 500, the corresponding element of the resolution matrix is forced to be smaller than 1 so that all the elements of 1 in the resolution matrix indicate the corresponding moment tensor component can be reliably resolved.

6.4.2. MOMENT-TENSOR RESOLVABILITY FROM A SINGLE DAS CABLE IN A VERTICAL BOREHOLE

In this section, the resolution matrix is constructed for the case of one DAS cable in a vertical borehole This resolvability analysis is performed to be compared with the results from Vera Rodriguez & Wuestefeld (2020) to verify our method and demonstrate why some of the diagonal elements with a value 1 in the resolution matrix cannot be viewed as an indication of reliable resolvable moment tensor components. The source and the DAS cable are in the $x-z$ or North-Down plane with an azimuth of 0 ° (i.e. the fibre is to the North of the source) at epicentral distances ranging from 5 m to 100 m. The other aspects of the configuration including source parameters, DAS positions and gauge length are the same as in the base example.

The resolution matrix is obtained for both P and S wave separately, by evaluating the **G** matrix at corresponding theoretical arrival time.

Fig. 6.15 demonstrates that four components (M_{xx}, M_{xz}, M_{yy} and M_{zz}) are resolvable from the P wave when the epicentral distance is 5 m or 10 m. In contrast, when the epicentral is 40 m, only three components (i.e. M_{xx}, M_{xz} and M_{zz}) are resolvable from the P-wave, showing consistent results with the analytical solution from Vera Rodriguez & Wuestefeld (2020), in which results show the component M_{yy} can only be retrieved when the intermediate-field term is included in the solution. In addition, the constraints

provided by S wave is redundant, mostly useful only to improve the robustness of the solution (Vera Rodriguez & Wuestefeld, 2020).

Fig. 6.16 show the influence of increasing epicentral distance on the condition number, defined as the ratio of the largest to smallest non-zero eigenvalues, using single-cable and dual-cable signals (which will be discussed in next section). The azimuth from source to receiver is either 0° or 90°. It shows that. for both azimuths, the condition number is smaller than 500 only when the epicentral distance is 5 using single-cable signal. This is because the near- and intermediate-field terms have minor contributions beyond the area of 10 m, while M_{yy} cannot be resolved robustly with only far-field terms (Vera Rodriguez & Wuestefeld, 2020). In addition, a smaller condition number for the P-wave signal compared to that for the S-wave signal can be observed because the P-wave signal gives more constraint, as is shown in Fig. 6.15. The reason is likely that the P-wave signals show more variations along the cable vertically while S-wave signals show more similarities, as is shown in Fig. 6.17. When the epicentral distance increases up to 40 m - 100 m, the condition number shows an oscillatory pattern. The reason for this is that the numerical noise now plays a role as the signals weaken. This trend is also evident in Fig. 6.17, which depicts the DAS signals from an M_{yy} source gradually fading into the noise background as the epicentral distance increases.

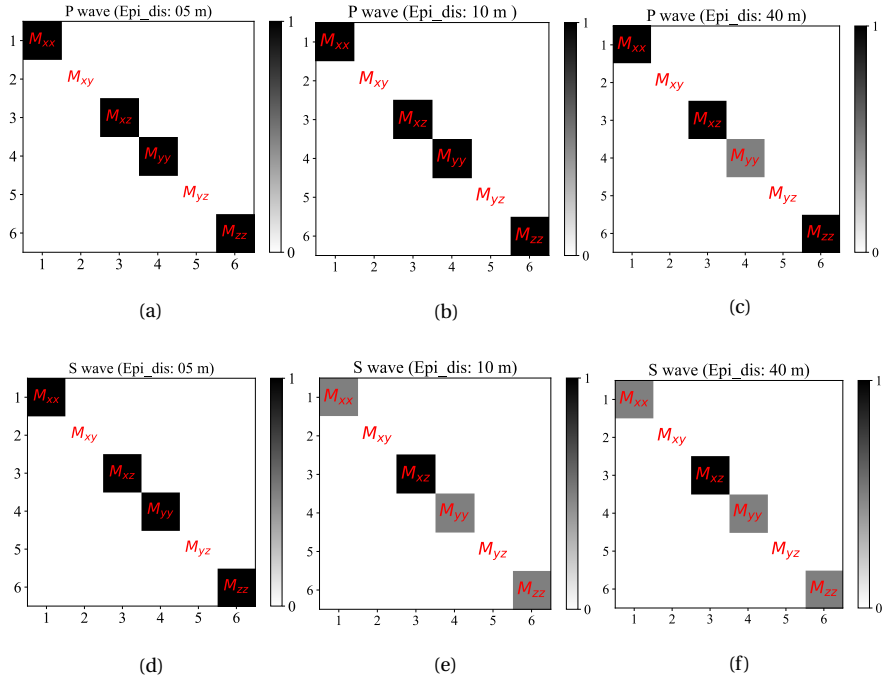
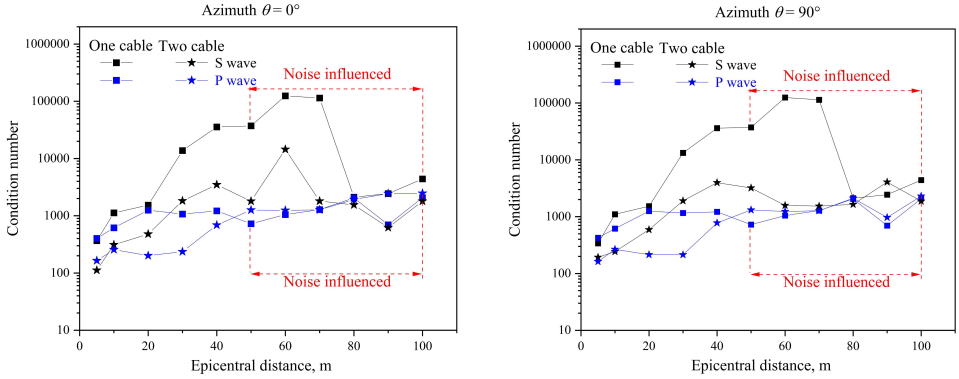
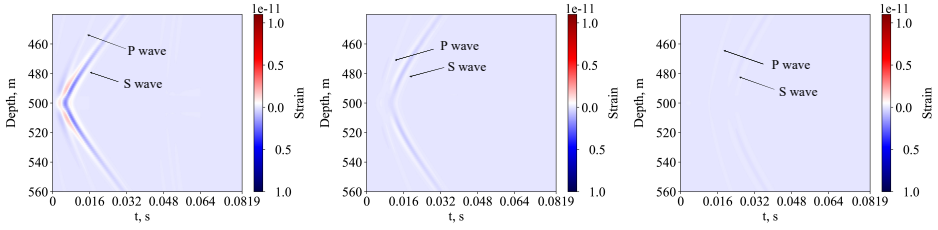


Figure 6.15: Resolution matrix of (a) - (c): P-wave (top row); and (d) - (e): S-wave (bottom row) signal for different epicentral distances for the case of one DAS cable in a vertical borehole. The configuration geometry is that the source and the DAS cable is in the x - z plane, so that the source to DAS azimuth is 0 °. The epicentral distance is 5 (left column), 10 (middle column), and 40 m (right column).



(a) Azimuth $\theta = 0°$ (b) Azimuth $\theta = 90°$

Figure 6.16: Comparison of condition number of matrix $\boldsymbol{A}^{\dagger}$ for different epicentral distances using single-cable and dual-cable signals.



(a) (b) (c)

Figure 6.17: Strain signals on one DAS cable in a vertical borehole due to a M_{yy} source for different epicentral distances (a) $D_0 = 10$ m, (b) $D_0 = 20$ m, and (c) $D_0 = 40$ m. Source and DAS cable are in the $x - z$ plane. With increasing epicentral distance, signals weaken and become comparable to the numerical noise background. P-wave signal is much weaker and therefore shows more sensitivity to the noise than S-wave signal in this case.

6.4.3. MOMENT-TENSOR RESOLVABILITY FROM DUAL DAS CABLE IN A VERTICAL BOREHOLE

The above discussion demonstrated that the moment tensor cannot be fully resolved from a single vertical DAS cable, although at a smaller epicentral distance, near- and intermediate-field terms can improve the resolvability of some of the components, showing results consistent with previous studies (Vavryčuk, 2007; Vera Rodriguez *et al.*, 2011; Vera Rodriguez & Wuestefeld, 2020). In this section, the resolvability from the dual cable in one single vertical well is examined. In the previous section, the DAS cable lay in the same plane as the source. In this configuration, an additional cable will not improve the focal coverage which refers to the capability of the network of seimsic sensors to constrain source location and mechanism. Therefore, we assume that the configuration is as shown in Fig. 6.18. That is, the source-to-borehole azimuth is 90°, located West of the borehole, while the two DAS cables are placed at opposite sides of the borehole, i.e., in the North and South.

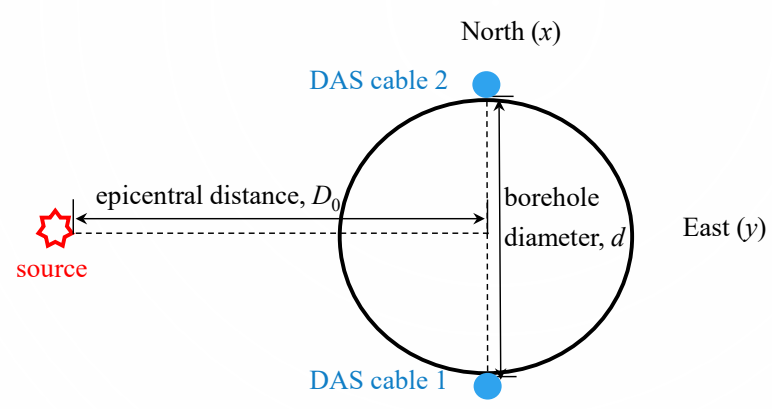


Figure 6.18: Schematic diagrams of the horizontal cross-section of the dual-cable configuration in a vertical well. Source to borehole azimuth is 90°.

First, the influence of the source to DAS-cable azimuth angle on the resolvability for the single-cable and dual-cable cases is investigated, assuming an epicentral distance of 40 m and a borehole diameter of 0.36 m. This is shown in Fig. 6.19. It shows reasonably well that, for both cases, when the azimuth is 0°, M_{xx}, M_{xz} and M_{zz} are resolvable, while at 90°, M_{yy}, M_{yz} and M_{zz} are resolvable. In addition, when the azimuth is 45°, neither M_{xx} nor M_{yy} is resolvable, since both produce identical DAS signals and are thus linearly dependent, as is indicated by the off-diagonal non-zero elements. The dual-cable installation does not provide significant improvement for the investigated azimuths, compared with the resolvability for the single-cable case. The reason is likely the small borehole size and the large epicentral distance. To further examine the resolvability using dual-cable DAS, the condition number using dual-cable signals is compared with that using single-cable signals in Fig. 6.16. It demonstrates that the condition number using dual-cable signals is significantly smaller than that using single-cable signals within the epicentral distance of 50 m, in which the noise plays a minor role. The condition number

using dual-cable DAS can be smaller than 500 m, even until an epicentral distance of 20 m, which improved considerably compared to only 5 m if using single-cable signals. Yet, when the epicentral distance is equal to or larger than 40 m, the condition number becomes larger than 500 and is consistent with Fig. 6.19 that shows no improvement in resolvability when the epicentral distance is 40 m. In addition, in the noise-influenced area, the condition number using dual-cable signals shows less oscillation. This confirms the robustness of dual-cable signals over single-cable ones.

In the following, we further investigate the impact of the borehole size and the epicentral distance on the improvement on resolvability using the dual-cable installation and then the sensitivity of the resolvability to the location is performed. Since the previous sensitivity analysis of the localisation shows that with the aid of a third cable the error in the determined azimuth is less than 5°, the maximum uncertainty in the azimuth is therefore set at that number. Fig. 6.20 demonstrates that an error up to 5° in the azimuth does not influence the resolvability using the dual-cable signals, assuming the source-to-receiver azimuth being 90° and epicentral distance being 40 m.

The borehole diameter (d) and the epicentral distance (D_0) together control the focal coverage, while a shorter epicentral distance will also lead to stronger near- and intermediate-field terms that can improve the moment-tensor resolvability. In this section, the epicentral distance is first assumed to be 40 m to limit the effects of near- and intermediate-field terms, and we examine the effects of the borehole diameter on the improvement of the moment-tensor resolvability from a dual cable, compared to one cable only. The effects of the epicentral distance with a fixed borehole diameter will be examined afterwards.

Fig. 6.21 compares the resolvability of moment-tensor components from one DAS cable to the one from two DAS cables in a single vertical well, with varying borehole diameter and a fixed epicentral distance of 40 m. These diameters are chosen since 0.36 m is a reasonable value for deep boreholes while 2.5 m is a value of an expanded borehole reported in Van der Schans *et al.* (2022). The results demonstrate that with increasing the borehole diameter, additional components can be resolved with dual DAS cable in a single vertical well. But only when the diameter reaches 2.5 m, the component M_{xy} can additionally be resolved with robust resolution. This indicates that only installation of a dual DAS cable in shallow and expanded boreholes can improve the moment-tensor resolvability of a source that is triggered tens of meters away from the borehole. Considering that many geothermal doublets consist of two wells drilled at a close distance, it is also promising to install a DAS cable in each well to improve the moment-tensor resolvability. Since we are interested in the downhole micro-seismic monitoring in a vertical and deep well, the resolvability of near-borehole sources is next examined with a small borehole diameter ($d = 0.36$ m).

Fig. 6.22 compares the resolvability of near-borehole sources (with epicentral distance of 5 m, 10 m and 20 m) from one DAS cable and two DAS cables in a single vertical well, with a borehole diameter of 0.36 m. The results show that employing a dual-cable DAS configuration can resolve one additional component compared to the one-cable configuration for all the cases considered. In particular, if the source is 5 m away from the borehole, the moment tensor can be fully resolved from the dual-cable DAS configuration. With increasing epicentral distance, the number of resolvable components

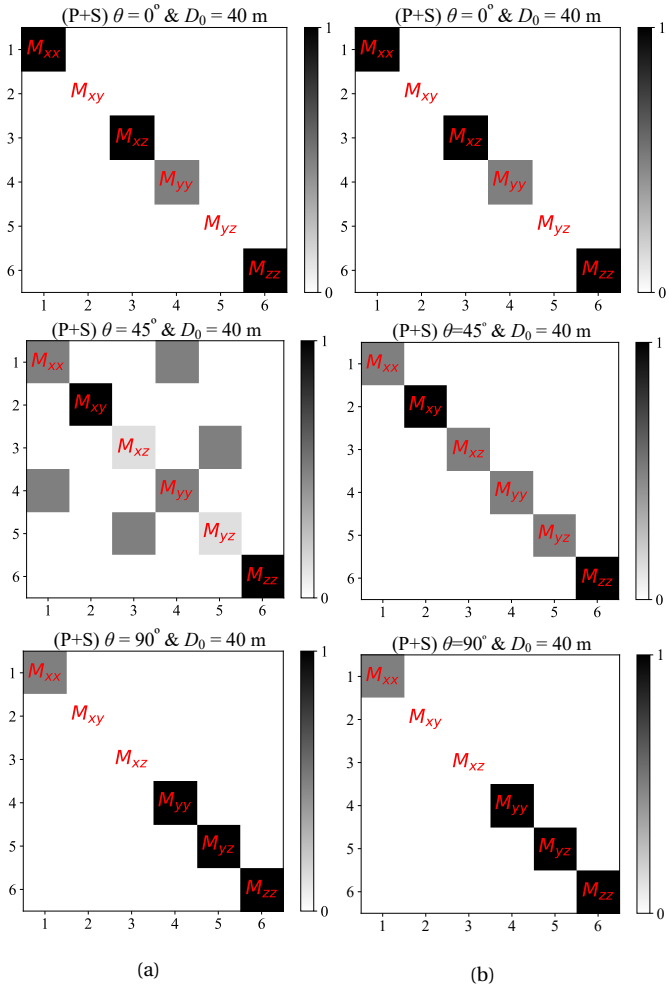


Figure 6.19: Resolution matrix of (P + S)-wave for different azimuths for the case of (a) one DAS cable and (b) two DAS cables in a vertical borehole. The epicentral distance is fixed at 40 m, while the azimuth from source to DAS cable is 0° (top row), 45° (middle row) and 90° (bottom row).

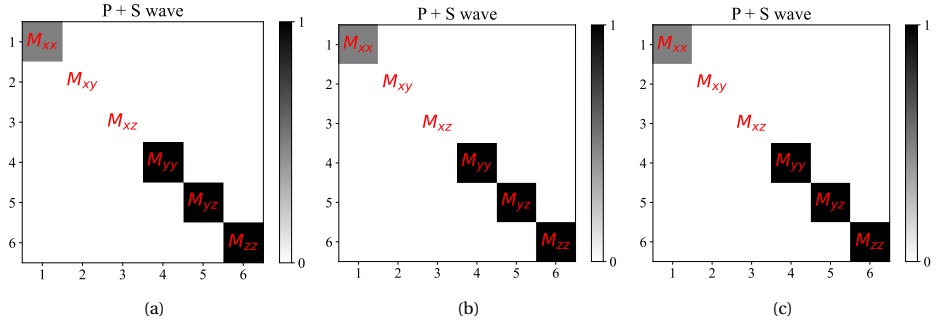


Figure 6.20: Sensitivity of the resolvability to the azimuth uncertainty (within 5°). (a) Error $\Delta\theta = 0°$, (b) Error $\Delta\theta = 2.5°$, and (c) Error $\Delta\theta = 5°$. The epicentral distance is 40 m with source to receiver azimuth of 90°. The borehole diameter is 0.36 m.

decreases. However, the dual-cable DAS configuration can guarantee the resolvability of the non-Double-Couple (non-DC) components (i.e. M_{xx}, M_{yy}, M_{zz}) even with an epicentral distance up to 20 m. In addition, as is shown in Fig. 6.19,when the epicentral distance increases to 40 m, more components become non-resolvable, including M_{xx}. The non-DC components determine the tensile failure of the events, therefore crucial for the application of monitoring micro-seismic events induced by reinjection/stimulation operations, during which tensile cracking events are most likely to happen in the near-borehole area. Therefore, installing a dual-cable DAS configuration can be concluded to provide valuable information.

6.5. DISCUSSION

The dual-cable DAS configuration proposed in this work has the potential to fully locate near-borehole rock failures, although at certain conditions (e.g. low S/N or azimuth close to 0°, i.e. aligned to the two cables) the accuracy decreases Yet, the accuracy under these conditions can be improved by an additional constraints from either surface receivers or a third DAS cable in the well. In addition, advanced arrival-picking techniques (for determining depth and epicentral distance, see section 6.3.2) and noise suppressing techniques can improve the localisation accuracy. The localisation method with the dual-cable DAS configuration is shown to be valid for a source with centre frequency from 50 Hz to 200 Hz, which, from literature, is commonly the dominant range of micro-seismic events induced during reinjection or small-scale stimulation operations. Compared to the case of only a single DAS cable, the additional constraint of the azimuth, due to the installation of the dual-cable DAS, can therefore provide valuable information on the in-situ stress state, the stress rotation and fracture propagation during operations. The full constraint on the location is also necessary to invert for the moment tensor to better understand the source mechanisms.

To construct the resolution matrix, the semi-analytical semi-numerical solution from CPS was used. This allows us to study inhomogeneous and anisotropic horizontally layered media, although our study is limited to homogenous and isotropic media in this paper for simplicity. The analysis of the moment-tensor resolvability shows that the installation

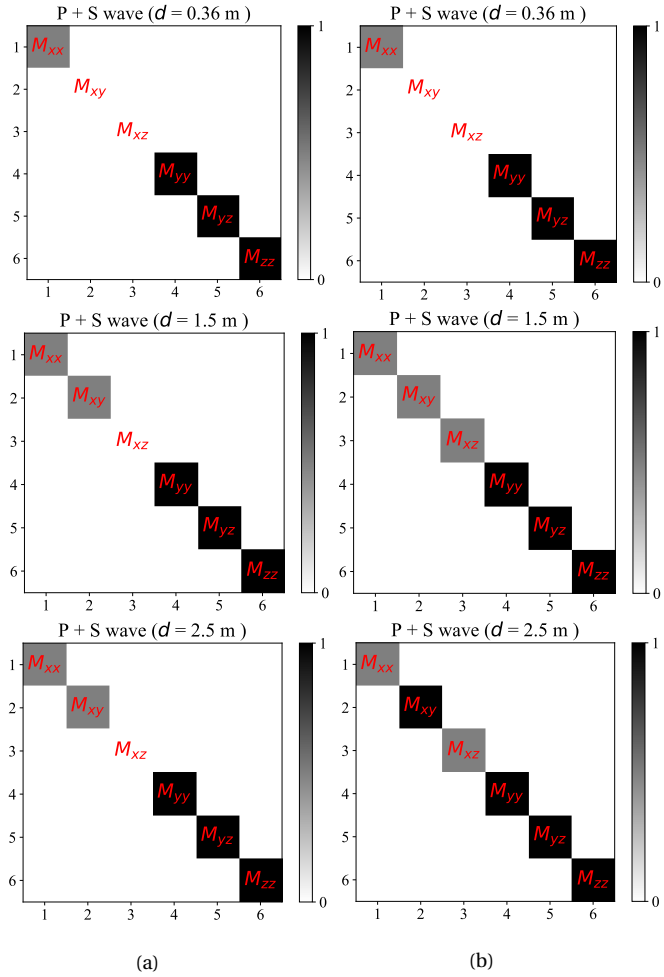


Figure 6.21: Comparison of resolution matrix from (a) one DAS cable, and (b) dual DAS cables for different borehole diameters of 0.36 (top row), 1.5 (middle row) and 2.5 m(bottom row), assuming an epicentral distance of 40 m and source-borehole azimuth of 90°.

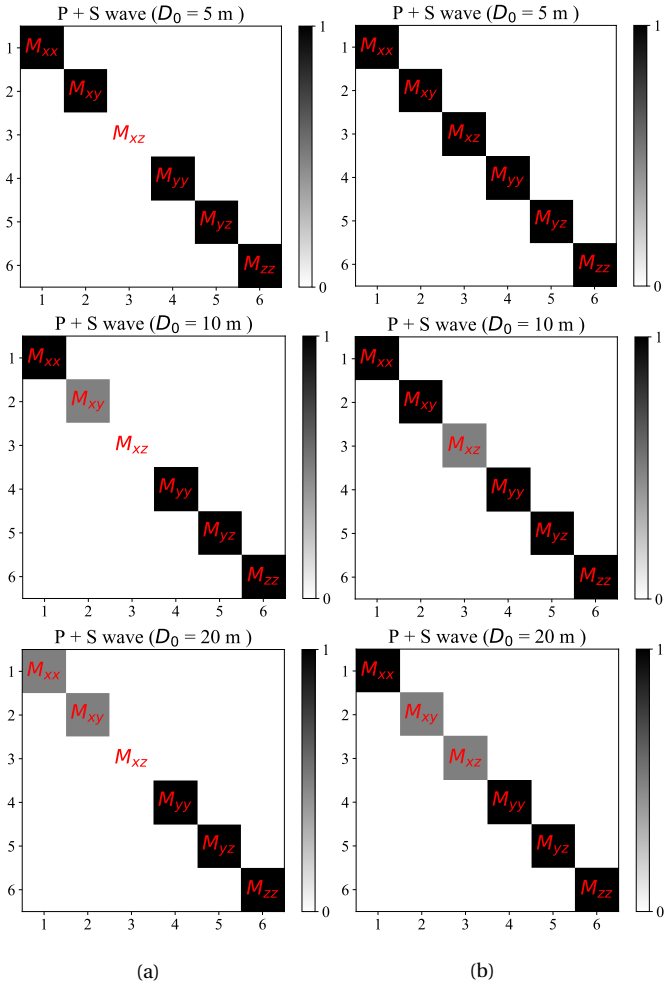


Figure 6.22: Comparison of resolution matrix from one and two DAS cables with different epicentral distances, assuming a borehole diameter of 0.36 m. Left column (a) one DAS cable, right column (b) two DAS cables.

of a dual-cable can help us to constrain the non-DC moment tensor components M_{xx}, M_{yy} and M_{zz} with an epicentral distance of, in this study, up to 20 m from the borehole. In contrast, for the DC components, M_{xy} and M_{xz} cannot be resolved with robust resolution with increasing epicentral distance while M_{yz} can be constrained even with an epicentral distance of 40 m. As mentioned early, the non-DC components indicate tensile failures while DC components indicate pure shear failures. Previous studies have shown non-DC components are related to the formation of hydraulic fractures (Šílený *et al.*, 2009), while DC components are linked to re-activation and development of natural fractures in shear mode (Sasaki, 1998). During hydraulic stimulation of homogeneous and non-fractured reservoirs, tensile failures dominate the micro-seismic response (Hampton *et al.*, 2018; Baird *et al.*, 2020; Tanaka *et al.*, 2021; Butt *et al.*, 2024).

To demonstrate the ability to monitor a stimulation campaign, a 2-D geo-mechanical simulation (assuming vertical fracture under normal-faulting environment) of thermal stimulation is performed to predict the tensile fractures in the near-borehole region. These fractures are then described by a moment tensor, which, based on the resolvability analysis, gives information about its resolvability via the dual-cable DAS. The moment tensors are then decomposed into elementary tensors to facilitate the interpretation. The following discussion focuses on tensile fractures, while the same procedure works also for shear fracture, which is not discussed here.

The problem of the thermal stimulation, together with the numerical model and input data, is presented in 5. The simulation result is presented in Fig. 6.23a (same result as Fig. 5.9c), showing three main fractures induced around the borehole at the end of the simulation (t = 120 h). Fracture B is propagating in the direction of the maximum intial stress σ_H, while fractures A and C propagate in the directions -45° and 45^circ deviated from fracture B respectively. With the fracture propagation, micro-seismicity will be continuously generated (Butt *et al.*, 2024). The micro-seismicity generated by the propagation of the induced main fractures A, B and C in Fig. 6.23a can therefore be described by the following moment tensor:

$$\mathbf{M}_A = \frac{1}{2} M_0 \begin{bmatrix} 1 & 1 & 0 \\ 1 & 1 & 0 \\ 0 & 0 & 0 \end{bmatrix} \quad \mathbf{M}_B = M_0 \begin{bmatrix} 1 & 0 & 0 \\ 0 & 0 & 0 \\ 0 & 0 & 0 \end{bmatrix} \quad \mathbf{M}_C = \frac{1}{2} M_0 \begin{bmatrix} 1 & -1 & 0 \\ -1 & 1 & 0 \\ 0 & 0 & 0 \end{bmatrix} \tag{6.9}$$

where M_0 [N·m] is the seismic moment, which is a quantitative measure of the amount of energy released in an seismic event, of the micro-seismicity resulted from the fracture opening. It is assumed that all the energy released due to the tensile fracture is transferred to seismic energy. Therefore, the seismic moment M_0 can be calculated from the specific fracture energy.

As is discussed earlier in relation to Fig. 6.22, the non-DC components M_{xx} and M_{yy} can be resolved at 20 m away from the borehole using the dual-cable DAS in a single vertical well, while M_{xy} can only be resolved at distances of 10 m or less. Therefore, only the initiation and propagation of fracture B can be well monitored and understood at a distance further than 20 m. The initiation and source mechanisms of fractures A and C can only be understood if they happen within 10 m, i.e. indicating a process of multiple fractures. The moment tensor can be decomposed into three elementary tensors, i.e. ISO, DC, and CLVD (Vavryčuk, 2015), and be represented in Hudson's source–type plot. The

details of the decomposition is presented in D. The decomposition of the moment tensors of three micro-seismic events resulted from the propagation of the three tensile fractures during the thermal stimulation is depicted in Hudson's source-type plot as is shown in Fig. 6.23b. The three tensile fractures contain the same portion of CLVD + and Explosion components, regardless of their different fracture directions. The results imply that the near-borehole tensile fractures induced during either geothermal operations or thermal stimulation can be characterised using the dual-cable DAS in a single vertical well, with the direction of fracture well resolved. However, the identification of the full moment tensor, which identifies the type of fracture (and therefore connecting to the changes in permeability) depends on the epicentral distance orientation of the two DAS cables. Several components of the moment can however be identified, and knowledge of the initial in-situ stresses and stress path imposed could be sufficient to estimate the moment tensor. Placing the two DAS cables aligned with the the direction of the maximum in-situ stress is the most advantageous choice, since it improves the focal coverage, and is shown to be able to identify tensile fractures.

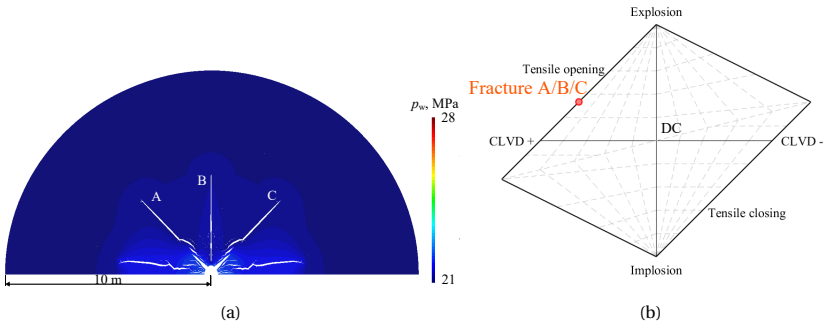


Figure 6.23: (a) Tensile fractures are induced in the near-borehole region to connect the borehole to the undamaged zone, and (b) the positions of the corresponding genrated micro-seismic events on the Hudson's source-type plot.

Although the above numerical results show the promising feasibility of the dual-cable DAS, its practical application to micro-seismic monitoring depends on several more practical considerations, including the minimum borehole diameter, the coupling between the cables and the formation, and the exact channel locations. In the above discussion, the borehole diameter is assumed to be 0.36 m. Yet, for deep geothermal wells, the diameter can be smaller. Numerically, there is hardly a minimum borehole diameter since the difference between the two cables can always be captured numerically; then, the numerical noise is the main factor. However, for field data, the minimum borehole diameter depends on their quality, namely the accuracy in retrieving full wave forms, the frequency band in which the desired signal is above the noise and the epicentral distance of the source. The difference in signals may not be well captured if the recorded frequencies are much lower (e.g. several Hz) due to the low-frequency characteristics of the source or if the epicentral distance is larger (e.g. hundreds of meters) such that the signals can severely attenuate. In addition, the coupling between the cables and the formation always has an impact on the data quality. Therefore, the dual-cable DAS is

suggested to be used with the cable being installed behind the casing to optimize the data quality. Moreover, in the above discussion, we assumed that the channels on both cables are at the same depth. However, for field data, this will often not be the case. The exact channel locations could introduce more difference between the two channels that are used to localise the source and could result in a larger $\Delta\theta$. Therefore, a calibration of the channel locations is suggested before any analysis can be done.

6.6. CONCLUSION

In this work, the configuration of a dual DAS cable in a single vertical well is proposed to provide constraints on source location and moment tensor that are additional to the case of a single DAS cable. The configuration consists of two DAS cables at opposite sides in one single vertical well. Synthetic signals are generated using an open-source code that assumes plane-layered media. A localisation method is introduced and demonstrated with a reference case to show the feasibility of using the difference in the signals of two DAS cables to determine source depth, epicentral distance and azimuth. Sensitivity analysis shows that a low S/N and azimuth close to 0° can lead to decreasing localisation accuracy, while the accuracy of the method is not sensitive to frequencies varying from 50 Hz to 200 Hz. In addition, the resolvability of the moment tensor is analysed, and results suggest non-DC components M_{xx}, M_{yy} and M_{zz} can be reliably resolved if the source epicentral distance is within 20 meters, showing improvement on the case of only one DAS cable in a well. Resolvability of the DC components M_{xy} and M_{xz} are more sensitive to large distances, since near- and intermediate-terms play an essential role to constrain additional components.

The two DAS cables within one well are optimally positioned in the direction of minimal horizontal stresses in normal-faulting geological condition. Geo-mechanical simulation shows tensile fractures can be induced in a homogeneous and non-fractured reservoir during thermal stimulation. The propagation of the main tensile fracture in the direction of maximum initial stress σ_H that happens within 20 m can be well monitored and understood, while the understanding of the tensile fracture branching in other directions relies on the resolvability of the moment tensor component M_{xy}. The results demonstrate that a single-well dual-cable configuration has the potential for monitoring and understanding near-borehole micro-seismic events induced during geothermal reinjection and stimulation operations.

7

CONCLUSIONS AND RECOMMENDATIONS

7.1. CONCLUSIONS

Near-borehole fracturing, a result of near-borehole coupled processes, is believed to be a major contributor to maintain or improve the re-injection performance in geothermal operations. Understanding the fracturing processes is therefore of great significance for both re-injection and stimulation operations. This thesis presents a geo-mechanical tool to simulate the coupled processes and a proposal of a dual-cable DAS installed downhole in the injection well to monitor the fracturing. The developed geo-mechanical tool is then used to perform simulations on stimulation scenarios for a synthetic clogged reservoir. The feasibility of using the single-well dual-cable DAS is examined based on synthetic signals. The main conclusions of this thesis are summarised in the following.

7.1.1. A NUMERICAL TOOL TO STUDY NEAR-BOREHOLE CYCLIC AND COUPLED THM PROCESSES

A method is developed to simulate fracturing processes under geothermal conditions using the cohesive zone model considering full THM couplings. Possible discontinuities are represented by zero-thickness triple-nodded interface elements, which allow solid elements to separate with mechanical damage and the simulation of longitudinal and transversal fluid/heat flow in the discontinuity. The cubic law is used to update the fracture transmissivity as a function of its aperture, while a elasto-damage law to characterise the mechanical response of the discontinuity. The nature of the interface element, i.e. triple-nodded with node-to-node contact approach, assure the flexible applications of the interface element, where an explicit representation of the mid-plane pressure and temperature is convenient, with pre-determined contact faces. This feature makes it possible to model fracture initiation and propagation from highly-permeable intact rock under coupled THM processes. The modelling approach is to insert interface elements in-between all the continuum elements that represent the intact rock, while assigning high stiffnesses and transversal hydraulic coefficients to the interface elements to reduce the artificial compliance / conductivity.

Since high heat convection (Péclet > 1) can lead to numerical divergence, a stabilisation technique is implemented. The method is then verified against a thermo-hydraulic problem and a hydro-mechanical problem, of which analytic solutions exist. The verification shows that the numerical solutions match well with the analytical solutions, illustrating the correctness of the numerical scheme. In addition, the method is validated against a thermal fracturing experiment, and the numerical result shows a good agreement with the experimental result, demonstrating that the model is capable of simulating the THM processes, and, in particular, cracking around a wellbore impacting the inflow ability during and after the cold water injection.

In order to study the cyclic thermal stimulation scheme, in which fatigue damage plays a key role, a new elasto-damage law is developed by incorporating a fatigue damage variable into the tensile branch of the conventional law. The fatigue damage variable is calibrated using the S-N curve. With this formulation, the tensile strength and stiffness of the interface element degrade with increasing cycle number. In addition, the Palmgren-Miner's rule is used to account for varying-amplitude cyclic loading. The proposed model is then validated against three experiments from literature with different THM coupling, including cyclic Brazilian test, cyclic hydraulic fracturing test and cyclic thermo-hydraulic

fracturing test. All three validation results show the fatigue damage due to cyclic loading or reduced breakdown pressure due to cyclic injection/cyclic cooling-heating treatment can be well reproduced. The ability of the method to handle varying-amplitude cyclic loading is also demonstrated by the simulation of a synthetic cyclic loading based on the Brazilian test. The validations confirm that the method can be used in simulations to support the design of cyclic thermal stimulation strategies for geothermal projects.

7.1.2. PERFORMANCE OF DIFFERENT STIMULATION SCHEMES

Maintaining the injectivity is challenging but necessary for the long-term successful re-injection operations, therefore also for the whole geothermal projects. However, injectivity decline has been long reported, particularly in sandstone reservoirs, which are the main contributor to Dutch geothermal energy sector. Inspired by the TU Delft campus geothermal project and surrounding regional experience, a synthetic sedimentary reservoir is used, i.e. it is assumed to be homogeneous and non-fractured, and have typical Delft Sandstone Formation reservoir properties.

The previously developed tool is first used to examine the effect of injection temperature on the well performance under normal operation (i.e. no clogging happens). Thermo-hydro-mechanical (THM) simulations of cold-water injection into the unclogged reservoir indicate that reducing the injection temperature significantly impacts well performance. In particular, when the injection temperature is lowered to 293 K, new fractures can be induced around the borehole, increasing the risk of sandstone production.

For a clogged reservoir, THM simulations of various stimulation strategies - monotonic, stepwise, cyclic, and stepwise combined with cyclic - demonstrate that stepwise stimulation yields generally the most favourable outcomes. Specifically, it enables the lowest peak pressure with the maximum injection rate at $Q_{\text{inj}} = 216$ m^3/h and $\Delta T = 40$ K, compared with corresponding monotonic, cyclic, and stepwise combined with cyclic stimulation. And the long-term injection pressures after stepwise stimulation is lower than those observed in the monotonic, cyclic or stepwise combined with cases. Cyclic-temperature stimulation (within the bounds of the scenarios considered here) is generally neither better or worse than monotonic stimulation, but has slightly different characteristics. Monotonic injection creates a larger single fracture which breaks through the clogged zone, whereas thermal cycles create more local damage controlled by the period of the cyclic injection. Conversely, cyclic-injection-rate stimulation slightly underperform (under higher injection rate) or slightly outperforms (under lower injection rate) the monotonic stimulation, with fatigue effect playing a negligible role. A combined approach incorporating both cyclic and stepwise strategies may offer enhanced stimulation performance compared to monotonic stimulation, but is inferior than stepwise stimulation alone.

7.1.3. FEASIBILITY OF THE DUAL-CABLE DAS IN A SINGLE VERTICAL WELL

A dual-cable DAS configuration in a single vertical well is proposed to provide constraints on source location and moment tensor that are additional to the case of a single DAS cable. A synthetic study is performed to show its feasibility and advantages. Synthetic signals are generated using an open-source code, CPS, that assumes plane-layered media. A localisation method is introduced and demonstrated with a reference case to show

the feasibility of using the signals and the difference in the signals of two DAS cables to determine source depth, epicentral distance and azimuth. Sensitivity analysis shows that a low S/N and/or source-to-receiver azimuth close to 0° can lead to decreasing localisation accuracy, while the accuracy is not sensitive to frequency varying from 50 Hz and 200 Hz.

In addition, the resolvability of the moment tensor is analysed, and results suggest non-DC components M_{xx}, M_{yy} and M_{zz} can be reliably resolved if the source epicentral distance is within 20 meters, showing improvement on the case of only one DAS cable in a well. Resolvability of the DC components M_{xy} and M_{xz} relies more on the near- and intermediate-field terms, therefore restricted in 5 m - 10 m, though also showing improvement compared to the case of only one DAS cable.

The two DAS cables within one well are optimally positioned in the direction of minimal horizontal stresses in a normal-faulting geological setting. Geo-mechanical simulation shows tensile fractures can be induced in a homogeneous and non-fractured reservoir during thermal stimulation. The propagation of the main tensile fracture in the direction of maximum initial stress σ_H that happens within 20 m can be well monitored and understood, while the understanding of the tensile fracture branching in other directions relies on the resolvability of the moment tensor component M_{xy}. The results demonstrate that a single-well dual-cable configuration has the potential for monitoring and understanding near-borehole micro-seismic events induced during geothermal reinjection and stimulation operations.

The results demonstrate that a single-well dual-cable configuration has the potential for monitoring and understanding near-borehole micro-seismic events induced during geothermal reinjection and stimulation operations. Yet, practical issues need to considered. Installing the cable outside of the casing can improve the data quality and therefore improve the applicability of this single-well duall cable DAS. Since the minimum diameter size depends on the data quality, source frequency and epicentral distance, the effectiveness of the single-well dual-cable DAS can be influenced for deep geothermal wells. Yet, many existing geothermal systems come as a doublet that includes two closely located wells. Therefore, installing the two cables separately in the geothermal doublet can be an alternative option, therefore has better focal coverage. In addition, calibration of the exact channel location is suggested before any analysis to improve the localisation accuracy of the proposed method.

7.2. LIMITATIONS AND FUTURE RECOMMENDATIONS

This thesis focuses on the near-borehole fracturing processes under cyclic and coupled THM processes and proposes a single-well dual-cable DAS configuration to monitor and understand the near-borehole cracking events. The proposed method to simulate complex coupled processes with discontinuities, especially modelling of the THM processes in highly-permeable intact rock with interface elements inserted in-between all the continuum elements to provide potential cracking paths, provides valuable tool to study geothermal operations, including re-injection and soft stimulation. The tool also has several other potential applications beyond geothermal reservoirs, including but not limited to optimising other geo-energy processes, e.g. hydrogen or carbon dioxide storage where soft stimulation technologies may be needed and coupled processes in

radioactive waste repository. Specifically, the study of the cyclic thermal stimulation, which requires methods similar to those developed here, gives valuable information for the design and optimisation of the novel soft stimulation technology that has rarely been reported and studied. Moreover, the proposed single-well dual-cable DAS provides a new possibility of installing DAS in a single well to fully localise and understand near-borehole micro-seismic events, and the work in this thesis confirms its feasibility. Yet, limitations still exist and future research is needed to further strengthen the conclusions.

7.2.1. NUMERICAL METHODS FOR COUPLED THM PROCESSES WITH DISCONTINUOUS PROBLEMS

In Chapter 5, the synthetic reservoir is assumed to be homogeneous. However, many reservoirs have strong heterogeneity, with the Delft Sandstone Formation being an example (Vardon *et al.*, 2024). The consideration of heterogeneity is not difficult to be introduced into the current model, however, it has not been considered in this work. One reason is the computational cost of the coupled THM model, which can require several hours to several weeks of computation and the impact of heterogeneity usually requires running ensembles of models. Therefore, more advanced algorithm or method to speed up the simulation is needed.

In addition, the calibration of the reservoir properties needs more research. History matching has been widely used in the field to calibrate the hydraulic properties, e.g. permeability. However, calibrating subsurface geo-mechanical properties, e.g. rock strengths and in-situ stress, is more challenging. Micro-seismic data provides valuable information of the rock failures, therefore the geo-mechanical properties, in the subsurface. Thus, using the micro-seismic data to calibrate the subsurface geo-mechanical properties is an important research topic to help manage the geothermal reservoirs.

Moreover, this thesis presents a stress-based method (i.e. counting the S-N curve) to measure the fatigue damage in the new elasto-damage law. Yet, limitation exists for current method to determine the fatigue damage variable D_f. For every different cyclic loading scenarios (except for the varying amplitude that has been considered in current model), e.g. different frequency or mean amplitude of the loading, experiments need to be conducted first to get enough data to obtain the S-N relation. This results in a substantial amount of laboratory work for even same types of rock or reservoir. Future efforts can be paid in formulating the fatigue damage variable as a function of the cumulative total strain energy (Branco *et al.*, 2022). In that way, the fatigue damage can be determined independent from the loading scenarios and without counting the cycle numbers. However, difficulty is expected in obtaining experimental data of the stress-strain curve under cyclic tensile loading (e.g. cyclic hydraulic fracturing test), which is needed to determine the cumulative total strain energy at tensile failure.

7.2.2. STIMULATION STRATEGY FOR GEOTHERMAL RESERVOIRS

This thesis numerically investigates the stimulation strategy based on a synthetic sedimentary reservoir considering fully coupled THM processes. The results suggest that stepwise stimulation strategy is a good strategy, and is superior than a combination of cyclic-injection-rate and stepwise stimulation. Therefore, cyclic stimulation is not suggested for highly permeable reservoirs with partly clogged zone. In contrast, stepwise

stimulation is more suitable for these reservoirs.

This conclusion has only been established for reservoirs with considerable permeability. For low or non-permeable reservoirs, e.g. for hot dry rock projects, this can be different. As is reported in Hofmann *et al.* (2019), field cyclic stimulation to a fractured granodiorite reservoir shows clear advantages in reducing the stimulation pressure and induced micro-seismicity. However, the underlying mechanisms are not yet clear. Whether the fatigue effects play a dominant role or not needs further evidence. Therefore, more simulations or field tests on the comparison of cyclic and stepwise stimulation to low-permeability reservoirs need to be performed to investigate the controlling factors.

7.2.3. MICRO-SEISMIC MONITORING USING DAS

Initial analysis in this thesis demonstrates the feasibility of using the single-well dual-cable DAS to fully localise and understand the near-borehole micro-seismic events. Yet, some limitations exist in the curret proposal and more research is needed to further confirm the practical efficacy of this DAS configuration.

Due the one-dimension nature of the DAS measurement, the signals at/close to the broadside channel are null/weak. Consequently, localisation based on these channels are largely influenced by the noise and can lead to significant error. Therefore, additional measurements of signals at and near the broadside channels are needed. Installation of downhole geophones or the use of helically wound fibres can be a possible solution.

In addition, as is mentioned in 6.3, with current method, two possible solutions for the azimuth exist. This issue can be resolved by installing a third cable in the well or by utilising the signal attenuation due to the presence of fluid in the wellbore. Yet, it is not studied in this thesis. Further investigations are therefore needed to study the determination of the unique azimuth employing a third fibre or utilising the signal attenuation.

In addition, the resolvability analysis has demonstrated the feasibility to resolve moment tensor components using the single-well dual-cable DAS. A next step is to perform moment-tensor inversion based on the single-well dual-cable DAS. Moreover, the moment-tensor inversion can be investigated and how this would be influenced by noise level and source frequency.

So far, all the discussions are based on the synthetic signals, assuming homogeneous and isotropic media. The localisation and source inversion for sources in heterogenous and anisotropic reservoir are more complicated but doable since such methods are well-known in the seismology community. Therefore, future works on the localisation and source mechanism inversion using the single-well dual-cable DAS in complex reservoirs is needed, preferable using synthetic signals first. After the feasibility study, field tests are needed to confirm the practical efficacy of the proposed DAS configuration.

A

FINITE ELEMENT PROCEDURE

A

Finite element formulations are derived from a weak form formulation of the equilibrium equations (Cerfontaine *et al.*, 2015), which addresses the boundary-value problems over global domains. In LAGAMINE, the weak form is obtained based on the principle of virtual work and measured in current configuration (i.e. updated Lagrangian formulation). Compared to classical solid mechanics, contact problems need to further take into account the contributions of the interface elements as additional non-classical boundary conditions. Thus, in this section, classical boundary conditions are firstly introduced, on the basis of which the weak form considering the contact problem is presented. Thereafter, the discretisation of the domain and the local isoparametric coordinates are introduced, followed by an introduction to the global solution scheme.

A.1. INITIAL AND BOUNDARY CONDITIONS

A numerical model is a closed system. Therefore, initial and boundary conditions are required to close the governing equations mentioned above. The initial condition describes the state of all the degrees of freedom on the entire domain ($\mathscr{B}^1$ and $\mathscr{B}^2$, shown in Fig.A.1) at $t = t_0$:

$$\boldsymbol{x} = \boldsymbol{x}_0, \quad p_\mathrm{w} = p_{\mathrm{w}0}, \quad T = T_0 \tag{A.1}$$

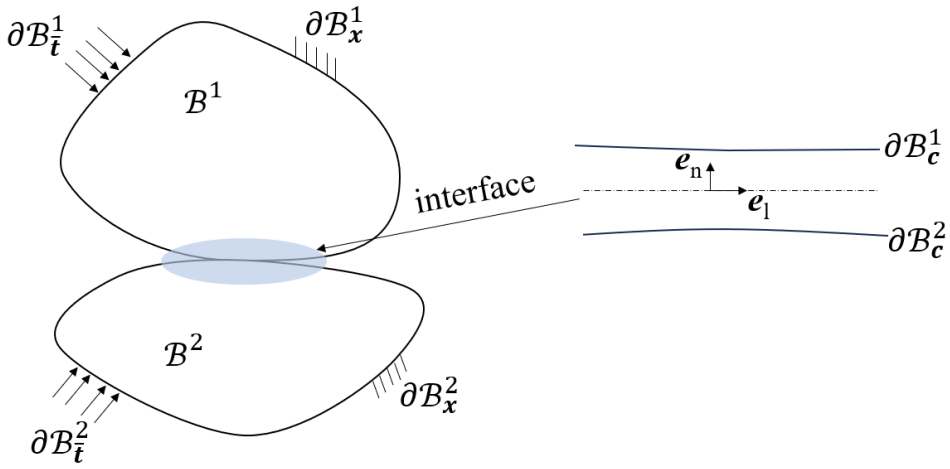


Figure A.1: Two bodies subjected to classical and contact constraints, modified from (Dieudonné, 2016). $\partial\mathscr{B}^i_{\boldsymbol{x}}$ is the generalised imposed displacement and $\partial\mathscr{B}^i_{\bar{\boldsymbol{t}}}$ is the generalised imposed traction. $\partial\mathscr{B}^i_c$ is the contact boundary.

At all time of interest, $t \geqq t_0$, classical boundary conditions should be defined on the reference boundary $\partial\mathscr{B}^i$ of the body $\mathscr{B}^i$. The classical boundary conditions include Dirichlet and Neumann conditions. The mechanical, hydraulic and thermal Dirichlet boundary condition can be expressed respectively as:

$$\boldsymbol{x} = \bar{\boldsymbol{x}} \quad \text{on} \quad \partial\mathscr{B}^i_{\bar{x}}, \quad p_\mathrm{w} = \bar{p}_\mathrm{w} \quad \text{on} \quad \partial\mathscr{B}^i_{\bar{p}_\mathrm{w}}, \quad T = \bar{T} \quad \text{on} \quad \partial\mathscr{B}^i_{\bar{T}} \tag{A.2}$$

where, $\bar{\boldsymbol{x}}$, $\bar{p}_{\mathrm{w}}$ and $\bar{T}$ are the imposed degrees of freedom. $\partial\mathscr{B}^i_{\bar{\boldsymbol{x}}}$, $\partial\mathscr{B}^i_{\bar{p}_{\mathrm{w}}}$ and $\partial\mathscr{B}^i_{\bar{T}}$ are the corresponding Dirichlet boundaries of the ith body, shown in Fig. A.1.

The corresponding Neumann conditions can be expressed as:

$$\bar{\boldsymbol{T}} = \boldsymbol{N}\cdot\boldsymbol{\sigma} \quad \text{on} \quad \partial\mathscr{B}^i_{\bar{t}} \tag{A.3}$$

$$\boldsymbol{N}\cdot\boldsymbol{q}^{\mathrm{w}}\mathrm{w} + \bar{q}^{\mathrm{w}} = 0 \quad \text{on} \quad \partial\mathscr{B}^i_{\bar{q}^{\mathrm{w}}} \tag{A.4}$$

$$\boldsymbol{N}\cdot\boldsymbol{q}^{\mathrm{T}} + \bar{q}^{\mathrm{T}} = 0 \quad \text{on} \quad \partial\mathscr{B}^i_{\bar{q}^{\mathrm{T}}} \tag{A.5}$$

where, $\bar{\boldsymbol{T}}$ is the imposed traction, $\bar{q}^{\mathrm{w}}$ and $\bar{q}^{\mathrm{T}}$ the imposed water and heat fluxes (positive if incoming). $\boldsymbol{N}$ is the unit vector normal to $\partial\mathscr{B}^i$. $\boldsymbol{\sigma}$, $\boldsymbol{q}^{\mathrm{w}}$ and $\boldsymbol{q}^{\mathrm{T}}$ are the total Cauchy stress, water and heat flux respectively.

A.2. WEAK FORM

According to the principle of virtual work, for any kinematically admissible virtual velocity field $\delta\dot{\boldsymbol{x}}$, equilibrium can be reached if the internal virtual power $\delta\dot{W}_{\mathrm{I}}$ is equal to the external virtual power $\delta\dot{W}_{\mathrm{E}}$ (Dieudonné, 2016). For contact problem, it is nothing but a classical continuum mechanical problems with an additional contact constraint (Cerfontaine *et al.*, 2015). The weak form of the finite element formulations for continuum elements can be found in (Cerfontaine *et al.*, 2015; Dieudonné, 2016). To further take into account the contact constraints, additional contributions from the interface element shall be added into the external and/or internal virtual power, which finally leads to the weak form of the mechanical formulation (measured in current configuration) :

$$\underbrace{\sum_{i=1}^{2}\int_{\mathscr{B}^i}[\nabla(\delta\dot{\boldsymbol{x}})]^{\mathrm{T}}\cdot\boldsymbol{\sigma}\,\mathrm{d}\Omega}_{\delta\dot{W}_{\mathrm{I,\,m}}} = \underbrace{\sum_{i=1}^{2}\left[\int_{\mathscr{B}^i}(\delta\dot{\boldsymbol{x}})^{\mathrm{T}}\cdot\boldsymbol{b}\,\mathrm{d}\Omega + \int_{\mathscr{B}^i_{\bar{t}}}(\delta\dot{\boldsymbol{x}})^{\mathrm{T}}\cdot\bar{\boldsymbol{T}}\,d\Gamma\right]}_{\delta\dot{W}_{\mathrm{E,\,m}}} + \delta\dot{W}^{\mathrm{c}}_{\mathrm{E,\,m}} \tag{A.6}$$

where, $\boldsymbol{b}$ is the body force, $\bar{\boldsymbol{T}}$ the imposed traction on boundary $\partial\mathscr{B}^i_{\bar{t}}$. $\delta\dot{W}_{\mathrm{I,\,m}}$ and $\delta\dot{W}_{\mathrm{E,\,m}}$ are the internal and external mechanical virtual power repsectively, and $\delta\dot{W}^{\mathrm{c}}_{\mathrm{E,\,m}}$ is the contribution of the contact constraint to external virtual power. According to (Liaudat *et al.*, 2023), it reads:

$$\delta\dot{W}^{\mathrm{c}}_{\mathrm{E,\,m}} = -\int_{lmp}(\delta r)^{\mathrm{T}}\boldsymbol{\sigma}_{\mathrm{c}}\,dl \tag{A.7}$$

where, δr is the virtual relative displacement vector within the interface element (Liaudat *et al.*, 2023), the minus sign before the right-hand term is because the virtual relative displacement is computed from the top to the bottom.

Similarly, the weak forms for hydraulic and thermal formulations can be obtained by considering an admissible virtual pressure field $\delta\dot{p}_{\mathrm{w}}$ and an admissible virtual temperature field $\delta\dot{T}$:

A

$$\underbrace{\sum_{i=1}^{2}\int_{\mathscr{B}^i}\left[\delta\dot{p}_{\mathrm{w}}\dot{S}-[\nabla(\delta\dot{p}_{\mathrm{w}})]^{\mathrm{T}}\cdot\boldsymbol{q}^{\mathrm{w}}w\right]\mathrm{d}\Omega}_{\delta\dot{W}_{\mathrm{I,f}}}+\delta\dot{W}^{\mathrm{c}}_{\mathrm{I,f}}=$$
$$\underbrace{\sum_{i=1}^{2}\left[\int_{\mathscr{B}^i}\delta\dot{p}_{\mathrm{w}}\cdot Q_{\mathrm{w}}\mathrm{d}\Omega+\int_{\mathscr{B}^i_{\bar{q}^{\mathrm{w}}}}\delta\dot{p}_{\mathrm{w}}\bar{q}^{\mathrm{w}}d\Gamma\right]}_{\delta\dot{W}_{\mathrm{E,f}}}+\delta\dot{W}^{\mathrm{c}}_{\mathrm{E,f}} \tag{A.8}$$

$$\underbrace{\sum_{i=1}^{2}\int_{\mathscr{B}^i}\left[\delta\dot{T}\dot{S}_{\mathrm{T}}-[\nabla(\delta\dot{T})]^{\mathrm{T}}\cdot\boldsymbol{q}^{\mathrm{T}}\right]\mathrm{d}\Omega}_{\delta\dot{W}_{\mathrm{I,T}}}+\delta\dot{W}^{\mathrm{c}}_{\mathrm{I,T}}=$$
$$\underbrace{\sum_{i=1}^{2}\left[\int_{\mathscr{B}^i}\delta\dot{T}\cdot Q_{\mathrm{T}}\mathrm{d}\Omega+\int_{\mathscr{B}^i_{\bar{q}^{\mathrm{T}}}}\delta\dot{T}\bar{q}^{\mathrm{T}}d\Gamma\right]}_{\delta\dot{W}_{\mathrm{E,T}}}+\delta\dot{W}^{\mathrm{c}}_{\mathrm{E,T}} \tag{A.9}$$

where, Q_{w} and Q_{T} are the water and heat source terms, $\bar{q}^{\mathrm{w}}$ and $\bar{q}^{\mathrm{T}}$ are the imposed water and heat fluxes on boundary $\partial\mathscr{B}^i_{\bar{q}^{\mathrm{w}}}$ and $\partial\mathscr{B}^i_{\bar{q}^{\mathrm{T}}}$ respectively. $\delta\dot{W}_{\mathrm{I,f}}/\delta\dot{W}_{\mathrm{I,T}}$ and $\delta\dot{W}_{\mathrm{E,f}}/\delta\dot{W}_{\mathrm{E,T}}$ are the internal and external hydraulic/thermal virtual power respectively, and $\delta\dot{W}^{\mathrm{c}}_{I,f}/\delta\dot{W}^{\mathrm{c}}_{\mathrm{I,T}}$ and $\delta\dot{W}^{\mathrm{c}}_{\mathrm{E,f}}/\delta\dot{W}^{\mathrm{c}}_{\mathrm{E,T}}$ are the contribution of the interface to internal and external hydraulic/thermal virtual power.

The contribution of the interface to internal hydraulic and thermal virtual powers read:

$$\delta\dot{W}^{\mathrm{c}}_{\mathrm{I,f}}=\int_{lmp}\delta p^{\mathrm{m}}_{\mathrm{w}}Q^{\mathrm{s}}_{\mathrm{w}}dl-\int_{lmp}\frac{\partial\delta p^{\mathrm{m}}_{\mathrm{w}}}{\partial l}Q^{\mathrm{l}}_{\mathrm{w}}dl \tag{A.10}$$

$$\delta\dot{W}^{\mathrm{c}}_{\mathrm{I,T}}=\int_{lmp}\delta T^{\mathrm{m}}Q^{\mathrm{s}}_{\mathrm{T}}dl-\int_{lmp}\frac{\partial\delta T^{\mathrm{m}}}{\partial l}Q^{\mathrm{l}}_{\mathrm{T}}dl \tag{A.11}$$

where, $\delta p^{\mathrm{m}}_{\mathrm{w}}$ and δT^{m} are the virtual pressure and temperature fields at the mid-plane of the interface element.

In contrast, the contribution of the interface to external hydraulic and thermal virtual powers come from the bottom and top faces of the interface element, if considering null source terms inside the interface. Therefore, they can be expressed as:

$$\delta\dot{W}^{\mathrm{c}}_{\mathrm{E,f}}=\int_{lmp}\delta\check{p}^{\mathrm{b}}_{\mathrm{w}}Q^{\mathrm{b}}_{\mathrm{w}}dl+\int_{lmp}\delta\check{p}^{\mathrm{T}}_{\mathrm{w}}Q^{\mathrm{T}}_{\mathrm{w}}dl \tag{A.12}$$

$$\delta\dot{W}^{\mathrm{c}}_{\mathrm{E,T}}=\int_{lmp}\delta\check{T}^{\mathrm{b}}Q^{\mathrm{b}}_{\mathrm{T}}dl+\int_{lmp}\delta\check{T}^{\mathrm{T}}Q^{\mathrm{T}}_{\mathrm{T}}dl \tag{A.13}$$

where, $\delta\check{p}^{\mathrm{b/t}}_{\mathrm{w}}$ and $\delta\check{T}^{\mathrm{b/t}}$ are the virtual pressure jumps and temperature jumps respectively.

A.3. DISCRETISATION AND INTRINSIC COORDINATES

In the finite element method, the continuum body $\mathscr{B}^i$ is discretised into small elements, which generally is isoparametric. In this work, the continuum element used has 8 nodes with 4 integration points, illustrated in Fig.A.2. Each node has four degrees of freedom, i.e. x and y coordinates, p_w and T. Therefore, a generalised nodal unknown vector of the Nth element can be defined in global coordinate as:

$$\bar{\boldsymbol{u}}_\mathrm{N} = [\bar{\boldsymbol{u}}_1 \quad \bar{\boldsymbol{u}}_2 \quad \bar{\boldsymbol{u}}_3 \quad \bar{\boldsymbol{u}}_4 \quad \bar{\boldsymbol{u}}_5 \quad \bar{\boldsymbol{u}}_6 \quad \bar{\boldsymbol{u}}_7 \quad \bar{\boldsymbol{u}}_8]^\mathrm{T} \tag{A.14}$$

where,

$$\bar{\boldsymbol{u}}_i = \begin{bmatrix} x_\mathrm{i} & y_\mathrm{i} & p_{\mathrm{w}i} & T_\mathrm{i} \end{bmatrix}^\mathrm{T}, i = 1, \ldots, 8 \tag{A.15}$$

With the quadratic serendipity shape functions (Dieudonné, 2016), nodal unknowns can be computed over the element. The details of the continuum isoparametric element and corresponding shape functions can be found in any FEM textbooks or in (Dieudonné, 2016; Cerfontaine *et al.*, 2015).. The nodal unknowns over the element read:

$$\boldsymbol{u}_\mathrm{N} = \boldsymbol{N}_{(\xi,\eta)} \cdot \bar{\boldsymbol{u}}_\mathrm{N} \tag{A.16}$$

where, $\boldsymbol{u}_\mathrm{N}$ is the generalised coordinate vector of any point belonging to the Nth element.

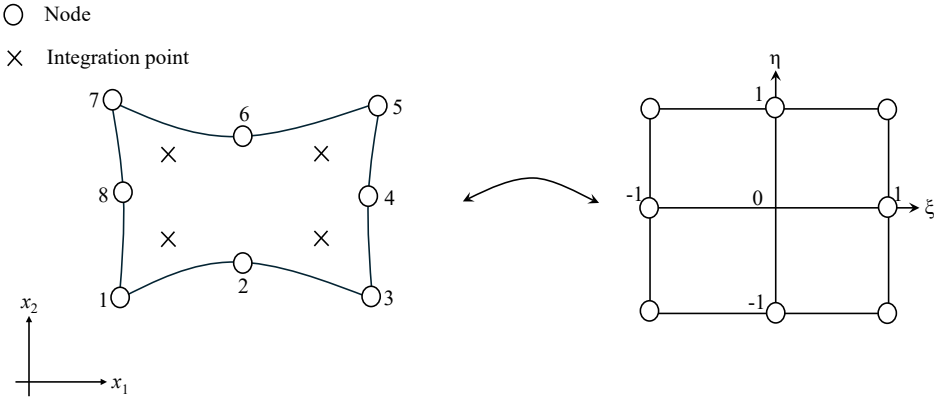


Figure A.2: 2D finite element (left) used in this work and its corresponding isoparametric element (right), modified from (Dieudonné, 2016)

In contrast, the interface element has 9 nodes with 3 integration points. While the nodes on the top and bottom faces have four degrees of freedom, i.e. x and y coordinates, p_w and T, the same with the continuum element, the nodes at the mid plane have only 2 degrees of freedom (p_w and T). Thence, the generalised unknown vector of the Nth interface element can be defined in global coordinate as:

A

$$\bar{\boldsymbol{u}}_{\mathrm{IN}} = \begin{bmatrix} \bar{\boldsymbol{x}} \\ \bar{\boldsymbol{p}}_{\mathrm{w}} \\ \bar{\boldsymbol{T}} \end{bmatrix} = \begin{bmatrix} \bar{\boldsymbol{x}}^{\mathrm{b}} \\ \bar{\boldsymbol{x}}^{\mathrm{t}} \\ \bar{\boldsymbol{p}}_{\mathrm{w}}^{\mathrm{b}} \\ \bar{\boldsymbol{p}}_{\mathrm{w}}^{\mathrm{t}} \\ \bar{\boldsymbol{p}}_{\mathrm{w}}^{\mathrm{m}} \\ \bar{\boldsymbol{T}}^{\mathrm{b}} \\ \bar{\boldsymbol{T}}^{\mathrm{t}} \\ \bar{\boldsymbol{T}}^{\mathrm{m}} \end{bmatrix} \tag{A.17}$$

where, the superscript $^{\mathrm{b}}$, $^{\mathrm{t}}$ and $^{\mathrm{m}}$ mean the bottom, top and mid plane respectively. The details of $\bar{\boldsymbol{x}}^{\mathrm{b}}$, $\bar{\boldsymbol{x}}^{\mathrm{t}}$, $\bar{\boldsymbol{p}}_{\mathrm{w}}^{\mathrm{b}}$, $\bar{\boldsymbol{p}}_{\mathrm{w}}^{\mathrm{t}}$ and $\bar{\boldsymbol{p}}_{\mathrm{w}}^{\mathrm{m}}$ of the Nth interface element can be found in (Liaudat *et al.*, 2023). Here, the nodal temperature vectors $\bar{\boldsymbol{T}}^{\mathrm{b}}$, $\bar{\boldsymbol{T}}^{\mathrm{t}}$ and $\bar{\boldsymbol{T}})^{\mathrm{m}}$ are presented in detail as an example. In a single interface element, each face has 3 nodes. Thus, the nodal temperature vectors can be expressed as:

$$\bar{\boldsymbol{T}}^{\mathrm{b}} = [T_1^{\mathrm{b}}, \quad T_2^{\mathrm{b}}, \quad T_3^{\mathrm{b}}]^{\mathrm{T}} \tag{A.18}$$

$$\bar{\boldsymbol{T}}^{\mathrm{t}} = [T_1^{\mathrm{t}}, \quad T_2^{\mathrm{t}}, \quad T_3^{\mathrm{t}}]^{\mathrm{T}} \tag{A.19}$$

$$\bar{\boldsymbol{T}}^{\mathrm{m}} = [T_1^{\mathrm{m}}, \quad T_2^{\mathrm{m}}, \quad T_3^{\mathrm{m}}]^{\mathrm{T}} \tag{A.20}$$

where the subscript number indicates the node number, while N indicates the element number.

In the interface element, an isoparametric coordinate, ξ, is defined along the intrinsic axis, $\boldsymbol{e}_{\xi}$ that is an unit vector tangent to the mid-plane (the intrinsic axis normal to the mid-plane is $\boldsymbol{e}_{\eta}$, of which the details can be found in (Liaudat *et al.*, 2023)). Thus, the quadratic shape functions for interface element can be written as:

$$N_1 = \frac{1}{2}\xi(\xi - 1) \tag{A.21}$$

$$N_2 = (1 - \xi^2) \tag{A.22}$$

$$N_3 = \frac{1}{2}\xi(1 + \xi) \tag{A.23}$$

Thereafter, the nodal unknowns of the Nth interface element can be computed over the interface element:

$$\boldsymbol{u}_{\mathrm{IN}} = \boldsymbol{N}_{I(\xi)} \cdot \bar{\boldsymbol{u}}_{\mathrm{IN}} = \begin{bmatrix} \boldsymbol{N}^{\mathrm{x}} & \boldsymbol{0} & \boldsymbol{0} & \boldsymbol{0} & \boldsymbol{0} & \boldsymbol{0} & \boldsymbol{0} & \boldsymbol{0} \\ \boldsymbol{0} & \boldsymbol{N}^{\mathrm{x}} & \boldsymbol{0} & \boldsymbol{0} & \boldsymbol{0} & \boldsymbol{0} & \boldsymbol{0} & \boldsymbol{0} \\ \boldsymbol{0} & \boldsymbol{0} & \boldsymbol{N}^{\mathrm{p}} & \boldsymbol{0} & \boldsymbol{0} & \boldsymbol{0} & \boldsymbol{0} & \boldsymbol{0} \\ \boldsymbol{0} & \boldsymbol{0} & \boldsymbol{0} & \boldsymbol{N}^{\mathrm{p}} & \boldsymbol{0} & \boldsymbol{0} & \boldsymbol{0} & \boldsymbol{0} \\ \boldsymbol{0} & \boldsymbol{0} & \boldsymbol{0} & \boldsymbol{0} & \boldsymbol{N}^{\mathrm{p}} & \boldsymbol{0} & \boldsymbol{0} & \boldsymbol{0} \\ \boldsymbol{0} & \boldsymbol{0} & \boldsymbol{0} & \boldsymbol{0} & \boldsymbol{0} & \boldsymbol{N}^{\mathrm{p}} & \boldsymbol{0} & \boldsymbol{0} \\ \boldsymbol{0} & \boldsymbol{0} & \boldsymbol{0} & \boldsymbol{0} & \boldsymbol{0} & \boldsymbol{0} & \boldsymbol{N}^{\mathrm{p}} & \boldsymbol{0} \\ \boldsymbol{0} & \boldsymbol{0} & \boldsymbol{0} & \boldsymbol{0} & \boldsymbol{0} & \boldsymbol{0} & \boldsymbol{0} & \boldsymbol{N}^{\mathrm{p}} \end{bmatrix} \cdot \bar{\boldsymbol{u}}_{\mathrm{IN}} \tag{A.24}$$

where, $\boldsymbol{N}_{I(\xi)}$ is the generalised interpolation matrix for interface element, $\boldsymbol{0}$ is the null matrix. $\boldsymbol{N}^{\mathrm{x}}$ is the interpolation matrix for nodal coordinates, while $\boldsymbol{N}^{\mathrm{p}}$ the interpolation matrix for nodal pressure and temperature. They can be expressed as:

$$\boldsymbol{N}^{\mathrm{x}} = \begin{bmatrix} N_1 & 0 & N_2 & 0 & N_3 & 0 \\ 0 & N_1 & 0 & N_2 & 0 & N_3 \end{bmatrix} \tag{A.25}$$

$$\boldsymbol{N}^{\mathrm{p}} = \begin{bmatrix} N_1 & N_2 & N_3 \end{bmatrix} \tag{A.26}$$

A.4. GLOBAL SOLUTION AND STIFFNESS MATRIX

As said by the principle of virtual work, equilibrium is reached when the energetically equivalent internal nodal forces F_{I} are equal to the external nodal forces F_{E} (Cerfontaine *et al.*, 2015). When the analysis includes time-dependent path, such as the evolution of the loading, the equilibrium need to be found for the complete time range of interest (Cerfontaine *et al.*, 2015; Bathe, 1982). The nodal forces are likely not balanced at the beginning of an arbitray time step, thus an out-of-balance force is defined as (Cerfontaine *et al.*, 2015):

$$\boldsymbol{F}_{\mathrm{OB}} = \boldsymbol{F}_{\mathrm{I}} - \boldsymbol{F}_{\mathrm{E}} \tag{A.27}$$

Let's assume at time t the solution is known, and the solution at time $t + \Delta t$ is to be solved. The out-of-balance force at time step $t + \Delta t$ can be expressed in Taylor series (Cerfontaine *et al.*, 2015):

$$\boldsymbol{F}_{\mathrm{OB}}^{(t+\Delta t)} = \boldsymbol{F}_{\mathrm{OB}}^{(t)} + \frac{\partial \boldsymbol{F}_{\mathrm{OB}}^{(t)}}{\partial \Delta \boldsymbol{U}} \cdot \Delta \boldsymbol{U} \tag{A.28}$$

where, $\boldsymbol{F}_{\mathrm{OB}}^{(t+\Delta t)}$ is the global out-of-balance force at time step $t + \Delta t$, $\Delta \boldsymbol{U}$ is the global generalised displacement. The equilibrium at time step $t + \Delta t$ can be found if:

$$\boldsymbol{F}_{\mathrm{OB}}^{(t+\Delta t)} = 0 \tag{A.29}$$

Thus, after some transformations, it arrives:

$$\boldsymbol{F}_{\mathrm{OB}}^{(t)} = -\frac{\partial \boldsymbol{F}_{\mathrm{OB}}^{(t)}}{\partial \Delta \boldsymbol{U}} \cdot \Delta \boldsymbol{U} = -\boldsymbol{K}^{(t)} \cdot \Delta \boldsymbol{U} \tag{A.30}$$

where, $\boldsymbol{K}^{(t)}$ is the global stiffness matrix at time step t. As $\boldsymbol{F}_{\mathrm{OB}}^{(t)}$ is known, once the global stiffness matrix $\boldsymbol{K}^{(t)}$ is obtained, the global generalised displacement $\Delta \boldsymbol{U}$ can be computed, after which all the degrees of freedom at time step $t + \Delta t$ can be obtained:

$$\boldsymbol{U}^{(t+\Delta t)} = \boldsymbol{U}^{(t)} + \Delta \boldsymbol{U} \tag{A.31}$$

where, $\boldsymbol{U}^{(t+\Delta t)}$ is the generalised global unknown vector that is expected at time step $t + \Delta t$. Note that the solution may be suffering from significant errors and be unstable, due to the time or load step size used (Cerfontaine *et al.*, 2015; Bathe, 1982). Therefore, the Newton-Raphson scheme is used in each time step to iterate the solution until required accuracy is achieved.

In LAGAMINE, the global stiffness matrix is obtained by assembling element stiffness matrices, which are evaluated individually. For the continuum element stiffness and

nodal forces, the evaluations can be found in (Dieudonné, 2016; Cerfontaine *et al.*, 2015). Here, only the interface element stiffness matrix is introduced.

Similarly to the generalised nodal unknowns $\bar{\boldsymbol{u}}_{\mathrm{IN}}$, the generalised nodal forces of the Nth interface element can be expressed as:

$$\bar{\boldsymbol{f}}_{\mathrm{IN}} = \begin{bmatrix} \bar{\boldsymbol{f}}_{\mathrm{x}} & \bar{\boldsymbol{f}}_{\mathrm{w}} & \bar{\boldsymbol{f}}_{\mathrm{T}} \end{bmatrix}^{\mathrm{T}} \tag{A.32}$$

Therefore, the element stiffness matrix of the Nth interface element, k_{IN} reads:

$$k_{IN,30\times30} = \frac{\partial \bar{\boldsymbol{f}}_{\mathrm{IN}}}{\partial \bar{\boldsymbol{u}}_{\mathrm{IN}}} = \begin{bmatrix} \frac{\partial \bar{\boldsymbol{f}}_{\mathrm{x}}}{\partial \bar{\boldsymbol{x}}} & \frac{\partial \bar{\boldsymbol{f}}_{\mathrm{x}}}{\partial \bar{\boldsymbol{p}}_{\mathrm{w}}} & \frac{\partial \bar{\boldsymbol{f}}_{\mathrm{x}}}{\partial \bar{\boldsymbol{T}}} \\ \frac{\partial \bar{\boldsymbol{f}}_{\mathrm{w}}}{\partial \bar{\boldsymbol{x}}} & \frac{\partial \bar{\boldsymbol{f}}_{\mathrm{w}}}{\partial \bar{\boldsymbol{p}}_{\mathrm{w}}} & \frac{\partial \bar{\boldsymbol{f}}_{\mathrm{w}}}{\partial \bar{\boldsymbol{T}}} \\ \frac{\partial \bar{\boldsymbol{f}}_{T}}{\partial \bar{\boldsymbol{x}}} & \frac{\partial \bar{\boldsymbol{f}}_{\mathrm{T}}}{\partial \bar{\boldsymbol{p}}_{\mathrm{w}}} & \frac{\partial \bar{\boldsymbol{f}}_{T}}{\partial \bar{\boldsymbol{T}}} \end{bmatrix} \tag{A.33}$$

The mechanical and hydraulic nodal forces of interface element can be found in (Liaudat *et al.*, 2023). The thermal nodal forces and corresponding components in the element stiffness matrix can be obtained accordingly. To make the paper easy to read, the details are not presented here.

B

METHOD TO REDUCE HYDRAULIC AND THERMAL ARTIFICIAL COMPLIANCE

The placement of interface elements between continuum elements has been shown not to affect the stress, pressure or temperature fields of intact rock when parameters are appropriately chosen. In particular, the stiffness of the interface elements should be set high enough to reduce the mechanical artificial compliance without causing numerical instability. Similarly, to properly address the thermal and hydraulic artificial conductivity, the transversal hydraulic transmissivity should be set as high as possible to minimise the pressure and temperature drops across the interface elements.

However, a high transversal hydraulic transmissivity can result in fast heat convection accross the interface elements. It is well known that fast heat convection in comparison to conduction can lead to numerical oscillation. The Péclet number, a dimensionless number that quantifies the relative importance of convective heat transport compared to conductive heat transport, is used to characterise the dominant heat transfer mechanism. It is defined as:

$$Pe = \frac{\rho_{\mathrm{w}} c_{\mathrm{pw}} h v_{\mathrm{w}}^{b/t}}{2\lambda_{\mathrm{w}}} \quad \text{(transversal)} \tag{B.1}$$

where ρ_{w} [m^3/h], c_{pw} [J/kg·K] and λ_{w} [W/m·K] are the water density, specific heat capacity and heat conductivity respectively. $v_{\mathrm{w}}^{b/t}$ [m/s] is the transversal fluid velocity (from bottom or top side of the interface element). h [m] is the element length.

A high Péclet corresponds to a convection-dominated transfer mechanism. In Section 3.3.1, it is shown that high longitudinal heat convection within the interface elements can result in numerical oscillation, and that adding an artificial conductivity can stabilise the solution. In the present case, transversal heat convection will also be high due to the imposed high transversal transmissivity. Therefore, in this section, an artificial conductivity is added to the transversal heat transfer terms. It is expressed as:

$$\lambda_{\mathrm{a}} = \delta \rho_{\mathrm{w}} c_{\mathrm{pw}} h \left| v_{\mathrm{w}}^{b/t} \right| \quad \text{(transversal)} \tag{B.2}$$

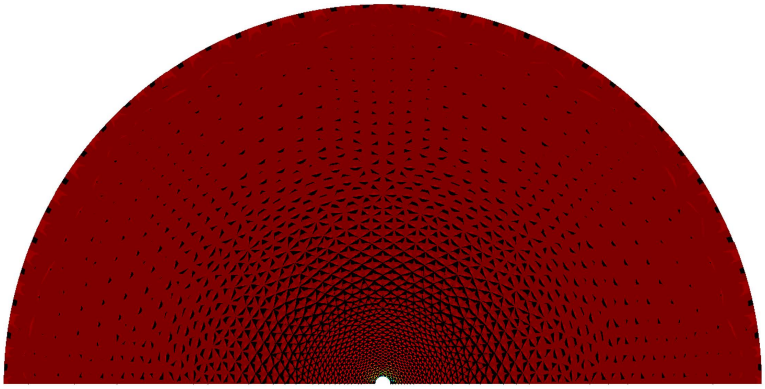
where δ is a tuning parameter. Consequently, the Péclet number with stabilisation reads:

$$Pe = \frac{\rho_{\mathrm{w}} c_{\mathrm{pw}} h v_{\mathrm{w}}^{b/t}}{2(\lambda_{\mathrm{a}} + \lambda_{\mathrm{w}})} \quad \text{(transversal)} \tag{B.3}$$

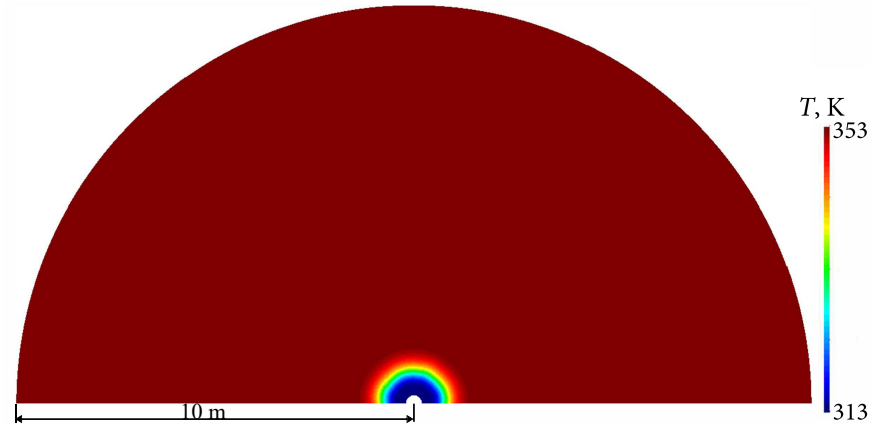
To demonstrate the stabilisation technique, thermo-hydraulic (T-H) simulations of the injection of cold water using the model equipped with interface elements with and without stabilisation are first compared. Then, T-H simulations using the model with interface elements and the model without interface elements are compared to demonstrate the capability of the modelling approach (i.e. increasing the transversal hydraulic conductivity of the interface element with stabilised technique) to reproduce the thermal and hydraulic fields of the intact rock. The parameters of the continuum and interface elements as well as boundary and initial conditions are the same as is presented earlier in Tab. 5.1 and Tab. 5.2. The injection rate Q_{inj} is assumed to be 72 m^3/h with injection temperature at 313 K.

Fig. B.1 compares temperature fields calculated without and with stabilisation technique, of simulations on the domain including interface elements. Significant oscillation is seen to occur if no stabilisation technique is used, and the simulation stops at t = 30 s due to lack of numerical convergence. In contrast, when the stabilisation technique is used

(with $\delta \times h = 10$ m), the simulation is seen to run smoothly and continuously without any numerical oscillation.



(a) Temperature field without stabilisation. t = 30 s

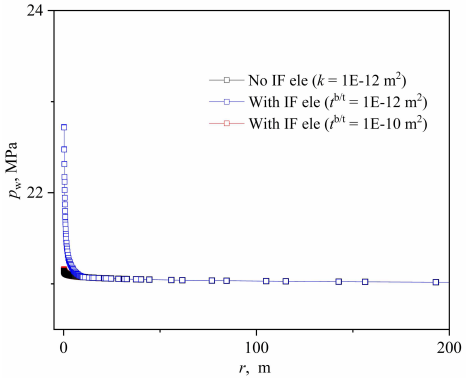


(b) Temperature field with stabilisation ($\delta \times h = 10$). t = 2000 s

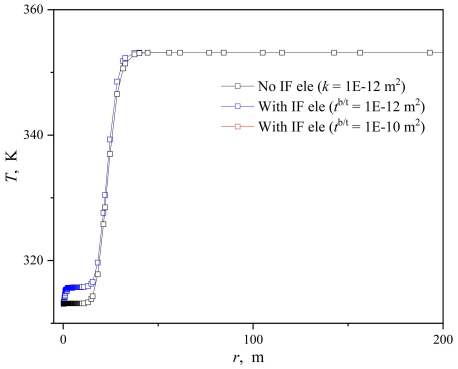
Figure B.1: Comparison of temperature fields (model region within radius of 10 meters is shown here) with and without stabilisation technique for high Péclet number. The simulation without stabilisation is stopped at t = 30 s due to numerical divergence and temperature solution is with numerical oscillation. The black spots indicate values outside the legend range 313 K - 353 K. In contrast, the simulation with stabilisation can run smoothly without oscillation.

The second set of simulations investigates whether the model equipped with interface elements, utilising high transversal transmissivity and stabilisation, can reproduce the hydraulic and thermal fields of intact rock. To investigate this, two model domains are used and the results compared. The first model only consists of continuum elements, representing intact rock, while the other is composed of continuum elements and interface elements. Two variants of the model with interface elements are used to investigate the impact of the transversal hydraulic transmissivity. As before, thermo-hydraulic simulations with same boundary and initial conditions are performed. Figs. B.2a and

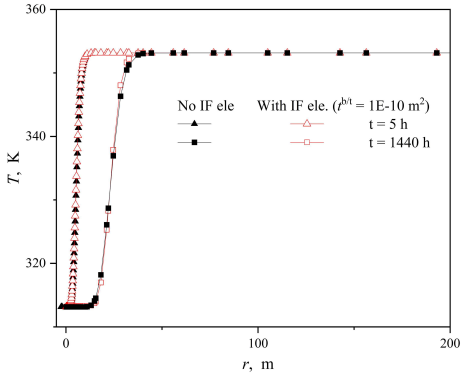
B.2b compare the spatial distribution of pressure and temperature of all three results. Fig. B.2c presents the temperature results for an additional time step of the intact and most successful stabilised solution. The results show that when the transversal hydraulic transmissivity of the interface elements is 1E-10 m^2, the temperature and pressure distributions are imperceptibly different from those of the model without interface elements. In contrast, when the transversal hydraulic transmissivity is 1E-12 m^2, there is a large difference in the zone with the interface elements. The comparison confirms that the values of transversal fluid/heat transmissivity must be carefully selected, in order to have realistic results, but this may require the use of a stabilisation technique to address the resulting numerical oscillation due to high Péclet number.



(a) Pressure profile at t = 1440 h



(b) Temperature profile at t = 1440 h



(c) Temperature profile after 5 and 1440 hours of cold water injection

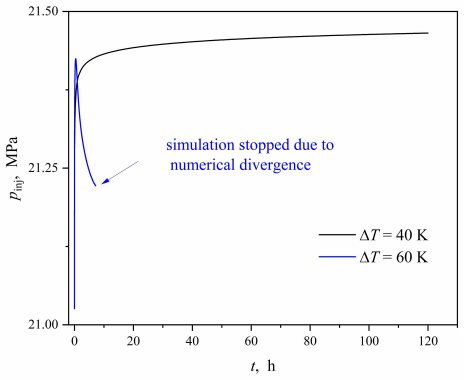
Figure B.2: Comparison of (a) pressure (t = 1440 h) and (b) temperature (t = 1440 h) distributions with and without interface elements inserted in between all the continuum elements in the region with a radius of 10 meters. When the transversal hydraulic conductivity is 1E-10 m^2 respectively, the pressure and temperature distribution can be reproduced. (c) Comparison of temperature distribution evolving with time, of the model equipped with interface element ($t^{h/t}$ = 1E-10 m^2) and without interface element.

C

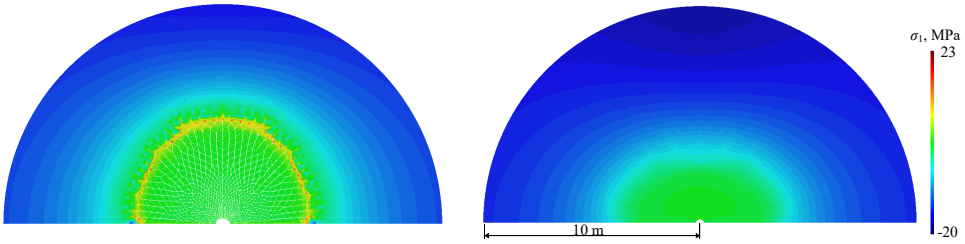
SIMULATION OF THE NORMAL INJECTION SCENARIO

In the normal scenario, labelled as $N1$, the performance of cold water injection into the synthetic non-clogged formation is investigated to evaluate the cooling effects, with injection temperatures of 353 K (i.e. same temperature as the reservoir, $\Delta T = T_{\text{inj}} - T_{\text{i}} = 0$ K, thus no cooling effects) to give a control simulation, 313 K (i.e. a temperature difference of $\Delta T = 40K$, which is representative of multiple geothermal heating projects) and 293 K (i.e. a temperature difference of $\Delta T = 60K$, which is considered to be a reasonably extreme lower bound).

Fig. C.1a presents the injection pressure evolution under fixed injection rate of 360 m^3/h with two different ΔT. A slight but continuous increase in p_{inj} under $\Delta T = 40$ K is observed, due to the increasing water viscosity of cold water. In contrast, when the $\Delta T = 60$ K, a sharp decrease in injection pressure is observed and the simulation stops early due to numerical divergence. This is a result of thermal contraction causing tension and the opening of almost all interface elements, as shown in Fig. C.1b. Fractures are induced almost in every direction within the cooled-down area is separated as a result of thermal stress, though fractures have to follow the element edges. Some elements are completely separated from others, leading to the unstable numerical solution. In contrast, Fig. C.1c shows almost no fracturing when the $\Delta T = 40$ K. Fig. C.2 presents the distribution of the first principal stress from an elastic analysis, i.e. without interface elements inserted, under the same boundary conditions. It shows that strong tensile stress is induced at and near the borehole when $\Delta T = 60$ K, since fracturing is not allowed to happen (thus no stress relaxation). In contrast, Fig. C.2b tensile stress is much less when $\Delta T = 40$ K, showing almost identical level of stresses with the result shown in Fig. C.1c, where interface elements are inserted in the near-borehole zone thus allowing fracture to happen. The results implies that even though lower injection temperatures can cause thermal fracturing which can improve injectivity, large thermal stresses could lead to severe damage in the near-borehole zone, which can trigger several unfavourable processes, such as sand production, even in normal operating conditions where clogging has not occurred.

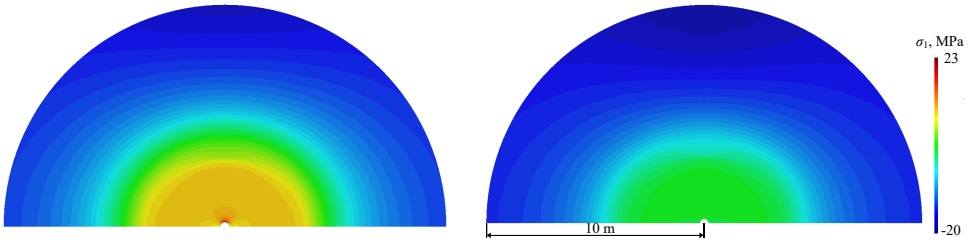


(a)



(b) (c)

Figure C.1: Results from THM (with interface elements inserted in the near-borehole zone until a radius of 10 m) analysis of the normal scenario $N1$. (a) Injection pressure changes with time under ΔT = 60 K and 40 K, and (b) and (c) corresponding first principal stress (σ_1) distributions with deformed mesh at t = 7.4 h. When ΔT = 60 K, the simulation is stopped due to numerical divergence, a result of large fracture networks at the near-borehole zone. The deformation is 50 times enlarged.



(a) (b)

Figure C.2: Results from elastic (without interface elements) analysis of the normal scenario $N1$. (a) and (b) first principal stress (σ_1) distributions under ΔT = 60 K and 40 K, respectively, with deformed mesh at t = 7.4 h.

D

MOMENT TENSOR DECOMPOSITION

The moment tensor can be decomposed into three elementary tensors, i.e. ISO, DC, and CLVD as follows (Vavryčuk, 2015):

$$\mathbf{M}' = M_{\mathrm{ISO}}\mathbf{E}_{\mathrm{ISO}} + M_{\mathrm{DC}}\mathbf{E}_{\mathrm{DC}} + M_{\mathrm{CLVD}}\mathbf{E}_{\mathrm{CLVD}} \tag{D.1}$$

where $\mathbf{M}'$ is the principal moment tensor in the principal coordinate system, and $\mathbf{E}_{\mathrm{ISO}}$, $\mathbf{E}_{\mathrm{DC}}$ and $\mathbf{E}_{\mathrm{CLVD}}$ are the ISO, DC and CLVD elementary tensors, and read:

$$\mathbf{E}_{\mathrm{ISO}} = \begin{bmatrix} 1 & 0 & 0 \\ 0 & 1 & 0 \\ 0 & 0 & 1 \end{bmatrix} \quad \mathbf{E}_{\mathrm{DC}} = \begin{bmatrix} 1 & 0 & 0 \\ 0 & 0 & 0 \\ 0 & 0 & -1 \end{bmatrix} \quad \mathbf{E}^{+}_{\mathrm{CLVD}} = \frac{1}{2}\begin{bmatrix} 2 & 0 & 0 \\ 0 & -1 & 0 \\ 0 & 0 & -1 \end{bmatrix} \quad \text{or} \quad \mathbf{E}^{-}_{\mathrm{CLVD}} = \frac{1}{2}\begin{bmatrix} 1 & 0 & 0 \\ 0 & 1 & 0 \\ 0 & 0 & -2 \end{bmatrix} \tag{D.2}$$

where $\mathbf{E}^{+}_{\mathrm{CLVD}}$ or $\mathbf{E}^{-}_{\mathrm{CLVD}}$ is used if $M_1 + M_3 - 2M_2 \geq 0$ or $M_1 + M_3 - 2M_2 < 0$ (M_1, M_2 and M_3 are the eigenvalues of the principal moment tensor $\mathbf{M}'$ and $M_1 \geq M_2 \geq M_3$). The corresponding elementary scalar moments read:

$$M_{\mathrm{ISO}} = \frac{1}{3}(M_1+M_2+M_3), \quad M_{\mathrm{DC}} = \frac{1}{2}(M_1-M_3-|M_1+M_3-2M_2|), \quad M_{\mathrm{CLVD}} = \frac{2}{3}(M_1+M_3-2M_2) \tag{D.3}$$

The values of M_{ISO}, M_{DC} and M_{ISO} are generally normalised to obtain the contribution of each elementary source mechanism:

$$\begin{bmatrix} C_{\mathrm{ISO}} \\ C_{\mathrm{DC}} \\ C_{\mathrm{CLVD}} \end{bmatrix} = \frac{1}{M}\begin{bmatrix} M_{\mathrm{ISO}} \\ M_{\mathrm{DC}} \\ M_{\mathrm{CLVD}} \end{bmatrix} \tag{D.4}$$

where $M = |M_{\mathrm{ISO}}| + |M_{\mathrm{CLVD}}| + M_{\mathrm{DC}}$, so that $|C_{\mathrm{ISO}}| + |C_{\mathrm{CLVD}}| + C_{\mathrm{DC}} = 1$ is always satisfied. Physically, $C_{\mathrm{ISO}} = \pm 1$ indicates pure explosion/implosion. $C_{\mathrm{DC}} = 1$ indicates pure shear failures while $C_{\mathrm{DC}} = 0$ indicates tensile failures that contain both ISO and CLVD components (Vavryčuk, 2015).

REFERENCES

Abrams, A. (1977). Mud design to minimize rock impairment due to particle invasion. *J Petrol Technol* **29**, No. 05, 586–592, doi:10.2118/5713-PA.

Adachi, J. I. & Detournay, E. (2002). Self-similar solution of a plane-strain fracture driven by a power-law fluid. *Int J Numer Anal Met* **26**, No. 6, 579–604, doi:10.1002/nag.213.

Akdas, S. B. & Onur, M. (2022). Analytical solutions for predicting and optimizing geothermal energy extraction from an enhanced geothermal system with a multiple hydraulically fractured horizontal-well doublet. *Renew Energ* **181**, 567–580, doi:10.1016/j.renene.2021.09.051.

Aliabadi, M. A. & Rooke, D. P. (1991). *Numerical fracture mechanics*. Dordrecht: Springer Dordrecht, URL https://link.springer.com/book/9780792311751.

Allis, R. G. (2000). Review of subsidence at Wairakei field, New Zealand. *Geothermics* **29**, No. 4-5, 455–478, doi:10.1016/S0375-6505(00)00016-X.

Alonso, E., Zandarín, M. & Olivella, S. (2013). Joints in unsaturated rocks: Thermo-hydro-mechanical formulation and constitutive behaviour. *J Rock Mech Geotech Eng* **5**, No. 3, 200–213, doi:10.1016/j.jrmge.2013.05.004.

Aramburo Velez, D. A. (2017). *Synergy between geothermal and stranded oil fields to add value to geothermal projects*. Master's thesis, Delft University of Technology, URL https://www.ebn.nl/wp-content/uploads/2017/11/Aramburo_D._Synergy_between_geothermal_and_stranded_oil_fields_to_add_value_to_geothermal_projects.pdf.

Axelsson, G., Thórhallsson, S. & Björnsson, G. (2006). Stimulation of geothermal wells in basaltic rock in iceland. In *Enhanced geothermal innovative network for Europe Workshop 3: Stimulation of Reservoir and Microseismicity*, URL https://www.researchgate.net/publication/242234259_Stimulation_of_geothermal_wells_in_basaltic_rock_in_Iceland/citations.

Bader, M., Clapp, R. G., Nihei, K. T. & Biondi, B. (2023). Moment tensor inversion of perforation shots using distributed-acoustic sensing. *Geophysics* **88**, No. 6, WC37–WC45, doi:10.1190/geo2023-0040.1.

Baig, A. & Urbancic, T. (2010). Microseismic moment tensors: A path to understanding frac growth. *The Leading Edge* **29**, No. 3, 320–324, doi:10.1190/1.3353729.

Baiocchi, C., Brezzi, F. & Franca, L. P. (1993). Virtual bubbles and Galerkin-least-squares type methods (Ga.L.S.). *Comput Method Appl M* **105**, No. 1, 125–141, doi:10.1016/0045-7825(93)90119-I.

Baird, A. F., Stork, A. L., Horne, S. A., Naldrett, G., Kendall, J.-M., Wookey, J., Verdon, J. P. & Clarke, A. (2020). Characteristics of microseismic data recorded by distributed acoustic sensing systems in anisotropic media. *Geophysics* **85**, No. 4, KS139–KS147, doi:10.1190/geo2019-0776.1.

Baisch, S., Vörös, R., Rothert, E., Stang, H., Jung, R. & Schellschmidt, R. (2010). A numerical model for fluid injection induced seismicity at soultz-sous-forêts. *Int J Rock Mech Min Sci* **47**, No. 3, 405–413, doi:10.1016/j.ijrmms.2009.10.001.

Barenblatt, G. (1962). The mathematical theory of equilibrium cracks in brittle fracture. *Adv Appl Mech* **7**, 55–129, doi:10.1016/S0065-2156(08)70121-2.

Barends, F. B. J. (2010). Complete solution for transient heat transport in porous media, following Lauwerier's concept. In *SPE Annual Technical Conference and Exhibition*, Florence, pp. 19–22, URL http://onepetro.org/SPEATCE/proceedings-pdf/10ATCE/All-10ATCE/SPE-134670-MS/1726378/spe-134670-ms.pdf/1.

Bathe, K.-J. (1982). *Finite element procedures in engineering analysis*. Prentice-Hall.

Baumann, T., Bartels, J., Lafogler, M. & Wenderoth, F. (2017). Assessment of heat mining and hydrogeochemical reactions with data from a former geothermal injection well in the Malm Aquifer, Bavarian Molasse Basin, Germany. *Geothermics* **66**, 50–60, doi:10.1016/j.geothermics.2016.11.008.

Baveye, P., Vandevivere, P., Hoyle, B. L., DeLeo, P. C. & de Lozada, D. S. (1998). Environmental impact and mechanisms of the biological clogging of saturated soils and aquifer materials. *Crit Rev Environ Sci Technol* **28**, No. 2, 123–191, doi:10.1080/10643389891254197.

Bennion, D. B. (2002). An overview of formation damage mechanisms causing a reduction in the productivity and injectivity of oil and gas producing formations. *J Can Petrol Technol* **41**, No. 11, doi:10.2118/02-11-DAS.

Bijay, K. C. & Ghazanfari, E. (2021). Geothermal reservoir stimulation through hydroshearing: an experimental study under conditions close to enhanced geothermal systems. *Geothermics* **96**, 102200, doi:10.1016/j.geothermics.2021.102200.

Birner, J., Seibt, A., Hinrichs, T., Seibt, P. & Wolfgramm, M. (2015). Removing and reducing scalings - Practical experience in the operation of geothermal systems. In *World Geothermal Congress 2015*, Melbourne, Australia.

Blöcher, G., Reinsch, T., Henninges, J., Milsch, H., Regenspurg, S., Kummerow, J., Francke, H., Kranz, S., Saadat, A. & Zimmermann, G. (2016). Hydraulic history and current state of the deep geothermal reservoir Groß Schönebeck. *Geothermics* **63**, 27–43, doi:10.1016/j.geothermics.2015.07.008.

Boeije, C. S., Verweij, C. B., Zitha, P. L. J. & Pluymakers, A. M. H. (2022). CO2 degassing of fluid in coreflood experiments. In *European Geothermal Congress 2022*, Berlin, URL https://research.tudelft.nl/en/publications/co2-degassing-of-fluid-in-coreflood-experiments.

Boisdet, A., Cautru, J. & Czernichowski, I. (1989). Experiments on reinjection of geothermal brines in deep Triassic sandstones. In *The 4th International Seminar on the Results of EC Geothermal Energy*, Italy, pp. 419–428.

Bouwer, H. (2002). Artificial recharge of groundwater: hydrogeology and engineering. *Hydrogeol J* **10**, 121–142, doi:10.1007/s10040-001-0182-4.

Branco, R., Prates, P., Costa, J. D., Cruces, A., Lopez-Crespo, P. & Berto, F. (2022). On the applicability of the cumulative strain energy density for notch fatigue analysis under multiaxial loading. *Theor Appl Fract Mec* **120**, doi:10.1016/j.tafmec.2022.103405.

Brehme, M., Nowak, K., Banks, D., Petrauskas, S., Valickas, R., Bauer, K., Burnside, N. & Boyce, A. (2019). A review of the hydrochemistry of a deep sedimentary aquifer and its consequences for geothermal operation: Klaipeda, Lithuania. *Geofluids* **2019**, No. 1, 4363592, doi:10.1155/2019/4363592.

Brehme, M., Regenspurg, S., Leary, P., Bulut, F., Milsch, H., Petrauskas, S., Valickas, R. & Blöcher, G. (2018). Injection-triggered occlusion of flow pathways in geothermal operations. *Geofluids* **2018**, No. 1, 4694829, doi:10.1155/2018/4694829.

Bressers, P. M. M. C. & Wilschut, F. (2014). Lead deposition in geothermal installations. *Technical Report R11416*, TNO, Utrecht, URL https://www.nlog.nl/sites/default/files/2014%20r11416%20lead%20deposition%20in%20geothermal%20installations.pdf.

Burté, L., Cravotta III, C. A., Bethencourt, L., Farasin, J., Pédrot, M., Dufresne, A., Gerard, M.-F., Baranger, C., Le Borgne, T. & Aquilina, L. (2019). Kinetic study on clogging of a geothermal pumping well triggered by mixing-induced biogeochemical reactions. *Environ Sci Technol* **53**, No. 10, 5848–5857, doi:10.1021/acs.est.9b00453.

Butt, A., Hedayat, A. & Moradian, O. (2024). Microseismic monitoring of laboratory hydraulic fracturing experiments in granitic rocks for different fracture propagation regimes. *Rock Mech Rock Eng* **57**, No. 3, 2035–2059, doi:10.1007/s00603-023-03669-6.

Carrier, B. & Granet, S. (2012). Numerical modeling of hydraulic fracture problem in permeable medium using cohesive zone model. *Eng Fract Mech* **79**, 312–328, doi:10.1016/j.engfracmech.2011.11.012.

Castro, M. R., López, D. L., Reyes-López, R. L., Montalvo, F. E., Romero, R., Ramírez-Hernández, J. & Lázaro-Mancilla, O. (2006). Modeling scaling of silica from reinjection waters at wellhead conditions in the Berlin geothermal field, El Salvador, Central America. In *31th Workshop on Geothermal Reservoir Engineering*, SGP-TR-177, Stanford, California: Stanford University, URL https://pangea.stanford.edu/ERE/pdf/IGAstandard/SGW/2006/castro.pdf.

Centraal Bureau voor de Statistiek (2014). Hernieuwbare energie in Nederland 2013. *Technical report*, Centraal Bureau voor de Statistiek, The Hague/Heerlen, URL https://www.cbs.nl/nl-nl/publicatie/2014/35/hernieuwbare-energie-in-nederland-2013.

Cerfontaine, B. & Collin, F. (2018). Cyclic and fatigue behaviour of rock materials: Review, interpretation and research perspectives. *Rock Mech Rock Eng* **51**, No. 2, 391–414, doi:10.1007/s00603-017-1337-5.

Cerfontaine, B., Dieudonné, A., Radu, J., Collin, F. & Charlier, R. (2015). 3D zero-thickness coupled interface finite element: formulation and application. *Comput Geotech* **69**, 124–140, doi:10.1016/j.compgeo.2015.04.016.

Chai, R., Liu, Y., Xue, L., Rui, Z., Zhao, R. & Wang, J. (2022). Formation damage of sandstone geothermal reservoirs: During decreased salinity water injection. *Appl Energ* **322**, 119465, doi:10.1016/j.apenergy.2022.119465.

Chapman, C. H. & Leaney, W. S. (2012). A new moment-tensor decomposition for seismic events in anisotropic media. *Geophys J Int* **188**, No. 1, 343–370, doi:10.1111/j.1365-246X.2011.05265.x.

Charlier, R. (1987). *Approche unifiée de quelques problèmes non linéaires de mécanique des milieux continus par la méthode des éléments finis (grandes déformations des métaux et des sols, contact unilatéral de solides, conduction thermique et écoulements en milieu poreux)*. Ph.D. thesis, University of Liège, Liège, URL https://hdl.handle.net/2268/315205.

Chen, J., Xu, T., Jiang, Z., Feng, B. & Liang, X. (2020). Reducing formation damage by artificially controlling the fluid-rock chemical interaction in a double-well geothermal heat production system. *Renew Energ* **149**, 455–467, doi:10.1016/j.renene.2019.12.038.

Chen, X., Bu, J., Fan, X., Lu, J. & Xu, L. (2017). Effect of loading frequency and stress level on low cycle fatigue behavior of plain concrete in direct tension. *Constr Build Mater* **133**, 367–375, doi:10.1016/j.conbuildmat.2016.12.085.

Cheng, Y., Zhang, Y., Yu, Z., Hu, Z., Ma, Y. & Yang, Y. (2021). Experimental and numerical studies on hydraulic fracturing characteristics with different injection flow rates in granite geothermal reservoir. *Energy Sci Eng* **9**, No. 1, 142–168, doi:10.1002/ese3.816.

Choi, H., Park, K. & Paulino, G. H. (2020). Mixed-mode fatigue crack growth using cohesive zone modeling. *Eng Fract Mech* **240**, 107234, doi:10.1016/j.engfracmech.2020.107234.

Ciezobka, J. (2021). Overview of hydraulic fracturing test site 2 in the Permian Delaware basin (HFTS-2). In *The 9th Unconventional Resources Technology Conference*, URTEC-2021-5514-MS, Houston, Texas, USA: American Association of Petroleum Geologists, doi:10.15530/urtec-2021-5514.

Cladouhos, T. T., Petty, S., Swyer, M. W., Uddenberg, M. E., Grasso, K. & Nordin, Y. (2016). Results from newberry volcano egs demonstration, 2010–2014. *Geothermics* **63**, 44–61, doi:10.1016/j.geothermics.2015.08.009.

Clotworthy, A. W. (1989). Selection and testing of reinjection wells for the Ohaaki geothermal field. In *11th New Zealand Geothermal Workshop*, Auckland, New Zealand, pp. 67–72, URL https://pangea.stanford.edu/ERE/pdf/IGAstandard/NZGW/1989/Clotworthy.pdf.

Collin, F., Li, X., Radu, J. & Charlier, R. (2002). Thermo-hydro-mechanical coupling in clay barriers. *Eng Geol* **64**, No. 2-3, 179–193, doi:10.1016/S0013-7952(01)00124-7.

Cornet, F. H. & Jianmin, Y. (1995). Analysis of induced seismicity for stress field determination and pore pressure mapping. *Pure Appl Geophys* **145**, No. 3-4, 677–700, doi:10.1007/BF00879595.

Corsi, R. (1986). Scaling and corrosion in geothermal equipment: problems and preventive measures. *Geothermics* **15**, No. 5-6, 839–856, doi:10.1016/0375-6505(86)90097-0.

Croese, E., Doddema, S. & Veeger, F. (2019). Microbiology in geothermal operations. In *Corrosion 2019*, Nashville, Tennessee, pp. 2019–12818, URL https://onepetro.org/NACECORR/proceedings-abstract/CORR19/All-CORR19/NACE-2019-12818/127158.

Cuenot, N., Charléty, J., Dorbath, L. & Haessler, H. (2006). Faulting mechanisms and stress regime at the European HDR site of Soultz-sous-Forêts, France. *Geothermics* **35**, No. 5-6, 561–575, doi:10.1016/j.geothermics.2006.11.007.

Cui, W., Potts, D. M., Zdravković, L., Gawecka, K. A. & Tsiampousi, A. (2019). Formulation and application of 3D THM-coupled zero-thickness interface elements. *Comput Geotech* **116**, 103204, doi:10.1016/j.compgeo.2019.103204.

Dadi, S., Norbeck, J., Titov, A., Payeur, T., Machovoe, S. & Joern, K. (2024). Microseismic monitoring of a horizontal EGS system: Case study and state of the art. In *49th Workshop on Geothermal Reservoir Engineering*, SGP-TR-227, Stanford, California: Stanford University, URL https://pangea.stanford.edu/ERE/db/GeoConf/papers/SGW/2024/Dadi.pdf.

Dally, T., Bilgen, C., Werner, M. & Weinberg, K. (2020). Cohesive elements or phase-field fracture: which method is better for dynamic fracture analyses? In *Modeling and Simulation in Engineering - Selected Problems*, IntechOpen, doi:10.5772/intechopen.92180.

De Moura, M. & Gonçalves, J. (2015). Cohesive zone model for high-cycle fatigue of composite bonded joints under mixed-mode i+ ii loading. *Eng Fract Mech* **140**, 31–42, doi:10.1016/j.engfracmech.2015.03.044.

De Simone, S. (2017). *Induced sesimicity in enhanced geothermal systems: assessment of thermo-hydro-mechanical effects*. Ph.D. thesis, Universitat Politécnica de Catalunya, Catalunya, URL https://upcommons.upc.edu/bitstream/handle/2117/107946/TSdS1de1.pdf?sequence=1&isAllowed=y.

De Simone, S., Vilarrasa, V., Carrera, J., Alcolea, A. & Meier, P. (2013). Thermal coupling may control mechanical stability of geothermal reservoirs during cold water injection. *Phys Chem Earth* **64**, 117–126, doi:10.1016/j.pce.2013.01.001.

Dempsey, D., Rowland, J., Zyvoloski, G. & Archer, R. (2012). Modeling the effects of silica deposition and fault rupture on natural geothermal systems. *J Geophys Res: Solid Earth* **117**, No. B5, doi:10.1029/2012JB009218.

Diaz, A. R., Kaya, E. & Zarrouk, S. J. (2016). Reinjection in geothermal fields- a worldwide review update. *Renew Sustain Energy Rev* **53**, 105–162, doi:10.1016/j.rser.2015.07.151.

Diersch, H.-J. G. (2014). *FEFLOW: finite element modeling of flow, mass and heat transport in porous and fracturedmedia*. 1 edn., Springer Berlin, Heidelberg, doi:10.1007/978-3-642-38739-5.

Dieudonné, A., Cerfontaine, B., Collin, F. & Charlier, R. (2015). Hydromechanical modelling of shaft sealing for CO_2 storage. *Eng Geol* **193**, 97–105, doi:10.1016/j.enggeo.2015.04.016.

Dieudonné, A.-C. (2016). *Hydromechanical behaviour of compacted bentonite: from micro-scale analysis to macro-scale modelling*. Ph.D. thesis, Université de Liège, Liège, doi:https://hdl.handle.net/2268/201397.

Diller, D. E. & Gardner, S. P. (2012). Observations and implications from simultaneous recording of microseismic surface and borehole data. *The Leading Edge* **31**, No. 11, 1310–1317, doi:10.1190/tle31111310.1.

Dobbie, T. P., Maunder, B. R. & Sarit, A. D. (1982). Reinjection experience in the Philippines. In *4th New Zealand Geothermal Workshop*, Auckand, New Zealand: University of Auckland, pp. 223–228, URL https://pangea.stanford.edu/ERE/db/IGAstandard/record_detail.php?id=3283.

Doughty, C. (2013). User's guide for hysteretic capillary pressure and relative permeability functions in TOUGH2. *Technical Report LBNL-6533E*, Lawrence Berkeley National Laboratory, Berkeley, California, doi:10.2172/1164322.

Dudani, N., Bhalla, U. S. & Ray, S. (2014). *MOOSE, the multiscale object-oriented simulation environment*. New York: Springer, doi:10.1007/978-1-4614-7320-6_257-1.

Dugdale, D. (1960). Yielding of steel sheets containing slits. *J Mech Phys Solids* **8**, No. 2, 100–104, doi:10.1016/0022-5096(60)90013-2.

Dutch Government (2024). Mining act. URL https://wetten.overheid.nl/BWBR0014168/2024-05-01, accessed: 2025-03-29.

Dutch Government (2025). Water act. URL https://wetten.overheid.nl/BWBR0025458/2024-01-01, accessed: 2025-03-29.

Eaton, D. W. & Forouhideh, F. (2011). Solid angles and the impact of receiver-array geometry on microseismic moment-tensor inversion. *Geophysics* **76**, No. 6, WC77–WC85, doi:10.1190/geo2011-0077.1.

EGU Seismology ECS Team (2023). What is das? URL https://blogs.egu.eu/divisions/sm/2023/12/02/what-is-das/, accessed: 2025-06-19.

Eisner, L., Thornton, M. & Griffin, J. (2011). Challenges for microseismic monitoring. In *SEG Technical Program Expanded Abstracts 2011*, Society of Exploration Geophysicists, pp. 1519–1523, doi:10.1190/1.3627491.

Elices, M., Guinea, G. V., Gomez, J. & Planas, J. (2002). The cohesive zone model: advantages, limitations and challenges. *Eng Fract Mech* **69**, No. 2, 137–163, doi:https://doi.org/10.1016/S0013-7944(01)00083-2.

Erarslan, N. & Williams, D. J. (2012). Investigating the effect of cyclic loading on the indirect tensile strength of rocks. *Rock Mech Rock Eng* **45**, No. 3, 327–340, doi:10.1007/s00603-011-0209-7.

European Parliament and Council (2000). Directive 2000/60/EC establishing a framework for Community action in the field of water policy. *Official Journal of the European Communities* **L 327**, 1–73, URL https://eur-lex.europa.eu/legal-content/EN/TXT/?uri=CELEX%3A32000L0060.

Evans, K. F., Moriya, H., Niitsuma, H., Jones, R., Phillips, W., Genter, A., Sausse, J., Jung, R. & Baria, R. (2005). Microseismicity and permeability enhancement of hydrogeologic structures during massive fluid injections into granite at 3 km depth at the Soultz HDR site. *Geophys J Int* **160**, No. 1, 388–412, doi:10.1111/j.1365-246X.2004.02474.x.

Fadili, A., Murtaza, A. & Zitha, P. (2022). Injectivity decline by nanoparticles transport in high permeable rock. *J Petrol Sci Eng* **211**, 110121, doi:10.1016/j.petrol.2022.110121.

Fallahzadeh, S., Hossain, M., Cornwell, A. J. & Rasouli, V. (2017). Near wellbore hydraulic fracture propagation from perforations in tight rocks: the roles of fracturing fluid viscosity and injection rate. *Energies* **10**, No. 3, 359, doi:10.3390/en10030359.

Faoro, I., Elsworth, D. & Candela, T. (2016). Evolution of the transport properties of fractures subject to thermally and mechanically activated mineral alteration and redistribution. *Geofluids* **16**, No. 3, 396–407, doi:10.1111/gfl.12157.

Feng, J., Zhao, Y., Ji, D., Gao, Z. *et al.* (2021). An experimental study on bio-clogging in porous media during geothermal water reinjection. *J Water Resour Prot* **13**, No. 02, 139, doi:10.4236/jwarp.2021.132008.

Finster, M., Clark, C., Schroeder, J. & Martino, L. (2015). Geothermal produced fluids: Characteristics, treatment technologies, and management options. *Renew Sustain Energy Rev* **50**, 952–966, doi:10.1016/j.rser.2015.05.059.

Fox, D. B., Koch, D. L. & Tester, J. W. (2016). An analytical thermohydraulic model for discretely fractured geothermal reservoirs. *Water Resour Res* **52**, No. 9, 6792–6817, doi:10.1002/2016WR018666.

Franco, J., Ortiz, M., De, G., Renlie, L. & Williams, S. (2006). Sonic investigation in and around the borehole. *Oilfield Rev* **18**, 14–31, URL https://www.researchgate.net/profile/Masaei-Ito/publication/266460849_Sonic_Investigations_In_and_Around_the_Borehole/links/54b7bea90cf2bd04be33c579/Sonic-Investigations-In-and-Around-the-Borehole.pdf.

Fujita, C., Akhtar, M. S., Hidaka, R. & Nishigaki, M. (2022). Mitigation of groundwater iron-induced clogging by low-cost bioadsorbent in open loop geothermal heat pump systems. *Appl Water Sci* **12**, No. 3, 30, doi:10.1007/s13201-022-01574-x.

Garipov, T. T., Tomin, P., Rin, R., Voskov, D. V. & Tchelepi, H. A. (2018). Unified thermo-compositional-mechanical framework for reservoir simulation. *Computat Geosci* **22**, No. 4, 1039–1057, doi:10.1007/s10596-018-9737-5.

Garolera Vinent, D. (2017). *Zero-thickness interface elements in petroleum geomechanics: sand production and hydraulic fractureproblems*. Ph.D. thesis, Universitat Politècnica de Catalunya · BarcelonaTech, Barcelona, URL https://upcommons.upc.edu/bitstream/2117/168575/1/TDGV1de1.pdf.

Gasc-Barbier, M., Girma, G. & Gendre, V. (2014). Laboratory analysis of thermal fatigue in limestone. In *ISRM Regional Symposium - EUROCK 2014*, Vigo, Spain, pp. 2014–043, URL https://onepetro.org/ISRMEUROCK/proceedings/EUROCK14/EUROCK14/ISRM-EUROCK-2014-043/41646.

Geertsma, J. & De Klerk, F. (1969). A rapid method of predicting width and extent of hydraulically induced fractures. *J Petrol Technol* **21**, No. 12, 1571–1581, doi:10.2118/2458-PA.

German Environment Agency (UBA) (2011). Follow-up benchmark study – geothermal power and heat generation in Hungary. *Technical report*, Umweltbundesamt, URL https://www.umweltbundesamt.de/sites/default/files/abschlussbericht_en.pdf, accessed: 2025-05-16.

Ghassemi, A. (2012). A review of some rock mechanics issues in geothermal reservoir development. *Geotech Geol Eng* **30**, 647–664, doi:10.1007/s10706-012-9508-3.

Ghassemi, A., Tarasovs, S. & Cheng, A.-D. (2007). A 3-d study of the effects of thermomechanical loads on fracture slip in enhanced geothermal reservoirs. *Int J Rock Mech Min Sci* **44**, No. 8, 1132–1148, doi:10.1016/j.ijrmms.2007.07.016.

Gino, E., Starosvetsky, J., Kurzbaum, E. & Armon, R. (2010). Combined chemical-biological treatment for prevention/rehabilitation of clogged wells by an iron-oxidizing bacterium. *Environ Sci Technol* **44**, No. 8, 3123–3129, doi:10.1021/es903703v.

Goyal, K. & Conant, T. (2010). Performance history of The Geysers steam field, California, USA. *Geothermics* **39**, No. 4, 321–328, doi:10.1016/j.geothermics.2010.09.007.

Grant, M. A., Clearwater, J., Quinão, J., Bixley, P. F. & Brun, M. L. (2013). Thermal stimulation of geothermal wells: a review of field data. In *38th Workshop on Geothermal Reservoir Engineering*, Stanford, Canifornia: Stanford University, URL https://pangea.stanford.edu/ERE/pdf/IGAstandard/SGW/2013/Grant1.pdf.

Grechka, V., Howell, B., Li, Z., Furtado, D. & Straus, C. (2021). Microseismic at HFTS2: A story of three stimulated wells. In *The 9th Unconventional Resources Technology Conference*, Houston, Texas, USA: American Association of Petroleum Geologists, doi:10.15530/urtec-2021-5517, URL URTEC-2021-5517-MS.

Guinot, F. & Marnat, S. (2021). Death by injection: reopening the Klaipėda geothermal cold case. In *46th Workshop on Geothermal Reservoir Engineering*, Stanford, California, URL https://pangea.stanford.edu/ERE/db/IGAstandard/record_detail.php?id=29561.

Gunnarsson, G. (2011). Mastering reinjection in the Hellishóidi field, SW-Iceland: A story of successes and failures. In *36th Workshop on Geothermal Reservoir Gngineering*, Stanford, Canifornia: Stanford University, URL https://es.stanford.edu/ERE/pdf/IGAstandard/SGW/2011/gunnarsson1.pdf.

Guo, F., Morgenstern, N. & Scott, J. (1993). Interpretation of hydraulic fracturing breakdown pressure. *Int. J. Rock Mech. Min. Sci. Geomech. Abstrs.* **30**, No. 6, 617–626, doi:10.1016/0148-9062(93)91221-4.

Haklıdır, F. S. T. & Balaban, T. Ö. (2019). A review of mineral precipitation and effective scale inhibition methods at geothermal power plants in West Anatolia (Turkey). *Geothermics* **80**, 103–118, doi:10.1016/j.geothermics.2019.02.013.

Hampton, J., Gutierrez, M., Matzar, L., Hu, D. & Frash, L. (2018). Acoustic emission characterization of microcracking in laboratory-scale hydraulic fracturing tests. *J Rock Mech Geotech Eng* **10**, No. 5, 805–817, doi:10.1016/j.jrmge.2018.03.007.

Häring, M. O., Schanz, U., Ladner, F. & Dyer, B. C. (2008). Characterisation of the Basel 1 enhanced geothermal system. *Geothermics* **37**, No. 5, 469–495, doi:10.1016/j.geothermics.2008.06.002.

Hartog, A. H. (2017). *An introduction to distributed optical fibre sensors*. CRC Press, doi:10.1201/9781315119014.

Hasani, A. (2024). *Distributed Acoustic Sensing using straight, sinusoidally and helically shaped fibres for seismic applications*. Ph.D. thesis, Delft University of Technology, doi:https://doi.org/10.4233/uuid:3b23b63b-69be-4c0e-90c0-3312eae1d871.

He, H., Xiong, X., Wu, T., Hu, R., Chen, Y.-F. & Yang, Z. (2025). Pore-scale study of particle transport and clogging mechanisms in a porous micromodel. *Sep Purif Technol* **362**, 131929, doi:10.1016/j.seppur.2025.131929.

Heinrich, J. C., Huyakorn, P. S., Zienkiewicz, O. C. & Mitchell, A. R. (1977). An 'upwind' finite element scheme for two-dimensional convective transport equation. *Int J Numer Meth Eng* **11**, No. 1, 131–143, doi:10.1002/nme.1620110113.

Herrmann, R. B. (2013). Computer Programs in Seismology: An evolving tool for instruction and research. *Seismol Res Lett* **84**, No. 6, 1081–1088, doi:10.1785/0220110096.

Hillerborg, A., Modéer, M. & Petersson, P.-E. (1976). Analysis of crack formation and crack growth in concrete by means of fracture mechanics and finite elements. *Cement Concrete Res* **6**, No. 6, 773–781, doi:10.1016/0008-8846(76)90007-7.

Hofmann, H., Zimmermann, G., Farkas, M., Huenges, E., Zang, A., Leonhardt, M., Kwiatek, G., Martinez-Garzon, P., Bohnhoff, M., Min, K.-B., Fokker, P., Westaway, R., Bethmann, F., Meier, P., Yoon, K. S., Choi, J. W., Lee, T. J. & Kim, K. Y. (2019). First field application of cyclic soft stimulation at the Pohang Enhanced Geothermal System site in Korea. *Geophys J Int* **217**, No. 2, 926–949, doi:10.1093/gji/ggz058.

Hofmann, H., Zimmermann, G., Huenges, E., Regenspurg, S., Aldaz, S., Milkereit, C., Heimann, S., Dahm, T., Zang, A., Grigoli, F., Karvounis, D., Broccardo, M., Wiemer, S., Hjörleifsdóttir, V., Kristjánsson, B. R., Hersir, G. P., Ásgeirsdóttir, R. S., Magnússon, R. & Árnadóttir, S. (2021). Soft stimulation treatment of geothermal well RV-43 to meet the growing heat demand of Reykjavik. *Geothermics* **96**, 102146, doi:10.1016/j.geothermics.2021.102146.

Holl, H.-G., Hurter, S., Saadat, A., Köhler, S., Wolfgramm, M., Zimmermann, G., Trautwein, U., Winter, H., Legarth, B. & Huenges, E. (2003). First hand experience in a second hand borehole: Hydraulic experiments and scaling in the geothermal well Groß Schönebeck after reopening. In *The International Geothermal Conference*, S01-Paper060, Reykjavík, Iceland, pp. 8–13, URL https://gfzpublic.gfz-potsdam.de/pubman/item/item_229995.

Hong, C.-Y., Yang, R.-Y., Huang, Z.-W., Zhuang, X.-Y., Wen, H.-T. & Hu, X.-L. (2023). Enhance liquid nitrogen fracturing performance on hot dry rock by cyclic injection. *Petrol Sci* **20**, No. 2, 951–972, doi:10.1016/j.petsci.2022.07.004.

Horne, R. N. (1982). Effects of water injection into fractured geothermal reservoirs: a summary of experience worldwide. *Technical Report 860855*, Stanford University, Stanford California, doi:https://doi.org/10.2172/860855, URL https://pangea.stanford.edu/ERE/pdf/SGPreports/SGP-TR-057.pdf.

Hou, J., Wei, B., Du, Q., Wang, J., Wang, Q. & Zhang, G. (2016). Production prediction of cyclic multi-thermal fluid stimulation in a horizontal well. *J Pet Sci Eng* **146**, 949–958, doi:10.1016/j.petrol.2016.08.008.

IEA (2024a). The future of geothermal energy. *Technical report*, IEA, Paris, URL https://www.iea.org/reports/the-future-of-geothermal-energy.

IEA (2024b). World energy outlook 2024. *Technical report*, International Energy Agency, Paris, URL https://www.iea.org/reports/world-energy-outlook-2024.

IGA (2024). Geothermal energy database. URL https://worldgeothermal.org/geothermal-data/geothermal-energy-database, accessed: 2025-03-26.

International Society for Rock Mechanics (1978). Suggested methods for determining the strength of rock materials in triaxial compression. *Int J Rock Mech Min Sci Geomech Abstr* **15**, No. 2, 47–51, doi:10.1016/0148-9062(78)91677-7.

Israelsson, J. I. (1996). Short descriptions of UDEC and 3DEC. *Dev Geotech Eng* **79**, 523–528, doi:10.1016/S0165-1250(96)80041-1.

Itoi, R., Fukuda, M., Jinno, K., Hirowatari, K., Shinohara, N. & Tomita, T. (1989). Long-term experiments of waste water injection in the Otake geothermal field, Japan. *Geothermics* **18**, No. 1-2, 153–159, doi:10.1016/0375-6505(89)90022-9.

Jacquey, A. B. (2017). *Coupled thermo-hydro-mechanical processes in geothermal reservoirs: a multiphysic and multiscale approach linking geology and 3D numerical modelling*. Ph.D. thesis, RWTH Aachen, Aachen, doi:10.18154/RWTH-2017-09790.

Jaeger, J. C., Cook, N. G. & Zimmerman, R. (2009). *Fundamentals of rock mechanics*. 4th edition edn., Wiley-Blackwell.

Jafari, A., Vahab, M., Broumand, P. & Khalili, N. (2023). An eXtended finite element method implementation in COMSOL multiphysics: Thermo-hydro-mechanical modeling of fluid flow in discontinuous porous media. *Comput Geotech* **159**, 103707, doi:10.1016/j.compgeo.2023.105458.

Jarrahian, K., Mackay, E., Singleton, M., Mohammadi, S., Heath, S. & Pessu, F. (2024). Scale control in geothermal wells – what are the options for effective and economic scale management? In *SPE Oilfield Scale Symposium*, SPE, doi:10.2118/218737-MS.

Jeanne, P., Rutqvist, J., Hartline, C., Garcia, J., Dobson, P. F. & Walters, M. (2014). Reservoir structure and properties from geomechanical modeling and microseismicity analyses associated with an enhanced geothermal system at the geysers, california. *Geothermics* **51**, 460–469, doi:10.1016/j.geothermics.2014.02.003.

Jeong, H. Y., Jun, S.-C., Cheon, J.-Y. & Park, M. (2018). A review on clogging mechanisms and managements in aquifer storage and recovery (asr) applications. *Geosci J* **22**, 667–679, doi:10.1007/s12303-017-0073-x.

Johnson, L. R. (2014). A source model for induced earthquakes at the geysers geothermal reservoir. *Pure Appl Geophys* **171**, No. 8, 1625–1640, doi:10.1007/s00024-014-0798-7.

Jost, M. L., Büßelberg, T., Jost, Ö. & Harjes, H.-P. (1998). Source parameters of injection-induced microearthquakes at 9 km depth at the KTB deep drilling site, Germany. *Bull Seismol Soc Am* **88**, No. 3, 815–832, doi:10.1785/BSSA0880030815.

Jost, M. L. & Herrmann, R. B. (1989). A student's guide to and review of moment tensors. *Seismol Res Lett* **60**, No. 2, 37–57, doi:10.1785/gssrl.60.2.37.

Julian, B. R., Foulger, G. R. & Monastero, F. (2007). Microearthquake moment tensors from the COSO geothermal area. In *32nd Workshop on Geothermal Reservoir Engineering*, SGP-TR-183, Stanford, Canifornia: Stanford University, URL https://pangaea.stanford.edu/ERE/pdf/IGAstandard/SGW/2007/julian.pdf.

Jung, S., Diaz, M. B., Kim, K. Y., Hofmann, H. & Zimmermann, G. (2021). Fatigue behavior of granite subjected to cyclic hydraulic fracturing and observations on pressure for fracture growth. *Rock Mech Rock Eng* , 1–14doi:10.1007/s00603-021-02383-5.

Kallesøe, A. J., Vangkilde-Pedersen T., Nielsen, J. E., Bakema, G., Egermann, P., Maragna, C., Hahn, F., Guglielmetti, L. & Koornneef, J. (2021). HEATSTORE–Underground thermal energy storage (UTES)-State of the art, example cases and lessons learned. In *World Geothermal Congress 2020+1*, Reykjavik, Iceland: International Geothermal Asssociation, p. 9, URL https://www.geothermal-energy.org/pdf/IGAstandard/WGC/2020/29091.pdf, accessed: 2025-05-16.

Kalvani, N., Mesdaghinia, A., Yaghmaeian, K., Abolli, S., Saadi, S., Alimohammadi, M. & Rashidi Mehrabadi, A. (2021). Evaluation of iron and manganese removal effectiveness

by treatment plant modules based on water pollution index; a comprehensive approach. *J Environ Health Sci Eng* **19**, 1005–1013, doi:10.1007/s40201-021-00665-2.

Kamila, Z., Kaya, E. & Zarrouk, S. J. (2021). Reinjection in geothermal fields: An updated worldwide review 2020. *Geothermics* **89**, 101970, doi:10.1016/j.geothermics.2020.101970.

Kang, H., Zhang, J., Fan, X. & Huang, Z. (2020). Cyclic injection to enhance hydraulic fracturing efficiency: Insights from laboratory experiments. *Geofluids* **2020**, 844293, doi:10.1155/2020/8844293.

Karrenbach, M., Cole, S., Ridge, A., Boone, K., Kahn, D., Rich, J., Silver, K. & Langton, D. (2019). Fiber-optic distributed acoustic sensing of microseismicity, strain and temperature during hydraulic fracturing. *Geophysics* **84**, No. 1, D11–D23, doi:10.1190/geo2017-0396.1.

Kaya, E., Zarrouk, S. J. & O'Sullivan, M. J. (2011). Reinjection in geothermal fields: a review of worldwide experience. *Renew Sustain Energy Rev* **15**, No. 1, 47–68, doi:10.1016/j.rser.2010.07.032.

Khoramishad, H., Crocombe, A., Katnam, K. & Ashcroft, I. (2010). Predicting fatigue damage in adhesively bonded joints using a cohesive zone model. *Int J Fatigue* **32**, No. 7, 1146–1158, doi:10.1016/j.ijfatigue.2009.12.013.

Khristianovic, S. A. & Zheltov, Y. P. (1955). Formation of vertical fractures by means of highly viscous liquid. In *The 4th World Petroleum Congress*, Rome, URL http://onepetro.org/WPCONGRESS/proceedings-pdf/WPC04/All-WPC04/WPC-6132/2082397/wpc-6132.pdf/1.

Kindle, C., Mercer, B., Elmore, R., Blair, S. & Myers, D. (1984). Geothermal injection treatment: process chemistry, field experiences, and design options. *Technical report*, Pacific Northwest National Laboratory (PNNL), Richland, WA, doi:10.2172/6281733.

Kluge, C., Blöcher, G., Barnhoorn, A., Schmittbuhl, J. & Bruhn, D. (2021). Permeability evolution during shear zone initiation in low-porosity rocks. *Rock Mech Rock Eng* **54**, No. 10, 5221–5244, doi:10.1007/s00603-020-02356-0.

Koh, J., Roshan, H. & Rahman, S. S. (2011). A numerical study on the long term thermo-poroelastic effects of cold water injection into naturally fractured geothermal reservoirs. *Comput Geotech* **38**, No. 5, 669–682, doi:10.1016/j.compgeo.2011.03.007.

Kolditz, O., Bauer, S., Bilke, L., Böttcher, N., Delfs, J. O., Fischer, T., Görke, U. J., Kalbacher, T., Kosakowski, G., McDermott, C. I., Park, C. H., Radu, F., Rink, K., Shao, H., Shao, H. B., Sun, F., Sun, Y. Y., Singh, A. K., Taron, J., Walther, M., Wang, W., Watanabe, N., Wu, Y., Xie, M., Xu, W. & Zehner, B. (2012). OpenGeoSys: an open-source initiative for numerical simulation of thermo-hydro-mechanical/chemical (THM/C) processes in porous media. *Environ Earth Sci* **67**, No. 2, 589–599, doi:10.1007/s12665-012-1546-x.

Kottsova, A., Bruhn, D., Saar, M. O., Veeger, F. & Brehme, M. (2022). Clogging mechanisms in geothermal operations: theoretical examples and an applied study. In *European Geothermal Congress 2022*, Berlin, Germany, URL https://publica-rest.fraunhofer.de/server/api/core/bitstreams/472349af-77af-47c8-8208-7b5f9aa8cf5d/content.

Kramers, L., van Wees, J.-D., Pluymaekers, M., Kronimus, A. & Boxem, T. (2012). Direct heat resource assessment and subsurface information systems for geothermal aquifers; the Dutch perspective. *Neth J Geosci* **91**, No. 4, 637–649, doi:10.1017/S0016774600000421.

Krishna Mohan, K., Reed, M. G. & Scott Fogler, H. (1999). Formation damage in smectitic sandstones by high ionic strength brines. *Colloids Surf , A* **154**, No. 3, 249–257, doi:10.1016/S0927-7757(98)00338-0.

Krogstad, S., Lie, K. A., Møyner, O., Nilsen, H. M., Raynaud, X. & Skaflestad, B. (2015). MRST-AD - an open-source framework for rapid prototyping and evaluation of reservoir simulation problems. In *2015 SPE Reservoir Simulation Symposium*, vol. 3, Houston, Texas: Society of Petroleum Engineers, pp. 2080–2105, doi:10.2118/173317-ms.

Köhl, B., Elsner, M. & Baumann, T. (2020). Hydrochemical and operational parameters driving carbonate scale kinetics at geothermal facilities in the Bavarian Molasse Basin. *Geotherm Energy* **8**, No. 1, 26, doi:10.1186/s40517-020-00180-x.

Lanru, J. & Ove, S. (2007). *Fundamentals of discrete element methods for rock engineering*, vol. 85. Amsterdam: Elsevier, URL https://www.sciencedirect.com/bookseries/developments-in-geotechnical-engineering/vol/85/suppl/C.

Lauwerier, H. A. (1955). The transport of heat in an oil layer caused by the injection of hot fluid. *J. Appl. Sci. Res.* **5**, No. 2-3, 145–150, doi:10.1007/BF03184614.

Le Calvez, J. H., Klem, R. C., Bennett, L., Erwemi, A., Craven, M. & Palacio, J. C. (2007). Real-time microseismic monitoring of hydraulic fracture treatment: A tool to improve completion and reservoir management. In *Hydraulic Fracturing Technology Conference*, SPE-106159-MS, College Station, Texas, USA: SPE, doi:10.2118/106159-MS.

Lei, Q. & Barton, N. (2022). On the selection of joint constitutive models for geomechanics simulation of fractured rocks. *Comput Geotech* **145**, 104707, doi:10.1016/j.compgeo.2022.104707.

Lellouch, A., Lindsey, N. J., Ellsworth, W. L. & Biondi, B. L. (2020). Comparison between distributed acoustic sensing and geophones: Downhole microseismic monitoring of the FORGE geothermal experiment. *Seismol Res Lett* **91**, No. 6, 3256–3268, doi:10.1785/0220200149.

Lellouch, A., Luo, B., Huot, F., Clapp, R. G., Given, P., Biondi, E., Nemeth, T., Nihei, K. T. & Biondi, B. L. (2022). Microseismic analysis over a single horizontal distributed acoustic sensing fiber using guided waves. *Geophysics* **87**, No. 3, KS83–KS95, doi:10.1190/geo2021-0418.1.

Lepillier, B., Yoshioka, K., Parisio, F., Bakker, R. & Bruhn, D. (2020). Variational phase-field modeling of hydraulic fracture interaction with natural fractures and application to enhanced geothermal systems. *J Geophys Res Solid Earth* **125**, No. 7, doi:10.1029/2020JB019856.

Lequesne, C. (2009). *Modeling of fracture in heavy steel welded beam-to-column connection submitted to cyclic loading by finite elements*. Ph.D. thesis, Université de Liège, Liège, URL https://orbi.uliege.be/handle/2268/315091.

Lequesne, C., Plumier, A., Degee, H. & Habraken, A. M. (2006). Numerical study of the fatigue crack in welded beam-to-column connection using cohesive zone model. *Key Eng Mater* **324-325**, 847–850, doi:10.4028/www.scientific.net/kem.324-325.847.

Li, L., Tan, J., Wood, D. A., Zhao, Z., Becker, D., Lyu, Q., Shu, B. & Chen, H. (2019). A review of the current status of induced seismicity monitoring for hydraulic fracturing in unconventional tight oil and gas reservoirs. *Fuel* **242**, 195–210, doi:10.1016/j.fuel.2019.01.026.

Li, Y., Karrenbach, M. & Ajo-Franklin, J. (2022). *Distributed acoustic sensing in geophysics: Methods and applications*. John Wiley & Sons, doi:10.1002/9781119521808.

Liaudat, J., Dieudonné, A. C. & Vardon, P. J. (2023). Modelling gas fracturing in saturated clay samples using triple-node zero-thickness interface elements. *Comput Geotech* **154**, 105128, doi:10.1016/j.compgeo.2022.105128.

Lima, M. G., Vogler, D., Querci, L., Madonna, C., Hattendorf, B., Saar, M. O. & Kong, X.-Z. (2019). Thermally driven fracture aperture variation in naturally fractured granites. *Geotherm Energy* **7**, 1–28, doi:10.1186/s40517-019-0140-9.

Liu, Y., Dai, F., Xu, N., Zhao, T. & Feng, P. (2018). Experimental and numerical investigation on the tensile fatigue properties of rocks using the cyclic flattened Brazilian disc method. *Soil Dyn. Earthq. Eng.* **105**, 68–82, doi:10.1016/j.soildyn.2017.11.025.

Livermore Software Technology (2007). LS-DYNA ® keyword user's manual: Volume I. URL www.lstc.com.

Lu, Y., Elsworth, D. & Wang, L. (2013). Microcrack-based coupled damage and flow modeling of fracturing evolution in permeable brittle rocks. *Comput Geotech* **49**, 226–244, doi:10.1016/j.compgeo.2012.11.009.

Luo, W., Dieudonné, A.-C., Ouf, J., Amann, F. & Vardon, P. (2025a). A cohesive zone model for fatigue under cyclic thermo-hydro-mechanical loading. *Submitted* .

Luo, W., Dieudonné, A.-C., Ouf, J., Amann, F. & Vardon, P. (2025b). Numerical study of near-borehole coupled thermo-hydro-mechanical processes during stimulation to a synthetic geothermal reservoir. *Submitted* .

Luo, W., Drijkoningen, G., Eltayieb, M., Amann, F. & Vardon, P. (2025c). Feasibility study of single-well dual-cable das for micro-seismic monitoring of geothermal operations. *Submitted* .

Luo, W., Kottsova, A., Vardon, P., Dieudonné, A. & Brehme, M. (2023). Mechanisms causing injectivity decline and enhancement in geothermal projects. *Renew Sustain Energy Rev* **185**, 113623, doi:10.1016/j.rser.2023.113623.

Luo, W., Liaudat, J., Ouf, J., Dieudonné, A.-C., Amann, F. & Vardon, P. J. (2025d). Numerical modelling of fracturing processes during cold water injection into geothermal reservoirs: Verification and qualitative validation. *Comput Geotech* **183**, 107186, doi:10.1016/j.compgeo.2025.107186.

Luviano, M. S., Flores Armenta, M. & Montes, M. R. (2015). Thermal stimulation to improve the permeability of geothermal wells in Los Humeros geothermal field, Mexico. In *World Geothermal Congress 2015*, Melbourne, Australia, URL https://www.worldgeothermal.org/pdf/IGAstandard/WGC/2015//22017.pdf.

Ma, L., She, W., Wu, G., Yang, J., Phurbu, D. & Jiang, H. (2021). Influence of temperature and sulfate concentration on the sulfate/sulfite reduction prokaryotic communities in the Tibetan hot springs. *Microorganisms* **9**, No. 3, 583, doi:10.3390/microorganisms9030583.

Ma, Z.-y., Xu, Y., Zhai, M.-j. & Wu, M. (2017). Clogging mechanism in the process of reinjection of used geothermal water: A simulation research on Xianyang No. 2 reinjection well in a super-deep and porous geothermal reservoir. *J Groundw Sci Eng Vol* **5**, No. 4, URL https://gwse.iheg.org.cn/en/article/dxskxygc/2017/4/311.

Mad Zahir, M. H., Abdul Aziz, K. M., Ghazali, A. R. & Abdul Latiff, A. H. (2023). Effectiveness of fiber optic distributed acoustic sensing (DAS) in vertical seismic profiling (VSP) field survey. *Appl Sci* **13**, No. 8, 5002, doi:10.3390/app13085002.

Maiti, S. & Geubelle, P. H. (2005). A cohesive model for fatigue failure of polymers. *Eng Fract Mech* **72**, No. 5, 691–708, doi:10.1016/j.engfracmech.2004.06.005.

Manzella, A., Giamberini, S., Montegrossi, G., Scrocca, D., Chiarabba, C., Valkering, P., Delvaux, S., Harcouët-Menou, V., Branchu, F., Maurel, C., Bozkurt, C., Nádor, A., Guðjónsdóttir, S. R., Guðmundsdóttir, M., Ravier, G., Cuenot, N., Bonciani, D., Torsello, L., Luchini, M., Batini, F. & Dumas, P. (2021). Compilation of recommendations on environmental regulations. *Technical Report D4.2*, GEOENVI project technical report, URL https://www.geoenvi.eu/wp-content/uploads/2021/03/D4.2-Recommendations-on-environmental-regulations.pdf, accessed: 2025-05-16.

Markó, Á., Brehme, M., Pedretti, D., Zimmermann, G. & Huenges, E. (2024). Controls of low injectivity caused by interaction of reservoir and clogging processes in a sedimentary geothermal aquifer (Mezőberény, Hungary). *Geotherm Energy* **12**, No. 1, 40, doi:10.1186/s40517-024-00317-2.

Markó, Á., Mádl-Szőnyi, J. & Brehme, M. (2021). Injection related issues of a doublet system in a sandstone aquifer - A generalized concept to understand and avoid problem sources in geothermal systems. *Geothermics* **97**, 102234, doi:10.1016/j.geothermics.2021.102234.

Martyushev, D. A., Yang, Y., Kazemzadeh, Y., Wang, D. & Li, Y. (2024). Understanding the mechanism of hydraulic fracturing in naturally fractured carbonate reservoirs: Microseismic monitoring and well testing. *Arab J Sci Eng* **49**, No. 6, 8573–8586, doi:10.1007/s13369-023-08513-1.

Maxwell, S. C. & Cipolla, C. (2011). What Does microseismicity tell us about hydraulic fracturing? In *SPE Annual Technical Conference and Exhibition*, Denver, Colorado, USA: SPE, doi:10.2118/146932-MS.

McClure, M. W. & Horne, R. N. (2014). An investigation of stimulation mechanisms in enhanced geothermal systems. *Int J Rock Mech Min Sci* **72**, 242–260, doi:10.1016/j.ijrmms.2014.07.011.

Meng, X., Chen, H., Niu, F., Tang, Y., Yin, C. & Wu, F. (2018). Microseismic monitoring of stimulating shale gas reservoir in SW China: 1. An improved matching and locating technique for downhole monitoring. *J Geophys Res Solid Earth* **123**, No. 2, 1643–1658, doi:10.1002/2017JB014488.

Meng, X., Liu, Y., Ning, Z., Dong, J., Liang, G. & Wang, Y. (2023). Fatigue performance of hydraulic asphalt concrete under uniaxial constant-amplitude tensile cycle loading. *J Buld Eng* **80**, 108070, doi:10.1016/j.jobe.2023.108070.

Messer, P., Pye, D. & Gallus, J. (1978). Injectivity restoration of a hot-brine geothermal injection well. *J Petrol Technol* **30**, No. 09, 1225–1230, doi:10.2118/6761-PA.

Mi, Y., Crisfield, M. A., Davies, G. A. O. & Hellweg, H. B. (1998). Progressive delamination using interface elements. *J Compos Mater* **32**, No. 14, 1246–1272, doi:10.1177/002199839803201401.

Mijnlieff, H. F. (2020). Introduction to the geothermal play and reservoir geology of the Netherlands. *Neth J Geosci* **99**, e2, doi:10.1017/njg.2020.2.

Min, K. (2013). *Numerical modelling of hydraulic fracture propagation using thermo-hydro-mechanical analysis with brittle damage model by finite element method*. Ph.D. thesis, Texas A & M University, College Station, Texas, URL `https://hdl.handle.net/1969.1/150961`.

Moghadasi, J., Müller-Steinhagen, H., Jamialahmadi, M. & Sharif, A. (2004). Theoretical and experimental study of particle movement and deposition in porous media during water injection. *J Pet Sci Eng* **43**, No. 3-4, 163–181, doi:10.1016/j.petrol.2004.01.005.

Munoz, J. J., Galvanetto, U. & Robinson, P. (2006). On the numerical simulation of fatigue driven delamination with interface elements. *Int J Fatigue* **28**, No. 10, 1136–1146, doi:10.1016/j.ijfatigue.2006.02.003.

Navidtehrani, Y., Betegón, C., Zimmerman, R. W. & Martínez-Pañeda, E. (2022). Griffith-based analysis of crack initiation location in a brazilian test. *Int J Rock Mech Min Sci* **159**, 105227, doi:https://doi.org/10.1016/j.ijrmms.2022.105227.

Newcomer, M. E., Hubbard, S. S., Fleckenstein, J. H., Maier, U., Schmidt, C., Thullner, M., Ulrich, C., Flipo, N. & Rubin, Y. (2016). Simulating bioclogging effects on dynamic riverbed permeability and infiltration. *Water Resour Res* **52**, No. 4, 2883–2900, doi:10.1002/2015WR018351.

Nguyen, M. C., Dejam, M., Fazelalavi, M., Zhang, Y., Gay, G. W., Bowen, D. W., Spangler, L. H., Zaluski, W. & Stauffer, P. H. (2021). Skin factor and potential formation damage from chemical and mechanical processes in a naturally fractured carbonate aquifer with implications to co_2 sequestration. *Int J Greenh Gas Control* **108**, 103326, doi:10.1016/j.ijggc.2021.103326.

Nguyen, V. P., Lian, H., Rabczuk, T. & Bordas, S. (2017). Modelling hydraulic fractures in porous media using flow cohesive interface elements. *Eng Geol* **225**, 68–82, doi:10.1016/j.enggeo.2017.04.010.

Niu, Y., Wang, G., Wang, J., Liu, X., Zhang, R., Qiao, J. & Zhang, J. (2023). Experimental study on thermal fatigue damage and failure mechanisms of basalt exposed to high-temperature treatments. *Fatigue Fract Eng Mater Struct* **46**, No. 8, 2909–2928, doi:10.1111/ffe.14052.

Nojavan, S., Schesser, D. & Yang, Q. (2016a). A two-dimensional in situ fatigue cohesive zone model for crack propagation in composites under cyclic loading. *Int J Fatigue* **82**, 449–461, doi:10.1016/j.ijfatigue.2015.08.029.

Nojavan, S., Schesser, D. & Yang, Q. D. (2016b). An in situ fatigue-CZM for unified crack initiation and propagation in composites under cyclic loading. *Compos Struct* **146**, 34–49, doi:10.1016/j.compstruct.2016.02.060.

Nolen-Hoeksema, R. C. & Ruff, L. J. (2001). Moment tensor inversion of microseisms from the B-sand propped hydrofracture, M-site, Colorado. *Tectonophysics* **336**, No. 1-4, 163–181, doi:10.1016/S0040-1951(01)00100-7.

Norbeck, J. H., McClure, M. W. & Horne, R. N. (2018). Field observations at the Fenton Hill enhanced geothermal system test site support mixed-mechanism stimulation. *Geothermics* **74**, 135–149, doi:10.1016/j.geothermics.2018.03.003.

Ochi, J. & Vernoux, J.-F. (1998). Permeability decrease in sandstone reservoirs by fluid injection. *J Hydrol* **208**, No. 3-4, 237–248, doi:10.1016/S0022-1694(98)00169-3.

Ohtsu, M. (1991). Simplified moment tensor analysis and unified decomposition of acoustic emission source: Application to in situ hydrofracturing test. *J Geophys Res Solid Earth* **96**, No. B4, 6211–6221, doi:10.1029/90JB02689.

Ontoy, Y., Molling, P., Xu, T., SpycherM, N., Parini, M. & Pruess, K. (2003). Scaling of hot brine injection wells: supplementing field studies with reactive transport modeling. In *TOUGH Symposium*, Berkeley, California: Lawrence Berkeley National Laboratory, URL https://tough.lbl.gov/assets/files/02/documentation/proceedings/2003-OntoyMollingXuSpycher.pdf.

Owen, A. (1984). Artificial diffusion in the numerical modelling of the advective transport of salinity. *Appl Math Model* **8**, No. 2, 116–120, doi:10.1016/0307-904X(84)90063-5.

Pambudi, N. A., Itoi, R., Yamashiro, R., Alam, B. Y. C. S., Tusara, L., Jalilinasrabady, S. & Khasani, J. (2015). The behavior of silica in geothermal brine from dieng geothermal power plant, Indonesia. *Geothermics* **54**, 109–114, doi:10.1016/j.geothermics.2014.12.003.

Park, S., Xie, L., Kim, K.-I., Kwon, S., Min, K.-B., Choi, J., Yoon, W.-S. & Song, Y. (2017). First hydraulic stimulation in fractured geothermal reservoir in pohang PX-2 well. *Procedia Engineer* **191**, 829–837, doi:10.1016/j.proeng.2017.05.250.

Patel, S. M., Sondergeld, C. H. & Rai, C. S. (2017). Laboratory studies of hydraulic fracturing by cyclic injection. *Int J Rock Mech Min Sci* **95**, 8–15, doi:10.1016/j.ijrmms.2017.03.008.

Peyret, O., Drew, J., Mack, M., Brook, K., Maxwell, S. & Cipolla, C. (2012). Subsurface to surface microseismic monitoring for hydraulic fracturing. In *SPE Annual Technical Conference and Exhibition*, SPE-159670-MS, San Antonio, Texas, USA: SPE, doi:10.2118/159670-MS.

Planbureau voor de Leefomgeving (2020). Netherlands climate and energy outlook 2020 - Summary. *Technical report*, Planbureau voor de Leefomgeving, The Hague, URL https://www.pbl.nl/uploads/default/downloads/pbl-2020-netherlands-climate-and-energy-outlook-2020-summary-4299.pdf.

Platform Geothermie, DAGO, Wartenetwerk & EBN (2018). Master plan geothermal energy in the Netherlands. *Technical report*, URL @techreport{2018-EBN-MasterPlan, title={{Masterplangeothermalenergyintheh Netherlands}}, year={2018}, institution={{PlatformGeothermie}and{DAGO}and{Wartenetwerk}and{EBN}}}.

Pluymakers, A., Muntendam-Bos, A. G. & Niemeijer, A. (2023). Induced seismicity: a global phenomenon with special relevance to the Dutch subsurface. *Neth J Geosci* **102**, e2, doi:10.1017/njg.2023.2.

Podgorney, R., Finnila, A., Simmons, S. & McLennan, J. (2021). A reference thermal-hydrologic-mechanical native state model of the Utah FORGE enhanced geothermal site. *Energies* **14**, No. 16, 4758, doi:10.3390/en14164758.

Portier, S., Vuataz, F.-D., Nami, P., Sanjuan, B. & Gérard, A. (2009). Chemical stimulation techniques for geothermal wells: experiments on the three-well EGS system at Soultz-sous-Forêts, France. *Geothermics* **38**, No. 4, 349–359, doi:10.1016/j.geothermics.2009.07.001.

Priisholm, S., Nielsen, B. L. & Haslund, O. (1987). Fines migration, blocking, and clay swelling of potential geothermal sandstone reservoirs, Denmark. *SPE Formation Evaluation* **2**, No. 02, 168–178, doi:10.2118/15199-PA.

Pérez Carreras, A. (2018). *T-H-M coupling with large advection in fractured rock masses using zero-thickness interface elements*. Ph.D. thesis, Universitat Politècnica de Catalunya · BarcelonaTech, Barcelona, URL http://hdl.handle.net/2117/341611.

Qazvini, S., Golkari, A., Azdarpour, A., Santos, R. M., Safavi, M. S. & Norouzpour, M. (2021). Experimental and modelling approach to investigate the mechanisms of formation damage due to calcium carbonate precipitation in carbonate reservoirs. *J Petrol Sci Eng* **205**, 108801, doi:10.1016/j.petrol.2021.108801.

Ranjbar, A., Hassani, H. & Shahriar, M. J. A., K.and Shahrabi (2020). Thermo-hydro-mechanical modeling of fault discontinuities using zero-thickness interface element. *J Rock Mech Geotech Eng* **12**, No. 1, 74–88, doi:10.1016/j.jrmge.2019.05.005.

Rezaeizadeh, M., Hajiabadi, S. H., Aghaei, H. & Blunt, M. J. (2021). Pore-scale analysis of formation damage; a review of existing digital and analytical approaches. *Adv Colloid Interface Sci* **288**, 102345, doi:10.1016/j.cis.2020.102345.

Rinck-Pfeiffer, S., Ragusa, S., Sztajnbok, P. & Vandevelde, T. (2000). Interrelationships between biological, chemical, and physical processes as an analog to clogging in aquifer storage and recovery (ASR) wells. *Water Res* **34**, No. 7, 2110–2118, doi:10.1016/S0043-1354(99)00356-5.

Robinson, P., Galvanetto, U., Tumino, D., Bellucci, G. & Violeau, D. (2005). Numerical simulation of fatigue-driven delamination using interface elements. *Int J Numer Meth Eng* **63**, No. 13, 1824–1848, doi:10.1002/nme.1338 .

Roe, K. & Siegmund, T. (2003). An irreversible cohesive zone model for interface fatigue crack growth simulation. *Eng Fract Mech* **70**, No. 2, 209–232, doi:10.1016/S0013-7944(02)00034-6.

Rosenbrand, E., Kjøller, C., Riis, J. F., Kets, F. & Fabricius, I. L. (2015). Different effects of temperature and salinity on permeability reduction by fines migration in berea sandstone. *Geothermics* **53**, 225–235, doi:10.1016/j.geothermics.2014.06.004.

Rosnes, J., Graue, A. & Lien, T. (1991). Activity of sulfate-reducing bacteria under simulated reservoir conditions. *SPE Prod Eng* **6**, No. 02, 217–220, doi:10.2118/19429-PA.

Rühaak, W., Heldmann, C.-D., Pei, L. & Sass, I. (2017). Thermo-hydro-mechanical-chemical coupled modeling of a geothermally used fractured limestone. *Int J Rock Mech Min Sci* **100**, 40–47, doi:10.1016/j.ijrmms.2017.10.019.

Rybach, L. (2003). Regulatory framework for geothermal in Europe–with special reference to Germany, France, Hungary, Romania, and Switzerland. In *Geothermal Training Programme*, IGC2003, Reykjavík, Iceland: The United Nations University, URL `https://rafhladan.is/bitstream/handle/10802/4808/UNU-GTP-2003-01-04.pdf?sequence=1`.

Sasaki, S. (1998). Characteristics of microseismic events induced during hydraulic fracturing experiments at the Hijiori hot dry rock geothermal energy site, Yamagata, Japan. *Tectonophysics* **289**, No. 1-3, 171–188, doi:10.1016/S0040-1951(97)00314-4.

Scheider, I. (2001). Cohesive model for crack propagation analyses of structures with elastic-plastic material behavior Foundations and implementation. URL

https://www.climate-service.info/imperia/md/content/gkss/institut_fuer_werkstoffforschung/wms/czm-doku.pdf.

Schijve, J. (2009). *Fatigue of structures and materials*. Dordrecht: Springer Netherlands, doi:10.1007/978-1-4020-6808-9.

Schoenball, M., Ajo-Franklin, J. B., Blankenship, D., Chai, C., Chakravarty, A., Dobson, P., Hopp, C., Kneafsey, T., Knox, H. A., Maceira, M., Robertson, M. C., Sprinkle, P., Strickland, C., Templeton, D., Schwering, P. C., Ulrich, C. & Wood, T. (2020). Creation of a mixed-mode fracture network at mesoscale through hydraulic fracturing and shear stimulation. *J Geophys Res Solid Earth* **125**, No. 12, doi:10.1029/2020JB019807.

Schrefler, B. A., Secchi, S. & Simoni, L. (2006). On adaptive refinement techniques in multi-field problems including cohesive fracture. *Comput Method Appl M* **195**, No. 4-6, 444–461, doi:10.1016/j.cma.2004.10.014.

Setiawan, F. A., Rahayuningsih, E., Petrus, H. T. B. M., Nurpratama, M. I. & Perdana, I. (2019). Kinetics of silica precipitation in geothermal brine with seeds addition: minimizing silica scaling in a cold re-injection system. *Geotherm Energy* **7**, No. 1, 22, doi:10.1186/s40517-019-0138-3.

Settgast, R. R., Fu, P., Walsh, S. D., White, J. A., Annavarapu, C. & Ryerson, F. J. (2017). A fully coupled method for massively parallel simulation of hydraulically driven fractures in 3-dimensions. *Int J Numer Anal Met* **41**, No. 5, 627–653, doi:10.1002/nag.2557.

Shapiro, S. A., Dinske, C. & Rothert, E. (2006). Hydraulic-fracturing controlled dynamics of microseismic clouds. *Geophys Res Lett* **33**, No. 14, doi:10.1029/2006GL026365.

Shirazi, S. M., Kazama, H., Kuwano, J. & Rashid, M. (2010). The influence of temperature on swelling characteristics of compacted bentonite for waste disposal. *Environ Asia* **3**, No. 1, 60–64, doi:10.14456/ea.2010.9.

Šílený, J., Hill, D. P., Eisner, L. & Cornet, F. H. (2009). Non–double-couple mechanisms of microearthquakes induced by hydraulic fracturing. *J Geophys Res Solid Earth* **114**, No. B8, doi:10.1029/2008JB005987.

Siratovich, P. A., Sass, I., Homuth, S. & Bjornsson, A. (2011). Thermal stimulation of geothermal reservoirs and laboratory investigation of thermally induced fractures. *GRC Transactions* **35**, 1529–1536, URL https://www.geothermal-library.org/index.php?mode=pubs&action=view&record=1029450.

Skog, G. (2019). *Current status and future outlook of geothermal reinjection: a review of the ongoing debate*. Bachelor's thesis, Uppsala University, Uppsala, URL urn:nbn:se:uu:diva-383963.

Song, W., Liu, X., Zheng, T. & Yang, J. (2020). A review of recharge and clogging in sandstone aquifer. *Geothermics* **87**, 101857, doi:10.1016/j.geothermics.2020.101857.

Soustelle, V., ter Heege Jan, Buijze, L. & Wassing, B. (2022). Thermomechanical parameters of geothermal analogue reservoir sandstone in the West Netherlands Basin. *Technical report*, TNO, Utrecht, URL https://www.warmingup.info/documenten/thermomechanical-parameters-of-geothermal.pdf.

Spence, D. & Sharp, P. (1985). Self-similar solutions for elastohydrodynamic cavity flow. *Proc Roy Soc London* **400**, No. 1819, 289–313, doi:10.1098/rspa.1985.0081.

Staatstoezicht op de Mijnen (2020). Toezichtsignaal integriteit afsluitende laag geothermie. URL https://www.sodm.nl/documenten/brieven/2021/01/19/toezichtsignaal-integriteit-afsluitende-laag-geothermie, accessed: 2025-03-29.

Stefansson, V.-d. u. (1997). Geothermal reinjection experience. *Geothermics* **26**, No. 1, 99–139, doi:10.1016/S0375-6505(96)00035-1.

Szpunar, T. & Budak, P. (2012). How to assess a depth of permeability impairment of the wellbore zone using drillstem-testing flow-period data. *J Can Petrol Technol* **51**, No. 03, 215–222, doi:10.2118/157852-PA.

Tanaka, R., Naoi, M., Chen, Y., Yamamoto, K., Imakita, K., Tsutsumi, N., Shimoda, A., Hiramatsu, D., Kawakata, H., Ishida, T. *et al.* (2021). Preparatory acoustic emission activity of hydraulic fracture in granite with various viscous fluids revealed by deep learning technique. *Geophys J Int* **226**, No. 1, 493–510, doi:10.1093/gji/ggab096.

Tang, X., Zhu, X., Huang, K., Wang, J., Guo, Y., Xie, B., Li, G. & Liang, H. (2021). Can ultrafiltration singly treat the iron-and manganese-containing groundwater? *J Hazard Mater* **409**, 124983, doi:10.1016/j.jhazmat.2020.124983.

Tang, Y., Yao, X., Chen, Y., Zhou, Y., Zhu, D. Z., Zhang, Y., Zhang, T. & Peng, Y. (2020). Experiment research on physical clogging mechanism in the porous media and its impact on permeability. *Granul Matter* **22**, No. 2, 37, doi:10.1007/s10035-020-1001-8.

Terzaghi, K. (1943). *Theoretical soil mechanics*. John Wiley & Sons, Inc., doi:10.1002/9780470172766, URL https://onlinelibrary.wiley.com/doi/book/10.1002/9780470172766.

Tester, J., Murphy, H., Grigsby, C., Potter, R. & Robinson, B. (1989). Fractured geothermal reservoir growth induced by heat extraction. *SPE Res Eng* **4**, No. 01, 97–104, doi:10.2118/15124-PA.

Thullner, M. (2010). Comparison of bioclogging effects in saturated porous media within one-and two-dimensional flow systems. *Ecol Eng* **36**, No. 2, 176–196, doi:10.1016/j.ecoleng.2008.12.037.

Timmer, H., Verdel, J.-D. & Jongmans, A. G. (2003). Well clogging by particles in dutch well fields. *J Am Water Works Assoc* **95**, No. 8, 112–118, doi:10.1002/j.1551-8833.2003.tb10434.x.

TNO (2024). Natural resources and geothermal energy in the Netherlands. *Technical report*, Ministry of Climate and Green Growth, The Hague, URL https://www.nlog.nl/media/3298.

TNO - GDN (2024). ThermoGIS. URL https://www.thermogis.nl/.

Tranter, M., De Lucia, M., Wolfgramm, M. & Kühn, M. (2020). Barite Scale Formation and Injectivity Loss Models for Geothermal Systems. *Water* **12**, No. 11, 3078, doi:10.3390/w12113078.

Turon, A., Costa, J., Camanho, P. & Dávila, C. (2007). Simulation of delamination in composites under high-cycle fatigue. *Compos Part A Appl Sci Manuf* **38**, No. 11, 2270–2282, doi:10.1016/j.compositesa.2006.11.009.

Tut Haklidir, F. S. & Özen Balaban, T. (2019). A review of mineral precipitation and effective scale inhibition methods at geothermal power plants in West Anatolia (Turkey). *Geothermics* **80**, 103–118, doi:10.1016/j.geothermics.2019.02.013.

Ungemach, P. (2003). Reinjection of cooled geothermal brines into sandstone reservoirs. *Geothermics* **32**, No. 4-6, 743–761, doi:10.1016/S0375-6505(03)00074-9.

Valkó, P. & Economides, M. J. (1995). *Hydraulic fracture mechanics*. Wiley.

Van Den Bogert, P. A. J. (2015). Impact of various modelling options on the onset of fault slip and the fault slip response using 2-dimensional Finite-Element modelling. *Technical Report SR.15.11455*, Shell, URL https://nam-feitenencijfers.data-app.nl/download/rapport/604ef59b-5ac5-4770-93b1-e501c87da3a9?open=true.

Van der Baan, M., Eaton, D. & Dusseault, M. (2013). Microseismic monitoring developments in hydraulic fracture stimulation. In *Effective and Sustainable Hydraulic Fracturing*, InTech, doi:10.5772/56444.

Van der Schans, M. L., Bloemendal, M., Robat, N., Oosterhof, A., Stuyfzand, P. J. & Hartog, N. (2022). Field testing of a novel drilling technique to expand well diameters at depth in unconsolidated formations. *Groundwater* **60**, No. 6, 808–819, doi:10.1111/gwat.13203.

Vardon, P. J. (2009). *A three-dimensional numerical investigation of the thermo-hydro-mechanical behaviour of a large-scale prototype repository*. Ph.D. thesis, Cardiff University, Cardiff, URL https://orca.cardiff.ac.uk/id/eprint/54832/.

Vardon, P. J., Abels, H. A., Barnhoorn, A., Daniilidis, A., Bruhn, D., Drijkoningen, G., Elliott, K., van Esser, B., Laumann, S., van Paassen, P., Vargas Meleza, L., Vondrak, A. G. & Voskov, D. (2024). A research and energy production geothermal project on the TU Delft campus: project implementation and initial data collection. In *49th Workshop on Geothermal Reservoir Engineering*, Stanford, California: Stanford University, URL https://pangea.stanford.edu/ERE/db/GeoConf/papers/SGW/2024/Vardon.pdf.

Vavryčuk, V. (2007). On the retrieval of moment tensors from borehole data. *Geophys Prospect* **55**, No. 3, 381–391, doi:10.1111/j.1365-2478.2007.00624.x.

Vavryčuk, V. (2015). Moment tensors: Decomposition and visualization. In *Encyclopedia of Earthquake Engineering*, Berlin, Heidelberg: Springer Berlin Heidelberg, pp. 1–16, doi:10.1007/978-3-642-36197-5_288-1.

Vavryčuk, V. & Kühn, D. (2012). Moment tensor inversion of waveforms: a two-step time-frequency approach. *Geophys J Int* **190**, No. 3, 1761–1776, doi:10.1111/j.1365-246X.2012.05592.x.

Veldkamp, J. G., Goldberg, T. V., Bressers, P. M. M. C. & Wilschut, F. (2016a). Corrosion in dutch geothermal systems. *Technical Report R10160*, TNO, Utrecht, URL https://www.nlog.nl/sites/default/files/2023-11/2016.03.15_tno%202015%20r10160_corrosion%20in%20dutch%20geothermal%20systems_public.pdf.

Veldkamp, J. G., Loeve, D., Peters, E., Nair, R., Pizzocolo, F. & Wilschut, F. (2016b). Thermal fracturing due to low injection temperatures in geothermal doublets. *Technical Report R11739*, TNO, Utrecht, URL https://publications.tno.nl/publication/34620511/yg2gxI/TNO-2015-R11739.pdf.

Vera Rodriguez, I., Gu, Y. J. & Sacchi, M. D. (2011). Resolution of seismic-moment tensor inversions from a single array of receivers. *Bull Seismol Soc Am* **101**, No. 6, 2634–2642, doi:10.1785/0120110016.

Vera Rodriguez, I. & Wuestefeld, A. (2020). Strain microseismics: Radiation patterns, synthetics, and moment tensor resolvability with distributed acoustic sensing in isotropic media. *Geophysics* **85**, No. 3, KS101–KS114, doi:10.1190/geo2019-0373.1.

Verdon, J. P., Horne, S. A., Clarke, A., Stork, A. L., Baird, A. F. & Kendall, J. M. (2020). Microseismic monitoring using a fiber-optic distributed acoustic sensor array. *Geophysics* **85**, No. 3, KS89–KS99, doi:10.1190/geo2019-0752.1.

Vogler, D., Amann, F., Bayer, P. & Elsworth, D. (2016). Permeability evolution in natural fractures subject to cyclic loading and gouge formation. *Rock Mech Rock Eng* **49**, 3463–3479, doi:10.1007/s00603-016-1022-0.

Voskov, D., Abels, H., Barnhoorn, A., Chen, Y., Daniilidis, A., Bruhn, D., Drijkoningen, G., Geiger, S., Laumann, S., Song, G., Vardon, P. J., Vargas Meleza, L., Verschuur, E. & Vondrak, A. (2024). A research and production geothermal project on the TU Delft campus: initial modeling and establishment of a digital twin. In *49th Workshop on Geothermal Reservoir Engineering*, California: Stanford University, URL https://pangea.stanford.edu/ERE/db/GeoConf/papers/SGW/2024/Voskov.pdf.

Voskov, D. V. (2017). Operator-based linearization approach for modeling of multiphase multi-component flow in porous media. *J Comput Phys* **337**, 275–288, doi:10.1016/j.jcp.2017.02.041.

Vrijlandt, M. A. W., Struijk, E. L. M., Brunner, L. G., Veldkamp, J. G., Witmans, N., Maljers, D. & Van Weesm, J. D. (2019). ThermoGIS update: a renewed view on geothermal potential in the Netherlands. In *European Geothermal Congress*, Den Haag, URL https://www.thermogis.nl/sites/default/files/2019-09/Vrijlandt_etal_ThermoGIS_Paper-EGC-2019.pdf.

Wang, H. F., Bonner, B. P., Carlson, S. R., Kowallis, B. J. & Heard, H. C. (1989). Thermal stress cracking in granite. *J Geophys Res: Solid Earth* **94**, No. B2, 1745–1758, doi:10.1029/JB094iB02p01745.

Wang, X., Wang, J., Yan, G., Liu, X., Huang, Y., Tian, S. & Xu, Q. (2023). Study on prevention and control measures of sandstone geothermal reinjection plugging. *Water Sci Technol* **87**, No. 6, 1571–1581, doi:10.2166/wst.2023.078.

Wang, Z., Du, X., Yang, Y. & Ye, X. (2012). Surface clogging process modeling of suspended solids during urban stormwater aquifer recharge. *J Environ Sci* **24**, No. 8, 1418–1424, doi:10.1016/S1001-0742(11)60961-3.

Warpinski, N. (2009). Microseismic monitoring: Inside and out. *J Pet Technol* **61**, No. 11, 80–85, doi:10.2118/118537-JPT.

Warpinski, N. R., Wright, T. B., Uhl, J. E., Engler, B. P., Drozda, P. M., Peterson, R. E. & Branagan, P. T. (1999). Microseismic monitoring of the B-sand hydraulic-fracture experiment at the DOE/GRI multisite project. *SPE Journal* **4**, No. 03, 242–250, doi:10.2118/57593-PA.

Water Research Institute (KWR) (2015). Report assessment of injectivity problems in geothermal greenhouse heating wells. *Technical report*, Water Research Institute (KWR), URL https://www.kasalsenergiebron.nl/content/research/14898_Injectiviteitsproblemen_bij_geothermische_bronnen_in_Nederland.pdf.

Webster, P., Wall, J., Perkins, C. & Molenaar, M. (2013). Micro-seismic detection using distributed acoustic sensing. In *Society of Exploration Geophysicists International Exposition and 83rd Annual Meeting, SEG 2013: Expanding Geophysical Frontiers*, Society of Exploration Geophysicists, pp. 2459–2463, doi:10.1190/segam2013-0182.1.

Wei, C., Li, S., Yu, L., Zhang, B., Liu, R., Pan, D. & Zhang, F. (2023). Study on mchanism of strength deterioration of rock-like specimen and fracture damage deterioration model under pulse hydraulic fracturing. *Rock Mech Rock Eng* **56**, No. 7, 4959–4973, doi:10.1007/s00603-023-03313-3.

Wu, J.-Y., Nguyen, V. P., Nguyen, C. T., Sutula, D., Sinaie, S. & Bordas, S. P. (2020). Phase-field modeling of fracture. *Adv Appl Mech* **53**, 1–183, doi:10.1016/bs.aams.2019.08.001.

Wu, S., Wang, Y. & Liang, X. (2023). Hydraulic fracturing distributed acoustic sensing monitoring data source mechanism inversion: A Hessian-based method. *Geophysics* **88**, No. 6, WC133–WC143, doi:10.1190/geo2023-0073.1.

Wu, Y., Zhao, X., Zinno, R., Wu, H., Vaidya, V., Yang, M. & Qin, J. (2016). The application of microseismic monitoring in unconventional reservoirs. In *Unconventional Oil and Gas Resources Handbook*, Elsevier, pp. 243–287, doi:10.1016/B978-0-12-802238-2.00009-2.

www.nlog.nl (2025). Geotherm energy. URL https://www.nlog.nl/en/geothermal-energy, accessed: 2025-03-29.

Xi, X., Yang, S., McDermott, C. I., Shipton, Z. K., Fraser-Harris, A. & Edlmann, K. (2021). Modelling rock fracture induced by hydraulic pulses. *Rock Mech Rock Eng* **54**, No. 8, 3977–3994, doi:10.1007/s00603-021-02477-0.

Xiao, J.-Q., Ding, D.-X., Jiang, F.-L. & Xu, G. (2010). Fatigue damage variable and evolution of rock subjected to cyclic loading. *Int J Rock Mech Min Sci* **47**, No. 3, 461–468, doi:10.1016/j.ijrmms.2009.11.003.

Yanaze, T., Yoo, S., Marumo, K. & Ueda, A. (2019). Prediction of permeability reduction due to silica scale deposition with a geochemical clogging model at sumikawa geothermal power plant. *Geothermics* **79**, 114–128, doi:10.1016/j.geothermics.2019.01.002.

Yasuhara, H., Kinoshita, N., Ohfuji, H., Lee, D. S., Nakashima, S. & Kishida, K. (2011). Temporal alteration of fracture permeability in granite under hydrothermal conditions and its interpretation by coupled chemo-mechanical model. *Appl Geochem* **26**, No. 12, 2074–2088, doi:10.1016/j.apgeochem.2011.07.005.

Ye, Z. & Ghassemi, A. (2018). Injection-induced shear slip and permeability enhancement in granite fractures. *J Geophys Res: Solid Earth* **123**, No. 10, 9009–9032, doi:10.1029/2018JB016045.

Yeltekin, K. & Parlaktuna, M. (2006). Interpretation of reinjection tests in Kizildere geothermal field, Turkey. In *31st Workshop on Geothermal Reservoir Engineering*, SGP-TR-179, Stanford, California: Stanford University, URL https://pangea.stanford.edu/ERE/pdf/IGAstandard/SGW/2006/yeltekn1.pdf.

Yoshitaka, N., Makoto, N. *et al.* (2021). Clogging mechanisms and preventive measures in artificial recharge systems. *J Groundw Sci Eng* **9**, No. 3, 181–201, doi:10.19637/j.cnki.2305-7068.2021.03.002.

Yu, M., Hussain, F., Arns, J.-Y., Bedrikovetsky, P., Genolet, L., Behr, A., Kowollik, P. & Arns, C. (2018). Imaging analysis of fines migration during water flow with salinity alteration. *Adv Water Resour* **121**, 150–161, doi:10.1016/j.advwatres.2018.08.006.

Yuan, B. & Wood, D. A. (2018). A comprehensive review of formation damage during enhanced oil recovery. *J Petrol Sci Eng* **167**, 287–299, doi:10.1016/j.petrol.2018.04.018.

Zang, A., Hofmann, H., Ji, Y., Zhuang, L., Lu, G. & Bunger, A. (2025). How rock hydraulic fatigue methods from mining and petroleum industry assist in unlocking deep heat for a clean energy future. *Renew. Sustain. Energy Rev.* **217**, 115683, doi:https://doi.org/10.1016/j.rser.2025.115683.

Zang, A., Zimmermann, G., Hofmann, H., Niemz, P., Kim, K. Y., Diaz, M., Zhuang, L. & Yoon, J. S. (2021). Relaxation damage control via fatigue-hydraulic fracturing in granitic rock as inferred from laboratory-, mine-, and field-scale experiments. *Sci Rep* **11**, No. 1, 6780, doi:10.1038/s41598-021-86094-5.

Zhang, W., Guo, T. K., Qu, Z. Q. & Wang, Z. Y. (2019). Research of fracture initiation and propagation in HDR fracturing under thermal stress from meso-damage perspective. *Energy* **178**, 508–521, doi:10.1016/j.energy.2019.04.131.

Zhou, X., Aydin, A., Liu, F. & Pollard, D. D. (2010). Numerical modeling of secondary thermal fractures in hot dry geothermal reservoirs. In *35th Work-shop on Geothermal Reservoir Engineering*, SGP-TR-188, Stanford, California: Stanford University, URL https://earthsciences.stanford.edu/ERE/pdf/IGAstandard/SGW/2010/zhou.pdf.

Zhu, D., Jing, H., Yin, Q., Ding, S. & Zhang, J. (2020). Mechanical characteristics of granite after heating and water-cooling cycles. *Rock Mech Rock Eng* **53**, 2015–2025, doi:https://doi.org/10.1007/s00603-019-01991-6.

Zhuang, L., Kim, K. Y., Jung, S. G., Diaz, M. & Min, K.-B. (2019a). Effect of water infiltration, injection rate and anisotropy on hydraulic fracturing behavior of granite. *Rock Mech Rock Eng* **52**, No. 2, 575–589, doi:10.1007/s00603-018-1431-3.

Zhuang, L., Kim, K. Y., Jung, S. G., Diaz, M., Min, K. B., Zang, A., Stephansson, O., Zimmermann, G., Yoon, J. S. & Hofmann, H. (2019b). Cyclic hydraulic fracturing of pocheon granite cores and its impact on breakdown pressure, acoustic emission amplitudes and injectivity. *Int J Rock Mech Min Sci* **122**, 104065, doi:10.1016/j.ijrmms.2019.104065.

Zimmerman, R. W. (2000). Coupling in poroelasticity and thermoelasticity. *Int J Rock Mech Min Sci* **37**, No. 1-2, 79–87, doi:10.1016/S1365-1609(99)00094-5.

Zimmerman, R. W. & Yeo, I.-W. (2000). Fluid flow in rock fractures: From the Navier-Stokes equations to the cubic law. In *Dynamics of Fluids in Fractured Rock*, vol. 122, Wiley, pp. 213–224, doi:10.1029/GM122p0213.

Zyvoloski, G. (2007). FEHM: A control volume finite element code for simulating subsurface multi-phase multi-fluid heat and mass transfer. *Technical Report LAUR-07-3359*, Los Alamos National Laboratory, Los Alamos, New Mexico, URL https://www.lanl.gov/orgs/ees/fehm/pdfs/FEHM_LAUR-07-3359.pdf.

ACKNOWLEDGEMENTS

Finally, I am here on the last page of my Ph.D thesis, which cannot be achieved without contribution and support from countless individuals.

I would like to begin by expressing my deepest gratitude to Prof. Dr. Phil Vardon, my primary promotor. Without his guidance and support, I would not have been able to successfully complete this Ph.D journey. What can I say? He is simply the best promotor I could have ever wished for. His profound expertise in soil and rock mechanics, numerical methods, and both experimental and field insights has been invaluable. His critical thinking and scientific perspectives have continually guided and inspired me. Furthermore, his sense of humour has always added a lot of joys to our drinks and weekly meetings in the past four years. I am truly grateful for his unwavering support — he never says no to me, like he never says no to an extra beer.

I would also like to express my heartfelt gratitude to my co-promotor, Associate Prof. Dr. Anne-Catherine Dieudonné for her unwavering support and guidance, not only in science, but also in life. From the very beginning of this Ph.D journey, she has played a crucial role in my daily supervision. Her expertise in the LAGAMINE code and geomechanical modelling, combined with her patience and insightful guidance, have been instrumental in the successful completion of this thesis. Her meticulous feedback on my manuscripts has significantly enhanced their quality, for which I am deeply grateful. I am also grateful for the BBQs and various other group activities she organised each summer and winter. Her efforts in creating such a supportive and enjoyable environment made my Ph.D. journey all the more memorable.

My sincere gratitude also goes to my promotor, Associate Prof. Guy Drijkoningen, for his unwavering support and guidance in micro-seismic monitoring using distributed acoustic sensing. His expertise in geophysics has been instrumental in helping me develop new research skills and fostering my interest in the field of micro-seismic monitoring. I am especially thankful for his patience, as I had little background in micro-seismic monitoring when I started. Without his step-by-step guidance and support, completing Chapter 6 of this thesis would not have been possible.

I am deeply grateful to Prof. Dr. Florian Amann, my promotor from RWTH Aachen, for his warm welcome and unwavering support during my research and secondment. I sincerely appreciate his generosity in hosting me at RWTH Aachen for nine months and his encouraging feedback on my works, which has always been a great source of motivation. I would also like to thank Dr. Joaquin Liadut, whose unwavering support was indispensable for the completion of the geo-mechanical modelling work in this thesis. His expertise in the LAGAMINE code and numerical methods has been invaluable, making a significant contribution to this research. In addition, the support and help from Robert Herrmann, the author of the code Computer Programs in Seismology, are also gratefully acknowledged. I would also like to thank Barbara Cox and other people in Aardyn for hosting me six months in the company.

Special thanks to Prof. Dr. David Bruhn, and Prof. Dr. Florian Wellmann, Prof. Dr. Florian Wagner, Prof. Dr. Raul Fuentes, and Prof. Dr. Michael Hicks (as reserve member) for serving as committee members for my Ph.D. defence. In addition, special thanks to Dr. Maren Brehme, Dr. Paromita Deb, Prof. Dr. Paolo Silva and many others for their outstanding management of our EASYGO project, I would also like to take this chance to thank all the EASYGOers, including Anna, David, Mahmoud, Lorenzo, Hagen, Nicolás, Selvican, Josselin, Ryan, Andrea, Esteban, Tristan (Merbecks). I am especially grateful to Josselin (and Christina) for their generosity in hosting me for several weeks (well, two months) during a challenging period. I would also like to extend my special thanks to Hagen, whose warm support during that time was equally appreciated.

Furthermore, I would like to express my gratitude to my colleagues and friends in Delft, including — but not limited to — Tristan, Valentina, Nathali, Cristhian, Susan, Bihni, Joss, Inge, Kevin, Yasmin, Aoxi, Liang, Zhaojiang, Xiangcou, Andrea, Laura, Zheng, Yuen, and David (Leibold), Tessel, Thijs, Parvin, Stijn, Entela, Eli and many others. The time we spent together, along with the drinks and parties, will be cherished as lifelong memories. Special thanks go to Tristan (who also contributed to revising the Dutch abstract), Valentina, Nathali, Cristhian, Susan, Bihni, Aoxi, Liang and Zhaojiang for their kind helps and supports in my life and research. In addition, I would also like to thank my colleagues and friends in Aachen, including Deyan, Zhengyang, Menghao, Chengyi, Dima, and Kavan. The drinks, hotpots and running provided a much-needed way to relax and relieve stress.

This research is supported by the European Union's Horizon 2020 research and innovation programme under the Marie Skłodowska-Curie grant agreement No. 956965, for which I am deeply grateful. This generous funding has made it possible for me to conduct this research and participate in conferences and training weeks around the world.

Finally, I would like to express my heartfelt gratitude to my family, especially my parents. Without their sacrifice and unwavering support, I would not have reached this milestone as a Ph.D. I would also like to thank my extended family, including my grandparents, my aunts and uncles, my cousins, and my nephew and nieces, who have brought me so much happiness and joy. In addition, I would also like to appreciate Yawen's love and unwavering support. During my Ph.D, I spent quite some time in China with my families, because of whom the journeys were always fun and enjoyable, and because of whom the Ph.D journey was more enjoyable.

CURRICULUM VITÆ

Wen LUO

13–05–1995 Born in Chengdu, Sichuan, China.

EDUCATION

2021–2025 Joint Ph.D in Geo-Engineering at
Delft University of Technology, the Netherlands & RWTH Aachen, Germany
Promotor: Prof. dr. P. J. Vardon
Promotor: Prof. dr. rer. nat. F. Amann
Promotor: Dr. ir. G. G. Drijkoningen
Co-promotor: Dr. ir. A. C. Dieudonné

2017–2020 MSc, Oil and Gas Well Engineering
Southwest Petroleum University, Chengdu, China

2013–2017 BSc, Petroleum and Natural Gas Engineering
Southwest Petroleum University, Chengdu, China

WORK

08.2025–12.2025 Postdoc Researcher
Section of Applied Geophysics, TU Delft, the Netherlands

11.2023–02.2024 Intern
Aardyn, Dordrecht, the Netherlands

11.2021–02.2022 Intern
Aardyn, Dordrecht, the Netherlands

09.2020–01.2021 Assistant Fracturing Engineer
Xinjiang Oilfield Company (PetroChina), Xinjiang, China

List of Publications

Journal Publications

- **Luo, W.**, Dieudonné, A. C., Ouf, J., Amann, F., Vardon, P. J. (2025). Numerical study of the cyclic thermal stimulation scenarios. *Under review*

- **Luo, W.**, Dieudonné, A. C., Ouf, J., Amann, F., Vardon, P. J. (2025). A numerical tool to simulate fatigue damage under cyclic coupled thermo-hydro-mechanical processes. *Under review*

- **Luo, W.**, Drinjkoningen, G.G., Eltayieb, M., Amann, F., Vardon, P. J. (2025). Feasibility study of single-well dual-cable DAS for micro-seismic monitoring of geothermal operations. *Rock Mechanics and Rock Engineering*. DOI: https://doi.org/10.1007/s00603-025-04942-6

- **Luo, W.**, Liaudat, J., Ouf, J., Dieudonné, A. C., Amann, F., Vardon, P. J. (2025). Numerical modelling of fracturing processes during cold water injection into geothermal reservoirs: Verification and qualitative validation. *Computers and Geotechnics* 183: 107186. DOI: 10.1016/j.compgeo.2025.107186

- **Luo, W.**, Kottsova, A., Vardon, P. J., Dieudonné, A. C., Brehme, M. (2023). Mechanisms causing injectivity decline and enhancement in geothermal projects. *Renewable and Sustainable Energy Reviews* 185: 113623. DOI: 10.1016/j.rser.2023.113623

- Ouf, J., Vardon, P. J., Khaledi, K., **Luo, W.**, Jalali, M., Amann, F. (2025). Numerical analysis of far-field fault reactivation induced by reservoir cooling. *Geothermics*, 127(2): 103234. DOI: 10.1016/j.geothermics.2024.103234

- Ouf, J., Khaledi, K., Vardon, P. J., **Luo, W.**, Jalali, M., Amann, F. (2024). Numerical modeling of hydro-mechanical processes during hydraulic testing of pre-existing fractures at the Grimsel Test Site, Switzerland. *Geomechanics for Energy and the Environment* 40(1): 100608. DOI: 10.1016/j.gete.2024.100608

- Ouf, J., Osten, J., **Luo, W.**, Khaledi, K., Jalali, M., Vardon, P. J., Amann, F. (2024). Experimental and numerical analysis of injection-induced permeability changes in pre-existing fractures. *Geomechanics for Energy and the Environment* 39(B4):100576. 10.1016/j.gete.2024.100576

Conference and Workshop

- **Luo, W.**, Liaudat, J., Ouf, J., Dieudonné, A. C., Amann, F., Vardon, P. J. (2024). Thermo-hydro-mechanical coupled zero-thickness interface elements: benchmarking examples. *InterPore Annual Meeting 2024*; Qingdao, China. Oral Presentation.

- **Luo, W.**, Ouf, J., Vardon, P. J., Dieudonné, A. C., Liaudat, J., Khaledi, K., Jalali, M., Amann, F. (2023). Comparison of two approaches for modelling fracture opening due to cold water injection in geothermal reservoir. *Symposium on Energy Geotechnics 2023*; Delft, the Netherlands. Oral Presentation.

- **Luo, W.**, Drijkonigen, G., Amann, F., Vardon, P. J. (2023). How to better locate micro-seismic event using distributed acoustic sensing with fish-hook shaped layout. *14th European Geothermal Ph.D Days*; Glasgow, UK. Poster.
- **Luo, W.**, Cox, B., Dieudonné, A. C., Vardon, P. J. (2022). Numerical Study of Fluid Loss into a Thief Zone overlying a Geothermal Reservoir. *European Geothermal Congress 2022*; Berlin, Germany. Oral Presentation.

Other Academic Aactivities

- Organising Committee Member, *13rd European Geothermal Ph.D Days*; Aachen, Germany.
- Organising Committee Member, *15th European Geothermal Ph.D Days*; Delft, the Netherlands.
- Fellowship applications (all failed): Stanford Energy Postdoc Fellowship 2024, Newton Fellowship 2025, Forrest Fellowship 2025, Rubicon Fellowship 2025 Round 2.